UNIVERSITY OF CALIFORNIA SAN DIEGO

Seismic Performance Evaluation of Reinforced Masonry Wall Systems with Frame Modeling

A dissertation submitted in partial satisfaction of the requirements for the degree

Doctor of Philosophy

in

Structural Engineering

by

Jianyu Cheng

Committee in charge:

Professor P. Benson Shing, Chair

Professor Joel P. Conte

Professor Michael J. Holst

Professor Francesco Lanza di Scalea

Professor Chia-Ming Uang

2021

The Dissertation of Jianyu Cheng is approved, and it is acceptable in quality and form for publication on microfilm and electronically.

University of California San Diego

2021

DEDICATION

To my parents

TABLE OF CONTENTS

LIST OF NOTATIONS

CHAPTERS 3 AND 4

a	dimensionless parameter
A_n	net cross-sectional area of a wall
$A_{s,f}$	total area of steel within effective flange width
$A_{s,w}$	total area of steel in wall web
A_v	effective shear area
c	distance of the neutral axis of bending from extreme compression fiber of a section
Dmg1	ductility-proportional in-cycle damage factor
Dmg2	energy-proportional in-cycle damage factor
E_m	modulus of elasticity of masonry
f'_m	masonry compressive strength
f_y	yield strength of vertical reinforcing bar
G_m	masonry shear modulus
h	height of a wall
h_{eff}	effective height of the wall
I	moment of inertia of an uncracked wall section

k	effective initial stiffness
k_v	stiffness of shear spring
l_b	center-to-center spacing of vertical bars
l_e	center-to-center distance between two extreme bars in a section
l_f	width of wall flange
l_f'	effective width of flange
l_w	length of wall section
L_p	effective plastic-hinge length
M	moment resistance of a wall section
M'	dimensionless moment resistance of a section
M_{max}	maximum moment resistance developed by a wall section
M'_{max}	dimensionless maximum moment resistance of a section
pinchX	pinching factor 1 in hysteresis model
pinchY	pinching factor 2 in hysteresis model
P	axial force on a wall
Q_{max}	expected maximum lateral load resistance
Q_r	residual lateral load resistance
t	wall thickness

t_w width of wall web

V_{nm} contribution of masonry to the shear strength of an RM wall

V_{ns} contribution of horizontal reinforcement to the shear strength of an RM wall

α vertical reinforcement index

β axial load ratio

Δ_m lateral displacement at which maximum resistance develops

Δ_{75} lateral displacement at which post-peak resistance drops to 75% of maximum resistance

Δ_c capping lateral displacement

ε normal strain

ε_0 strain at which the tensile strength of reinforcing bar drops to zero after fracture

ε_{10} compressive strain at which residual strength is reached after bar buckling

ε_b strain at which buckling of vertical reinforcing bar occurs

ε_p masonry compressive strain at which peak stress is reached

ε_{ps} strain at which the peak tensile strength of reinforcing bar is reached

ε_r masonry compressive strain at which residual strength is first reached

ζ_f flexural stiffness reduction factor

ζ_v shear stiffness reduction factor (before peak wall lateral resistance is reached)

ζ_{v0} shear stiffness reduction factor (after peak wall lateral resistance is reached)

η ratio of total reinforcing bar area in wall web to that in wall flange

ξ reduction factor to unloading stiffness

ρ_v vertical reinforcement ratio

$\rho_{v,web}$ web steel ratio

σ_m normal stress in masonry

σ'_m normalized stress of masonry

σ_s normal stress in steel reinforcement

σ'_s normalized stress of vertical steel reinforcement

ϕ wall curvature

ϕ_m sectional curvature at which maximum moment resistance develops

ϕ_{75} sectional curvature at which moment resistance drops to 75% of maximum moment resistance

ϕ_c sectional curvature at which moment resistance drops to 50% of maximum moment resistance

CHAPTER 6

A_{sf} total area of vertical reinforcing bars in flange

A_w net cross sectional area of web

b	width of compressive stress block
C_1	constant to define web strength reduction factor
C_2	constant to define web strength reduction factor
C_3	constant to define web strength reduction factor
dmg1	in-cycle damage parameter
dmg2	in-cycle damage parameter
dmg3	in-cycle damage parameter
dmg4	in-cycle damage parameter
D_0	accumulative in-cycle damage factor
E_A	normalization term for energy dissipation
E_D	total energy dissipated
E_{i-1}	energy dissipated in last cycle
f'_m	compressive strength of masonry
f_y	yield strength of vertical reinforcing bars in flange
G_m	masonry shear modulus
H_{eff}	effective wall height
k_1	initial stiffness of shear force-vs.-shear strain envelope curve
k_{un}	unloading stiffness

$\boldsymbol{K}_{ii}^{e}$ sectional stiffness matrix at integration pint *i*

$K_{shear,y}$ shear stiffness in local *x*-*y* plane

$K_{shear,z}$ shear stiffness in local *x*-*z* plane

$\tilde{\boldsymbol{K}}_{\boldsymbol{a}}$ condensed stiffness matrix

$\tilde{\boldsymbol{K}}^{\boldsymbol{e}}$ condensed stiffness matrix

l_f flange width

L element length

L/H depth-to-height ratio of web

M_f moment capacity of flange section

M_y moment about local *y* axis

M_z moment about local *z* axis

$\bar{M}_y$ moment about local *y* axis given by constitutive law

$\bar{M}_z$ moment about local *z* axis given by constitutive law

M_{y1} nodal moment about local *y* axis

M_{y2} nodal moment about local *y* axis

M_{z1} nodal moment about local *z* axis

M_{z2} nodal moment about local *z* axis

$\hat{M}_{y1}$ applied nodal moment about local *y* axis

$\hat{M}_{y2}$ applied nodal moment about local *y* axis

$\hat{M}_{z1}$ applied nodal moment about local *z* axis

$\hat{M}_{z2}$ applied nodal moment about local *z* axis

n_s number of integration points

N axial force

$\bar{N}$ axial force given by constitutive law

$\hat{N}$ applied axial force

N_0 nodal axial force

P_w fiber axial stress resultant of wall web

P_f fiber axial stress resultant of wall flange

$\boldsymbol{R}_u$ residual sub-vector

$\boldsymbol{R}_\sigma$ residual sub-vector

$\boldsymbol{R}_\varepsilon$ residual sub-vector

$\tilde{\boldsymbol{R}}_a$ condensed residual vector

$\tilde{\boldsymbol{R}}_{\sigma}$ condensed residual vector

t_f flange thickness

T torque

$\bar{T}$ torque given by constitutive law

$\hat{T}$ applied torque

T_0 nodal torque

$\hat{u}_x$ displcement in local x direction

$\hat{u}_y$ displcement in local y direction

$\hat{u}_z$ displcement in local z direction

$\hat{u}_{x0}$ nodal axial displacement

$\boldsymbol{u}$ displacement vector in local coordinate system

V_y shear force in local y direction

V_z shear force in local z direction

$\bar{V}_y$ shear force in local y direction given by constitutive law

$\bar{V}_z$ shear force in local z direction given by constitutive law

V_{cr} shear force at which major diagonal cracks initiate

V_0 shear strength of a wall subjected to zero axial load

V_p peak shear resistance

V_{res} residual shear strength on envelope

V_w shear resistance provided by web

V_f shear resistance provided by flange

W_0 weight associated with shear strains

W_l weight of the l^{th} integration point

χ_l coordinate of the l^{th} integration point

α web strength reduction factor

α_{res} residual web strength reduction factor

β_w axial load ratio of web

γ_{xy} shear strain in local *x*-*y* plane

γ_{xz} shear strain in local *x*-*z* plane

γ_{y0} approximated constant shear strain in local *x*-*y* plane

γ_{z0} approximated constant shear strain in local *x*-*z* plane

γ_p shear strain at which peak shear resistance is reached

γ_{res} shear strain at which residual shear strength is reached

γ_{max} maximum shear strain reached during analysis

$\Delta\gamma$ shift of target shear strain

$\boldsymbol{\varepsilon}$ element strain vector

ε axial strain

ε_l axial strain at the l^{th} integration point

$\hat{\theta}_x$ rotation (torsion) about local *x* axis

$\hat{\theta}_y$ rotation about local *y* axis

$\hat{\theta}_z$ rotation about local *z* axis

$\hat{\theta}_{x0}$ nodal torsional rotation

$\hat{\theta}_{y1}$ nodal rotation about local *y* axis

$\hat{\theta}_{y2}$ nodal rotation about local *y* axis

$\hat{\theta}_{z1}$ nodal rotation about local *z* axis

$\hat{\theta}_{z2}$ nodal rotation about local *z* axis

κ_y curvature about local *y* axis

κ_z curvature about local *z* axis

κ_{yl} curvature about local *y* axis at the l^{th} integration point

κ_{zl} curvature about local *z* axis at the l^{th} integration point

Π_{bc} work done by applied nodal forces

σ force vector in local coordinate system

$\bar{\sigma}$ internal force vector given by constitutive laws

ϕ torsional strain

ϕ_l torsional strain at the l^{th} integration point

LIST OF FIGURES

LIST OF TABLES

ACKNOWLEDGEMENTS

The research presented in this dissertation was conducted under the supervision of Professor P. Benson Shing at University of California San Diego (UC San Diego). The work conducted on the numerical modeling of flexure-dominated reinforced masonry shear walls was carried out as part of the ATC 114 project of the Applied Technical Council, which was supported by National Institute of Standards and Technology (NIST). The rest of the work presented in this dissertation was supported with funding from the National Science Foundation (NSF) under Award No. CMMI-1728685. The support of the NHERI program of the NSF for the shake-table tests conducted at UC San Diego is also gratefully acknowledged. I would also like to acknowledge a Graduate Fellowship from UC San Diego, which supported my first-year graduate study.

I would like to thank the members of my committee, Professors Joel P. Conte, Chia-Ming Uang, Francesco Lanza di Scalea, and Michael J. Holst for their suggestions to my research, feedback on my dissertation, and offering the courses which were invaluable for my research.

I would like to express my deepest gratitude to my advisor, Professor P. Benson Shing, for his guidance, patience, and understanding through all these years. I have benefited greatly from his knowledge in structural engineering and advice on my research. I would like to thank him for giving me the opportunity to work with an individual with expertise, righteousness, and integrity.

I would like to express my sincere gratitude to Dr. Andreas A. Koutras for his suggestions on my research. We had excellent collaboration over various projects during my study in UC San Diego.

I would like to thank the technical staff members of the Englekirk Structural Engineering Center and the Powell Structural Laboratories of UC San Diego for their professionalism and help in conducting the shake-table tests presented in this dissertation.

I would like to acknowledge RCP Block and Brick for their generous donation of concrete masonry units. The generous support of Concrete Masonry Association of California and Nevada, Masonry Institute of America, and Northwest Concrete Masonry Association are also gratefully acknowledged.

I would like to thank Jeffrey Lee and Joyner Deamer, undergraduate students supported by the NSF REU program, and Richard Šusták, a visiting Master student at UC San Diego, for their assistance in the preparation of the shake-table tests.

Finally, I would like to thank my parents, Qinxian Cheng and Amei Shan, for their relentless love and support through these years. It is to them I dedicate this dissertation. I would also like to thank Ms. Yidi Fang, for her encouragement and support.

Chapters 3 and 4, in part, are a reprint of the material in a manuscript titled "Practical Nonlinear Analysis Methods for Flexure-Dominated Reinforced Masonry Shear Walls" that has been submitted to *ASCE Journal of Structural Engineering* in 2021 (under review). The authors of the manuscript are: the author of the dissertation and P. Benson Shing. The author of the dissertation is the primary author and the main contributor of the work presented in the manuscript.

Chapter 5, in part, is a reprint of the material in a research paper titled “Evaluation of Collapse Resistance of Reinforced Masonry Wall Systems by Shake-Table Tests” that appears in the journal of *Earthquake Engineering and Structural Dynamics* in 2020. The authors of the research paper are: the author of the dissertation, Andreas A. Koutras, and P. Benson Shing. The author of the dissertation is the primary author and the main contributor of the work presented in the paper.

Chapter 6, in part, is a reprint of the material currently being prepared for submission for publication, Cheng, J. and Shing P. B. under the title “A Beam-Column Model for Nonlinear Flexural and Shear Behavior of Reinforced Masonry Walls”. The author of the dissertation is the primary author and the main contributor of the work presented in the paper.

VITA

2010-2014 B. S. in Civil Engineering, Tongji University

2014-2016 M. S. in Structural Engineering, University of California San Diego

2016-2021 Ph. D. in Structural Engineering, University of California San Diego

ABSTRACT OF THE DISSERTATION

Seismic Performance Evaluation of Reinforced Masonry Wall Systems with Frame Modeling

by

Jianyu Cheng

Doctor of Philosophy in Structural Engineering

University of California San Diego, 2021

Professor P. Benson Shing, Chair

This study is aimed to acquire a better understanding of the seismic behavior of reinforced masonry (RM) structures at a system level, and to develop frame models for simulating the nonlinear flexural and shear behaviors of these wall systems. To capture the

nonlinear, in-plane, cyclic behavior of flexure-dominated RM walls, a rational modeling method along with suitable material models, using a fiber-section beam-column element idealization is presented. The modeling method accounts for the buckling and low-cycle fatigue of vertical reinforcing bars as well as plastic strain localization, which may develop in RM walls under severe seismic actions. The model has been validated by experimental data on fully grouted planar walls and T-walls. In addition, a rational and simple method to construct lateral force-vs.-lateral displacement backbone curves is also presented. The proposed method produces backbone curves that show a good agreement with experimental data from the quasi-static, cyclic, loading tests of walls with rectangular and T sections.

There had been a lack of experimental data showing the ultimate displacement capacity of shear-dominated RM wall systems. To fill this data gap, a shake-table test program was carried out to investigate the displacement capacity of shear-dominated RM wall systems, and the influence of wall flanges and planar walls perpendicular to the direction of shaking (out-of-plane walls) on the seismic performance of a wall system. Two full-scale, single-story, fully grouted, RM wall specimens were tested to the verge of collapse. Each specimen had two T-walls as the seismic force resisting elements and a stiff roof diaphragm. The second specimen had six additional planar walls perpendicular to the direction of shaking. The two specimens reached maximum roof drift ratios of 17% and 13%, respectively, without collapsing. The high displacement capacities can be largely attributed to the presence of wall flanges and, for the second specimen, also the out-of-plane walls, which provided an alternative load path to carry the gravity load when the webs of the T-walls had been severely damaged.

A computationally efficient beam-column model is proposed to simulate the

nonlinear flexural and shear behaviors of reinforced masonry shear walls for time-history analysis. A three-field mixed formulation based on the Hu-Washizu variational principle is adopted. This mixed element is free of shear locking, and allows a wall to be modeled with one element. To capture the nonlinear behavior of a reinforced masonry wall, the axial and flexural responses are evaluated at each integration point along the element with a fiber-section model, while the shear response in each loading direction is represented by a macro material model. The model accounts for the influence of the axial load, wall aspect ratio, and the flange on the shear response of a wall. To consider axial-flexure-shear interaction, the shear model accounts for the axial stress resultant from the fiber-section model, and the compressive strength of masonry in the fiber-section model decreases when severe shear damage developed. The model has been calibrated and validated with extensive test data. It has been demonstrated that the model is able to reproduce the experimental results from quasi-static cyclic loading tests of single walls as well as shake-table tests of wall systems with good accuracy.

CHAPTER 1 INTRODUCTION

1.1. Background

Masonry structures are widely used in north America and other countries of the world due to its beneficial features, such as cost-effectiveness, durability, and fire resistance. Traditional plain masonry structures with concrete or clay masonry units can develop brittle failures during an earthquake event, and therefore are not allowed to be used in high seismic areas, such as California. In North America, reinforced masonry (RM) is typically constructed of hollow concrete masonry units (CMU) with horizontal and vertical steel bars placed inside the units. The units may be fully or partially grouted. RM shear walls are the main seismic force resisting elements in RM structures. They can develop flexural and shear deformation mechanisms. These shear walls can have different cross-sectional shapes, such as rectangular sections, T-sections, L-sections, etc. In an RM structure, walls are normally oriented in two orthogonal directions to resist the seismic forces in the respective directions.

Modern RM structures may have all or part of the interior cells filled with grout. RM walls with all the interior cells filled with grout are referred as fully grouted. In many parts of the United States, it is more common to only place grout in cells containing vertical or horizontal reinforcing bars. This type of RM walls is called partially grouted.

Past experimental studies (Shing et al., 1991) show that the ultimate lateral strength and strength deterioration of an RM shear wall can be governed by flexure, diagonal shear, and/or shear sliding, depending on its shear-span ratio, the applied axial load, and the reinforcement contents. Slender walls with high shear-span ratios tend to develop flexure-

dominated failure, whereas walls with low shear-span ratios and insufficient amount of shear reinforcement are most likely to exhibit shear-dominated behavior, or shear slding.

A flexure-dominated mechanism may include flexural cracking, the yielding, buckling, and fracture of the vertical reinforcement, masonry crushing at wall toes, and the failure of lap splices if any. Figures 1-1 and 1-2 show a flexure-dominated cantilever wall tested by Sherman (2011), together with its in-plane lateral force-vs.-displacement hysteresis curves. As shown, in the crushed toe regions, the exposed extreme vertical reinforcing bars were vulnerable to buckling due to severe spalling of the surrounding masonry. After a buckled bar has been subjected to a few cycles of straightening and bending as the wall has been pushed back and forth with cyclic load reversals, bar fracture may soon follow. This will lead to severe strength degradation in the wall. As can be seen from the hysteresis curves in Figure 1-2, walls dominated by flexure can exhibit a relatively ductile behavior. In general, a wall with a higher axial compressive load and/or a higher amount of vertical reinforcement will have less ductile flexural behavior. In reinforced concrete (RC) walls, it has been a common practice to have confined boundary elements to prevent the walls from severe toe crushing. However, because of the spatial constraints of masonry units for steel confinement, boundary elements are rarely used in RM walls. In recent years, experimental studies have been carried out to examine the effectiveness of different boundary element options in improving the displacement capacity of flexure-dominated RM walls (Cyrier, 2012; Shedid and El-Dakhakhni, 2013; Banting and El-Dakhakhni, 2012, 2014).

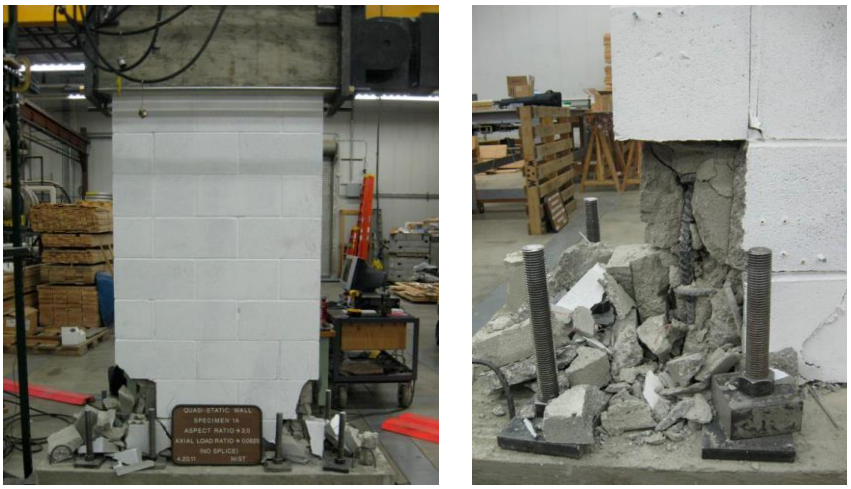

(a) overall damage on the wall (b) crushing and bar buckling at the toe

Figure 1-1. Damage in a flexure-dominated wall (WSU-W-1A tested by Sherman, 2011)

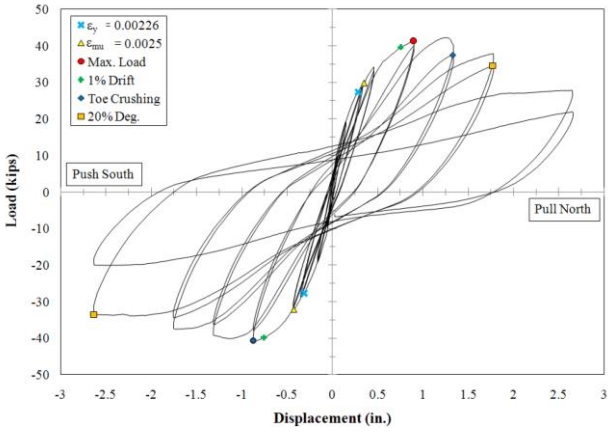

Figure 1-2. In-plane lateral load-vs.-displacement curves for a flexure-dominated wall (WSU-W-1A tested by Sherman, 2011).

The behavior of walls dominated by diagonal shear cracks is often very brittle, as shown by the lateral load-vs.-displacement hysteresis curves in Figure 1-3 for a wall tested by Ahmadi (2012). The failure of a shear-dominated wall is normally preceded by the development of diagonal shear cracks, which at the beginning may be restrained from opening by the horizontal shear reinforcement. However, once the diagonal shear capacity has been reached, diagonal cracks will open, and the lateral resistance of the wall may drop

rapidly. This may be accompanied by the tensile fracture or anchorage failure of the horizontal shear reinforcement. Limited ductility can be developed by a planar shear-dominated wall if sufficient horizontal reinforcement is present. The vertical reinforcement may contribute to the shear resistance through the dowel action. However, this contribution is normally small as compared to that provided by the horizontal reinforcement. The shear strength of a wall depends on the wall aspect ratio, the strength of the masonry, the quantity of the shear reinforcement, and the applied axial compressive load. A portion of the shear resistance of a wall can be provided by the masonry in the compression toe of the wall. Because of this, diagonal shear failure may occur in some walls after the flexural strength of a wall has been reached and the masonry in the compressed toe has been crushed.

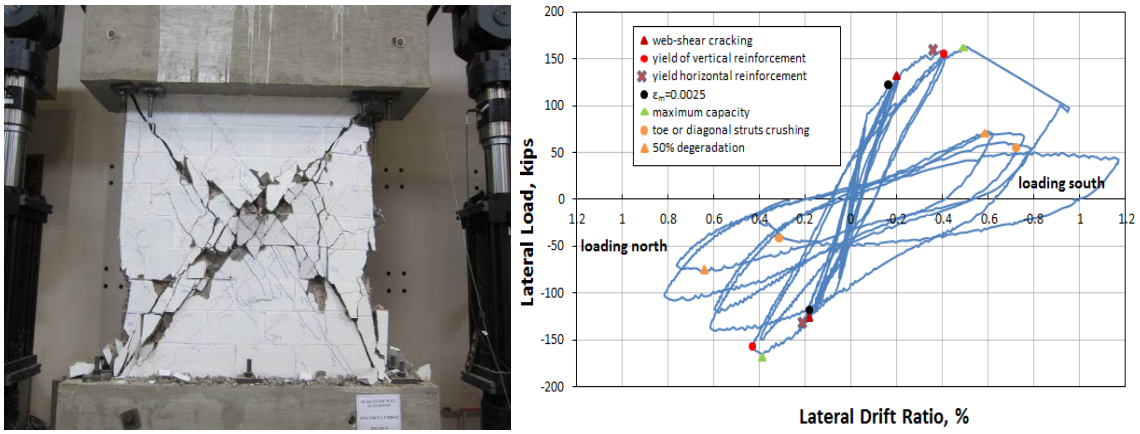

(a) Failure mode (b) lateral load-vs.-drift ratio hysteresis curves

Figure 1-3. A shear-dominated RM wall (UT-PBS-02 tested by Ahmadi, 2012)

RM walls with a low aspect ratio and low axial compressive load are likely to develop shear sliding failure along the base of a wall or in a bed joint a few courses away from the base. The sliding shear resistance of a wall depends on the surface roughness, the clamping force developed by the vertical reinforcement crossing the shear plane, the applied axial compressive load, and, to a lesser extent, the dowel action of the vertical

reinforcement. Walls dominated by shear sliding can exhibit a gradual degradation of the lateral load resistance, as shown in Figure 1-4. Shear sliding can exacerbate masonry crushing in the vicinity of the sliding plane, activating the dowel action of the vertical bars, which may cause damage to the surrounding masonry and lead to the shear fracture of the vertical bars at the shear plane. Significant base sliding may also induce severe damage to the other structural and non-structural components, such as the walls perpendicular to the direction of sliding, and may jeopardize the stability of the gravity frame that is present in the structure. Shear-sliding failure can be prevented by intentionally roughening the surface between an RM shear wall and the top surface of the footings.

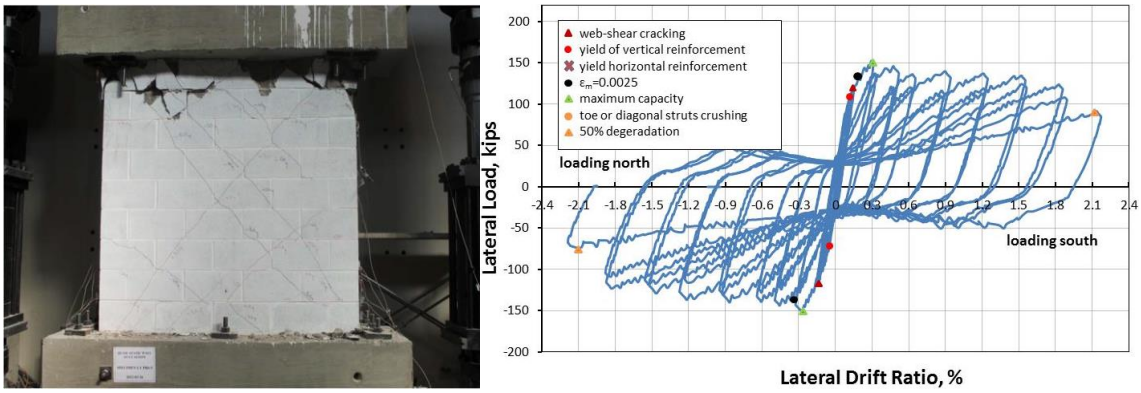

(a) Failure mode (b) In-plane lateral load-vs.-displacement curves

Figure 1-4. An RM wall dominated by shear sliding (UT-PBS-05 tested by Ahmadi, 2012).

TMS 402/602, *Building Code Requirements for Masonry Structures and Specifications for Masonry Structures* (TMS, 2016), are the main standards for RM construction in the United States. According to TMS 402, RM shear walls are categorized into ordinary, intermediate, and special walls based on the reinforcement details and reinforcement amount. Special RM shear walls are allowed to be used in high seismic areas,

corresponding to the Seismic Design Category (SDC) D, E, and F defined in ASCE 7 (ASCE, 2017).

For special RM shear walls, the value of the seismic force modification factor (*R*) is taken as 5 to ensure that the building has a low probability of collapse in the Maximum Considered Earthquake (MCE). This value of the *R* factor is based on the notion that the walls can develop the necessary flexural ductility to sustain a certain amount of story drifts without collapsing when subjected to severe seismic forces. In spite of the reinforcement and shear capacity design requirements in TMS 402/602 (TMS, 2016) for special RM walls, such wall systems could still be susceptible to shear-dominated behavior when there are wall components with a low shear–span ratio. This could be the case for perforated wall systems or when unintended coupling forces exerted by horizontal diaphragms significantly reduce the shear–span ratio of the walls. For example, the two-story RM structure tested by Stavridis et al. (2012) was designed as a cantilever wall system. However, due to the strong coupling forces exerted by the stiff horizontal diaphragms, RM shear walls in the test structure eventually developed diagonal shear failure, as shown in Figure 1-5.

In spite of the more brittle behavior of shear-dominated RM shear walls observed in the past cyclic loading tests, wall systems with such wall components sustained severe earthquake without collapse in some shake-table tests as well as past earthquake events. The high displacement capacity can be attributed to the existence of wall flanges and out-of-plane walls, which can carry the gravity load when the in-plane wall has been severely damaged. However, there had been no experimental data on the maximum displacement capacity of a shear-dominated RM wall system.

(a) Shear failure of reinforced masonry walls

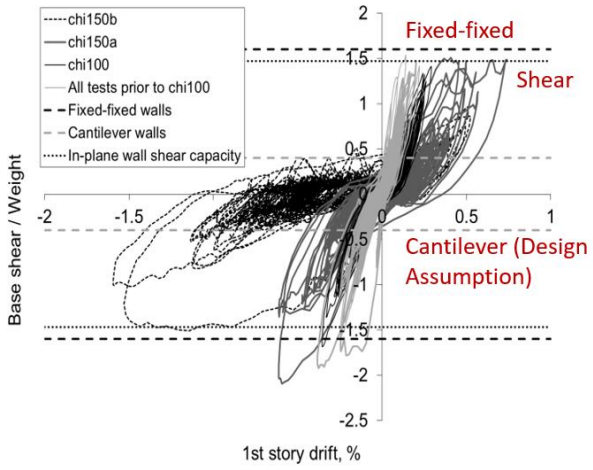

(b) Base shear-vs.-1st story drift responses of the test structure

Figure 1-5. A three-story building tested on a shake table (Stavridis et al., 2016).

The ability to model the aforementioned behaviors of a masonry wall system is of critical importance for performance-based seismic design and assessment. The numerical models developed in the past can be classified into two types: detailed finite element models and simplified models. In the detailed finite-element models, plane-stress elements or shell elements with a smeared-crack constitutive law and cohesive crack interface elements were used to simulate the cracking and crushing behavior of masonry; and beam or truss elements were used to model the behavior of reinforcing bars (Stavridis and Shing,

2010; Koutras and Shing, 2020, 2021). While the detailed finite element models are most general and accurate for capturing the different failure mechanisms that can be exhibited by a wall, they are computationally demanding, and therefore, are not suitable for use in engineering practice or computationally intensive procedures, such as the FEMA P695 procedure (FEMA, 2009), which requires incremental dynamic analysis to evaluate collapse probability of building archetypes. For these situations, computationally efficient models have to be used.

As one of the simplified modeling approaches, beam-column models provide a computationally efficient way to model RM structures. Traditional displacement-based and force-based beam-column elements with distributed plasticity have been adopted to model the flexural behavior of RM walls. With these elements, the inelastic behaviors of masonry and vertical reinforcement are represented in a fiber-section idealization. For this distributed plasticity approach, the sensitivity of numerical results to the element size has been an issue due to the localization of plastic strain in one element (for displacement-based elements) or one integration point (for force-based elements). Thus, the selection of the number of elements or number of integration points is of critical importance to have accurate and objective results. Beam-column elements with concentrated plasticity provide an alternative to distributed plasticity elements. They are computationally more efficient but require careful calibration to capture the plastic behavior of the structural components with zero-length hinges (Paulay and Priestley 1992; Priestley et al. 2007; Shedid and El-Dakhakhni 2014; Ezzeldin et al. 2018).

While the ability of these beam-column models to capture the nonlinear flexural behavior of RM and RC structural members has been well demonstrated, their extension

to simulate the shear behavior of a wall has faced many challenges. This is because the shear behavior of an RM or RC wall is associated with diagonal tensile cracking, which cannot be accurately represented by a constitutive law defined at the section level of a beam-column element. A number of beam-column models have been proposed with limited success to capture the shear behavior of RM and RC elements (D'Ambrisi and Filippou, 1999; Pentrageli et al, 1999; Martinelli,2008; Ceresa et al, 2009; Saritas and Filippou, 2009, 2013; Peruch et al, 2019). Hence, there is a significant need to develop a beam-column model that can capture both nonlinear shear and flexural behaviors of RM shear walls.

In engineering practice, ASCE 41 (ASCE, 2017), *Seismic Evaluation and Retrofit of Existing Buildings*, provides the lateral force-vs.-lateral displacement backbone curves for the nonlinear static and dynamic analyses of structural components and systems, including RM shear walls. However, the backbone curves adopted by ASCE 41 (ASCE, 2017) for RM shear walls are based on limited experimental data and have not been extensively verified with data that are currently available. Moreover, the proposed backbone curves do not distinguish fully grouted walls from partially grouted walls, or flanged wall sections from rectangular wall sections. Most importantly, these backbone curves tend to significantly under-estimate the displacement capacity of RM walls (NIST, 2017). Hence, these backbone curves need to be updated to realistically represent wall behaviors observed in experimental studies.

1.2 Research Objectives and Scope

The research presented in this dissertation consists of two parts. The first part was funded by NIST under the project ATC-114. This project was aimed to address the need to establish consistent modeling parameters and assumptions for nonlinear dynamic analysis

of common types of structural systems used in buildings. As a part of the project, this study was focused on the nonlinear analysis of RM shear walls. A force-based, fiber-section, beam-column element with predefined plastic hinge length was proposed to model the behavior of flexure-dominated RM shear walls. To capture the local failure mechanism in a flexure-dominated wall, a phenomenological material law was proposed to model the yielding, buckling, and low-cycle fatigue of the reinforcing bars. The proposed model has been calibrated and validated with extensive experimental data on fully grouted walls with rectangular and T-sections. Furthermore, a method has been proposed to determine force-vs.-displacement backbone curves for RM walls to replace the current backbone curves used in ASCE 41.

The second part of the dissertation was funded by the National Science Foundation (NSF). The main aim of this research was to investigate the displacement capacity of shear-dominated RM wall systems up to the point of collapse and to develop reliable and computationally efficient analytical models to simulate the nonlinear response of these systems. In this study, two one-story RM wall systems were tested to the verge of collapse on the outdoor shake table at the Natural Hazards Engineering Research Infrastructure (NHERI) site at the University of California San Diego. Each specimen had two T-walls as the main seismic force resisting elements. The second specimen had six additional out-of-plane walls. To investigate the influence of the out-of-plane walls, the T-walls in the two specimens had the same design and carried the same gravity load. The test program, results, and findings will be presented in this dissertation.

A beam-column model has been developed to model the nonlinear flexural and shear behaviors of RM shear walls. The proposed beam-column element is based on a

three-field mixed formulation based on Hu-Washizu variational principle. The axial-flexural behavior is modeled in a distributed plasticity manner with a fiber section model. For shear response, a macro phenomenological model has been proposed, which considers the influence of the axial load on the shear capacity and the contribution of the wall flanges. The model also considers the interaction between the axial-flexural and shear behaviors. The mixed beam-column element and the proposed shear model have been implemented in the open-source software platform, OpenSEES (McKenna et al. 2000). The model has been calibrated and validated with extensive test data, including the aforementioned shake-table tests. The mixed element formulation, details of the shear model, and the results of the validation analyses are presented in this dissertation.

1.3 Outline of Dissertation

Chapter 2 provides a literature review of the past experimental and numerical studies on RM shear walls and wall systems. Quasi-static cyclic tests and shake-table tests performed in the past on both flexure- and shear-dominated RM shear walls are briefly summarized. It also summarized detailed finite element models and simplified models developed in the past to model the flexure- and shear-dominated behaviors of RM shear walls.

Chapter 3 presents a force-based, fiber-section, beam-column model proposed to model the flexure-dominated RM shear walls. To capture the local failure mechanism in a flexure-dominated wall, a phenomenological material law proposed to model the yielding, buckling, and low-cycle fatigue of the reinforcing bars is presented. The proposed model has been calibrated and validated with extensive quasi-static cyclic loading test data on both planar and flanged walls.

Chapter 4 presents a method to construct force-vs.-displacement backbone curves of flexure-dominated RM shear walls. The method relies on the moment-curvature relation of a wall section, which can be generated with the constitutive laws presented in Chapter 3. The idealization schemes used to construct the backbone curves for walls with rectangular section and flanged section are discussed. The applicability of the proposed method on partially grouted RM walls is also discussed. Furthermore, an empirical backbone curve is presented for shear-dominated RM shear walls.

Chapter 5 presents the full-scale shake-table test program to investigate the collapse resistance of two shear-dominated RM shear wall systems. The design of the test structures, test setup, loading protocol, instrumentation schemes, and test observations are presented. The maximum lateral resistance reached by the two test structures are compared to the shear strengths given by the formula in TMS 402/602. Furthermore, the factors contributing to the high displacement capacities of the two test structures are discussed.

Chapter 6 presents the beam-column model proposed to model the nonlinear shear and flexural behaviors of RM walls. The beam-column model is based on a three-field (force, strain, and displacement) mixed beam formulation proposed by Taylor et al. (2003). The finite element approximation to the force and strain fields are discussed. The axial-flexural behavior of an RM shear wall is modeled as distributed plasticity with a fiber-section model. The macro model proposed to model the shear behavior is presented. It considers the resistance of the wall web(s), and, for a flanged wall, the flexural strength provided by the wall flange(s) to the shear resistance. The calibration and validation of the beam-column model with experimental data is also discussed.

Chapter 7 presents the conclusions of the study, and the needs and recommendations for future research.

Parts of Chapters 3 and 4 are a reprint of the material presented in a manuscript titled “Practical Nonlinear Analysis Methods for Flexure-Dominated Reinforced Masonry Shear Walls”, which has been submitted to *ASCE Journal of Structural Engineering* (under review). The authors of the manuscript are: the author of the dissertation and P. Benson Shing. The author of the dissertation is the primary author of the manuscript, and the main contributor of the work presented in the manuscript.

Part of Chapter 5 is a reprint of the material presented in a paper titled “Evaluation of Collapse Resistance of Reinforced Masonry Wall Systems by Shake-Table Tests”, which was published in the journal of *Earthquake Engineering and Structural Dynamics* in 2020. The authors of the research paper are: the author of the dissertation, Andreas A. Koutras, and P. Benson Shing. The author of the dissertation is the primary author of the paper, and the main contributor of the work presented in the paper.

Part of Chapter 6 is a reprint of the material currently being prepared for submission for publication, Cheng, J. and Shing P. B. under the title “A Beam-Column Model for Nonlinear Flexural and Shear Behavior of Reinforced Masonry Walls”. The author of the dissertation is the primary author and the main contributor of the work presented in the paper.

CHAPTER 2 LITERATURE REVIEW

2.1. Introduction

To investigate the factors influencing the strength and displacement capacity of RM shear walls, a number of quasi-static and shake-table tests were carried out on flexure- and shear-dominated walls and wall systems in the past decades. Nevertheless, the ultimate displacement capacity of RM wall systems has not been thoroughly investigated because most of the tests were stopped way before the collapse point. The test data on the collapse or near-collapse performance of masonry wall structures are very limited.

Based on the test data from the experimental studies, analytical models have been developed for nonlinear flexural and shear behaviors of RM shear walls. The models can be categorized into two types: detailed finite element models and simplified models. A detailed model utilizes continuum element and interface element to model the opening of cracks on masonry, and truss or beam element to model the nonlinear behavior of reinforcing bars embedded in masonry. In spite of the accuracy, the detailed finite models are computationally expensive. As one type of the simplified models, beam-column models provide a computationally efficient alternative to the sophisticated finite element models when a large number of analyses is required.

This chapter presents a summary of the past experimental studies on seismic behavior of RM shear walls, as well as the detailed finite element models and the simplified models (with a focus on beam-column models) developed for RM shear walls.

2.2. Experimental Investigations on RM Shear Walls

2.2.1. Single Wall Segments

Shing et al. (1991) performed quasi-static tests on 24 fully grouted, planar, cantilever RM shear walls. This study examined the influence of the axial load, amount of horizontal and vertical reinforcement, and loading history on the strength, failure mechanism, and ductility of RM shear walls. As shown in Figure 2-1, for each specimen, a constant axial load was first exerted by the loading beam through the two vertical actuators. A sequence of lateral displacement cycles with increasing amplitudes were applied at the top of the wall by the horizontal actuator. Of the 24 test specimens, seven specimens exhibited a flexure-dominated failure mode; twelve specimens exhibited diagonal shear failure, and the rest of the specimens had a combined flexural-shear failure mode. The results of the tests showed that the maximum lateral resistance of the flexure-dominated specimens increased with the increase of axial compressive load. However, the flexural ductility was reduced with the increase of axial compressive load. For shear-dominated wall specimens, the study showed that the lateral shear strength of a wall panel increased with the increase of axial compressive load due to the increase of aggregate interlock force along the diagonal cracks and the friction at the toes. Moreover, for a shear-dominated wall panel, the lateral strength and post-cracked ductility were significantly improved with an increase of the amount of horizontal and vertical reinforcement.

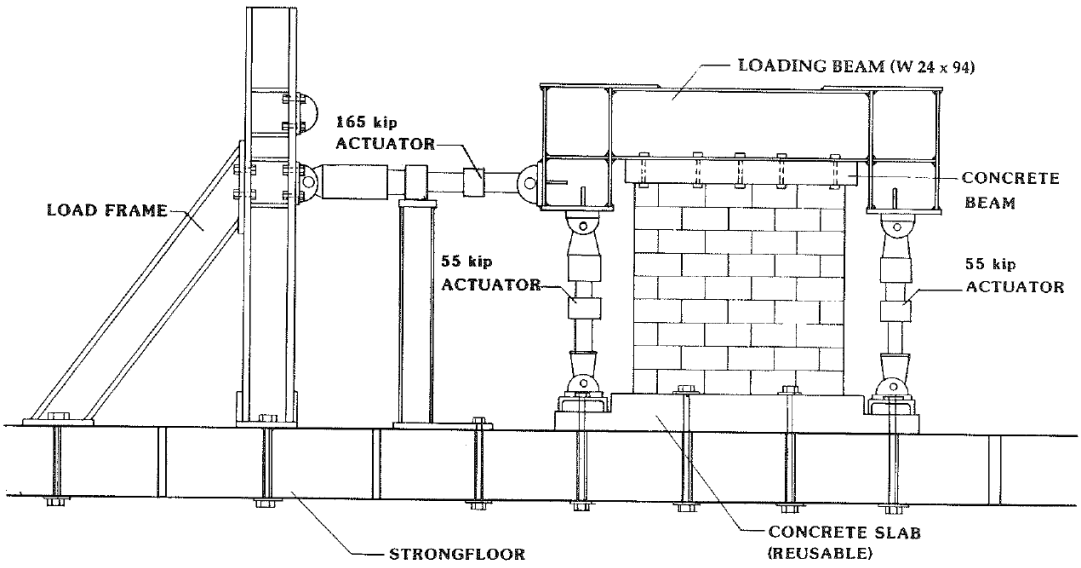

Figure 2-1. Test setup of Shing et al. (1989)

He and Priestley (1992) tested nine full-scale, fully grouted cantilever RM walls with T-sections. The test program consisted of two phases. In the first phase, quasi-static cyclic tests were performed on four T-walls to investigate the influence of the mount of the vertical reinforcement, flange width, and the confinement in the mortar bed at the toes of wall web on the strength and ductility of flanged RM walls. In the second phase, to simulate the behavior of RM shear walls in a real earthquake event, five wall specimens were tested on a shake-table. All of the nine wall specimens exhibited flexure-dominated behavior. The flanged RM walls had unsymmetric behaviors in the two loading directions parallel to the wall webs. Severe toe crushing and buckling of vertical reinforcing bars were observed in the webs, while the wall flanges had relatively minor damage near the base. As shown in Figure 2-2, the maximum lateral resistance of a T-wall was much higher and the post-peak ductility was lower in the loading direction in which the flange was in tension, compared to the behavior when the flange was in compression.

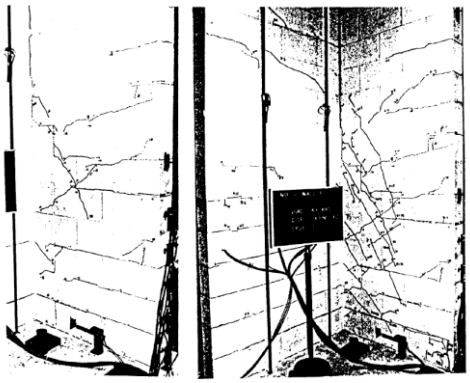

(a) Cracks developed on the wall before failure

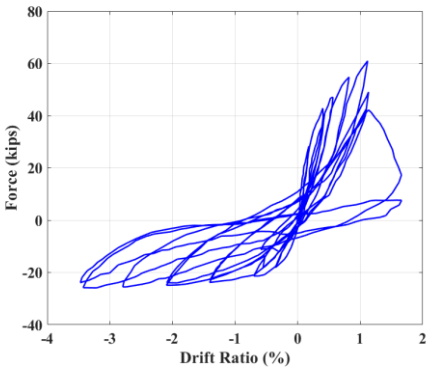

(b) Lateral force-vs.-drift ratio hysteresis curves

Figure 2-2. Wall UCSD-F1 tested by He and Priestley (1992)

Tomaževicˇ et al. (1996) tested 32 half-scale, cantilever RM shear walls subjected to two different axial stress levels (1MPa and 2MPa). For each axial stress level, the wall specimens were subjected to different types of displacement histories, including monotonic, cyclic, and simulated earthquake response, as shown in Figure 2-3. Moreover, each sequence of displacement history was applied in two levels of velocities, respectively, to compare the wall behaviors subjected to static and dynamic loads. The test results showed that the walls subjected to dynamic loads exhibited higher lateral resistance than those subjected to static loads. However, regardless of load type, the post-peak ductility was more or less the same. Comparing to the walls subjected to cyclic loads, those specimens subjected to monotonic loads exhibited higher lateral resistance and ductility, which could be attributed to the fact that they were subjected to less in-cycle damage.

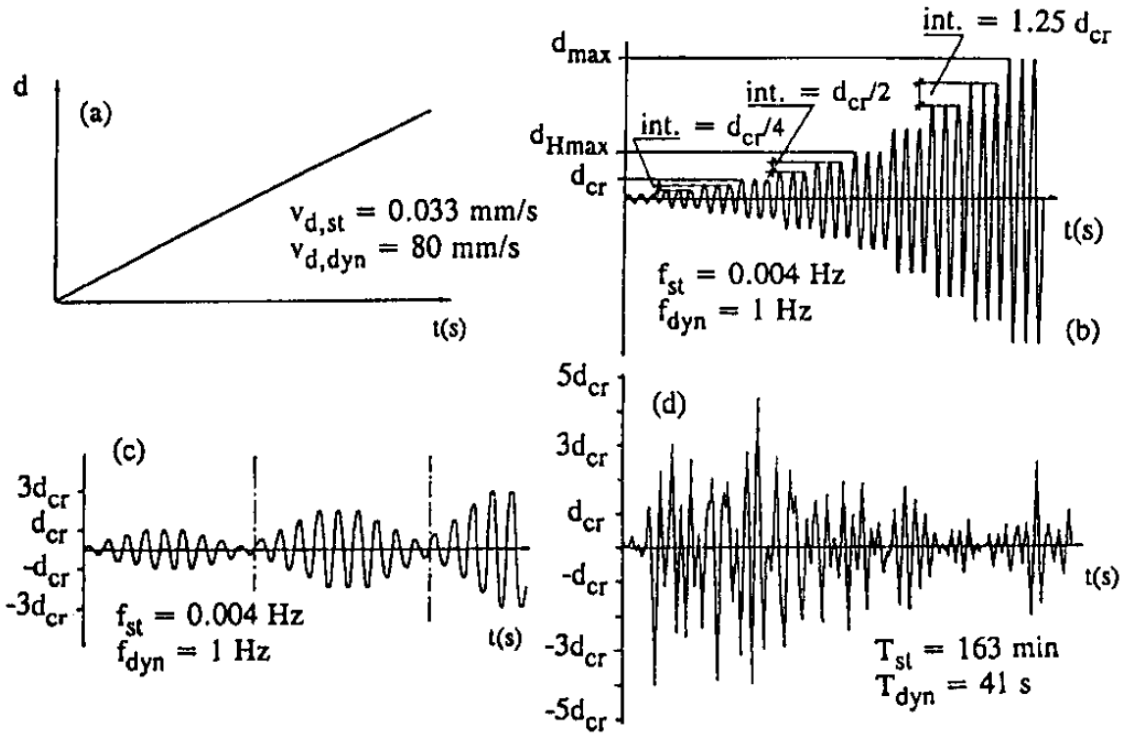

Figure 2-3. Four different types of input displacement histories adopted in the tests performed by Tomaževicˇ et al. (1996)

Ibrahim and Suter (1999) conducted quasi-static cyclic tests on five fully grouted RM cantilever walls with three height-to-length aspect ratios (0.467, 0.636, and 1.0) and two levels of axial compressive stress (100 psi and 250 psi). Although all the five wall specimens were designed to develop diagonal shear failure, the failure mode for one specimen was dominated by flexure. According to the test observations, with the increase of height-to-length aspect ratio, the shear strength decreased while the displacement ductility increased. The rest of test observations were in general consistent with those presented by Shing et al. (1991).

Eikanas (2003) examined the influence of wall aspect ratios and amount of vertical reinforcement on flexure-dominated RM shear walls by performing quasi-static, cyclic tests on seven fully grouted cantilever walls. These wall specimens had four different

height-to-length aspect ratios (0.72, 0.93, 1.5, and 2.1) and two vertical reinforcement ratios (0.26% and 0.52%). All the seven walls were subjected the same axial compressive stress (27 psi). The test results indicated that the walls with high height-to-length aspect ratios tended to exhibit more ductile behavior. Furthermore, comparing to the walls with low aspect ratios, those slender walls also had a shorter plastic hinge length. For the influence of the amount of flexural reinforcement, the conclusions were in general consistent with those reported by Shing et al. (1991).

Voon and Ingham (2006) performed quasi-static cyclic tests on ten single-story RM cantilever walls. All of the ten walls were designed to develop diagonal shear failure modes. These wall specimens had aspect three different height-to-length aspect ratios (0.6, 1.0, and 2.0) and three different levels of axial stress (zero, 0.25MPa, and 0.5MPa). The horizontal reinforcement ratios ranged from 0.01% to 0.14%. Eight out of the ten wall specimens were fully grouted, whereas the rest two walls were partially grouted. During the tests, most of the walls developed shear-dominated behavior as expected. However, one of the wall specimens exhibited severe sliding at the base. The test results indicated that the masonry shear strength decreased inversely with the height-to-length aspect ratio, which was consistent with the test observations by Ibrahim and Suter (1999). Additionally, the test results also demonstrated that, comparing to fully grouted RM walls, partial grouting significantly reduced the shear strength of the planar walls. The rest of the test observation were generally consistent with previous experimental studies (Shing et al., 1991, Ibrahim and Suter, 1999).

To evaluate the possibility to reach higher level of flexural ductility of RM walls, Shedid et al. (2008) tested six full-scale, fully grouted, RM shear walls to failure under

quasi-static cyclic loading. The test specimens consisted of three ordinary walls, two intermediate walls, and one special wall designed according to the provisions in TMS 402. The three ordinary walls had the same reinforcement details, but were subjected to three different levels of axial load (0, 0.75 MPa, and 1.50 MPa). The two intermediate walls were subjected to zero axial, and had the same amount of vertical and horizontal reinforcement. However, the arrangements of reinforcement were different: one wall had vertical #5 bars spaced at 8 inches, while the other one had #9 bars spaced at 16 inches. All the six walls exhibited ductile flexure-dominated behavior, with little strength degradation at drift ratios up to 2%, as shown in Figure 2-4. Furthermore, the wall responses showed that displacement ductility was highly dependent on the amount of vertical reinforcement, but was much less influenced by the axial load.

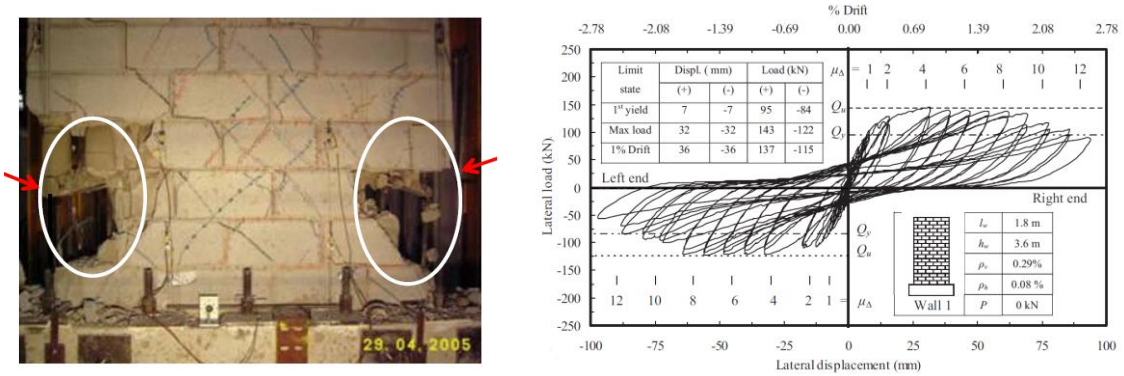

(a) Localized flexural failure (b) Force-vs.-displacement hysteresis curves

Figure 2-4. Response of a full-scale special RM shear wall tested by Shedid et al. (2008)

As part of a research project sponsored by National Institute for Standards and Technology (NIST) aimed to develop a displacement-based design procedure for masonry shear walls, quasi-static cyclic tests were performed on a number of wall segments with different design parameters and loading conditions. A total of 43 fully grouted RM wall

segments, which were classified to four groups, were tested at University of Texas at Austin and Washington State University (Ahmadi, 2012; Kapoi, 2012; Sherman, 2011; Cyrier, 2012).

The first group of wall specimens tested by Ahmadi and Sherman consisted of 16 flexure-dominated cantilever walls detailed as special and intermediate walls according to the design provision in TMS 402. The specimens had five height-to-depth aspect ratios (0.78, 1.0, 2.0, 3.0, and 4.5), six levels of axial compressive load ratios (0, 0.05, 0.0625, 0.10, 0.125, and 0.15). Furthermore, two pairs of wall specimens in this group were tested to compare the behaviors of RM walls with and without vertical reinforcing bars lap spliced near the base. The results showed that walls with vertical reinforcing bars lap spliced near the base exhibited more rapid strength degradation after toe crushing, due to the failure of lap splice.

The second group of wall specimens consisted of seven cantilever walls with confined boundary elements, which were tested by Cyrier to develop effective confining boundary elements in RM walls. Figure 2-5 shows the details of the two different types of boundary elements used by Cyrier, which were designed according to the requirements of ACI 318. Apart from the ordinary boundary element shown in Figure 2-5(a), the boundary element with a return shown in Figure 2-5(b) can also be used as the junction between two RM walls. The test results indicated that the boundary elements of this type can improve the displacement ductility of an RM shear wall significantly.

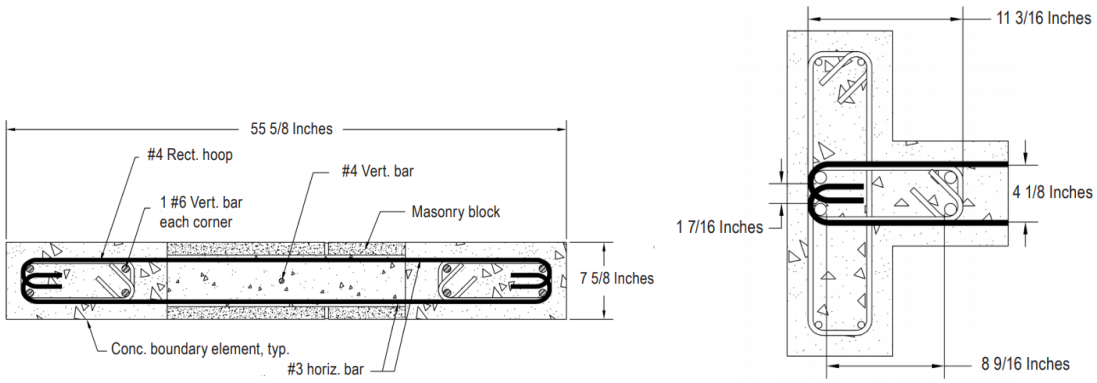

(a) a regular boundary element (b) a boundary element with return

Figure 2-5. Reinforced concrete boundary elements used by Cyrier (2012)

The third group consisted of 14 cantilever walls, where were tested by Ahmadi and Kapoi to investigate performance of RM wall with a wide range of reinforcement ratios, which might slightly violate the requirement of TMS 402. The influence of distribution of vertical reinforcement was also examined by testing two walls with jamb reinforcement (concentrated vertical reinforcement at each end of walls), as shown in Figure 2-6. The test results showed that the walls with jamb reinforcement had very similar behaviors as those with uniformly distributed vertical reinforcement. For the influence of axial load and reinforcement amount, the test observations on flexural-dominated RM shear walls were generally consistent with the previous studies (Shing et al. 1991).

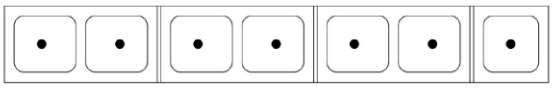

(a) Uniformly distributed reinforcement

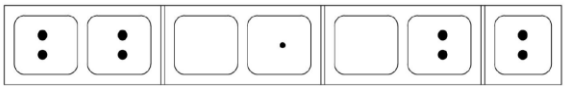

(b) Jamb reinforcement

Figure 2-6. Sections of RM walls with different arrangement of flexural reinforcement tested by Kapoi (2012)

For the fourth group, Ahmadi tested six RM shear walls with the same geometry and fixed-fixed end constraint conditions. Figure 2-7 shows the control system used to ensure the fixed-fixed end constrain conditions. As shown, the lateral load and restraining bending moment at the top of the specimen were applied by the horizontal actuator through an L-shaped loading beam. The rotation and vertical displacement of the loading beam were restrained by the out-of-plane bracing system, which consisted of three steel tubes with swivels at each end. Although all of the six wall specimens were designed to be dominated by diagonal shear cracks, only two wall specimens developed diagonal shear failure as expected. The rest four specimens developed shear-sliding failure. This could be attributed to two factors. One is the low axial compressive load, which reduces the friction along the wall base and concrete footing. The other is the amount of vertical reinforcement, which was not sufficient to resist sliding failure through dowel actions.

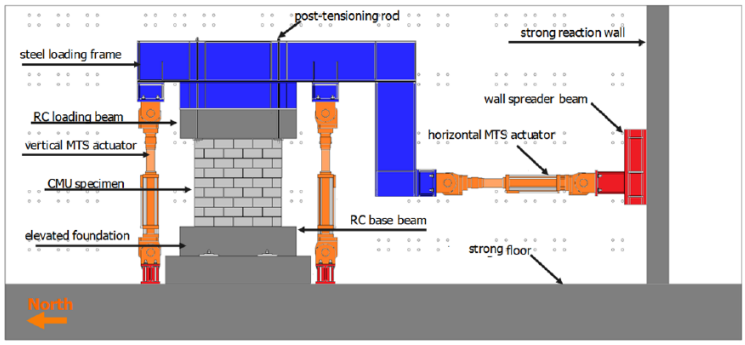

(a) Elevation view

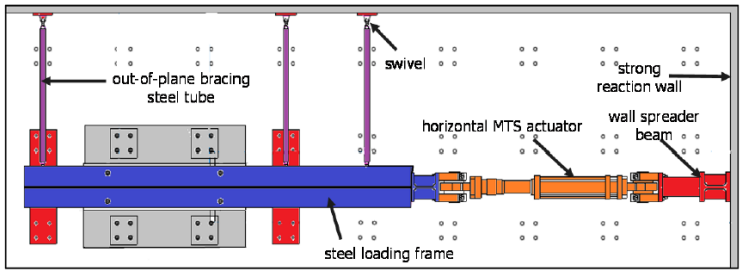

(b) Plan view

Figure 2-7. Control system for the fixed-fixed RM walls tested by Ahmadi (2012)

Banting and El-Dakhakhni (2012, 2014) performed cyclic quasi-static tests on nine half-scaled, fully grouted RM walls with confined boundary elements to develop a confinement scheme for the boundary elements. Figure 2-8 shows the confinement details a boundary element and the hysteresis curves of one of the specimens. The test results showed that the confined boundary elements were able to delay the toe crushing as well as buckling of flexural reinforcing bars. Hence, flexure-dominated RM shear walls could benefit significantly by providing lateral confinement in critical regions.

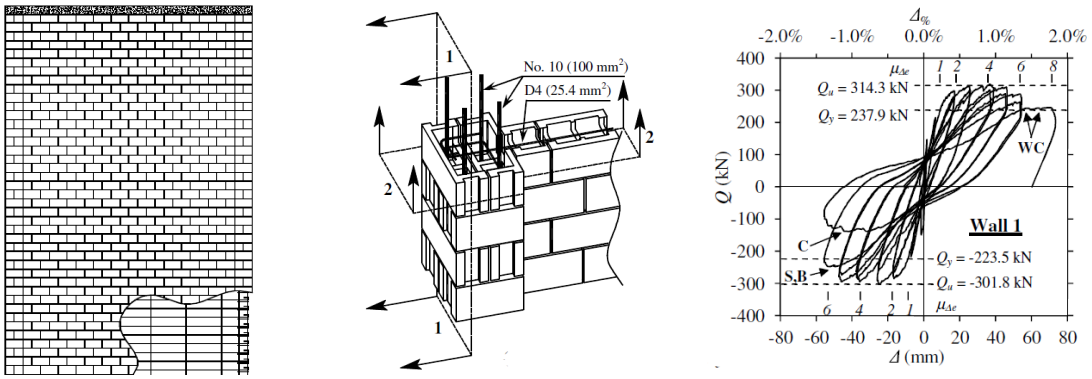

(a) Elevation view (b) Details of the confined boundary element (c) Force-vs.-displacement hysteresis curves

Figure 2-8. A wall specimen with confined boundary elements tested by Banting and El-Dakhakhni (2012)

Mojiri et al. (2014) performed shake-table tests on six 1/3-scale, fully grouted, lightly reinforced, flexure-dominated RM walls. The configurations of the test specimens were based on two one- and two-story prototype buildings. Each wall specimens were subjected to a ground motion recorded from 1989 Loma Prieta earthquake, which were scaled to four intensity levels.

Siyam et al. (2015) performed quasi-static cyclic tests on six 1/3-scale, fully grouted RM walls to investigate the influence of wall flanges and the slab-coupling effect. Among the six wall specimens, there were one flanged wall and two slab-coupled wall

systems, as shown in Figure 2-9. The six walls were designed as special RM shear walls based on TMS 402/602. All the wall components in the six specimens exhibited flexure-dominated behavior. However, comparing to the planar wall specimens, the flanged wall and the slab-coupled walls had significantly higher displacement capacity.

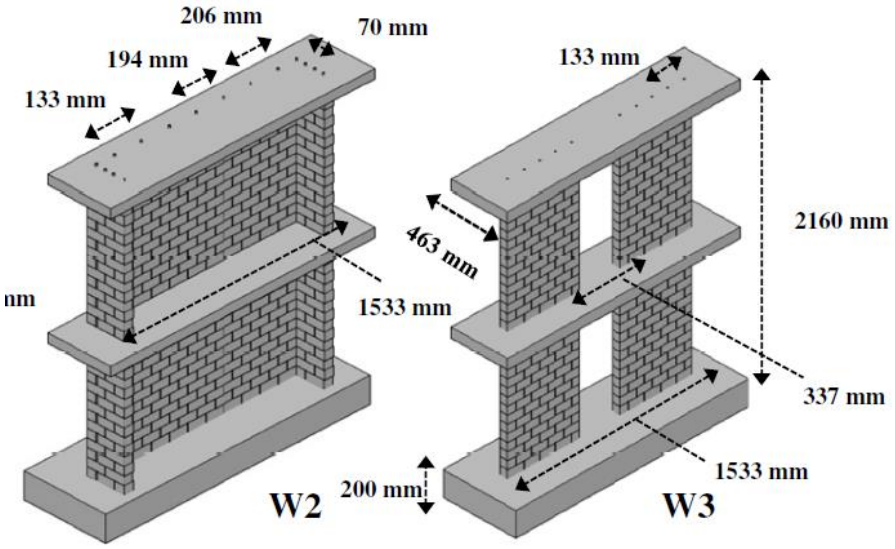

(a) A flanged wall specimen (b) A slab-coupled wall specimen

Figure 2-9. Wall specimens tested by Siyam et al. (2015)

2.2.2. Reinforced Masonry Wall Systems

Merryman et al (1990) tested two full-scale, fully grouted, flexure-dominated, two-story coupled RM wall systems. The two specimens, Specimens 2a and 2b, were designed to represent a coupled shear wall system in a two-story prototype building, as shown in Figure 2-10. The two specimens had the same geometry and reinforcement details, but different roof systems. Specimen 2a had a cast-in-place reinforced concrete slabs, while Specimen 2b had precast prestressed planks with a concrete topping. Both specimens were tested under quasi-static, cyclic lateral loads applied at the second floor and roof levels. In addition, Specimen 2a was subjected to a constant vertical load, which represented the

tributary gravity load transferred from the slab in the prototype structure. Comparing to the flexural strength calculated based on cantilever walls, the two specimens developed significantly higher maximum lateral strength due to the coupling effect of the horizontal diaphragms.

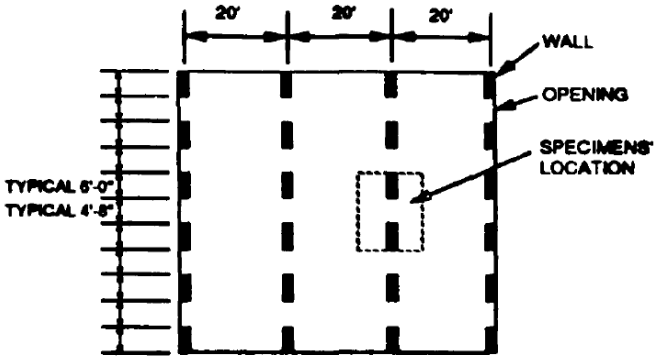

(a). elevation view of the prototype structure

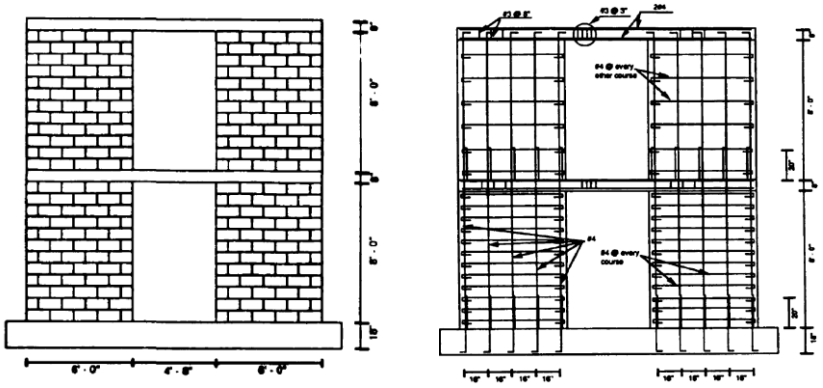

(b) block layout and reinforcement details of the two test wall specimens

Figure 2-10. Two-story slab-coupled wall specimens tested by Merryman et al. (1990)

Seible et al (1994) tested a flexure-dominated five-story RM building with the pseudo-dynamic test method. The five-story structure was subjected to a total of 75 separate tests, including generated sequential displacement tests, quasi-static inverse triangular load tests, and shakedown tests. The tests were stopped when the building had reached a maximum roof drift ratio of 1%, with the seismic resisting shear walls developed flexure-dominated behavior exhibiting little load degradation.

Tomaževič and Weiss (1994) tested two 1:5-scale, three-story building models on a shake table. The two models had the same configuration based on a prototype building representing three- to four-story residential buildings in central Europe. As shown in Figure 2-11, for each specimen, additional concrete mass blocks were fixed onto the roof to satisfy the dynamic similitude with the prototype structure. One of the test structures had plain masonry, and the other had wire reinforcement placed along the vertical edges of each wall, as well as the wire stirrups distributed horizontally. While the plain masonry structure collapsed at a first-story drift ratio of 2.5%, the RM structure was able to reach a first-story drift of nearly 4% without collapse.

Lourenço et al (2013) tested two 1:2-scale concrete masonry building models on a shake table. The first model was unreinforced, and the second one had truss-type steel reinforcement distributed vertically and horizontally in each wall. Both structures had two stories and were subjected to bidirectional base excitation. In the tests, the unreinforced model collapsed when reaching a maximum inter-story drift ratio of 2.5% at the second story. However, the model with truss-type reinforcement reached a maximum inter-story drift of 0.34% at the first story without collapse when the intensity of the base excitation was 60% stronger than that of the last excitation applied to the unreinforced model.

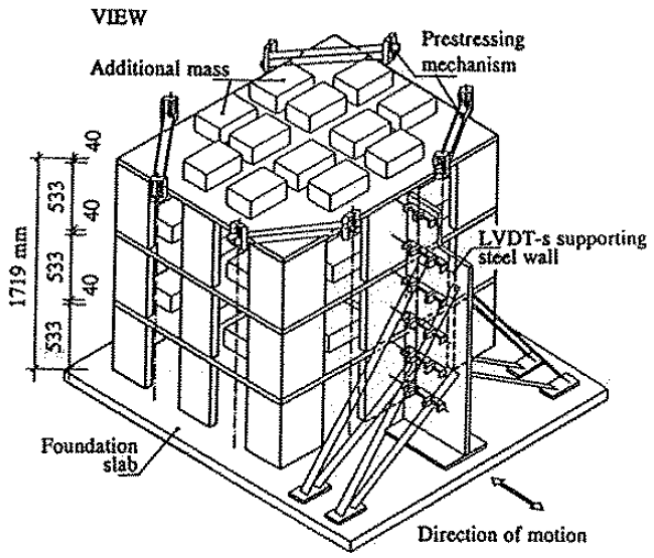

Figure 2-11. Test setup and specimen configuration of the wall systems tested by Tomaževič and Weiss (1994)

Heerema et al (2015) and Ashour et al (2016) performed quasi-static tests on two 1:3 scaled, two-story, asymmetric RM wall systems. These two wall systems had the same wall layouts but different diaphragm designs. As shown in Figure 2-12, the structure tested by Heerema et al. was detailed with hinge line in the diaphragm slabs to prevent the flexural coupling effect induced by the slabs, whereas the structure tested by Ashour et al. had stiffer slabs without the hinge lines. The system with the more flexible diaphragms reached a roof drift ratio of 2.5% with 38% loss in the lateral resistance. The system with the stronger diaphragms showed 50% higher peak lateral resistance but more brittle behavior with 72% strength degradation at a roof drift ratio of 2.5%. By comparing the behaviors of these two wall systems with those of the wall components tested by Siyam et al. (2015), Ashour et al. concluded that the difference between system-level and component level behavior can be attributed to two factors: slab flexural coupling and slab-induced twist, and the flexural coupling effect of the slabs had more significant impact on lateral resistance and stiffness deterioration of the RM shear walls.

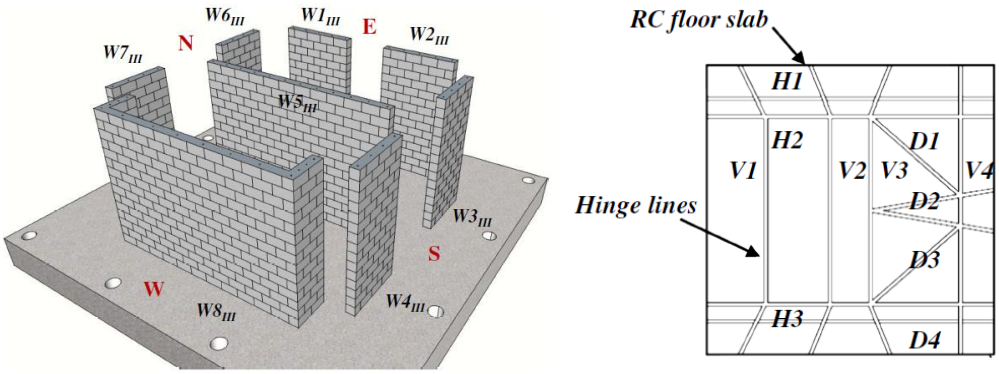

(a) Configuration of the walls in the first story (b) Hinge lines in the diaphragms

Figure 2-12. RM structure tested by Heerema et al. (2015)

Mavros et al (2016) conducted shake-table tests on a full-scale, fully grouted, two-story, RM shear wall structured designed by a displacement-based method. As shown in Figure 2-13, the test structure had two T-wall and a rectangular wall as the main seismic resisting elements. Meanwhile, there were four out-of-plane walls oriented perpendicular to the shaking direction. The structure was subjected to a sequence of scaled ground motion records from the El-Centro earthquake, and exhibited a shear-dominated failure mode. The structure exhibited 20% degradation of lateral strength at a maximum first-story drift ratio of 2%.

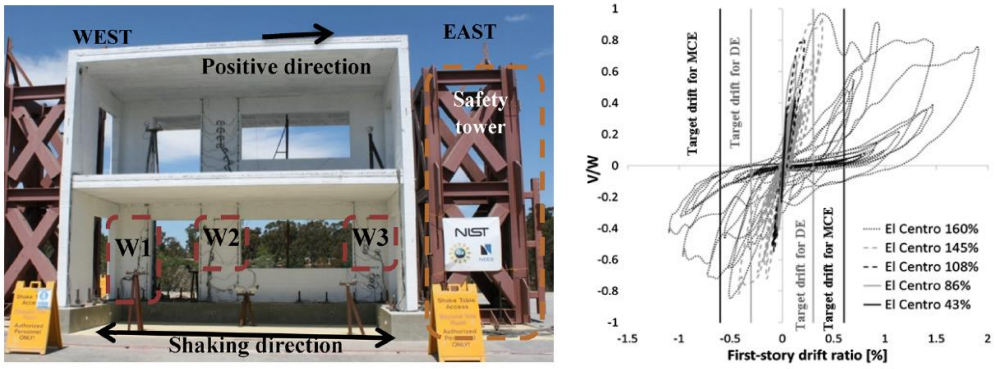

(a) Test setup (b) Hysteresis curves of the test structure

Figure 2-13. Two-story RM wall structure tested by Mavros et al. (2016)

Stavridis et al (2016) performed shake-table tests on a full-scale, fully grouted, three-story, RM shear wall structure. The test structure consisted of two T-walls and a planar wall as the main seismic resisting system. In addition, there were six out-of-plane walls oriented perpendicular to the loading direction. The seismic resisting wall elements were designed as flexure-dominated cantilever walls. However, the wall components eventually developed diagonal shear failure. This was attributed to the coupling forces exerted by the strong horizontal diaphragms, which effectively reduced the shear-span ratios. The three-story structure had a 27% strength degradation at a maximum first-story drift of 1.6%.

The displacement capacity observed in the shake-table tests (Mavros et al., 2015; Stavridis et al. 2016) is significantly higher than that of the previously referenced shear-dominated planar wall segments (Voon and Ingham, 2006; Shing et al., 1991; Ahmadi, 2012), which exhibited severe load degradations at drift ratios not exceeding 1%. The more ductile behavior observed in the wall systems in these shake-table tests could be attributed to the presence of wall flanges as well as displacement histories.

Koutras and Shing (2020) investigated the behavior of a single-story partially grouted RM structure that was designed for a low-to-moderate seismic zone based on TMS 402/602. The tests were conducted in two phases. In the first phase, the structure exhibited significant base sliding under the MCE-level motion. In the second phase, RC stoppers were installed to prevent the structure from developing further base sliding, and the structure developed a shear-dominated failure mode, as shown in Figure 2-14. At the end of the tests, the structure lost 85% of its lateral strength at a drift ratio of 2.2%. Collapse

was averted only because the walls perpendicular to the direction of shaking were able to carry the weight of the roof after the walls parallel to motion had been severely damaged.

Figure 2-14. Failure of the partially grouted structure tested by Koutras and Shing (2020)

2.3. Analytical Models of RM Shear Walls

2.3.1. Detailed Finite Element Model

Lotfi and Shing (1992) presented a smeared crack finite element formulation to represent the nonlinear behavior of RM shear walls. A J2 plasticity model was adopted for uncracked masonry and a nonlinear orthotropic model was adopted for cracked masonry. For reinforcing steel, an elastic-plastic model with strain hardening was adopted. By assuming that steel and masonry have compatibility in deformation, the steel reinforcement can be modeled as discrete bars or a smeared overlay on masonry. This model was examined by the diagonal compression tests on RM wall panels conducted by Hegemier et al. (1978) and the cantilever RM shear walls tested by Shing et al. (1991). While the flexural response of an RM shear wall could be well captured by this model, the smeared crack approach was not able to well represent the diagonal shear behavior due to the

assumed continuous displacement field. In spite of the simplicity, the assumption was unrealistic in representing the opening of diagonal cracks.

Mavros (2015) used a combination of smeared crack and discrete crack models to capture different failure modes of RM shear walls. A modeling scheme proposed by Stavridis and Shing (2010) for masonry infilled RC frames was adopted. As shown in Figure 2-15, smeared-crack plane-stress elements and cohesive crack interface elements were adopted for the infill masonry. Additionally, truss elements were used to model the vertical and horizontal reinforcing bars. The modeling scheme was validated with the quasi-static tests on the wall segments by Ahmadi (2012) and the shake-table tests on the two-story RM structure by Mavros et al. (2015).

Koutras (2019) presents an improved finite element modeling scheme, which is applicable to both fully grouted and partially grouted RM shear wall structures. As shown in Figure 2-16(a), for grouted reinforced masonry, a smeared-crack shell element and cohesive crack interface element were adopted. The smeared crack shell element consists of three layers, representing the grout filled into the hollow cells of the CMU blocks. For reinforcing steel, beam elements were adopted with a constitutive law to represent yielding, buckling, and fracture of reinforcing bars. The model also considers the bond-slip between the grout and steel bars as well as the dowel action of steel bars. For ungrouted masonry, a hollow layer was used between two masonry layers in the smeared crack shell element, as shown in Figure 2-16(b). Furthermore, an element removal scheme was proposed to model spalling of masonry due to the crack opening and crushing. The model was calibrated and validated by extensive test data on wall segments and RM wall systems (Shing et al., 1991; Ahmadi, 2012; Mavros, 2015; Koutras, 2019).

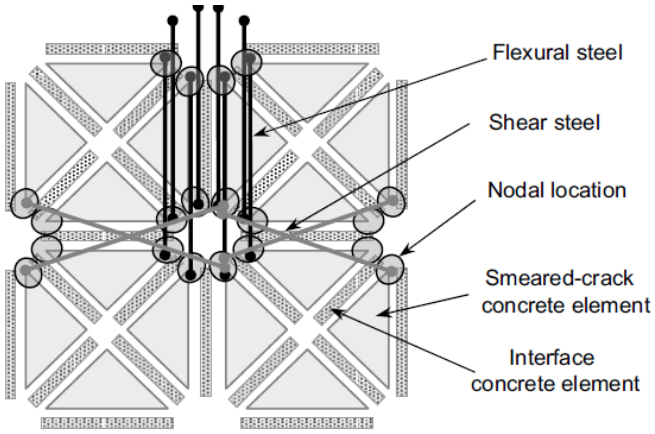

Figure 2-15. Finite element discretization of RC/RM members (Starvridis and Shing, 2010)

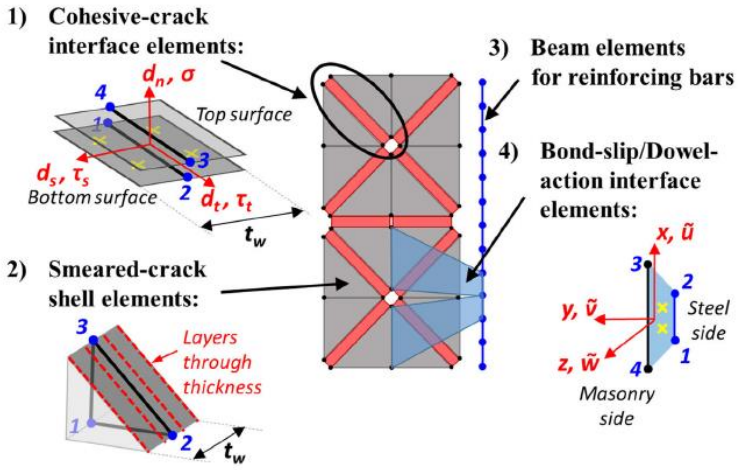

(a) discretization for grouted reinforced masonry

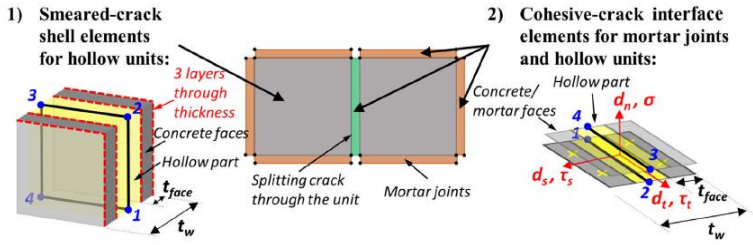

(b) discretization for ungrouted masonry

Figure 2-16. A detailed finite element modeling approach proposed by Koutras (2019)

2.3.2. Beam-Column Model

Spacone et al. (1996) presents a fiber beam-column element with distributed plasticity to perform static and dynamic analysis for RC frames. This model can be adopted to simulate the flexural behavior of RM walls. The element formulation is flexibility-based and the equilibrium between bending moment and shear is strictly satisfied along the element. With the assumption that plane sections remain plane, the nonlinear moment-curvature relation is modeled by a fiber section model, in which nonlinear uniaxial material models for concrete and vertical reinforcing steel are adopted, as shown in Figure 2-17. With this assumption, the effects of shear and bond-slip are neglected.

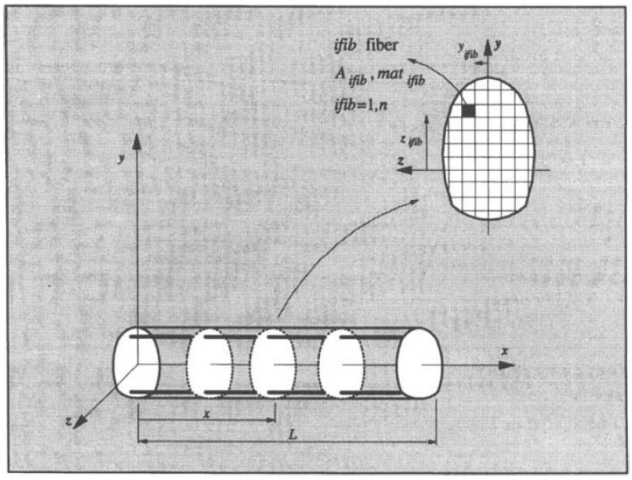

Figure 2-17. A force-based beam-column model with fiber sections (Spacone et al., 1996)

Petrangeli et al. (1999) proposed a fiber-section, beam-column element, which can be adopted for shear-dominated RC and RM members. The element formulation is flexibility-based with the consideration of shear deformation, in which the equilibrium between shear and moment is assumed to be satisfied. The shear mechanism is modeled in each concrete fiber at the cross sections with a 2-dimensional micro-plane model. The

deformation compatibility of concrete/masonry and vertical and horizontal reinforcement in the micro-plane model is assumed to be satisfied. The vertical strain and the shear strain were given by the element formulation, whereas the transverse strain is obtained by satisfying the equilibrium between concrete/masonry and horizontal steel bars. This element can be computationally demanding because it requires iteration in element level as well as in the micro-plane model in each fiber of the cross sections. In a companion study (Petrangeli, 1999), the beam-column model was verified by the data of the cyclic tests on a shear critical RC pier.

D'Ambrisi and Filippou (1999) proposed a frame element to model shear-dominated RC members, which consisted of an elastic sub-element, a spread plastic sub-element, an interface bond-slip sub-element, and a shear spring sub-element, as shown in Figure 2-18. A phenomenological hysteretic law was adopted in the shear sub-element to represent the shear sliding in the critical area as well as shear distortion of the entire member, in which the influence of axial load on the opening and closing of shear cracks was considered. The element was validated by the quasi-static cyclic test data on shear critical RC structural members, such as beam, column, and bridge pier. In spite of the simplicity, the strain compatibility is not enforced in this model. Moreover, these sub-elements are uncoupled, and the moment-shear interaction cannot be modeled appropriately.

Martinelli (2008) proposed a beam-column model by adopting an enhanced displacement-based Timoshenko beam-column element and a 2D truss model as constitutive law of reinforced concrete. The truss model consists of two diagonal concrete elements in tension and compression respectively, and one horizontal element representing

shear reinforcement. Cyclic loading test data from an RC beam and a short bridge pier, both had mixed flexure-shear behavior, have been used to validate the model. In spite of the good agreement between the test data and analysis, the ability of the model to capture the post-peak behaviors of the two specimens has not been demonstrated because the specimens did not show significant strength degradation.

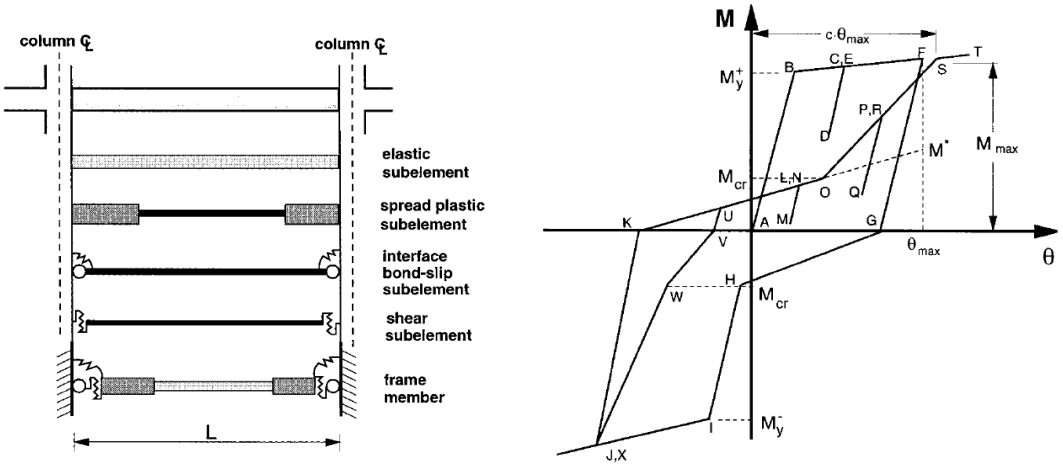

(a) Sub-elements in the model

(b) A phenomenological hysteretic law for shear behavior

Figure 2-18. A frame model proposed by D'Ambrisi and Filippou (1999)

Ceresa et al. (2009) presented a displacement-based beam-column element enriched with a bubble term to overcome the shear locking issue. A bi-axial constitutive law was developed for axial-flexure-shear interaction based on the modified compression field theory (MCFT). The model has been validated with cyclic loading test data from a shear-dominated planar RC wall. However, the ability of the model to capture the post-peak strength degradation has not been demonstrated as the wall did not exhibit strength degradation.

Saritas and Filippou (2009, 2013) proposed a mixed beam-column element, which can be used to model cyclic behavior of RM or RC walls. A mixed beam formulation

proposed by Taylor et al. (2003), which is based on a three-field (displacement, strain, and stress) Hu-Washizu variational principle, was adopted in this study. This element is free of shear locking, and allows a wall to be modeled with a very coarse mesh. The nonlinear flexural and shear behavior of a shear wall was modeled by a fiber section model in a distributed plasticity manner. For each fiber, a three-dimensional plastic damage concrete material model was adopted. The model has been validated with extensive test data, including three flexure-dominated RC planar walls and two shear-dominated RC columns. Similar to the beam-column model proposed by Pentrageli (1999), this model is computationally expensive because iteration is required in both element and material levels.

Ezzeldin et al. (2016) evaluated 20 archetypes of RM shear walls with boundary elements with two-dimensional frame models. To model the flexural behavior of the selected walls, two displacement-based elements with fiber sections are used. An additional nonlinear zero-length element was connected to the beam-column model in series to account for strain penetration at the support.

Ezzeldin et al. (2018) presents a concentrated plasticity beam-column model to represent the nonlinear behavior of flexure-dominated RM shear walls. As shown in Figure 2-19, this model consists of an elastic beam-column element connected in series of a zero-length rotational spring. A phenomenological moment-curvature hysteretic relation was proposed and adopted in the rotational spring. Different modeling parameters were calibrated for the walls with confined boundary elements, the flanged walls, and the slab-coupled wall systems, respectively. The proposed model has been validated with extensive test data on RM shear walls and wall systems with different configurations (Ashour et al. 2016, Ezzeldin et al. 2017).

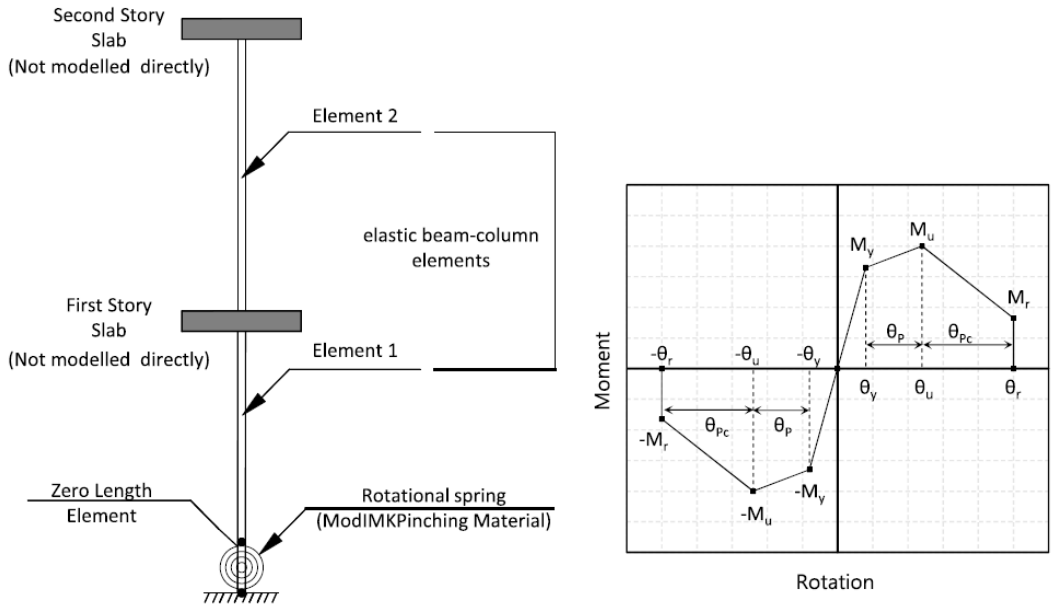

(a) Modeling scheme of a two-story RM wall (b) A phenomenological moment-curvature relation for shear

Figure 2-19. A concentrated plasticity beam-column model proposed by Ezzeldin et al. (2018)

Peruch et al. (2019) used a force-based Timoshenko beam element to model RM shear walls. In this model, the axial-flexural behavior was modeled with a fiber-section approach, and a phenomenological nonlinear shear law was proposed for shear response. This model was validated with the test data of six shear-dominated planar RM walls tested by Shing et al. (1991), with the maximum drift ratio less than 2%.

2.3.3. Other Simplified Models

Orakcal and Wallace (2006) proposed a macroscopic model for nonlinear flexural and shear behaviors of RC and RM walls. Figure 2-20 shows the idealization of a wall with the proposed Multiple-Vertical-Line-Element-Model (MVLEM). As shown, the macro-element consists of two rigid beams connected with multiple vertical line elements and a horizontal spring placed at the center of the element. Uniaxial nonlinear material properties of vertical reinforcement and concrete/masonry are assigned to the vertical line elements for axial-flexural behavior, whereas the horizontal spring is used to simulate shear response of a wall. An RC or RM structural wall can be modeled as a stack of the MVLEM elements in series. The model has been calibrated and validated with the two slender flexure-dominated RM walls tested by Thomsen and Wallace (1995). In spite of the good agreement between test data and analytical results, the model is not intended to capture diagonal shear failure and axial-flexural-shear interaction.

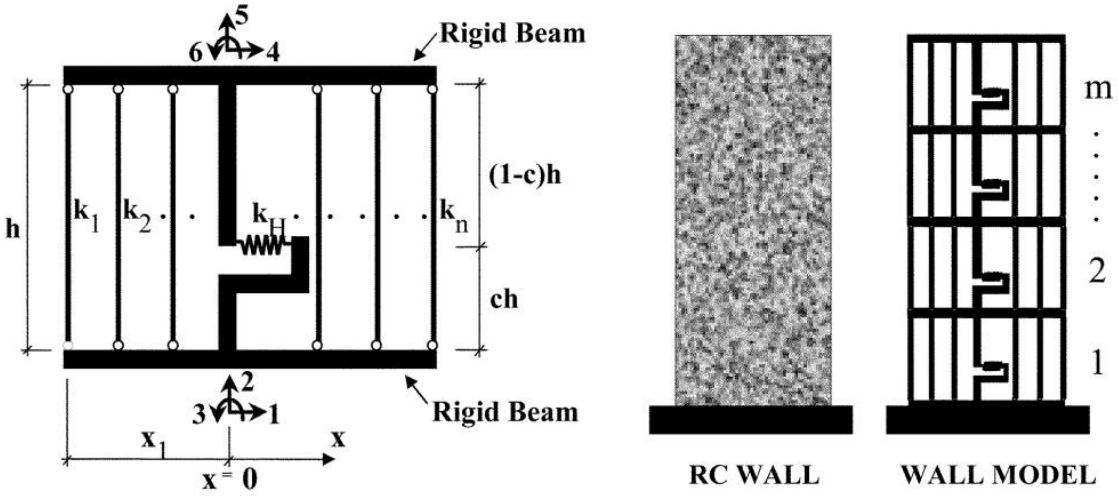

(a) MVLEM macro-element (b) Model idealization of a slender RC wall

Figure 2-20. Idealization of an RC wall with Multiple-Vertical-Line-Element-Model (Orakcal and Wallace, 2006)

To improve the MVLEM model (Orakcal and Wallace, 2006), Kolozvari et al. (2015) proposed an SFI-MVLEM model with the consideration of axial-flexural-shear interaction. As shown in Figure 2-21, for each vertical line element in this model, a two-dimensional fixed-strut-angle RC panel model is adopted. The RC panel model accounts for the coupling of axial and shear responses, and also allows coupling of flexural and shear responses at the element level. In a companion study (Kolozvari et al., 2014), the SFI-MVLEM model was calibrated and validated with the test data one five moderately reinforced slender concrete walls. The results indicated that the proposed model was able to capture the flexural-shear interaction in the five selected RC walls. However, the strength degradation of the five walls was not well represented due to the inability of the model in capturing the various failure mechanisms, such as buckling of reinforcing bars and sliding near the wall base.

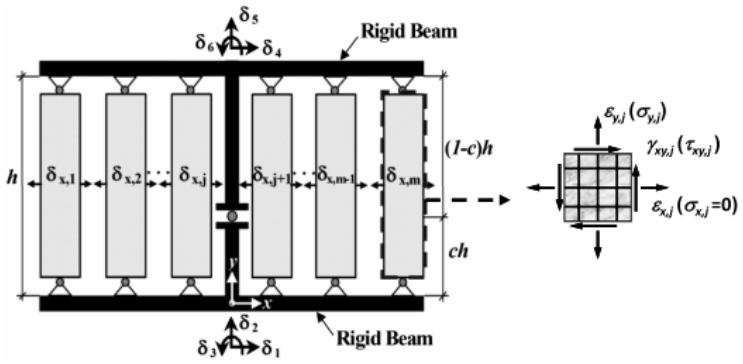

Figure 2-21. RC panel element and SFI-MVLEM element (Kolovzari et al., 2015)

Another simplified modeling approach for RC and RM walls is beam-truss models. Lu and Panagiotou (2014) presented a three-dimensional beam-truss model to capture nonlinear flexural and shear behaviors of nonplanar RC walls. As shown in Figure 2-22, nonlinear Euler-Bernoulli fiber-section beam elements are used to represent reinforcement and concrete in vertical direction, whereas nonlinear truss elements are used to represent

the horizontal reinforcement and the concrete in horizontal and diagonal directions. The model has been validated with the test data on three RC walls with T-shape, C-shape, and I-shape sections, respectively.

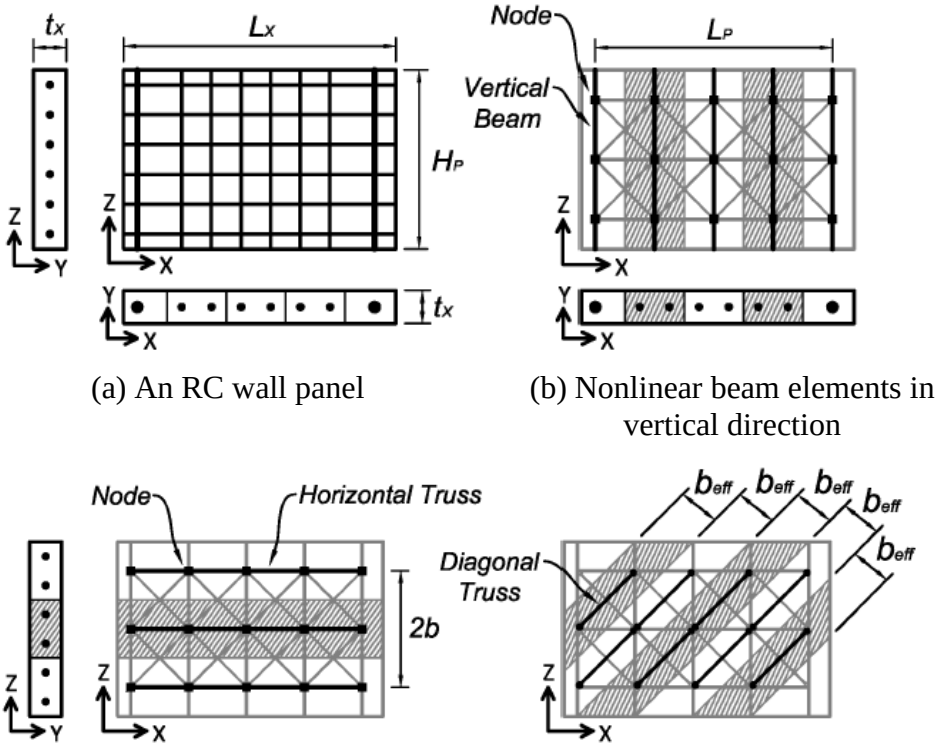

(a) An RC wall panel

(b) Nonlinear beam elements in vertical direction

(c) Nonlinear truss elements in horizontal direction

(d) Nonlinear truss elements in diagonal direction

Figure 2-22. A beam-truss model for RC shear walls (Lu and Panagiotou, 2014)

CHAPTER 3 A BEAM-COLUMN MODEL FOR FLEXURE-DOMINATED REINFORCED MASONRY SHEAR WALLS

This chapter presents a beam-column model to represent nonlinear seismic behavior of flexure-dominated RM shear walls. The work presented in this chapter is built upon the efforts in the ATC-114 project (NIST, 2017). A rational modeling approach using a force-based, fiber-section, beam-column element with predefined plastic-hinge lengths is proposed along with material models that can capture local failure mechanisms of flexure-dominated RM walls. The model accounts for the buckling and low-cycle fatigue of vertical reinforcing bars as well as plastic strain localization. The proposed model has been calibrated and validated with experimental data on walls with rectangular and T-sections.

3.1. Modeling Approach

3.1.1. Beam-Column Model

A simple approach to model the nonlinear behavior of a flexure-dominated RM wall is by means of a beam-column element. However, to capture the post-peak load degradation of a wall in an accurate manner, it is important that the model appropriately accounts for the crushing and spalling behavior of masonry, and the buckling and low-cycle fatigue of the reinforcing bars after the adjacent masonry has spalled off. For this purpose, a nonlinear modeling method using a force-based beam-column element and appropriately calibrated nonlinear material models, all available in the software platform OpenSEES (McKenna et al. 2000), is presented here. The beam-column element has a pre-defined plastic-hinge zone at each end (Scott and Fenves, 2006). In the plastic-hinge zone, a fiber section is used to simulate the nonlinear axial and flexural behaviors of a wall

section. Each fiber is assigned a uniaxial material law to describe the nonlinear behavior of masonry or flexural reinforcement. The material laws are so calibrated that they can account for the spalling of masonry after crushing, and the subsequent buckling and fracture of the reinforcing bars, with the latter caused by low-cycle fatigue. The material models are phenomenological rather than physics based. However, this approach affords computational efficiency without ignoring the essential failure mechanisms that govern the post-peak behavior of a flexure-dominated wall. Details of these material models will be discussed in the following sections.

In this modeling approach, one needs to assume an effective plastic-hinge length (L_p) for the wall, which is represented by the predefined plastic-hinge zone of the beam-column element, to capture the localization of plastic deformation. In theory, L_p should be a function of the wall dimensions as well as the loading condition, and it should provide an accurate description of the post-peak behavior of the wall when appropriate material models are used, with the assumption that the plastic deformation within this zone is uniform. Hence, the use of this beam-column model will ensure the objectivity of numerical results regardless of the element size, as long as the predefined plastic-hinge zone accurately reflects the effective plastic-hinge length of the wall. Several formulas have been proposed to estimate L_p for an RM wall, e.g., Priestley et al. (2007). Here, L_p is assumed to be 20% of the effective height of the wall (h_{eff}), which has been shown to provide good numerical results with beam-column models for walls of different height-to-length ratios (NIST, 2010). The effective height is defined as the distance between the end of the wall where plastic deformation is considered and the point of zero moment (or the point of inflection). Figure 3-1 shows an example of the beam-column model for a

cantilever wall. In this model, the shear deformation of the wall is modeled with a linear elastic spring, as shown in Figure 3-1(b). However, the stiffness of this spring should account for the effect of wall cracking as will be discussed later.

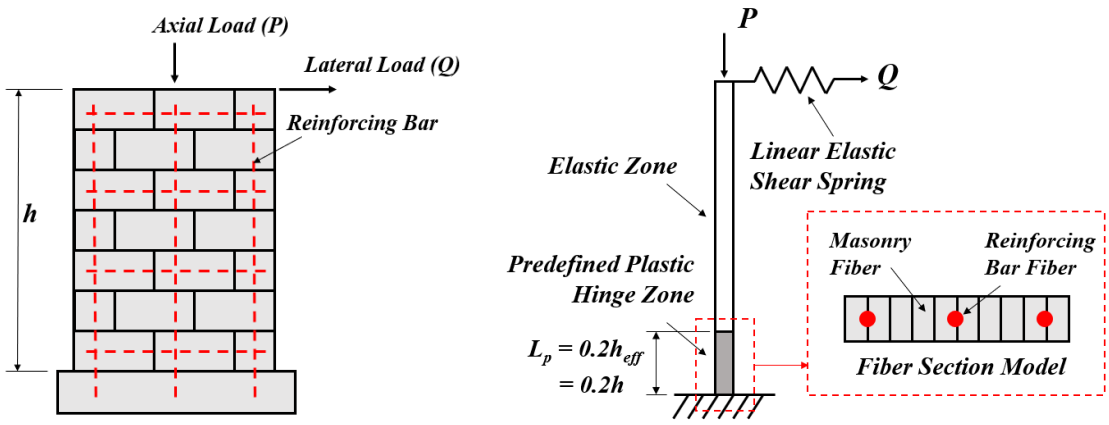

(a) (b)

Figure 3-1. (a) Cantilever reinforced masonry wall; (b) Beam-column model with a shear spring

3.1.2. Material Model for Masonry

Figure 3-2 shows the uniaxial stress-strain law selected for masonry, which is based on the concrete model proposed by Kent and Park (1990). The tensile strength of masonry is assumed to be zero. The peak compressive strength, f'_m, is to be determined from masonry prism tests, and the compressive strain (ε_p) at which the peak stress is reached is taken as 0.003. The post-peak residual strength is assumed to be 20% of the peak strength. The post-peak compressive behavior of the model is controlled by the strain parameter ε_r, which is the strain at which the residual strength is first reached, and it is selected to be 0.006. The proposed compressive stress-strain relation is based on masonry prism test data (e.g., Atkinson and Kingsley, 1985) and additional calibration with cyclic quasi-static wall test data (Ahmadi 2012; Sherman 2011; Kapoi 2012; Shing et al. 1991; Shedid et al. 2008)

using beam-column elements with the effective plastic-hinge length assumed to be $0.2h_{eff}$. The residual compressive strength is assumed to remain constant as strain increases to ensure the robustness of the numerical solution.

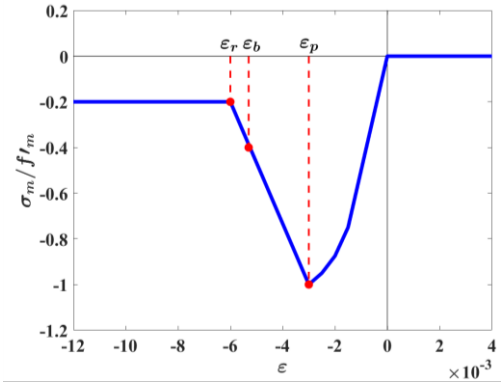

Figure 3-2. Normalized stress-strain relation for masonry

3.1.3. Material Model for Vertical Reinforcing Steel

Under severe seismic loading, the vertical reinforcing bars in a wall may undergo yielding, buckling, and fracture caused by low-cycle fatigue. Figure 3-3(a) shows the material model proposed for vertical reinforcing steel. It is a phenomenological material law developed to represent the aforementioned behaviors in an approximate manner.

Bar buckling is represented by a sudden drop of the compressive stress in the stress-strain law when the compressive strain reaches a critical value ε_b. The value of ε_b is taken to be -0.0053, which is the strain at which the compressive strength of masonry drops to 40% of the peak stress, as shown in Figure 3-2, with the assumption that the strain in the bar is the same as that in the adjacent masonry. The strain ε_b is considered as the level at which severe masonry crushing and spalling occur. After buckling, the compressive stress in the bar drops linearly to 10% of the yield strength f_y. The value of ε_{10}, at which the

residual compressive strength is first reached, is taken to be -0.01 to represent a rapid strength drop due to buckling, but not too sudden a drop which could cause numerical problems.

Under a monotonically increasing load, the peak tensile strength of steel is assumed to be 1.5 times the yield strength, which is typical for steel bars with a nominal yield strength of 414 MPa (Grade 60 steel in US standard). The strain at which tensile fracture occurs depends on the loading history. When a wall is subjected to severe cyclic loading, toe crushing and the spalling of masonry will occur, and the exposed vertical bars may undergo repeated buckling and straightening, which will induce low-cyclic fatigue. As a result, compared to reinforcing bars subjected to monotonic loading, fracture will occur in a cyclically loaded bar at a lower strain level. Hence, two types of loading histories are considered in modeling the tensile behavior of a bar, and one has to determine the loading history *a priori*. One is monotonically increasing tensile loading. For this case, it is assumed that the peak tensile strength is reached at a strain (ε_{ps}) equal to 0.10, which is typically observed in uniaxial tension tests. After this, it is assumed that bar fracture initiates and the tensile stress drops linearly as the strain increases. The strain (ε_0) at which the tensile stress reaches zero is assumed to be 0.15, which is on the lower end to account for the fact that the actual plastic strain of a bar in the effective plastic-hinge zone may not be uniform. The other case is cyclic loading, for which it is assumed that the peak tensile stress is reached at a reduced value of ε_{ps}, between 0.03 and 0.072, to account for the low-cycle fatigue. The strain (ε_0) at which the tensile stress reaches zero is so determined that the stress drops at the same rate as in the monotonic loading case. For simplicity, the model does not consider the number or amplitude of the strain cycles. However, it accounts for

the fact that bars in a wall with a higher amount of vertical reinforcement or a higher axial compressive load are expected to have a lower fracture strain as masonry spalling tends to occur earlier. To model this, the relation shown in Figure 3-3(b) is used to determine the value of ε_{ps}. In this relation, ε_{ps} is a function of the sum of the vertical reinforcement index (α) and axial load ratio (β), which are defined as follows.

$$\alpha = \frac{f_y}{f_m^{'}} \rho_v \tag{3-1}$$

$$\beta = \frac{P}{f_m^{'} A_n} \tag{3-2}$$

in which ρ_v is the ratio of the vertical steel area to the net cross-sectional area, A_n, of the wall, and *P* is the axial compressive force.

The aforementioned parameters for the steel model were calibrated indirectly with cyclic quasi-static wall test data (Ahmadi 2012; Sherman 2011; Kapoi 2012; Shing et al. 1991; Shedid et al. 2008) using the beam-column element model considered here with the effective plastic-hinge length assumed to be $0.2h_{eff}$. However, data from monotonic loading wall tests are not available. It should be mentioned that a model calibrated this way may over-estimate the cyclic strength degradation of a wall subjected to earthquake loading because the cyclic loading history applied in a quasi-static test was often far more severe than what would be expected in an earthquake.

The material models for masonry and steel presented here can also be adopted for other types of beam-column elements. However, when the plastic-hinge length assumed in the model differs from 20% of the effective wall height, the post-peak slopes of the material

models need to be changed to ensure the objectivity of the numerical results under strain localization (Bazant and Oh,1983). For beam-column elements, methods to determine the post-peak slopes can be found in Coleman and Spacone (2001) and NIST (2010).

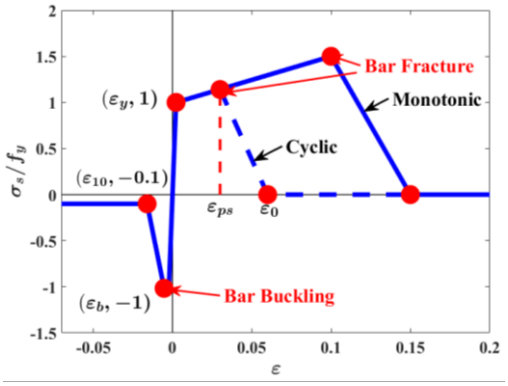

(a) Normalized stress-strain relation for steel accounting for bar buckling and fracture;

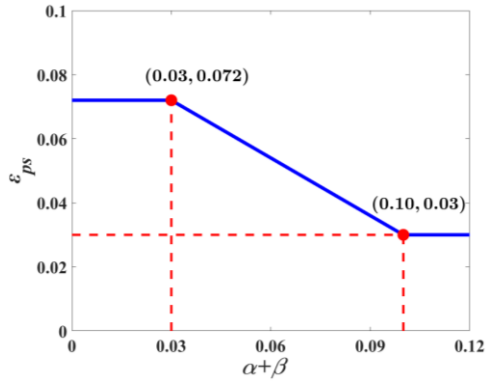

(b) Tensile strain at bar fracture as a function of steel and axial compressive load ratios for cyclic analysis

Figure 3-3**.** A steel model proposed for vertical reinforcing bars

3.1.4. Consideration of shear deformation

In this model, the shear deformation of a flexure-dominated wall is accounted for by introducing a linear elastic shear spring connected in series with the lateral degree of freedom at one end of the beam-column element, as shown in Figure 3-1(b). However, flexural and shear cracks may develop before the peak resistance of a wall has been reached, which can lead to a significant reduction of the shear stiffness. Test data of Shing et al.

(1989) have shown that the average shear stiffness of a reinforced masonry cantilever wall was around 50% of the theoretical elastic shear stiffness when the applied lateral force reached 50% of the shear capacity, and could be as low as 20% of the theoretical value when major shear cracks developed. Based on this observation, it is suggested that the stiffness (k_v) of the shear spring be 35% of the theoretical value as given in Eq. 3-3.

$$k_v = \frac{0.35 A_v G_m}{h} \tag{3-3}$$

in which A_v is the effective shear area of the wall section, G_m is the shear modulus of masonry, and h is the height of the wall. For a flanged wall, A_v can be taken as the cross-sectional area of the web.

3.2. Validation of the Proposed Model

Experimental data on flexure-dominated RM walls with both rectangular and T-sections have been selected to calibrate and validate the proposed frame model. Table 3-1 shows the dimensions, reinforcement amount, axial load, and material properties of 21 cantilever wall specimens with rectangular sections that have been selected (Ahmadi 2012; Sherman 2011; Kapoi 2012, Shing et al. 1990; Shedid et al. 2008). Eleven of these walls had the vertical reinforcement lap-spliced at the base. These specimens had aspect ratios (height-to-length ratio) ranging from 0.78 to 4.5, and the vertical reinforcement ratio ranging from 0.16% to 1.31%. The axial compressive load ratio, which is defined in Eq. 3-2, ranges from 0.0 to 0.125. Among these selected specimens, the experimental responses of the walls tested by Ahmadi (2012), Sherman (2011), and Kapoi (2012) were used to calibrate and validate the model parameters, whereas the responses of walls tested by Shing et al. (1990) and Shedid et al. (2008) were only used to verify the calibration. In addition,

three cantilever T-walls tested by He and Priestley (1992) are considered. The dimensions and material properties for these three flanged walls are shown in Tables 3-2 and 3-3. Figure 3-4 shows the cross-sections of the three specimens. These walls had the vertical reinforcing bars uniformly distributed in the flange and web. Wall UCSD-F1 and UCSD-F2 had the same dimensions and axial load ratio, but the amount of the vertical reinforcement of Wall UCSD-F2 is the half of that of Wall UCSD-F1. Wall UCSD-F3 had a very wide flange, with the ratio of the flange width to the web length equal to 1.38. For the flanged walls, the vertical reinforcement index (α), the axial compressive load ratio (β), and the ratio of the total reinforcing bars in wall web to that in wall flange (η) are shown in Table 3. The values of α and β are based on the total net sectional area (A_n) of the web and the flange. This is for the sake of simplicity, and the values are used to determine the tensile strain at peak stress (ε_{ps}) for the vertical reinforcement. Hence, the beneficial influence of the flange in delaying the buckling and low-cycle fatigue of the bars is ignored.

The software platform OpenSEES (Mazzoni et al. 2005; McKenna et al. 2000) is used to perform cyclic analyses on the selected wall specimens using the beam-column element (Beam-with-Hinge element) discussed in Section 3.1. Each wall is represented by one beam-column element with a pre-defined plastic hinge length to capture the plastic deformation at the wall base and a zero-length linear elastic shear spring element connected in series. For the cantilever walls, the effective wall height is identical to the actual wall height. Thus, the pre-defined plastic hinge length is set to 20% of the wall height. Masonry is modeled by the Kent-Park model (Concrete01 in OpenSEES), whereas the vertical reinforcement is modeled by the Hysteretic model in OpenSEES (McKenna et al. 2000). The calibration of the backbone curves for these models is discussed in the Section 3.1.

For the hysteretic behavior of the vertical reinforcing bars, the pinching and in-cycle damage parameters in the Hysteretic model are calibrated with the wall test data. The values of these parameters are shown in Table 3-4. The material strengths shown in Tables 3-1 to 3-3 are used.

Table 3-1. Selected cantilever wall specimens with rectangular sections

Specimen	Height (m)	Length (m)	Thickness (m)	Axial load Ratio (β)	f_y (MPa)	f'_m (MPa)	$\rho_v f_y / f'_m$ (α)
UT-PBS-03[1]	2.438	2.438	0.194	0	423	30.7	0.046
UT-PBS-04[1]	2.438	2.438	0.194	0	423	30.7	0.022
WSU-W-1A	2.032	1.016	0.194	0.0625	451	19.1	0.170
WSU-W-1B[1]	2.032	1.016	0.194	0.0625	456	21.0	0.170
WSU-W-2A	2.032	1.016	0.194	0.125	450	19.1	0.079
WSU-W-2B[1]	2.032	1.016	0.194	0.125	450	21.0	0.079
WSU-W-04[1]	1.829	1.829	0.194	0.0625	450	21.0	0.071
WSU-W-05[1]	1.422	1.829	0.194	0	450	21.0	0.071
WSU-W-06[1]	1.422	1.829	0.194	0.0625	450	21.0	0.071
WSU-W-07 (C1)[1]	2.032	1.016	0.194	0	450	20.9	0.071
WSU-W-08 (C2)[1]	2.032	1.016	0.194	0.0625	455	20.9	0.072
UT-W-13[1]	3.658	1.219	0.194	0.0281	421	30.7	0.099
UT-W-17[1]	3.658	0.813	0.194	0.0297	421	29.0	0.105
CU-Boulder-1	1.829	1.829	0.143	0.0833	441	20.1	0.101
CU-Boulder-2	1.829	1.829	0.143	0.0833	441	20.1	0.101
CU-Boulder-10	1.829	1.829	0.143	0.0394	441	22.3	0.096
CU-Boulder-12	1.829	1.829	0.143	0.0394	441	22.3	0.096
CU-Boulder-15	1.829	1.829	0.143	0.0347	448	23.0	0.122
McMaster-1	3.658	1.829	0.191	0	502	17.0	0.071
McMaster-2	3.658	1.829	0.191	0	502	17.0	0.191
McMaster-3	3.658	1.829	0.191	0	502	17.0	0.179

[1] vertical reinforcing bars lap spliced at the base

Table 3-2. Dimensions and material properties of the selected cantilever T-wall specimens

Specimen	Height (m)	Web Length (m)	Flange Length (m)	Thickness (in)	f_y (MPa)	f'_m (MPa)
UCSD-F1	3.658	1.168	2.642	0.143	491	19.9
UCSD-F2	3.658	1.168	2.642	0.143	523	19.9
UCSD-F3	3.658	1.168	5.080	0.143	523	15.9

Table 3-3. Dimensionless parameters of the selected cantilever T-wall specimens

Specimen	Axial Compression Ratio (β)	$\rho_v f_y / f'_m$ (α)	$A_{s,f}/A_{s,w}$ (η)
UCSD-F1	0.0347	0.168	1.5
UCSD-F2	0.0347	0.081	1.5
UCSD-F3	0.0435	0.102	3.0

Table 3-4. Calibrated hysteretic model parameters for the reinforcing steel (parameters are explained in OpenSEES)

Hysteretic Parameter	Value	Notes
PinchX	1.0	Pinching factor 1
PinchY	1.0	Pinching factor 2
ξ	0.0	Reduction factor to unloading stiffness
Dmg1	0.0	Ductility-proportional in-cycle damage factor
Dmg2	0.02	Energy-proportional in-cycle damage factor

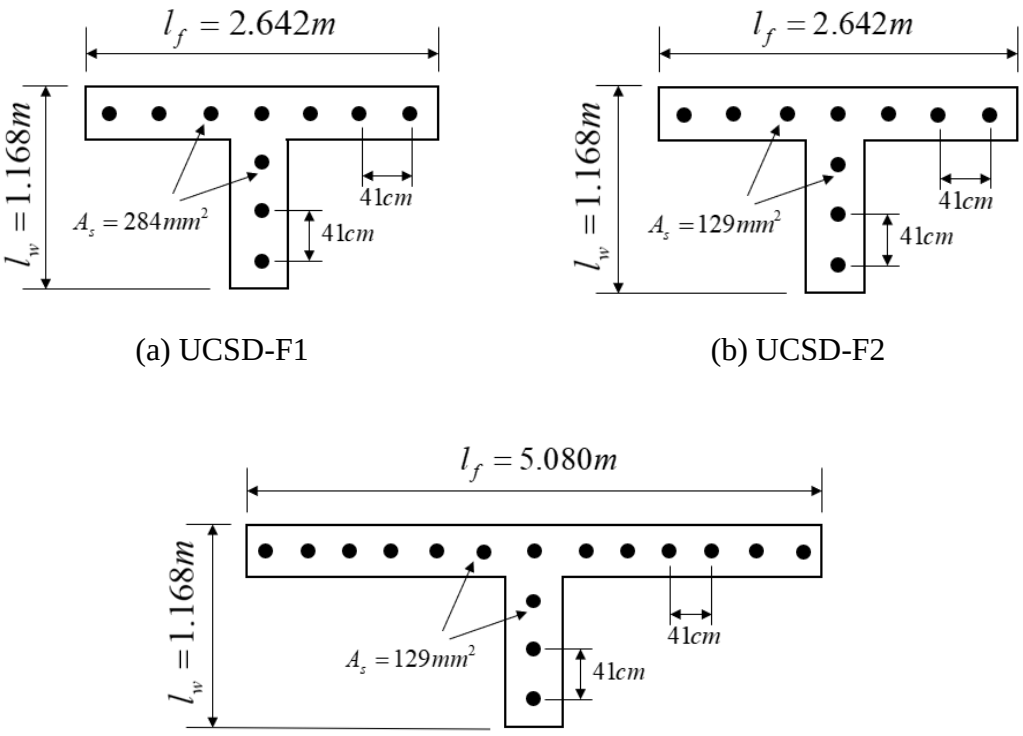

(a) UCSD-F1

(b) UCSD-F2

(c) UCSD-F3

Figure 3-4. Cross-sections of T-wall specimens

3.2.1. Rectangular-Sectioned Walls

The lateral load-vs.-lateral displacement hysteresis curves from the cyclic analyses the 21 selected planar walls in Table 3-1 are shown in Appendix I, together with the experimental results. Figure 3-5 shows the results of the selected six walls. As shown, the beam-column models can capture the peak strength, strength degradation, and hysteretic behavior of the wall specimens well, with the numerical results slightly under-estimating the peak strengths and over-estimating the strength degradation for most of the cases.

Some important observations are highlighted here. The results for walls UT-PBS-03 and UT-PBS-04 are shown in Figures 3-5(a) and 3-5(b). Both walls had an aspect ratio

of one and were not subjected to any axial load. Wall UT-PBS-03 had #4 vertical bars spaced at 20.3cm (8 in.) on center, whereas UT-PBS-04 had #4 bars spaced at 40.6cm (16 in.) on center. Because of the lower amount of vertical reinforcement, UT-PBS-04 exhibited a more ductile behavior in that its peak resistance was reached at a drift ratio of 1.75%, whereas the peak load for UT-PBS-03 was reached at about 0.80%. Nevertheless, UT-PBS-04 exhibited a more rapid strength drop after passing its peak strength. This is attributed to the fact that UT-PBS-04 had a smaller number of vertical bars with a wider bar spacing. As a result, the loss of the vertical bars due to fracture at the extreme ends in that wall had a more significant consequence than that in UT-PBS-03. As shown in Figures 3-5(a) and 3-5(b), this phenomenon is well captured by the beam-column model.

Figures 3-5(c) and 3-5(d) show the results for two slender walls (WSU-W-07 and WSU-W-08), which had an aspect ratio of two. They had the same amount of vertical reinforcement, but one of them had no axial load. With the axial compressive load, Wall WSU-W-08 developed a higher maximum lateral resistance than Wall WSU-W-07. Although the effect of axial load on lateral resistance is well captured by the model, the analyses under-estimate the maximum lateral resistance for both walls. This can be attributed to the fact that the models show bar fracture, whereas the tests did not have bar fracture. Nevertheless, necking was observed in one of the extreme vertical bars in wall WSU-W-08 during the test.

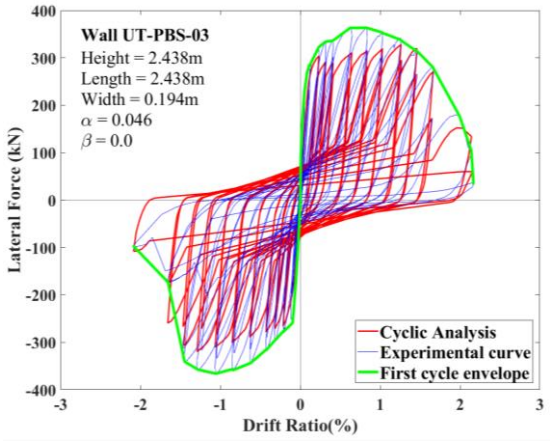

(a) UT-PBS-03

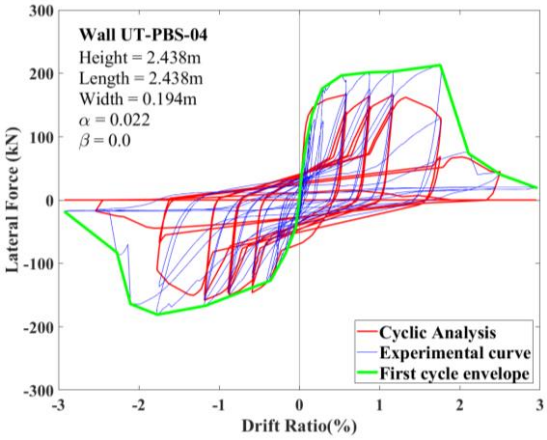

(b) UT-PBS-04

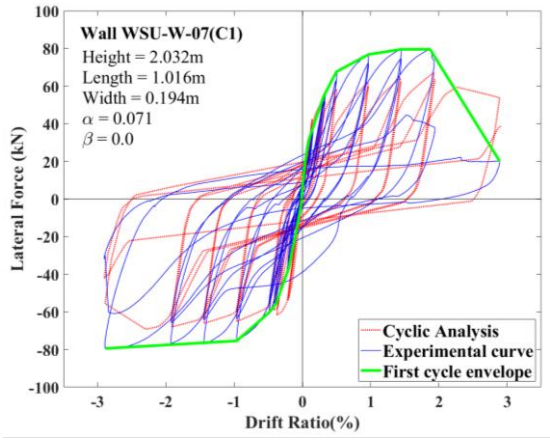

(c) WSU-W-07(C1)

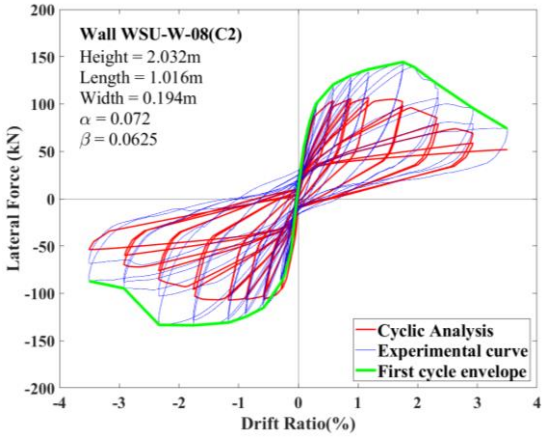

(d) WSU-W-08(C2)

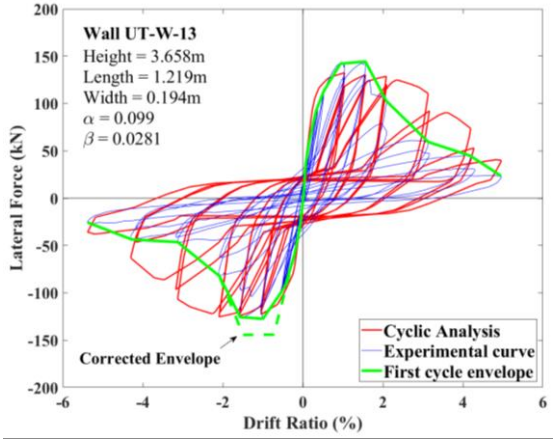

(e) UT-W-13

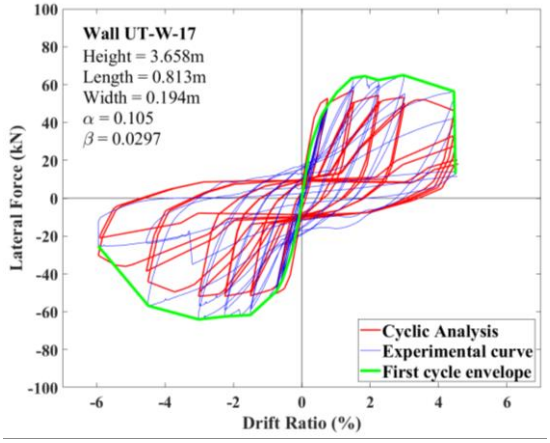

(f) UT-W-17

Figure 3-5**.** Comparison of numerical results with experimental data for planar RM walls

Figure 3-5(e) and 3-5(f) show the results for two very slender walls (UT-W-13 and UT-W-17), which had aspect ratios of 3 and 4.5, respectively. Both walls had an axial compressive load ratio of 5% and $\rho_v = 0.72\%$. While the load-displacement hysteresis curves for wall UT-W-17 are well captured, the analysis significantly under-estimates the strength degradation shown by UT-W-13. The severe strength degradation exhibited by that wall specimen is believed to be caused by the failure of the lap splices in the vertical reinforcement, which is not modeled in the analysis. The failure of the lap splices was caused by severe masonry spalling at the crushed toes.

3.2.1.1. Influence of Lap-Splice at Wall Base

Two pairs of wall specimens, WSU-W-1A/1B and WSU-W-2A/2B, were tested by Sherman (2011) to compare the behaviors of flexure-dominated walls that had vertical reinforcement with and without lap splices at the base. Each pair had identical designs and axial loads, except that one wall had lap splices at the base, while the other did not. The lengths of the lap splices complied with TMS 402/602 (TMS, 2016). The test results are compared in Figure 3-6. The numerical results obtained with the beam-column element models are also shown in the figure. Since the model does not account for the presence or absence of lap splices, only one analysis has been conducted for each pair. The test results show that the walls with lap splices had more rapid post-peak strength degradation and more pinched hysteresis curves than those without. The models better capture the behavior of the walls with lap splices. This is attributed to the fact that the database used to calibrate the hysteretic model for steel is slightly biased towards walls with lap splices. It is evident that the post-peak load degradation and pinching of the hysteresis loops are heavily influenced by the steel mode.

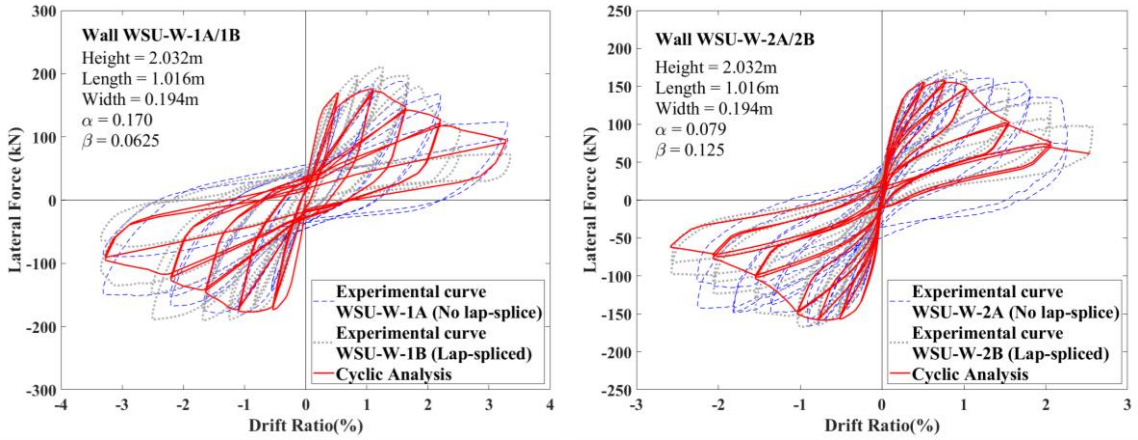

(a) WSU-W-1A/1B (b) WSU-W-2A/2B

Figure 3-6**.** Comparison of numerical results with experimental data for two pairs of walls with and without lap splices

3.2.1.2. Monotonically Increasing versus Cyclic Loading

As discussed previously, the material law for the steel reinforcement distinguishes the behavior of a bar under monotonically increasing loading from that under fully reversed cyclic loading. Under fully reversed cyclic loading, the model accounts for low-cycle fatigue. Here, the beam-column element model with the proposed steel material law is used to examine the behaviors of walls subjected to monotonic and cyclic loading histories. For these analyses, the respective tensile stress-strain curves corresponding to the two loading histories, as shown in Figure 3-3, are used for the vertical reinforcing steel. As shown in Figure 3-7, walls with three different values of $(\alpha + \beta)$, where α and β are the reinforcement index and axial load ratio, respectively, as defined in Eqs. 3-1 and 3-2, are considered. The numerical results show that the behavior of walls that have a lower amount of vertical steel and a lower axial compressive load ratio is more sensitive to the loading history, being significantly more ductile under monotonically increasing loads than under

cyclic loads. This can be attributed to the fact that the behavior of these walls is significantly influenced by that of the steel reinforcement, whereas the behavior of walls having a higher axial load and reinforcement ratio is dominated by the crushing of masonry. However, experimental data from monotonic loading tests are not available to confirm this observation.

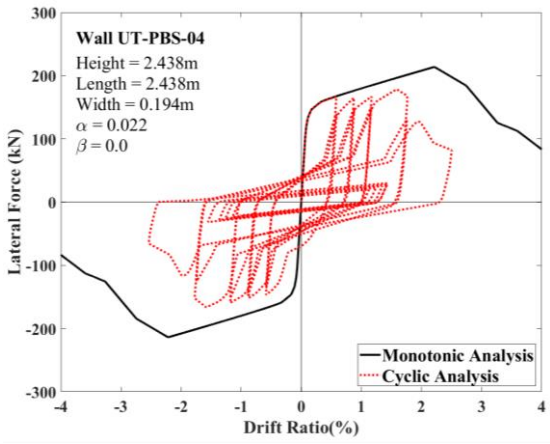

(a) $\alpha + \beta = 0.022$

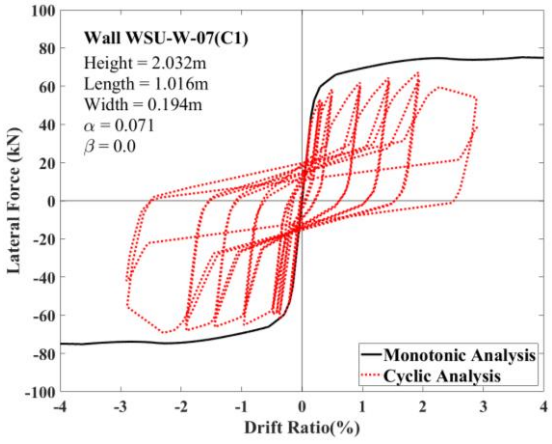

(b) $\alpha + \beta = 0.071$

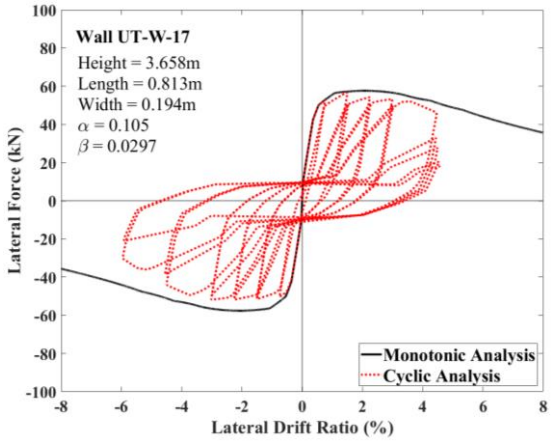

(c) $\alpha + \beta = 0.135$

Figure 3-7. Comparison of wall behaviors under monotonic and cyclic loads using beam-column models

3.2.2. T-Sectioned Walls

In Figure 3-8, the lateral load-vs.-drift ratio hysteresis curves obtained from the tests of the three T-walls by He and Priestley (1992) are compared to the numerical results. As expected for T-walls, both the experimental and numerical results show that the lateral resistance of the walls is weaker when loaded in the direction in which the flange is in compression than when the flange is in tension. The results also show that the post-peak load degradation is more rapid when the flange is in tension because of the crushing of the web toes. The dimensions and axial load ratios of UCSD-F1 and UCSD-F2 are identical, but the amount of flexural reinforcement in UCSD-F2 is half of that of UCSD-F1, as shown in Tables 3-2 and 3-3. However, in contrary to the expectation, UCSD-F2 exhibited a more rapid load degradation than UCSD-F1 when the flange was in tension in the tests. The numerical results show the opposite, which is consistent with the expectation. No explanation was provided in the original research report on the unexpected test results, but a picture of UCSD-F2 does show that it had more severe masonry spalling in the web than UCSD-F1. The amount of vertical reinforcement in the flange of UCSD-F3 is a little lower than that of UCSD-F1, but the former was subjected to a higher axial compressive load. The test results show that UCSD-F3 was a little stronger and more brittle than UCSD-F1 when the flange was in tension in both cases. However, the numerical results show that UCSD-F3 is a little weaker and much more brittle than UCSD-F1. This can be attributed to an over-estimation of the low-cycle fatigue phenomenon of the reinforcing bars in the model. For all three specimens, the models show a more rapid load degradation than the tests for the loading direction in which the flange is in compression. This can be attributed to the fracture of the web vertical reinforcement in the models, which was not observed in

the tests. Other than the above discrepancies, the beam-column models are able to capture the behaviors of the T-walls well.

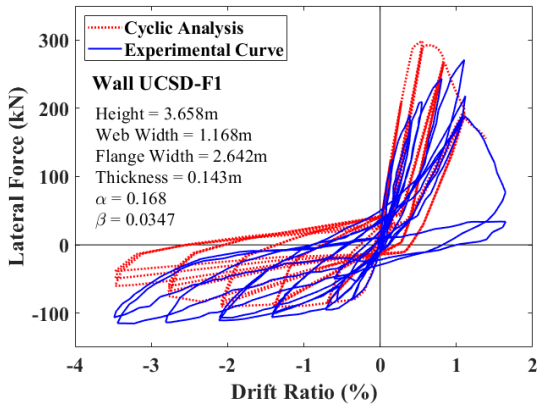

(a) UCSD-F1

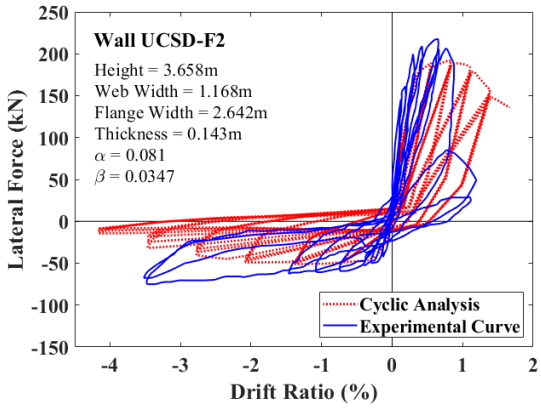

(b) UCSD-F2

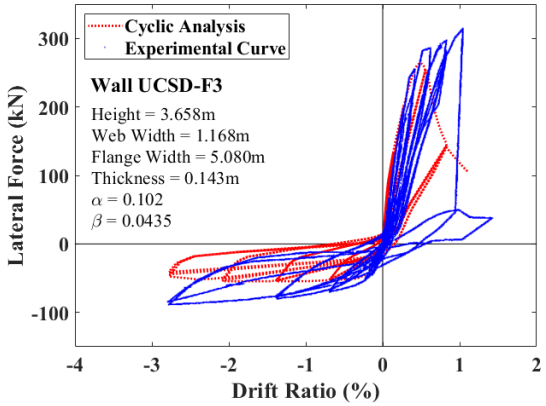

(c) UCSD-F3

Figure 3-8. Comparison of numerical results with experimental data for three T-walls

Chapter 3, in part, is a reprint of the material in a manuscript titled "Practical Nonlinear Analysis Methods for Flexure-Dominated Reinforced Masonry Shear Walls" that has been submitted to *ASCE Journal of Structural Engineering* in 2021 (under review). The authors of the manuscript are: the author of the dissertation and P. Benson Shing. The author of the dissertation is the primary author and the main contributor of the work presented in the manuscript.

CHAPTER 4 PROPOSED BACKBONE FORCE-VS.-DISPLACEMENT CURVES FOR REINFORCED MASONRY SHEAR WALLS

In this chapter, a method has been proposed to construct the lateral force-vs.-lateral displacement backbone curves for flexure-dominated RM walls in a simple and rational way. The proposed mothed is based on the moment-curvature relation of an RM wall section, which is generated with the fiber-section approach and the constitutive relations for masonry and steel presented in Chapter 3. It is applicable to walls with rectangular and flanged sections. While the method has been validated with experimental data from fully grouted walls, its possible application to partially grouted walls is suggested. Furthermore, based on experimental data, an empirical backbone curve has been proposed for fully grouted, shear-dominated, planar walls. Compared to the current recommendations in ASCE 41 (2017), the proposed backbone curves show significantly better agreement with past experimental data.

4.1. Flexure-dominated walls

As demonstrated in Chapter 3, the beam-column element and material laws presented in Section 3.1 are able to capture the lateral load capacities as well as the lateral load-vs.-displacement hysteretic relations for flexure-dominated walls with good accuracy. This chapter discusses how the material laws can be used to construct nonlinear lateral load-vs.-displacement backbone curves that can be adopted in ASCE 41 (2017) as specifications for the nonlinear analysis of flexure-dominated RM walls and for establishing improved acceptance criteria. Backbone curves based on current ASCE 41

(2017) specifications way under-estimate the displacement capacity of RM walls, as discussed in NIST (2017). The method proposed here for constructing the backbone curves is based on flexural theory and non-dimensional analysis, and is therefore, more general and rational than what is being used in ASCE 41 (2017).

The general lateral load-vs.-displacement backbone curve proposed here is shown in Figure 4-1. It represents the envelope of the load-displacement hysteresis curves for walls subjected to gradually increasing quasi-static displacement cycles, capturing the first-cycle response at each displacement amplitude. As shown in Figure 4-1, the backbone curve is defined in terms of five parameters: the effective initial stiffness (k), the expected maximum lateral load resistance (Q_{max}), the lateral displacement (Δ_m) at which the maximum resistance develops, the displacement (Δ_{75}) at which the post-peak resistance drops to 75% of Q_{max}, and the capping displacement (Δ_c), after which the lateral resistance of the wall can be ignored. The capping displacement is taken as the point at which the resistance drops to 50% of Q_{max}. The values of Q_{max}, Δ_m, Δ_{75}, and Δ_c can be computed with moment-curvature analysis and the assumed plastic-hinge length (L_p), as discussed in the following two sections using fully grouted cantilever walls with rectangular and T sections as examples. However, the methodology can be applied to walls with any boundary conditions resulting in a plastic hinge at one or both ends.

Figure 4-2 shows a moment-curvature curve obtained in an analysis using a fiber-section model with a monotonically increasing moment. The masonry and steel fibers assume the uniaxial material laws presented in Section 3.1. The values of M_{max}, ϕ_m, ϕ_{75}, and ϕ_c obtained can be used to determine the values of Q_{max}, Δ_m, Δ_{75}, and Δ_c, as explained in the following section. The monotonic moment-curvature relation ignores the

influence of in-cycle damage, which is controlled by the parameters *Dmg1* and *Dmg2* in the steel material law, whose values are shown in Table 3-3. However, the influence of the in-cycle damage is not significant and can therefore be ignored. In spite of this, the steel model that considers low-cycle fatigue due to cyclic loading is used. Hence, the resulting curve does represent the cyclic load effect. Since the material models are calibrated with quasi-static wall test results, the moment-curvature curve so obtained will provide a conservative backbone curve for assessing the performance under earthquake loading, which often induces less number of large displacement cycles.

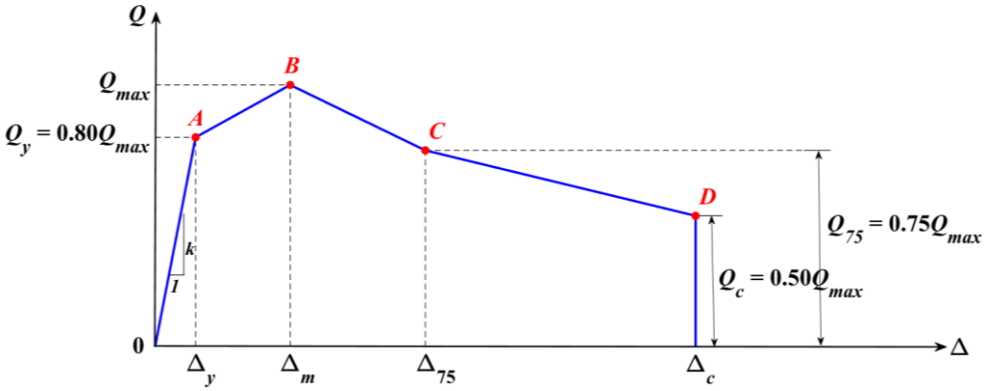

Figure 4-1. Backbone force-vs.-displacement curve for flexure-dominated RM walls.

Since only the values of M_{max}, ϕ_m, ϕ_{75}, and ϕ_c are of interest for the purpose of constructing the backbone curve, their non-dimensionalized values have been calculated and tabulated for walls with different axial compressive loads and reinforcement contents. This will be presented later in the following sections. With these tables, moment-curvature analysis need not be performed.

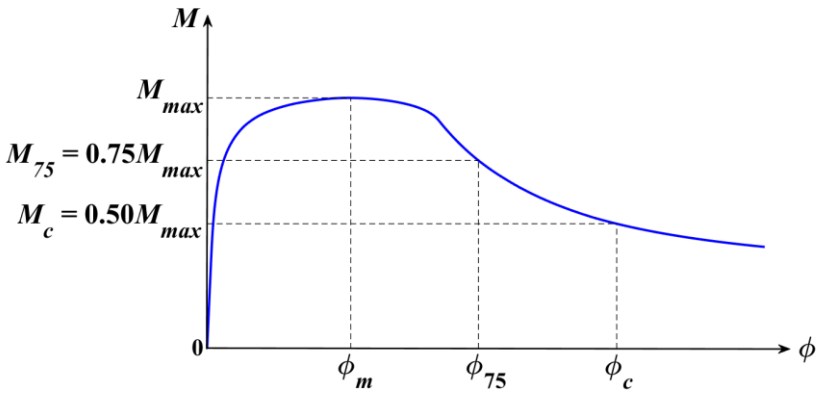

Figure 4-2. Moment-curvature relation for an RM wall section

4.1.1. Cantilever Walls with Rectangular Sections

Because of the abundance of experimental data, cantilever RM walls with rectangular sections are considered here. Similar to the specifications in ASCE 41 (2017), the effective initial stiffness (k) of an RM wall under in-plane loading, as shown in the backbone curve in Figure 4-1, is to be computed with elastic theory. Here, the reduction of the flexural and shear stiffnesses of a wall due to cracking is taken into account. The reduction factors proposed here are based on experimental data from Shing et al. (1991), Sherman (2011), and Ahmadi (2012). For a cantilever wall, the effective initial stiffness is calculated with the following equation.

$$k = \frac{1}{\frac{h^3}{3\zeta_f (E_m I)} + \frac{h}{\zeta_v (G_m A_v)}} \tag{4-1}$$

in which h is the wall height, A_v is the effective shear area of the wall section, I is the moment of inertia of an uncracked section, and E_m and G_m are the modulus of elasticity and shear modulus of masonry, respectively. The values of E_m and G_m can be calculated with the formulas specified in TMS 402 (2016) for the given compressive strength of

masonry. For a rectangular section, A_v is 5/6 of the net cross-sectional area of the wall. The flexural stiffness reduction factor (ζ_f) is suggested to be 0.15 and the shear stiffness reduction factor (ζ_v) is recommended to be 0.35. It should be noted that the value of ζ_f recommended here is significantly smaller than what is suggested in ASCE 41. However, since it is based on experimental observations, it also accounts for the plastic strain penetration effect.

With the values of M_{max}, ϕ_m, ϕ_{75}, and ϕ_c given by the moment-curvature relation, as shown in Figure 4-2 the values of the remaining critical parameters, Q_{max}, Δ_m, Δ_{75}, and Δ_c, for the backbone curve shown in Figure 4-1 can be calculated as follows. For a cantilever wall, the lateral resistance (Q_{max}) is equal to $\frac{M_{max}}{h}$. With the assumption that the plastic flexural deformation of a wall is uniformly distributed in the effect plastic-hinge length, L_p, the lateral displacements of a wall at different stages of strength degradation can be calculated with the following equations.

$$\Delta_{m/75/c} = \Delta_{fm/f75/fc} + \Delta_{vm/v75/vc} \tag{4-2}$$

$$\Delta_{fm/f75/fc} = \frac{M_{max/75/c}}{\zeta_f (E_m I)} \frac{h^2}{3} + \left(\phi_{m/75/c} - \frac{M_{max/75/c}}{\zeta_f (E_m I)} \right) L_p \left(1 - \frac{L_p}{2h} \right) \tag{4-3}$$

$$\Delta_{vm/v75/vc} = Q_{max/75/c} \frac{1}{\zeta_{v0} (G_m A_v)} \tag{4-4}$$

in which $M_{max/75/c}$ represents the peak moment, and moments at 75% and 50% of the peak, respectively, and $Q_{max/75/c}$ denotes the corresponding lateral resistances of the wall.

The corresponding lateral displacements ($\Delta_{m/75/c}$) consist of a flexural component, Δ_{fm}, Δ_{f75}, or Δ_{fc}, and a shear component, Δ_{vm}, Δ_{v75}, or Δ_{vc}. Here, ζ_f is suggested to be 0.15, the same as that for the initial effective stiffness, and the reduction factor ζ_{v0} for the shear stiffness is suggested to be 0.20 to account for the condition that extensive shear cracks may have developed when the peak lateral resistance is reached. The value of L_p is 20% of the wall height, the same as that for the beam-column element model considered in Section 3.1.

Furthermore, the capping lateral displacement (Δ_c) calculated with Eqs. (4-2) to (4-4) should not exceed 4% of the wall height, which is the maximum observed in the experimental studies used for the validation of this method (Shing et al. 1991; Shedid et al. 2008; Sherman, 2011; Ahmadi, 2012; Kapoi, 2012).

4.1.1.1. Non-Dimensionalized Moment-Curvature Relation

To simplify the determination of the critical parameters in the moment-curve relation required to construct a load-displacement backbone curve, these parameters are non-dimensionalized so that their values can be expressed as functions of a set of non-dimensionalized variables. Consider a fully grouted symmetric rectangular wall section, as shown in Figure 4-3(a). It is assumed that the flexural reinforcement has a uniform spacing and is distributed over a distance of $l_e = al_w$, where l_w is the length of the wall section and l_e is the center-to-center distance between the two extreme bars. For the simplicity of mathematical expressions, the reinforcement is assumed to be continuously distributed, as shown in Figure 4-3(b). As a result, the axial strength (P) and the moment resistance (M) about the centroidal axis can be expressed as follows.

$$P = -t\int_{-\frac{l_w}{2}}^{\frac{l_w}{2}} \sigma_m\left[\varepsilon(y)\right]dy - \frac{1}{a}\rho_v\int_{-\frac{l_e}{2}}^{\frac{l_e}{2}} \sigma_s\left[\varepsilon(y)\right]dy \tag{4-5}$$

$$M = -t\int_{-\frac{l_w}{2}}^{\frac{l_w}{2}} \sigma_m\left[\varepsilon(y)\right]ydy - \frac{t}{a}\rho_v\int_{-\frac{l_e}{2}}^{\frac{l_e}{2}} \sigma_s\left[\varepsilon(y)\right]ydy \tag{4-6}$$

in which y is the distance from the centroidal axis, t is the wall thickness, ρ_v is the vertical steel ratio with respect to the net cross-sectional area of the wall ($A_n = tl_w$), and σ_m and σ_s are the normal stresses in the masonry and the steel, respectively, which are functions of the strain ε and strain history associated with the axial deformation and curvature at the wall section. As shown in Figure 4-3(c), by assuming that the plane section remains plane during bending, the strain of each fiber along the section can be expressed as:

$$\varepsilon(y) = \phi\left(\frac{l_w}{2} - c - y\right) = \phi l_w\left(\frac{1}{2} - \frac{c}{l_w} - \frac{y}{l_w}\right) \tag{4-7}$$

in which c is the distance of the neutral axis of bending from the extreme compression fiber of the section, and ϕ is the wall curvature.

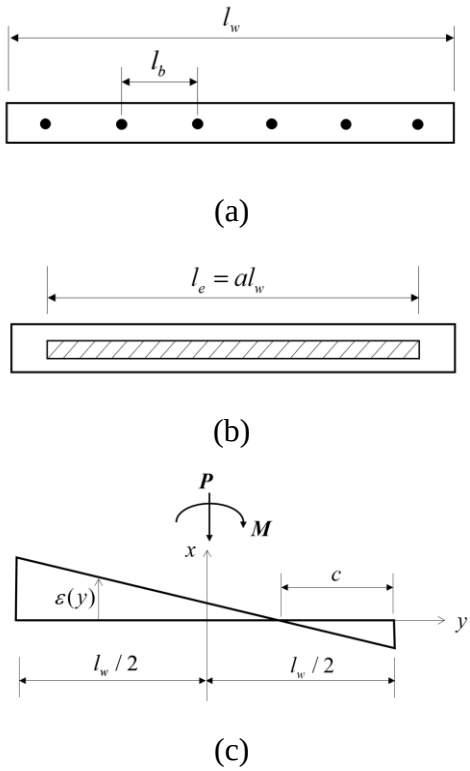

Figure 4-3. (a) Rectangular RM wall section with uniformly distributed vertical reinforcement; (b) Equivalent section with continuously distributed reinforcement; (c) Section strain profile

Dividing both sides of Eq. (4-5) by $f'_m l_w t$ and Eq. (4-6) by $f'_m l_w^2 t$, one can obtain the following non-dimensionalized equations.

$$\beta = -\int_{-\frac{1}{2}}^{\frac{1}{2}} \sigma'_m\left[\varepsilon(y')\right]dy' - \frac{1}{a}\alpha\int_{-\frac{a}{2}}^{\frac{a}{2}} \sigma'_s\left[\varepsilon(y')\right]dy' \tag{4-8}$$

$$M' = -\int_{-\frac{1}{2}}^{\frac{1}{2}} \sigma'_m\left[\varepsilon(y')\right]y'dy' - \frac{1}{a}\alpha\int_{-\frac{a}{2}}^{\frac{a}{2}} \sigma'_s\left[\varepsilon(y')\right]y'dy' \tag{4-9}$$

in which α is the reinforcement index, β is the axial compressive load ratio, as defined in Eqs. (3-1) and (3-2), respectively, $M' = \frac{M}{f'_m l_w^2 t}$, and $y' = y/l_w$. The bending strain $\varepsilon(y')$ is proportional to ϕl_w and is a linear function of y', as shown in Eq. (4-7), and σ'_m and σ'_s are the stresses in the masonry and vertical steel normalized by the masonry compressive strength f'_m and steel yield stress f_y, respectively. The stresses are to be calculated with the material laws shown in Figures 3-2 and 3-3. The parameter a is equal to l_e/l_w.

4.1.1.2. Sensitivity Analysis

For walls constructed of hollow concrete masonry units, the distance of the wall edge to the nearest reinforcing bar is typically 102 mm (4 in.). Hence, the value of $a = l_e/l_w$ depends on the wall length l_w. Furthermore, the adequacy of the assumption that the reinforcement is continuously distributed may depend on the actual bar spacing or more precisely the l_b/l_e ratio, in which l_b is the center-to-center spacing of the bars. To determine if the influence of $a = l_e/l_w$ and l_b/l_e could be ignored so that the number of independent variables can be minimized, a sensitive study has been performed. In this study, the moment-curvature relations are calculated with a fiber-section model in OpenSEES (McKenna et al. 2000) using the material laws presented in Section 3.1. The sensitivity of the moment-curvature relations to the value of *a* is shown in Figure 4-4, which considers the values of *a* between 0.80 and 0.97, corresponding to l_w ranging from 1.0 m (40 in.) to 6.1 m (240 in.). The results show that the influence of a is not significant for this wide range of wall lengths. However, the influence is a little more noticeable when the axial load is zero.

The sensitivity of the results to the values of l_b/l_e is shown in Figure 4-5. A wide range of l_b/l_e values is considered. The results indicate that the influence is very small except when the axial load is zero and l_b/l_e is equal to 0.5, which represents a very large bar spacing for a 1.83 m (72 in.) long wall (which corresponds to a = 0.89). Furthermore, based on these results, one can also expect that the non-dimensionalized moment-curvature relation presented here is also applicable to walls with non-uniform steel distribution.

4.1.1.3. Non-Dimensionalized Moment-Curvature Parameters

Based on the above results, one can conclude that the variables a and l_b/l_e need not be considered for the non-dimensionalized moment-curvature relations. As a result, α and β are the only independent variables that need to be considered. The values of the critical non-dimensionalized parameters $M'_{max} = M_{max} / (f'_m l_w^2 t)$, $\phi_m l_w$, $\phi_{75} l_w$, and $\phi_c l_w$ have been calculated for different values of α and β using the fiber section model in OpenSEES (McKenna et al. 2000). The results with the value of α ranging from 0.001 to 0.20 and the value of β ranging from zero to 0.25 are shown in Table 4-1. For the calculations, the wall length l_w considered is 1.83 m (72 in.), with a = 0.89 and l_b/l_e = 0.25. The wall thickness t is taken to be 0.194 m (7.625 in.).

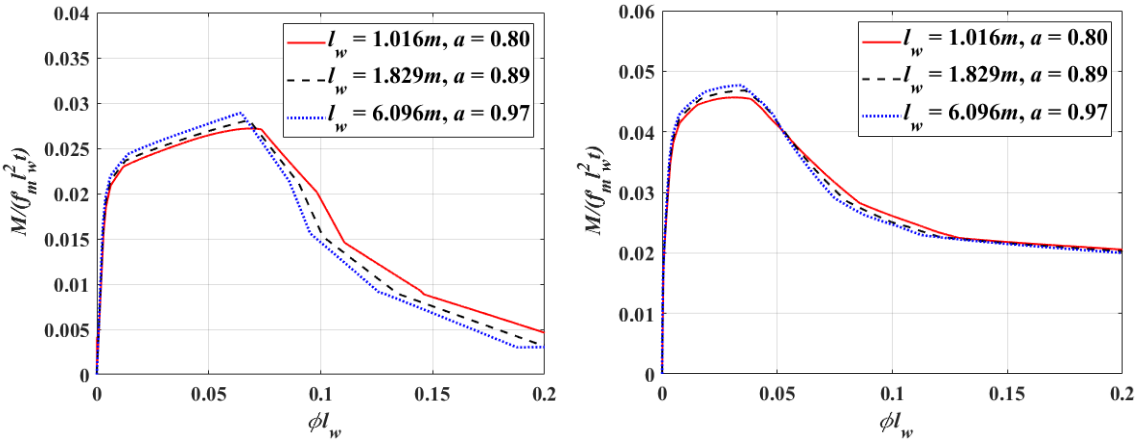

(a) $\beta = 0$ (b) $\beta = 0.05$

Figure 4-4. Influence of $a = l_e/l_w$ for walls with α = 0.05 and l_b/l_e = 0.25

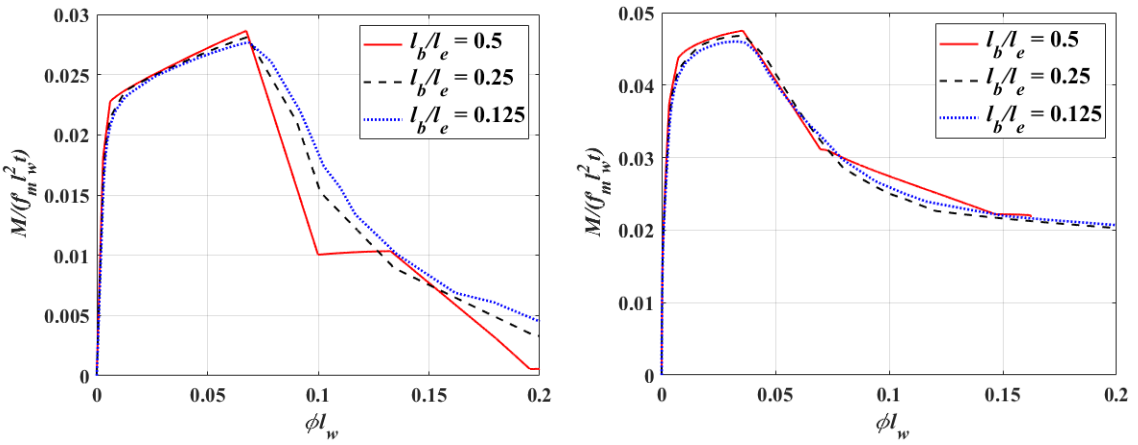

(a) $\beta = 0$ (b) $\beta = 0.05$

Figure 4-5. Influence of bar spacing for walls with α = 0.05 and l_e/l_w = 0.89

Table 4-1. Nondimensionalized moment-curvature values for fully grouted rectangular wall sections with uniform steel

Reinforcement Ratio $\alpha = (f_y/f'_m)\rho_y$	**Axial Compression Ratio** $\beta = P/(f'_m/A_n)$	$\phi_m l_w$	$\phi_{75} l_w$	$\phi_c l_w$	M'_{max}
0.001	0	0.0768	0.0992	0.1196	0.0006
	0.05	0.0495	Very Large	Very Large	0.02411
	0.10	0.0221	0.0535	Very Large	0.0449
	0.15	0.0152	0.0293	0.0443	0.063
	0.20	0.0115	0.0204	0.0251	0.0783
	0.25	0.0092	0.0157	0.0179	0.0909
0.005	0	0.0776	0.0998	0.1204	0.003
	0.05	0.0497	0.2226	Very Large	0.0261
	0.10	0.0224	0.0521	Very Large	0.0466
	0.15	0.0152	0.0292	0.0439	0.0644
	0.20	0.0114	0.0204	0.0252	0.0796
	0.25	0.0092	0.0157	0.018	0.092
0.01	0	0.0782	0.1002	0.1210	0.0060
	0.05	0.0481	0.1290	0.2099	0.0285
	0.10	0.0224	0.0505	0.0785	0.0487
	0.15	0.0151	0.0289	0.0435	0.0662
	0.20	0.0108	0.0203	0.0253	0.0812
	0.25	0.0089	0.0157	0.0181	0.0934
0.05	0	0.0681	0.0904	0.1073	0.0285
	0.05	0.0362	0.0631	0.1132	0.0472

Table 4-1. Nondimensionalized moment-curvature values for fully grouted rectangular wall sections with uniform steel, continued

Reinforcement Ratio $\alpha = (f_y/f'_m)\rho_y$	**Axial Compression Ratio** $\beta = P/(f'_m/A_n)$	$\phi_m l_w$	$\phi_{75} l_w$	$\phi_c l_w$	M'_{max}
0.05	0.10	0.0201	0.0415	0.0947	0.0653
	0.15	0.0139	0.0271	0.0408	0.0810
	0.20	0.0112	0.0198	0.0258	0.0946
	0.25	0.0093	0.0156	0.0188	0.1053
0.10	0	0.0355	0.0540	0.0673	0.0490
	0.05	0.0244	0.0535	0.0849	0.0677
	0.10	0.0171	0.0376	0.0767	0.0833
	0.15	0.0125	0.0260	0.0383	0.0978
	0.20	0.0109	0.0193	0.0262	0.1096
	0.25	0.0092	0.0157	0.0198	0.1191
0.15	0	0.0328	0.0567	0.0752	0.0712
	0.05	0.0206	0.0498	0.0841	0.0870
	0.10	0.0151	0.0350	0.0685	0.1012
	0.15	0.0115	0.0248	0.0363	0.1147
	0.20	0.0109	0.019	0.0266	0.1246
	0.25	0.009	0.0158	0.0207	0.1331
0.20	0	0.0232	0.0529	0.0763	0.0904
	0.05	0.0179	0.0478	0.0872	0.1042
	0.10	0.0136	0.0324	0.0616	0.1178
	0.15	0.0121	0.0238	0.0350	0.1302
	0.20	0.0103	0.0166	0.0227	0.1386
	0.25	0.0087	0.0159	0.0217	0.1465

4.1.1.4. Validation of Proposed Backbone Curve

The use of the tabulated non-dimensionalized parameters to construct load-displacement backbone curves has been validated with the wall tests shown in Table 4-1. The comparisons of the proposed backbone curves, the current backbone curve in ASCE 41, and experimental results are shown in Appendix II. Figure 4-6 shows the comparisons for three selected walls. The backbone curves show a good match with the first-cycle envelopes of the test results. In contrast, the backbone curves based on ASCE 41 show overly brittle behavior. Further comparisons can be found in NIST (2017).

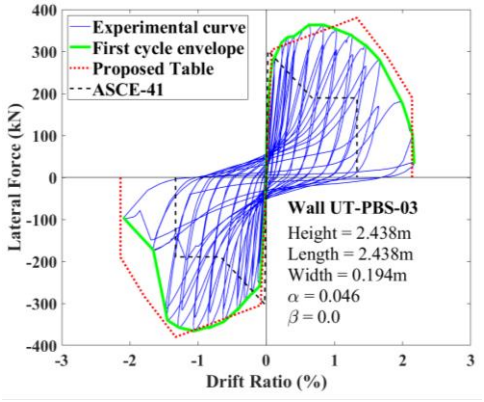

(a) UT-PBS-03

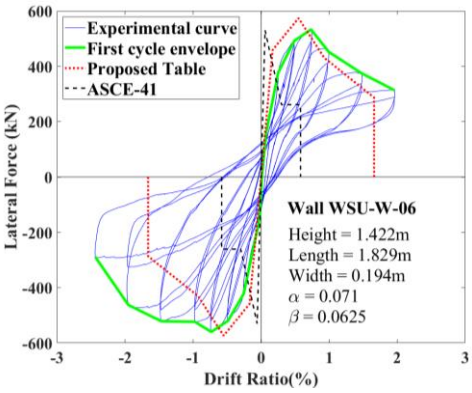

(b) WSU-W-06

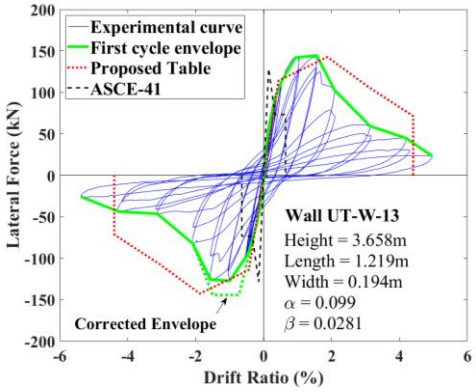

(c) UT-W-13

Figure 4-6. Comparison of backbone curves with test data for rectangular-sectioned cantilever walls

4.1.2. Cantilever Walls with T-sections

Comparing to walls with rectangular sections, flanged walls have additional variables to consider, such as the presence or absence of a wall flange on each side, the length of a flange compared to that of the web, and the distribution of the vertical reinforcement between the flange and the web. A general method accounting for these additional variables is proposed here for the construction of load-displacement backbone curves for flanged walls. The method is illustrated with T-walls but is also applicable to I-walls, L-walls, or C-walls. If the wall is asymmetric, two backbone curves are required to describe the nonlinear behavior, one for each direction. These backbone curves have the same general form as that shown in Figure 4-1.

For a T-wall, one backbone curve is required for each loading direction. The test data of He and Priestley (1992) have shown that RM T-walls subjected to cyclic loading exhibited symmetric behavior at the beginning before noticeable cracking had occurred. However, once cracks developed, stiffness degradation appeared to be more significant in the loading direction in which the flange is in compression than when the flange is in tension. Based on the test data, it is proposed that the effective initial stiffness (k) of the load-displacement backbone curve for a cantilever T-wall be calculated with Eq. (4-1) using the following stiffness reduction factors. For the loading direction in which the flange is in compression, the flexural stiffness reduction factor (ζ_f) is recommended to be 0.15, and the shear stiffness reduction factor (ζ_v) be 0.35, which are the same as those for walls with rectangular sections. For the direction in which the flange is in tension, ζ_f is recommended to be 0.5, and no reduction be applied to the shear stiffness (i.e., ζ_v =1.0). For calculating the values of Δ_m, Δ_{75}, and Δ_c using Eqs. (4-2) to (4-4), the values of ζ_f to

be used are the same as above, while the value of ζ_v is recommended to be 0.20 for both loading directions, similar to the case of rectangular-sectioned walls. When the flange is in tension, the capping displacement (Δ_c) should not exceed 4% of the wall height. When the flange is in compression, the aforereferenced test data have shown the wall can be very ductile, and the lateral resistance is much lower than that when the flange is in tension. Hence, for practical reasons, no limit needs to be assigned to the capping displacement.

4.1.2.1. Non-Dimensionalized Moment-Curvature Relations

For a T-section, the derivation of the moment-curvature relations needs to take into consideration whether the flange is in tension or compression. If the flange is in compression, then one needs to determine if the neutral axis of bending is in the flange or in the web. Hence, to develop simple non-dimensionalized moment-curve relations that can be used as analysis aids, the following assumptions are introduced. For the purpose of this discussion, consider a T-section with the dimensions and flexural reinforcement areas defined in Figure 4-7(a). The width of the flange (l'_f) is the effective width determined according to TMS 402 (2016). The steel area $A_{s,f}$ represents the total area of steel that is within the effective flange width, except for the steel that is in the intersection of the flange and the web. The latter is considered to be part of the web steel $A_{s,w}$. To simplify the analysis, the section is replaced by two equivalent rectangular sections that have different widths and reinforcement contents, as shown in Figures 4-7(b) and (c). When the flange is in tension, the equivalent rectangular section has a width equal to the width of the web (t_w), because masonry in tension is assumed to have zero strength, and the total flexural reinforcement consists of the web steel ($A_{s,w}$) and the flange steel ($A_{s,f}$), as shown in Figure 4-7(b). The web steel is assumed to be uniformly distributed over the length l_e, the center-

to-center distance between the extreme reinforcing bars, while $A_{s,f}$ is concentrated at the tension edge of the section. When the flange is in compression, the equivalent rectangular section has a width equal to the effective flange width (l'_f) in compression, and the contribution of the flange steel $A_{s,f}$ is neglected, as shown in Figure 4-7(c). The latter assumption is based on the fact that the flange steel is normally close to the neutral axis of bending when the moment capacity of the wall section is reached. If the axial load is applied at the centroid of a T-section, then the moment values calculated with the equivalent rectangular sections need correction needs to be corrected, as will be considered later.

For the case when the flange is in tension, the axial load (P) and the bending moment (M) about the centroidal axis of the equivalent rectangular section shown in Figure 4-7(c) can be expressed as:

$$P = -t_w \int_{-\frac{l_w}{2}}^{\frac{l_w}{2}} \sigma_m\left[\varepsilon(y)\right]dy - \frac{1}{a}\rho_{v,web} \int_{-\frac{l_e}{2}}^{\frac{l_e}{2}} \sigma_s\left[\varepsilon(y)\right]dy - A_{s,f}\sigma_s\left[\varepsilon\left(\frac{l_e}{2}\right)\right] \qquad (4\text{-}10)$$

$$M = -t_w \int_{-\frac{l_w}{2}}^{\frac{l_w}{2}} \sigma_m\left[\varepsilon(y)\right]ydy - \frac{t}{a}\rho_v \int_{-\frac{l_e}{2}}^{\frac{l_e}{2}} \sigma_s\left[\varepsilon(y)\right]ydy + A_{s,f}\sigma_s\left[\varepsilon\left(\frac{l_e}{2}\right)\right]\frac{l_e}{2} \qquad (4\text{-}11)$$

in which y is the distance from the centroidal axis of the equivalent rectangular section, $\rho_{v,web}$ is the web steel ratio defined as $\rho_{v,web} = \frac{A_{s,w}}{l_w t_w}$, where l_w is the length of the web, $a = l_e/l_w$, σ_m and σ_s are the stresses in the masonry and the steel.

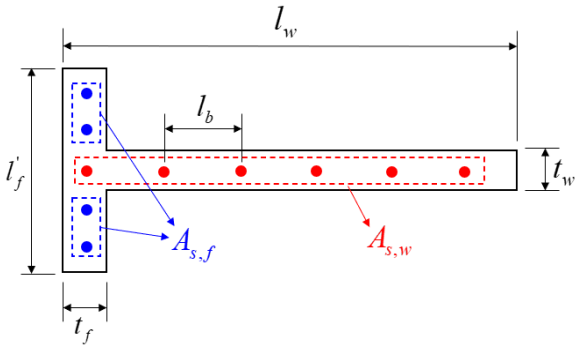

(a)

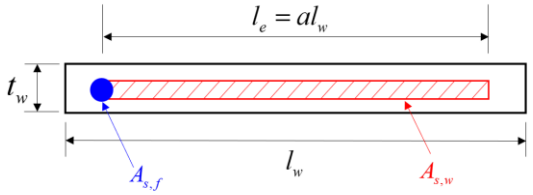

(b)

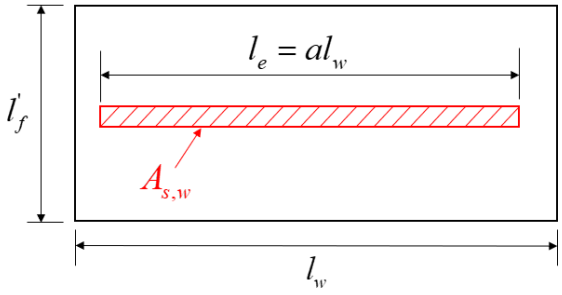

(c)

Figure 4-7. (a) T- section with uniformly distributed reinforcement; (b) Equivalent rectangular section for flange in tension; (c) Equivalent rectangular section for flange in compression

Dividing Eqs. (4-10) and (4-11) by $f_m' l_w t_w$ and $f_m' l_w^2 t_w$, respectively, one has the following non-dimensionalized equations.

$$\beta = -\int_{-\frac{1}{2}}^{\frac{1}{2}} \sigma_m'\left[\varepsilon(y')\right]dy' - \frac{1}{a}\alpha\int_{-\frac{a}{2}}^{\frac{a}{2}} \sigma_s'\left[\varepsilon(y')\right]dy' - \alpha\eta\sigma_s'\left[\varepsilon\left(\frac{a}{2}\right)\right] \tag{4-12}$$

$$M' = -\int_{-\frac{1}{2}}^{\frac{1}{2}} \sigma'_m\left[\varepsilon(y')\right] y' dy' - \frac{1}{a}\alpha \int_{-\frac{a}{2}}^{\frac{a}{2}} \sigma'_s\left[\varepsilon(y')\right] y' dy' + \alpha\eta\sigma'_s\left[\varepsilon\left(\frac{a}{2}\right)\right] \quad (4\text{-}13)$$

in which $\eta = \frac{A_{s,f}}{A_{s,w}}$ and the non-dimensionalized parameters are defined in the same way as in Section 3.1 for a rectangular section. Here, $M' = M/(f'_m l_w^2 t_w)$.The reinforcement index, α, is defined in Eq. (3-1) with ρ_v equal to $A_{s,web}/t_w l_w$ and the axial load ratio, β, is defined in Eq. (3-2) with A_n equal to $t_w l_w$.

When the flange is in compression, the non-dimensionalized equations derived for a rectangular section, as shown in Eqs. (4-8) and (4-9), apply. In this case, the width of the section is the effective flange width, l'_f, in compression, as shown in Figure 4-7(c), $M' = M/(f'_m l_w^2 l'_f)$, α is defined in Eq. (3-1) with ρ_v equal to $A_{s,web}/l'_f l_w$, and β is defined in Eq. (3-2) with A_n equal to $l'_f l_w$.

The equations developed here apply to I-sections, L-sections, or C-sections. For L- and C-sections, the conditions will be the same as those for T-sections. For I-sections, Eqs. (4-12) and (4-13) apply regardless of the loading directions. However, the width of the equivalent rectangular section for each loading direction will be the effective flange width, l'_f, in compression, α is defined in Eq. (3-1) with ρ_v equal to $A_{s,web}/l'_f l_w$, and β is defined in Eq. (3-2) with A_n equal to $l'_f l_w$. The flange steel in compression is ignored.

4.1.2.2. Non-Dimensionalized Moment-Curvature Parameters

Using the equivalent rectangular section assumptions as discussed above, the non-dimensionalized moment and curvature parameters, M'_{max}, $l_w\phi_m$, $l_w\phi_{75}$, and $l_w\phi_c$, for a

fully grouted T-section can be presented as functions of α, β and η, where η $\left(\text{which is the ratio of } A_{s,f} \text{ to } A_{s,w}\right)$ is required for the case that the flange is in tension. Similar to the case of a rectangular section, the influence of a and l_b/l_e on the moment-curvature relations can be ignored because the contribution of the web reinforcement to the moment capacity of a T-section is either the same or less than that for a rectangular section.

For the case that the flange is in compression, the non-dimensionalized moment and curvature parameters can be obtained from Table 4-1, with $M'_{max} = M_{max}/(f'_m l_w^2 l'_f)$, the value of α calculated from Eq. (3-1) with ρ_v equal to $A_{s,web}/l'_f l_w$, and the value of β from Eq. (3-2) with A_n equal to $l'_f l_w$, as explained before. For the case that the flange is in tension, the non-dimensionalized parameters are numerically generated using a fiber-section model of the equivalent rectangular section shown in Figure 4-7(b), for values of η equal to 1, 2, and 3. These η values cover a range of possible T-section properties. The values of the non-dimensionalized parameters for η values between 1 and 2, and 2 and 3, can be determined by linear interpretation. Here, $M'_{max} = M_{max}/(f'_m l_w^2 t_w)$, the value of α is calculated from Eq. (3-1) with ρ_v equal to $A_{s,web}/t l_w$ and the value of β from with Eq. (3-2) with A_n equal to $t_w l_w$. The analyses were conducted with a 1.83 m × 0.194 m (72 in. × 7.625 in.) equivalent rectangular section. The numerical results are presented in Table 4-2.

It should be noted that the values of M'_{max} presented in the aforementioned tables are moment capacities calculated about the centroid of the equivalent rectangular sections with the axial load applied at the same location. To calculate the moment capacity of a T-

section from the tabulated values, one has to apply a correction to account for the fact that the axial load is normally assumed to be located at the centroid of a T-section.

The correct moment capacity M_{max} for a T-section can be calculated from the non-dimensionalized value M'_{max} with a simple correction as follows.

$$M_{max} = f'_m l_w^2 t_w M'_{max} + Pe \quad \text{for flange in tension} \tag{4-14}$$

$$M_{max} = f'_m l_w^2 l'_f M'_{max} - Pe \quad \text{for flange in compression} \tag{4-15}$$

in which the eccentricity (e) is defined in Figure 4-8. According to TMS 402/602 (TMS, 2016), the effective flange width of a T-section can be different when the flange is in compression and tension. For simplicity, the eccentricity is calculated based on a T-section with actual flange width (l_f), rather than effective flange width (l'_f).

Strictly speaking, the moment in the entire moment-curvature curve has to be corrected by the same amount shown in Eqs. (4-14) and (4-15). As a result, the non-dimensionalized curvature values $l_w\phi_{75}$, and $l_w\phi_c$ from the equivalent rectangular sections will not reflect the actual moment degradations they are supposed to be associated with. For the case that the flange is in tension, they will under-estimate the corresponding curvature values, which will result in more severe load degradation being represented in the backbone curve. For the case that the flange is in compression, they will over-estimate the curvature values. However, for the latter case, the peak moment is much lower than that in the other loading direction, and the post-peak strength degradation is relatively mild. For these reasons, no corrections are needed for the corresponding lateral displacements calculated from $l_w\phi_{75}$, and $l_w\phi_c$ with Eqs. (4-2) - (4-4).

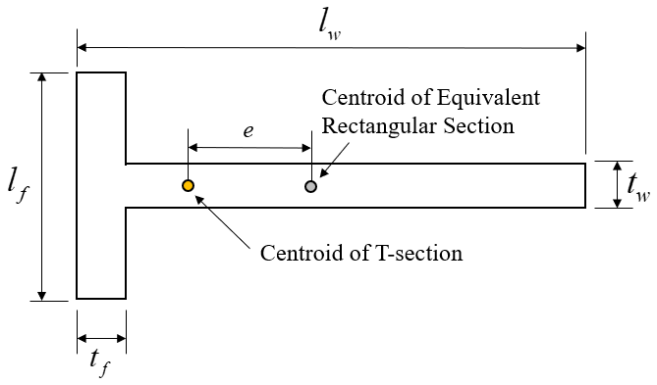

Figure 4-8**.** Eccentricity of axial force for a T-section represented by an equivalent rectangular section

4.1.2.3. Validation of Proposed Backbone Curves

The three T-walls presented in Table 3-2 and Figure 3-4 are used to validate the method proposed here for constructing the lateral load – displacement backbone curves for T-walls. Figure 4-9 shows the comparison of the test data with the backbone curves constructed by the interpolating the values of the non-dimensionalized parameters presented in Table 4-2. As shown, with the correction for axial load eccentricity applied, the proposed backbones curves show a good agreement with the first-cycle envelopes of the test data. The match is good except for UCSD-F2, which shows that the backbone curve is far more ductile than the test results in the positive loading direction. This discrepancy is also shown by the cyclic analysis with the beam-column model as shown in Figure 3-8(b).

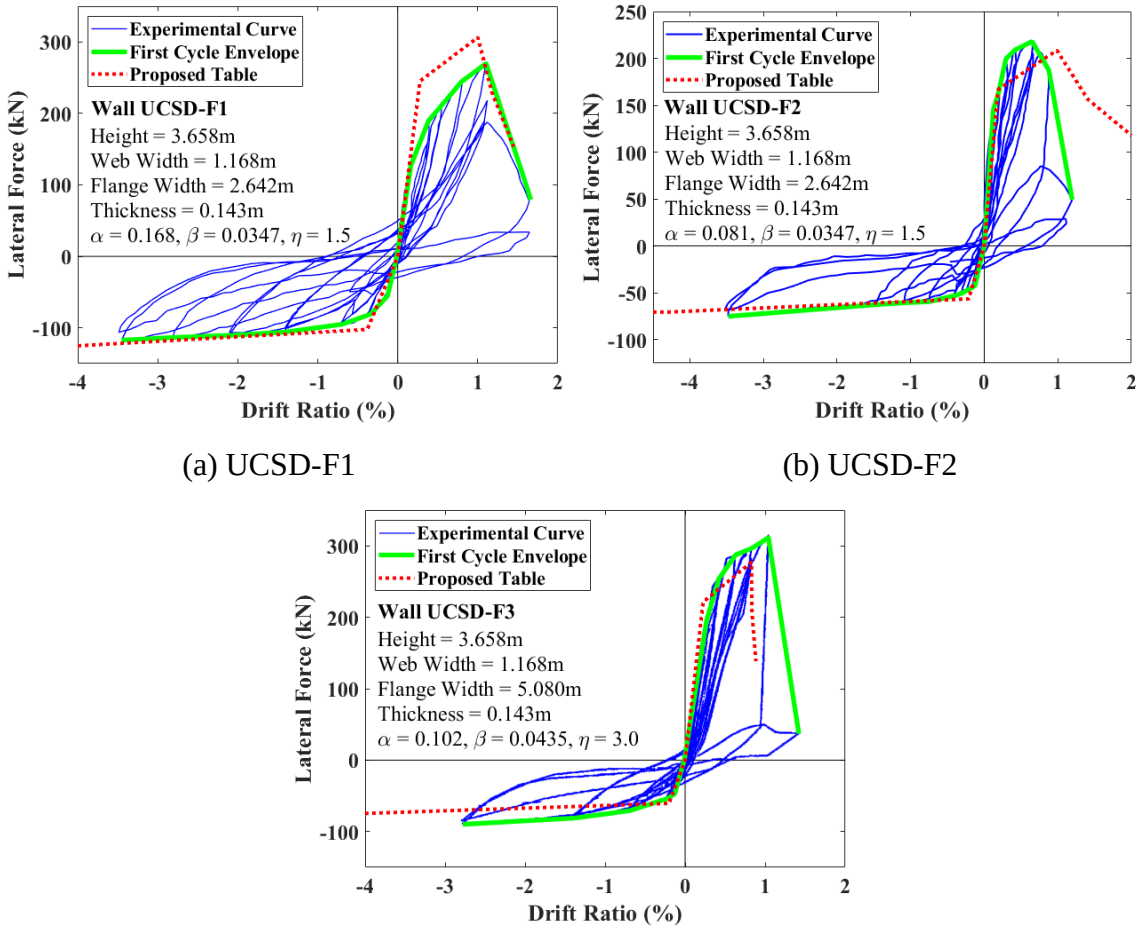

(a) UCSD-F1

(b) UCSD-F2

(c) UCSD-F3

Figure 4-9**.** Comparison of backbone curves with test data for T-walls

Table 4-2. Nondimensionalized moment-curvature values for fully grouted rectangular wall sections with additional steel at one end as quantified by the value of $\boldsymbol{\eta = A_{s,f}/A_{s,w}}$

Reinforcement Ratio $\boldsymbol{\alpha = \left(f_y/f_m^{'}\right)\rho_y}$	**Axial Compression Ratio** $\boldsymbol{\beta = P/(f_m^{'}/A_n)}$	$\boldsymbol{\phi_m l_w}$	$\boldsymbol{\phi_{75} l_w}$	$\boldsymbol{\phi_c l_w}$	$\boldsymbol{M'_{max}}$
$\boldsymbol{\eta = 1.0}$					
0.01	0	0.0781	0.09	0.0996	0.018
	0.05	0.0484	0.0761	0.2445	0.0385
	0.10	0.0207	0.0464	0.103	0.0571
	0.15	0.0137	0.0271	0.0405	0.074
	0.20	0.011	0.0194	0.024	0.0884
	0.25	0.0009	0.0151	0.0175	0.1
0.05	0	0.0366	0.0475	0.0567	0.0745
	0.05	0.0214	0.0523	0.079	0.0903
	0.10	0.0143	0.0299	0.0695	0.1051
	0.15	0.0116	0.0208	0.0302	0.1183
	0.20	0.0089	0.0161	0.0208	0.1286
	0.25	0.008	0.0132	0.0159	0.1372
0.10	0	0.0182	0.0533	0.088	0.1307
	0.05	0.0142	0.0308	0.1384	0.144
	0.10	0.0114	0.0214	0.0375	0.1553
	0.15	0.0094	0.0169	0.0245	0.1643
	0.20	0.0081	0.0138	0.0185	0.1721
	0.25	0.0072	0.0118	0.0147	0.1762
0.15	0	0.0127	0.0306	0.1612	0.184

Table 4-2. Nondimensionalized moment-curvature values for fully grouted rectangular wall sections with additional steel at one end as quantified by the value of $\eta = A_{s,f}/A_{s,w}$, continued

Reinforcement Ratio $\alpha = \left(f_y/f_m^{'}\right)\rho_y$	**Axial Compression Ratio** $\beta = P/(f_m^{'}/A_n)$	$\phi_m l_w$	$\phi_{75} l_w$	$\phi_c l_w$	M'_{max}
0.15	0.05	0.0109	0.0223	0.0441	0.1934
	0.10	0.0089	0.0178	0.0281	0.2014
	0.15	0.0083	0.0145	0.0209	0.2083
	0.20	0.0078	0.0124	0.0167	0.2112
	0.25	0.0065	0.0109	0.0139	0.2137
0.20	0	0.0114	0.0237	0.058	0.2288
	0.05	0.0009	0.02	0.0339	0.2365
	0.10	0.0085	0.0169	0.0247	0.2426
	0.15	0.0076	0.0142	0.0198	0.2452
	0.20	0.0068	0.0116	0.0157	0.2469
	0.25	0.0064	0.0102	0.0134	0.2475
$\eta = 2.0$					
0.01	0	0.0806	0.0896	0.0985	0.03
	0.05	0.0407	0.0636	0.0765	0.0478
	0.10	0.0196	0.0423	0.0907	0.0654
	0.15	0.0138	0.0256	0.0373	0.0816
	0.20	0.0103	0.0185	0.0229	0.0953
	0.25	0.0084	0.0146	0.0169	0.1064
0.05	0	0.0212	0.058	0.0757	0.1152
	0.05	0.0148	0.0409	0.1657	0.1291
	0.10	0.0115	0.0217	0.0368	0.1418

Table 4-2. Nondimensionalized moment-curvature values for fully grouted rectangular wall sections with additional steel at one end as quantified by the value of $\boldsymbol{\eta = A_{s,f}/A_{s,w}}$, continued

Reinforcement Ratio $\boldsymbol{\alpha = \left(f_y/f_m^{'}\right)\rho_y}$	**Axial Compression Ratio** $\boldsymbol{\beta = P/(f_m^{'}/A_n)}$	$\boldsymbol{\phi_m l_w}$	$\boldsymbol{\phi_{75} l_w}$	$\boldsymbol{\phi_c l_w}$	$\boldsymbol{M'_{max}}$
0.05	0.15	0.0091	0.01657	0.0232	0.1519
	0.20	0.0078	0.0135	0.0172	0.1602
	0.25	0.007	0.0114	0.0137	0.1655
0.10	0	0.0115	0.0242	0.0851	0.2006
	0.05	0.0095	0.0183	0.0314	0.2092
	0.10	0.0081	0.0147	0.0218	0.2168
	0.15	0.0073	0.0123	0.0169	0.2208
	0.20	0.0064	0.0107	0.0137	0.2237
	0.25	0.0066	0.0094	0.0116	0.2227
0.15	0	0.0084	0.0163	0.0279	0.2754
	0.05	0.0077	0.0135	0.0209	0.2783
	0.10	0.0065	0.0117	0.0169	0.2806
	0.15	0.0065	0.0103	0.014	0.2805
	0.20	0.0065	0.0094	0.0122	0.2688
	0.25	0.0063	0.0089	0.0112	0.2546
0.20	0	0.007	0.013	0.0207	0.3348
	0.05	0.0065	0.0113	0.0173	0.3353
	0.10	0.0067	0.0102	0.0148	0.3265
	0.15	0.0064	0.0097	0.0134	0.3111
	0.20	0.0061	0.0092	0.0122	0.2958
	0.25	0.0061	0.0088	0.0113	0.2806

Table 4-2. Nondimensionalized moment-curvature values for fully grouted rectangular wall sections with additional steel at one end as quantified by the value of $\eta = A_{s,f}/A_{s,w}$, continued

Reinforcement Ratio $\alpha = \left(f_y/f_m^{'}\right)\rho_y$	**Axial Compression Ratio** $\beta = P/(f_m^{'}/A_n)$	$\phi_m l_w$	$\phi_{75} l_w$	$\phi_c l_w$	M'_{max}
$\eta = 3.0$					
0.01	0	0.0755	0.0854	0.095	0.041
	0.05	0.0369	0.0539	0.0632	0.0567
	0.10	0.0185	0.0385	0.0889	0.0734
	0.15	0.013	0.024	0.0344	0.0891
	0.20	0.0102	0.0176	0.0219	0.1022
	0.25	0.0084	0.0141	0.0163	0.1127
0.05	0	0.0162	0.0352	Very Large	0.1528
	0.05	0.0111	0.0228	0.0491	0.1651
	0.10	0.009	0.0172	0.0258	0.175
	0.15	0.008	0.0139	0.0187	0.1832
	0.20	0.0073	0.0116	0.0146	0.1883
	0.25	0.0061	0.0101	0.0121	0.1918
0.10	0	0.0085	0.0157	0.0278	0.2608
	0.05	0.0074	0.013	0.02	0.265
	0.10	0.0063	0.0111	0.0158	0.2678
	0.15	0.0066	0.0098	0.013	0.2669
	0.20	0.0067	0.0091	0.0115	0.2531
	0.25	0.0061	0.0086	0.0105	0.2394
0.15	0	0.0065	0.0109	0.0174	0.3464
	0.05	0.0068	0.1	0.0149	0.3335

Table 4-2. Nondimensionalized moment-curvature values for fully grouted rectangular wall sections with additional steel at one end as quantified by the value of $\boldsymbol{\eta = A_{s,f}/A_{s,w}}$, continued

Reinforcement Ratio $\boldsymbol{\alpha = \left(f_y/f_m^{'}\right)\rho_y}$	**Axial Compression Ratio** $\boldsymbol{\beta = P/(f_m^{'}/A_n)}$	$\boldsymbol{\phi_m l_w}$	$\boldsymbol{\phi_{75} l_w}$	$\boldsymbol{\phi_c l_w}$	$\boldsymbol{M'_{max}}$
0.15	0.10	0.0064	0.0096	0.01344	0.3179
	0.15	0.0062	0.0091	0.0123	0.3021
	0.20	0.0061	0.0087	0.0113	0.2864
	0.25	0.0059	0.0083	0.0104	0.2707
0.20	0	0.0065	0.01	0.0161	0.3794
	0.05	0.0063	0.0096	0.0146	0.3627
	0.10	0.006	0.0092	0.0134	0.3463
	0.15	0.0058	0.0089	0.0122	0.3298
	0.20	0.0057	0.0085	0.0113	0.3134
	0.25	0.0055	0.0081	0.0106	0.2971

4.1.3. Partially Grouted Walls

While the general modeling method proposed here based on a fiber-section idealization is applicable to partially grouted walls, the non-dimensionalized moment and curvature parameters presented here are calculated and validated for fully grouted walls. Experimental data on flexure-dominated partially grouted walls are scarce. Most of the partially grouted walls tested were shear-dominated or had behavior resembling an infilled frame with weak infill walls. In the absence of data, one may use the non-dimensionalized moment and curvature parameters presented in the Tables 4-1 and 4-2 with the net wall cross-sectional area replaced by the gross cross-sectional area (including the wall cavity) and the masonry compressive strength based on the average over the gross cross-sectional area.

The validity of the aforementioned approach has been evaluated with the partially grouted rectangular wall section shown in Figure 4-10. As shown, the wall section has a length of 1.829 m (72 in). It has a vertical reinforcing bar in each of the two grouted cells, and the rest of cells are ungrouted. This section is representative of an ordinary partially grouted wall designed according to TMS 402 (TMS, 2016). Each reinforcing bar has a cross-sectional area of 129 mm^2 (#4 steel bar). A fiber-section model has been developed for this section, using the uniaxial material laws for masonry and steel presented in Section 3.1. The compressive strengths for the grouted and ungrouted masonry are based on the prism tests performed by Koutras (2019). The compressive strength for grouted masonry is 17.9 MPa (2.6 ksi), whereas that for ungrouted masonry is 6.8 MPa (1.0 ksi) based on the gross section. The yielding strength of the reinforcing steel is taken as 483 MPa (70.0 ksi). To determine the tensile strain at peak stress (ε_{ps}) for the moment-curvature analysis

as well as for determining the values of the non-dimensionalized moment and curvature values from Table 4-1, the vertical reinforcement index (α) and axial load ratio (β) are calculated with Eqs. (3-1) and (3-2). These two indices are based on the masonry compressive strength (f'_m) of 9.2 MPa (1.3 ksi), which is the average compressive strength based on the entire gross section of the wall.

Figure 4-10(b) shows the comparison of the moment-curvature curve with the critical moment and curvature values from the table for different values of the axial load ratio (β). As shown, for β equal to 0 and 0.05 (lower axial load), the values from the table tend to overestimate the ductility of the wall section. This is because the values in the table are generated with a section that has the vertical bars uniformly distributed over the section, while the vertical bars are actually concentrated at the wall ends. The failure of one bar in this section results in a significant drop of moment resistance, which is not accurately represented by a uniform steel distribution. For β equal to 0.10 and higher, the moment-curvature analyses stop before severe load degradation occurred, indicating the wall section is not able to carry the applied axial load due to extensive crushing of masonry. For these cases, the non-dimensionalized relation tends to underestimate the moment capacity and ductility of the wall section. This can be attributed to the use of the average compressive strength of masonry for the two grouted cells when calculating the moment values from the non-dimensionalized values. Hence, this approach is conservative when the axial load ratio (β) is greater than 0.10 and may over-estimate the ductility when β is less than 0.05. Even though the latter situation is more common for existing masonry structures, which are mostly low-rise, the method is acceptable considering that the post-peak curvature

range before complete crushing occurs, as shown in the figure, is short compared to the pre-peak range.

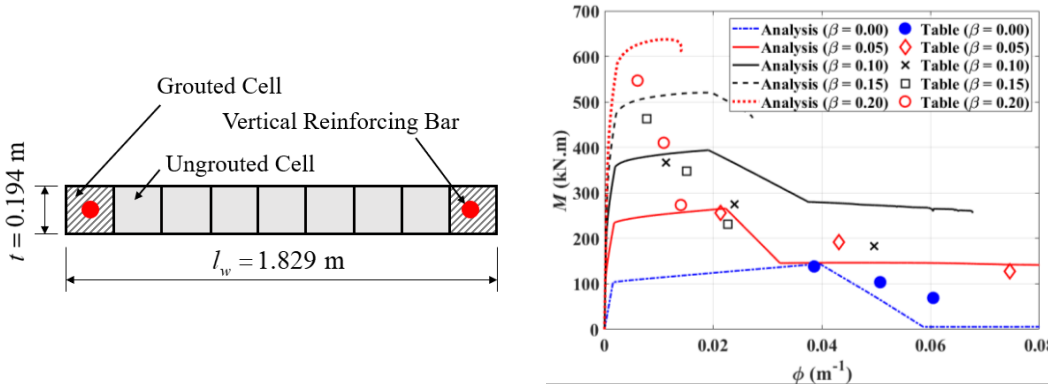

(a) (b)

Figure 4-10. (a) Partially grouted RM wall section; (b) Comparison of the moment-curvature curves with moment and curvature values calculated with the non-dimensionalized values from Table 4-1

4.2. Shear-Dominated Walls

For a fully grouted shear-dominated RM shear wall, the strength and ductility are influenced by the aspect ratio of the wall, the amount of vertical and horizontal reinforcement, and the axial compressive load. The influence of the vertical reinforcement on the shear strength and ductility is through the dowel action. In the absence of a simple rational model to account for all of these, an empirical backbone curve is proposed based on the test data of Shing et al. (1991), Voon and Ingham (2006), and Ahmadi (2012).

4.2.1. Proposed Empirical Backbone curve

Figure 4-11 shows the proposed lateral load-vs.-lateral drift ratio curve for fully grouted shear-dominated walls with rectangular section. For a cantilever wall, the effective initial stiffness (k) can be calculated with Eq. (4-1). For a wall with fixed-fixed end conditions, the flexure stiffness term in the equation should be modified accordingly. The peak shear strength (Q_{max}) of a wall can be calculated with the shear strength formula given in TMS 402/602 (2016), considering the contribution of the masonry (V_{nm}) and the contribution of the horizontal reinforcement (V_{ns}). The residual strength (Q_r) is assumed to be equal to V_{ns}. The drift ratio at the peak strength and the drift ratio at which the residual strength develops are taken as 0.5% and 1.0%, respectively. The maximum allowable drift ratio is taken as 2.0%, which is the same as that specified in ASCE 41 (2017).

Studies by Minaie et al. (2010) and Bolhassani (2015) show that partially grouted shear-dominated RM walls have lower strength and displacement capacity than fully grouted shear-dominated walls. Hence, for partially grouted walls, it is recommended that the backbone curve shown in Figure 4-11 be modified as follows. The peak strength (Q_{max})

and residual strength (Q_r) should be reduced by a factor of 0.75 as suggested in TMS 402/602 (2016). The drift ratio at the peak strength should be reduced from 0.5% to 0.2%, and that corresponding to the residual strength be reduced from 1% to 0.4%. The maximum allowable drift is to be capped at 0.8% rather than 2%.

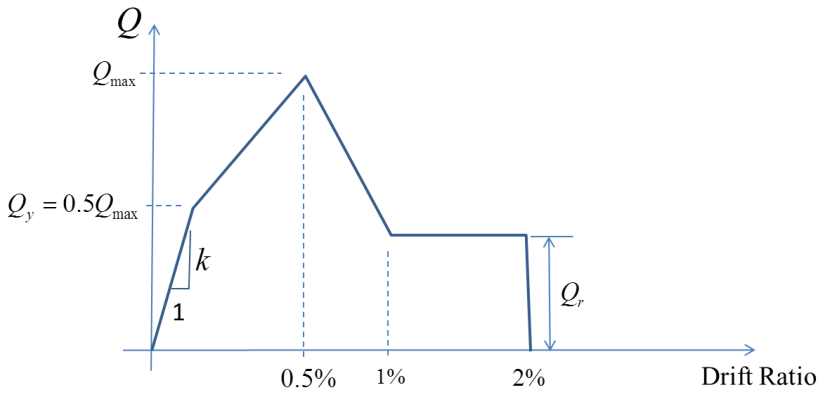

Figure 4-11. Backbone lateral load – lateral drift ratio curve for fully grouted shear-dominated reinforced masonry walls

4.2.2. Comparison with Experimental Data

Table 4-3 shows the dimensions, material strength, axial load ratios and reinforcement details of the 17 fully grouted, shear-dominated RM walls selected to evaluate the proposed backbone curve (Shing et al., 1991; Voon and Ingham, 2006; Ahmadi, 2012). These planar wall specimens had axial load ratios ranging from 0 to 0.109, and shear reinforcement ratios ranging from 0.025% to 0.33%. These walls also have different geometry and boundary conditions: 15 out of the 17 walls are cantilever walls with the length-to-height aspect ratios ranging from 0.5 to 1.67; the rest two specimens, tested by Ahmadi (2012) had fixed-fixed boundary conditions, with their depth-to-height ratios equal to one.

The comparison of the proposed backbone curve with the test data of these wall specimens are shown in Appendix III. Figure 4-12 shows the comparison for two selected walls, UT-PBS-01 and UT-PBS-02. The backbone curves match the test data well, while the backbone curves recommended in ASCE 41 (2017) show overly brittle behaviors.

Table 4-3. Properties of the selected shear-dominated RM wall specimens

Wall ID	**Height (m)**	**Length (m)**	**Width (m)**	**Axial load (kN)**	**Shear-span ratio**	**Horiz. Reinf.***	f'_m **(MPa)**	f_{yh}** **(MPa)**
Auck-02	1.80	1.80	0.140	0	1	#2@160cm	17.6	324.7
Auck-04	1.80	1.80	0.140	0	1	#3@79cm	17.0	319.9
Auck-07	1.80	1.80	0.140	126	1	#2@41cm	18.8	324.7
Auck-08	1.80	1.80	0.140	63.0	1	#2@41cm	18.8	324.7
Auck-09	3.60	1.80	0.140	63.0	2	#2@41cm	24.3	324.7
Auck-10	1.80	3.00	0.140	105	0.6	#2@41cm	24.3	324.7
CU-3	1.83	1.83	0.143	487	1	#3@41cm	20.4	393.0
CU-4	1.83	1.83	0.143	0	1	#3@41cm	18.2	393.0
CU-5	1.83	1.83	0.143	0.038	1	#3@41cm	18.2	393.0
CU-7	1.83	1.83	0.143	180	1	#3@41cm	22.4	393.0
CU-9	1.83	1.83	0.143	180	1	#3@41cm	22.4	393.0
CU-11	1.83	1.83	0.143	487	1	#4@41cm	22.3	461.9
CU-13	1.83	1.83	0.143	487	1	#4@41cm	23.0	461.9
CU-14	1.83	1.83	0.143	487	1	#3@41cm	23.0	393.0
CU-16	1.83	1.83	0.143	487	1	#4@41cm	17.1	461.9
UT-PBS-01	1.83	1.83	0.194	61.1	0.5	#4@20cm	21.5	430.2
UT-PBS-02	1.83	1.83	0.194	458	0.5	#4@41cm	21.5	430.2

* #2, #3, and #4 bars have nominal diameters of 6mm, 10mm, and 13mm, respectively.
** f_{yh} represents the yielding strength of horizontal bars.

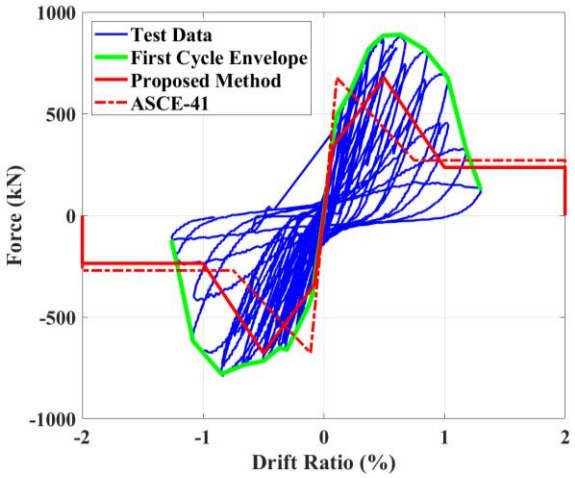

(a) Wall UT-PBS-01

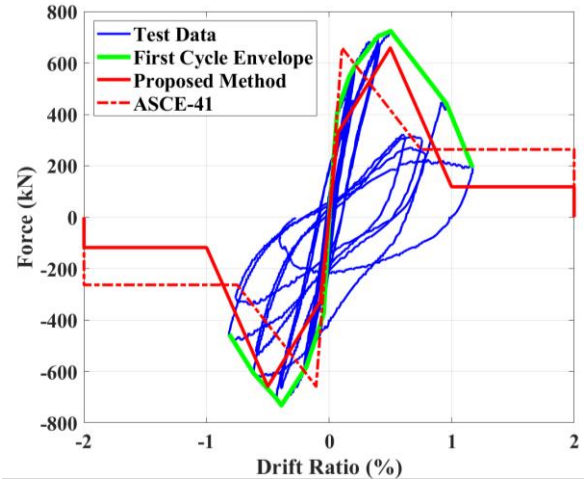

(b) Wall UT-PBS-02

Figure 4-12. Comparison of proposed backbone curves with experimental data and the backbone curves recommended in ASCE 41 for fully grouted shear-dominated walls

Chapter 4, in part, is a reprint of the material in a manuscript titled "Practical Nonlinear Analysis Methods for Flexure-Dominated Reinforced Masonry Shear Walls" that has been submitted to *ASCE Journal of Structural Engineering* in 2021 (under review). The authors of the manuscript are: the author of the dissertation and P. Benson Shing. The author of the dissertation is the primary author and the main contributor of the work presented in the manuscript.

CHAPTER 5 SHAKE-TABLE TESTS ON COLLAPSE RESISTANCE OF SHEAR-DOMINATED REINFORCED MASONRY SHEAR WALL SYSTEMS

This chapter presents a study to investigate the displacement capacity of shear-dominated fully grouted RM wall systems and the influence of wall flanges and planar walls perpendicular to the direction of the seismic force on the seismic performance of a wall system. Two full-scale, single-story, RM wall systems were tested on a shake table to the verge of collapse. The tests were carried out with unidirectional base excitation. The design of the two structures, the testing procedure, and the major results and findings from the shake-table tests will be presented. The influence of wall flanges and walls perpendicular to the direction of shaking has been analyzed and quantitively assessed. The responses of the test structures have been compared to a force-vs.-drift ratio backbone curve developed from previous quasi-static test data on shear-dominated planar wall segments. The results have been further used to assess the accuracy of the shear strength formula in TMS 402/602 (2016).

5.1. Design of Test Structures

Figure 5-1 shows the plan layouts of the two RM shear wall systems designed and tested under unidirectional motions on the outdoor shake table in the NHERI (Natural Hazards Engineering Research Infrastructure) facility at the University of California San Diego. Each specimen had two T-walls as the main seismic force resisting system. Specimen 2 had six additional rectangular walls with their planes oriented perpendicular to the direction of the shake-table motion. They are referred to as the out-of-plane walls in

this paper. One of the objectives of the tests was to investigate the influence of the out-of-plane walls on the seismic resistance of a wall system. To this end, the T-walls in the two specimens had the same design and carried the same gravity load, and the two specimens had the same effective seismic weight.

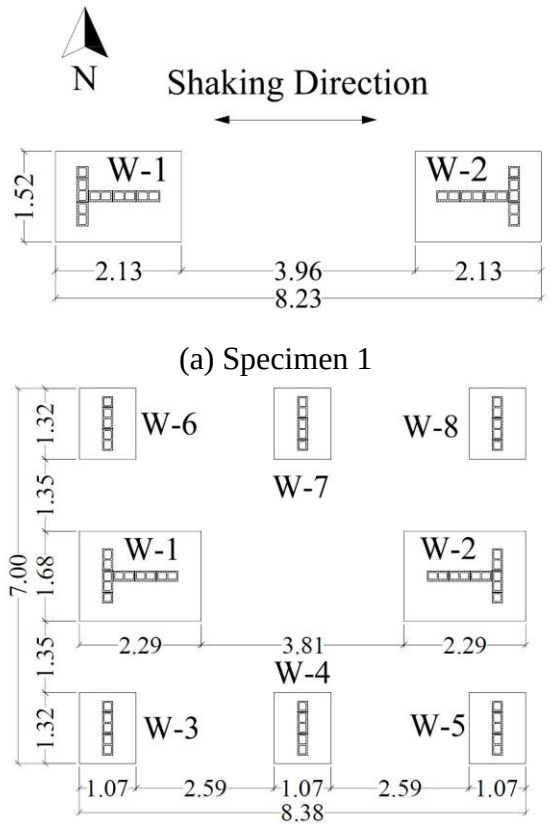

(a) Specimen 1

(b) Specimen 2

Figure 5-1. Plan views of footing and wall layout (in meters)

Figures 5-2 and 5-3 shows the reinforcement details for the two specimens. The reinforcing bars in the walls had a nominal yield strength of 414 MPa (Grade 60 in ASTM Standard[24]). Each T-wall had six No. 4 (13 mm) vertical bars spaced at 20 cm (8 in) on center in the web, and three No. 4 (13 mm) vertical bars spaced at 41 cm (16 in) in the flange. The horizontal bars in the web and the flange were No. 3's (10 mm) spaced at 41 cm (16 in) on center. In Specimen 2, each of the out-of-plane walls had No. 4 (13 mm) bars

for the vertical reinforcement, and No. 3 (10 mm) bars for the horizontal reinforcement, both spaced at 41 cm (16 in) on center. The reinforcement complied with the prescriptive requirements of TMS 402/602 for walls designed for high seismic areas, but the spacing of the reinforcing bars in the flanges of the T-walls slightly violated the maximum spacing requirement (which is no greater than one-third of the wall length). The vertical reinforcement ran continuously from the walls into the footings, and each bar ended with a 90-degree standard hook in the footing conforming to the ACI 318-14 specification[25] for the development of reinforcement in tension. The surface of the concrete footing underneath each wall was intentionally roughened to increase the frictional resistance.

As shown in Figure 5-2, the roof slab of Specimen 1 consisted of 25-cm-thick (10-in) precast prestressed hollow-core planks with a 13-cm-thick (5-inch) cast-in-place concrete topping. Two reinforced concrete slabs, each with dimensions of 3.0 × 3.0 × 0.36 m (10 ft × 10 ft × 14 in), were secured on top of the roof slab to achieve the target roof mass. For Specimen 2, the roof slab consisted of 20-cm-thick (8-in) hollow-core planks with a 7.6-cm (3-in) concrete topping, as shown in Figure 5-3. It had four additional concrete slabs, each with dimensions of 5.0 × 3.0 × 0.25 m (16.5 ft × 10 ft × 10 in), as added mass. The resulting roof weights of Specimens 1 and 2, including the added concrete slabs, were 245 kN (55.1 kips) and 601 kN (135 kips), respectively. The roof weights of the two specimens were so determined that the T-walls in the two specimens carried the same gravity load. Since the roof slabs were very stiff, the tributary roof load, P, on each wall was assumed to be proportional to the axial stiffness of the wall. The axial compressive load ratio, $P/f'_m A_g$, for each T-wall was 0.016, where A_g is the cross-sectional area of the wall. The compressive strength of masonry, f'_m, was specified to be 17 MPa (2.5 ksi).

Including the weight of the masonry walls from the mid-height to the top, Specimen 1 had an actual seismic weight of 268 kN (60 kips), while Specimen 2 had 661 kN (149 kips). To have the same effective seismic weight as Specimen 2, the input ground motions for Specimen 1 were scaled in time and amplitude to meet the dynamic similitude requirement.

The flexural, diagonal shear, and sliding shear strengths of the T-walls were calculated based on the recommendations and formulas in TMS 402/602 to ensure that the walls would develop diagonal shear-dominated behavior. The flexural strength was calculated using an axial force-moment interaction diagram. It was assumed that the T-walls had a fixed-fixed end condition due to the high stiffness of the roof diaphragms. The calculated flexural, diagonal shear, and sliding shear strengths were 355 kN (80 kips), 326 kN (73 kips), and 397 kN (89 kips), respectively, based on the masonry compressive strength of 17 MPa (2.5 ksi), and the expected yield strength of 469 MPa (68 ksi) for the reinforcing bars. A detailed finite element model (Koutras, 2019) was used to conduct pre-test analysis to determine the ground motion intensity scaling in the shake-table tests as discussed in a following section.

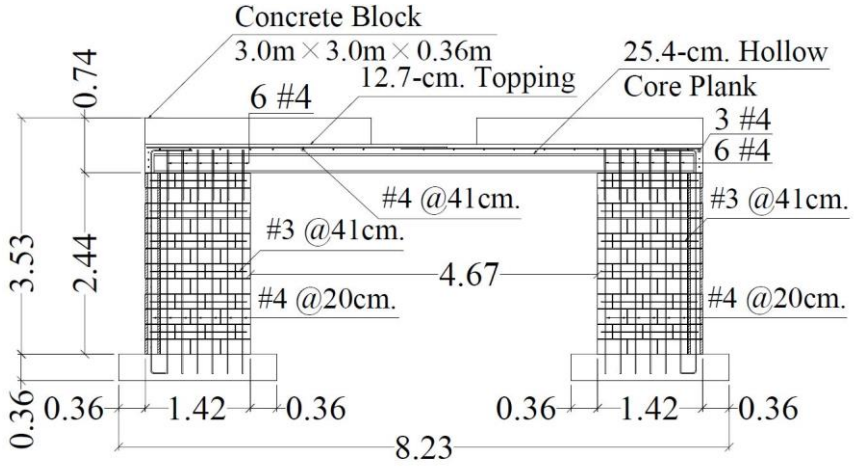

(a) South elevation view

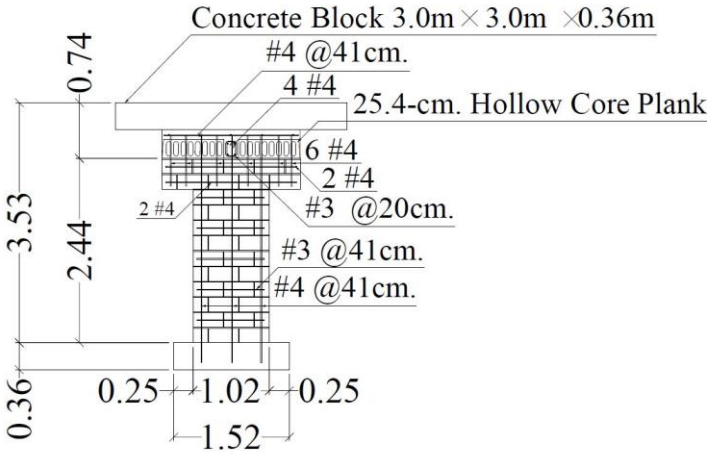

(b) West elevation view

Figure 5-2. Reinforcement details of Specimen 1 (in meters unless indicated)

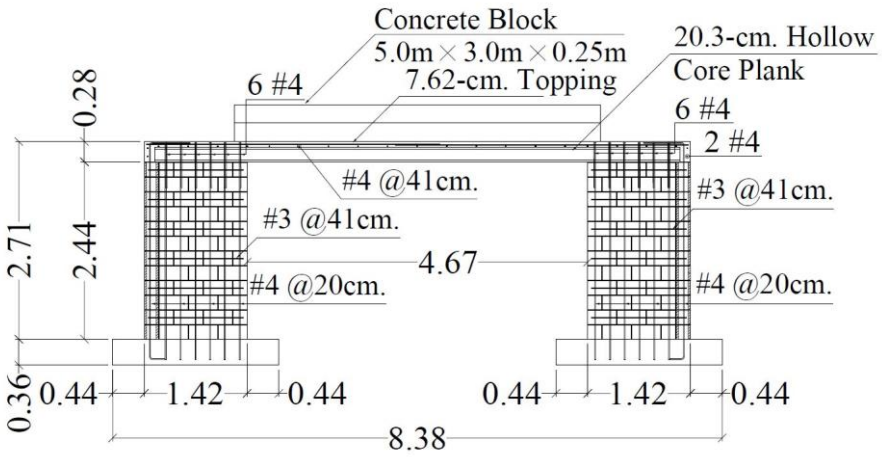

(a) South elevation view

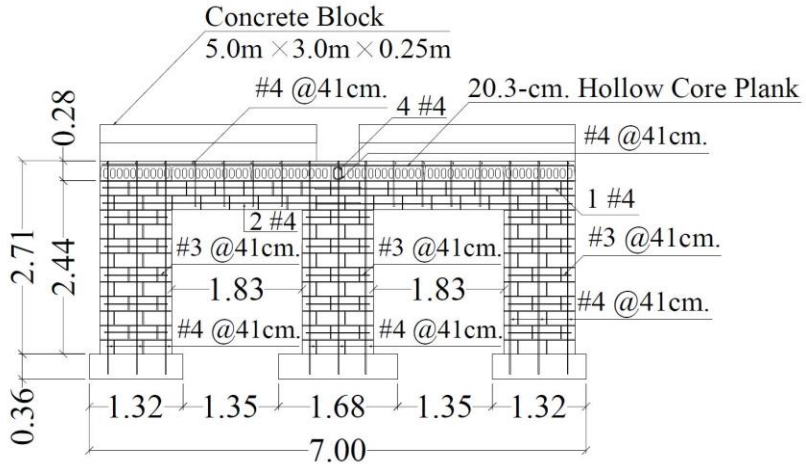

(b) West elevation view

Figure 5-3**.** Reinforcement details of Specimen 2(in meters unless indicated)

5.2. Material Properties

For both specimens, compression tests were performed on 203×102×102-mm (8×4×4-in.) grout prisms, 406×203×203-mm (16×8×8-in.) grouted CMU prisms and 152×305-mm (6×12-in.) concrete cylinders. For Specimen 2, compression tests were also performed on 102 ×203-mm (4×8-in.) grout cylinders and 51 ×102-mm (2×4-in.) mortar cylinders. The compression tests were conducted on the 28th day after the samples were prepared, and some samples were also tested several days after the first ground motion test was performed. The average compressive strengths of the masonry and concrete samples are shown in Table 5-1. Tension tests were conducted on reinforcing bar samples. The average tensile properties are presented in Table 5-2.

Table 5-1. Compressive Strengths of Masonry and Concrete Samples

Specimen	Type of Samples	Age (days)	Number of Samples	Compressive Strength		
				Average		COV
				MPa	ksi	
1	406×203×203-mm grouted CMU prisms	28	2	18	2.7	0.06
		68[b]	6	20	2.9	0.13
	203×102×102-mm grout prisms	28	2	27	3.9	0.01
		68[b]	3	32	4.7	0.02
	152×305-mm footing concrete cylinders	28	3	36	5.2	0.03
	152×305-mm roof concrete cylinders	28	3	35	5.0	0.02
2	406×203×203-mm grouted CMU prisms	28	7	27	3.9	0.07
	203×102×102-mm grout prisms	28	3	36	5.2	0.07
		70[c]	5	45	6.5	0.23
	102×203-mm grout cylinders	28	3	33	4.8	0.04
		70[c]	3	37	5.3	0.02
	51×102-mm mortar cylinders[a]	28	12	30	4.4	0.12
	152×305-mm footing concrete cylinders	28	3	36	5.3	0.03
	152×305-mm roof concrete cylinders	28	3	43	6.3	0.03

[a] Three batches with four samples in each batch
[b] Six days after the first ground motion test on Specimen 1
[c] Eight days after the first ground motion test on Specimen 2

Table 5-2. Average Tensile Properties of Reinforcing Bars

Bar Size	**Number of Samples**	**Yield Stress**		**Tensile Strength**		ϵ_y[a]	ϵ_{sh}[b]	ϵ_{su}[c]
		MPa	ksi	MPa	ksi	mm/mm (in./in.)	mm/mm (in./in.)	mm/mm (in./in.)
Specimen 1								
No.3	3	521	75.6	729	105.8	0.00474	-	0.107
No.4	3	462	67.0	671	97.3	0.00342	0.0106	0.116
Specimen 2								
No.3	3	523	75.9	730	105.9	0.00495	-	0.107
No.4	3	461	66.9	671	97.3	0.00339	0.0107	0.117

[a] Yield strain
[b] Strain at initiation of strain hardening
[c] Strain at peak stress

5.3. Instrumentation

Each specimen had a number of sensors installed to measure the response of the structure during the tests. Specimen 1 had 76 strain gauges, 24 accelerometers, and 56 displacement transducers. Specimen 2 had 136 strain gauges, 40 accelerometers, and 69 displacement transducers. Figures 5-4 and 5-5 shows the locations of the accelerometers and displacement transducers installed on the two specimens. Some locations had a set of three accelerometers to measure the acceleration in east-west, north-south and vertical directions, respectively. For Specimen 1, a set of three accelerometers were located at each corner of the roof slab. Eight sets of accelerometers were installed along the roof perimeter of Specimen 2. To record the table acceleration during the tests, 4 sets of accelerometers were installed on the top surfaces of the concrete footings of the T-walls in both specimens.

For both specimens, there were 7 string potentiometers installed on the north face of the web of each T-wall to measure the wall deformation. As shown in Figures 5-4(a) and 5-5(a), on the east and west sides of a T-wall, a string potentiometer was installed to measure the vertical displacement of the roof slab. For Specimen 2, one string potentiometer was installed along the center line of each out-of-plane wall to measure the vertical roof displacement, as shown in Figures 5-5(b), (c) and (d). The horizontal displacement of the roof relative to the table (the story drift) was measured by string potentiometers mounted along the east edge of the roof with the ends of the strings attached to a stiff reference frame, which was fixed on the table. As shown in Figures 5-4(b) and 5-5(d), Specimen 1 had two string potentiometers to measure the relative roof displacement, and Specimen 2 had three. The multiple string potentiometers were to check if there was horizontal rotation of the roof. Figures 5-4(a) and 5-5(a) also showed that 14 linear potentiometers were installed on the east and west sides of each T-wall to measure the flexural deformation (7 potentiometers on each side). The remaining linear potentiometers were used to measure the uplift and sliding of the base of each T-wall relative to the footing, the sliding between the top of each wall and the roof slab, and the sliding between the web and the flange if any.

For Specimen 2, sensors were installed to check if the concrete blocks secured on the roof slab slid during the tests. They included an accelerometer (along the shaking direction) attached to the west vertical surface of each block and linear potentiometers installed to measure the relative sliding between the roof top and the lower concrete block, and between two stacked blocks.

Strain gauges were installed on the vertical bars near the top and bottom of each wall to measure the flexural strains. Additional gauges were installed on vertical and horizontal bars in the webs of the T-walls along diagonal lines to measure strains induced by diagonal crack opening. The locations of the strain gauges will be shown later in Figures 5-16 and 17 together with the detected yielding.

(a) North view

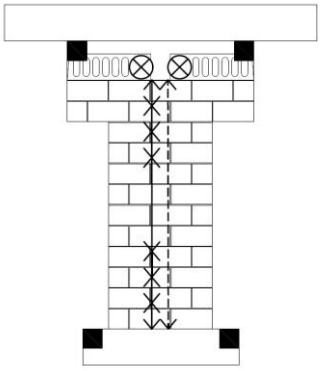

(b) East view

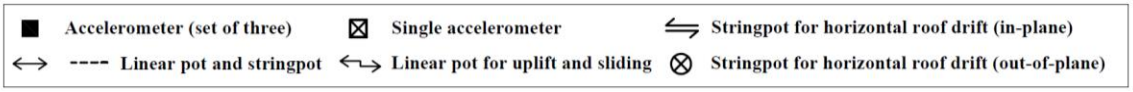

Figure 5-4. Instrumentation plans for Specimen 1

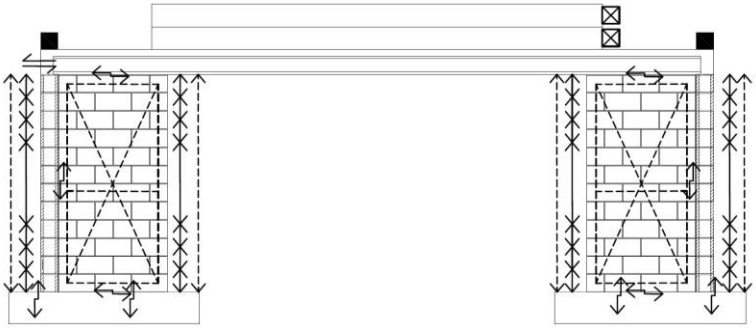

(a) North view North view of two T-walls

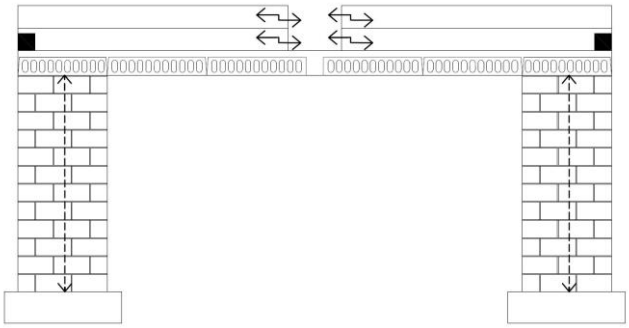

(b) West view of two central out-of-plane walls

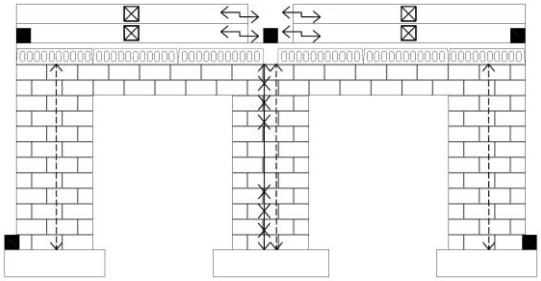

(c) West view

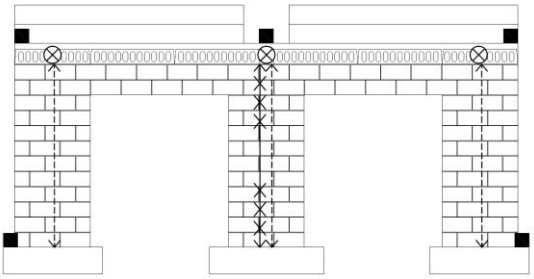

(d) East view

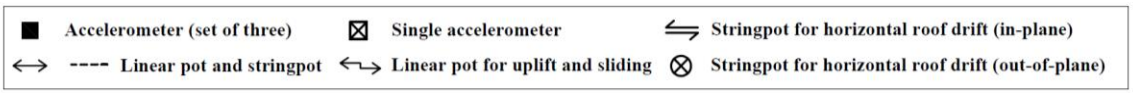

Figure 5-5. Instrumentation plans for Specimen 2

5.4. Test Setup and Loading Protocol

Figure 5-6 shows the two specimens with their footings secured on the shake table with post-tensioned rods. The table motion was in the east-west direction. For each specimen, four concrete pedestals, with two on each of the north and south sides, were used as a catch system to prevent the free fall of the roof slab onto the table in case the walls lost their vertical load carrying capacity. Four steel cables were used to tie the roof slab to the table platen with a slack to avoid uncontrolled drift of the roof. Specimen 1 was tested in two phases. In the first phase, the structure was subjected to a sequence of earthquake motions until it reached a roof drift ratio of 2.53% with a significant strength degradation at the end. In the second phase, the damaged structure was subjected to a quasi-static lateral load with the test setup shown in Figure 5-7. Two cables were used to pull the roof slab by moving the table away from a stiff steel reaction tower, to which the other ends of the cables were attached. During the quasi-static test, the lateral load was monitored with two load cells. The horizontal roof displacement was increased until the lateral resistance of the tested structure dropped close to zero. Specimen 2 was tested with a sequence of ground motions until the structure was on the verge of collapse.

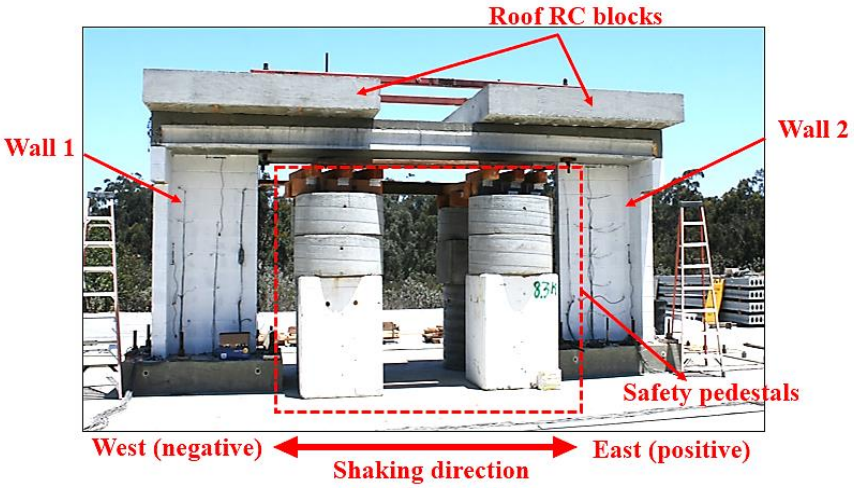

(a) Specimen 1

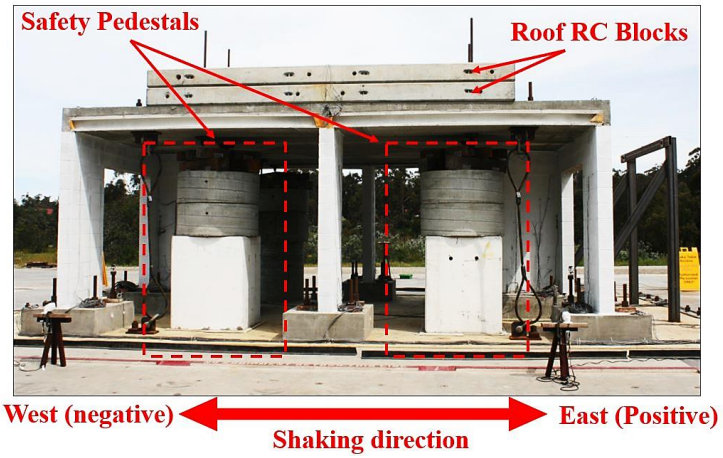

(b) Specimen 2

Figure 5-6. Shake-table test setups

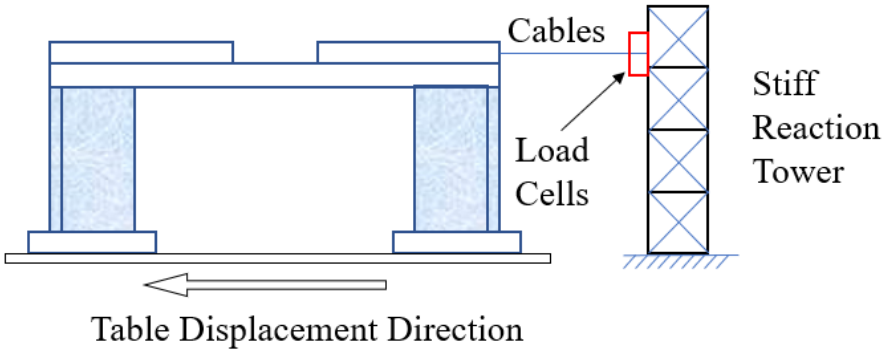

Figure 5-7. Pull test setup for Specimen 1

Two ground motion records from the 1994 Northridge Earthquake were selected for the shake-table tests: a far-field record from the Mulholland station (abbreviated as MUL below) and a near-fault record from the Rinaldi station (abbreviated as RIN below). Table 5-3 shows the sequences of input ground motions applied to the two specimens. After each earthquake motion, the specimen was subjected to white-noise excitation to identify any change in its natural period. The white noise had a root-mean-square amplitude of 0.03g and a duration of 3 minutes. The fundamental periods of both specimens before and after each motion are shown in Table 5-3. For Specimen 1, only the Mulholland record was used, with the acceleration scaled to 45%, 90%, 120%, and 133% of that of the original record in seven runs. For Specimen 2, the Mulholland record was used in the first six runs, with the acceleration scaled to 45%, 90%, 120%, 133%, and 160% of that of the original record. For the last run, the Rinaldi record was used with an intensity scaling of 130%. The Rinaldi record was selected for the last run because the fundamental period of the structure showed a significant elongation (to 0.328 s) after the sixth run, and the acceleration response spectrum of the record has a more or less uniform amplitude in the period range of 0.3 to 0.7 s, as shown in Figure 5-8(a). Moreover, as shown in Figure 5-8(c), the long-duration pulse in the acceleration time history of the Rinaldi record would induce a large displacement demand.

Table 5-3. Test Sequences for Specimens 1 and 2

Specimen 1			Specimen 2		
Test ID	**Input Motion**	**Period After Test (sec)**	**Test ID**	**Input Motion**	**Period After Test (sec)**
Initial	N/A	0.072	Initial	N/A	0.090
1	MUL-45%	0.072	1	MUL-45%	0.090
2	MUL-45%	0.074	2	MUL-90%	0.097
3	MUL-90%	0.090	3	MUL-120%	0.121
4	MUL-90%	0.095	4	MUL-90%	0.123
5	MUL-90%	0.107	5	MUL-133%	0.164
6	MUL-120%	0.166	6	MUL-160%	0.328
7	MUL-133%	0.751	7	RIN-130%*	-
8	Static Pull*	-			

* No white-noise test was performed because of the damage state of the specimens.

Since Specimens 1 and 2 had different roof weights, as mentioned before, additional scaling was applied to the time and amplitude of the earthquake records used for Specimen 1 to attain the dynamic similitude between the two specimens. The ground acceleration was scaled up by a factor of $S_a = 2.4$ (seismic weight of Specimen 2 / seismic weight of Specimen 1), and the time was compressed by a factor of $\sqrt{1/S_a} = 0.65$, with the assumption that both structures had the same lateral stiffness and strength as would be the case in design practice. The value of S_a was calculated with the seismic weights estimated prior to the construction of the specimens and it was 2.7% lower than the value calculated with the actual weights. Figure 5-8(b) shows the table acceleration histories for the 90%-level Mulholland records obtained from two tests performed on Specimens 1 and 2, respectively.

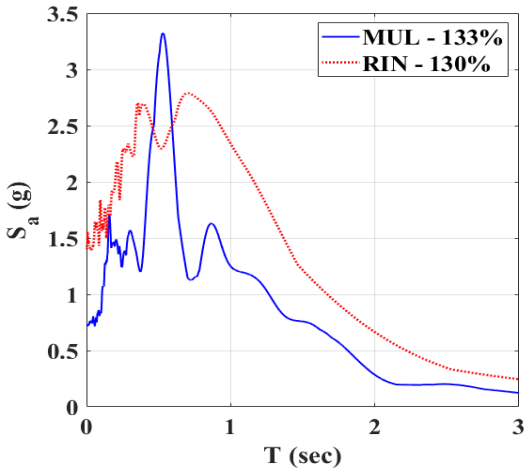

(a) Acceleration spectra of MUL-133% and RIN-130% from the tests of Specimen 2

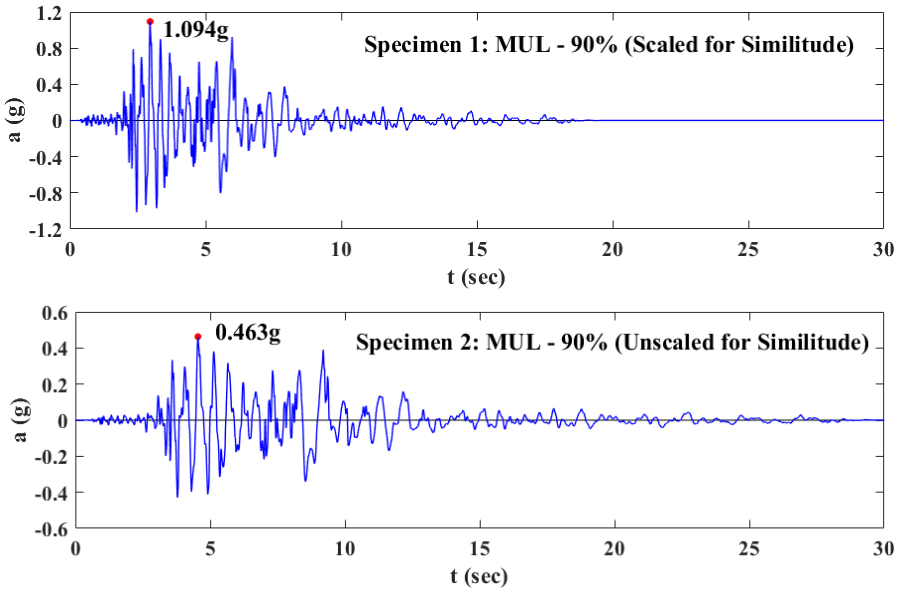

(b) Acceleration histories for MUL-90% from the tests of Specimens 1 and 2

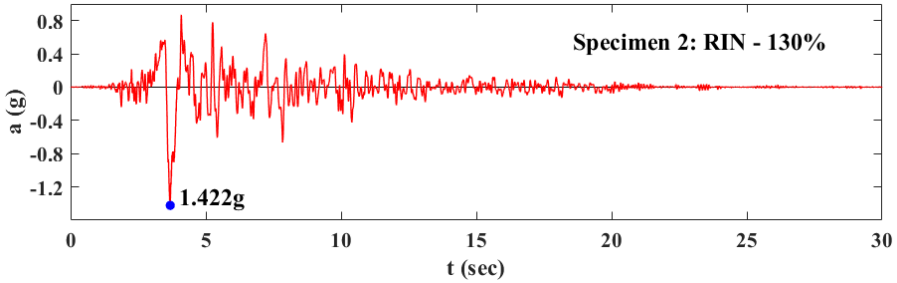

(c) Acceleration history for RIN-130% from the test of Specimen 2

Figure 5-8. Table motions recorded in shake-table tests

Table 5-4. Summary of Test Specimen Behaviors

Failure Mode	Maximum Lateral Resistance			Max. Roof Drift (%)	Occurrence of Collapse	Strength Degradation at Different Roof Drift Levels (%)		
	Test Value V_{max} (kN)	Code Formula V_n (kN) [a]	V_{max}/V_n			2% Drift	5% Drift	10% Drift
Specimen 1								
Shear	689	685	1.00	16.7	No	18.3	43.5	72.3
Specimen 2								
Shear	925	783	1.18	13.4	No	19.4	45.9	78.4

[a] The shear strength formulation in TMS 402/602 (TMS 2016).

Table 5-5. Peak Values of Structural Responses for Select Ground Motions

Test ID	Input Motion	Peak Roof Displacement (cm)		Peak Roof Drift[1] (%)		Peak Base Shear (kN)		Peak Base Sliding at Wall-1 (mm)		Peak Base Sliding at Wall-2 (mm)	
		Pos.	Neg.	Pos.	Neg.	Pos.	Neg.	Pos.	Neg.	Pos.	Neg.
Specimen 1											
5	MUL-90%	0.56	0.49	0.23	0.20	469	472	0.17	0.24	0.48	0.45
6	MUL-120%	1.01	1.14	0.42	0.47	598	561	0.37	0.50	1.00	1.01
7	MUL-133%	5.05	6.15	2.07	2.52	619	690	0.56	1.19	1.70	2.78
8	Static Pull[2]	40.7	-	16.7	-	394	-	-	-	-	-
Specimen 2											
2	MUL-90%	0.19	0.16	0.08	0.06	414	432	0.14	0.04	0.11	0.04
3	MUL-120%	0.29	0.35	0.12	0.14	521	598	0.34	0.25	0.35	0.21
5	MUL-133%	0.41	0.61	0.17	0.25	618	722	0.68	0.70	0.76	0.59
6	MUL-160%	1.18	2.20	0.48	0.90	777	925	2.21	3.00	2.63	2.58
7	RIN-130%	32.7	22.1	13.4	9.07	902	428	3.77	4.98	2.42	8.10

[1] Roof drift ratios are calculated based on a wall height of 2.44 m.

[2] Test 8 was a quasi-static test in which all displacement transducers measuring base sliding were removed.

5.5.1. Specimen 1

Tests up to MUL-90%

Two low-intensity and three mid-intensity tests were conducted on Specimen 1 by scaling the Mulholland record to 45% and 90%, respectively. The two low-intensity motions and the first mid-intensity motion were to check the instrumentation. No visible cracks were observed on the walls during the two 45%-level motions. As shown in Table 5-3, the fundamental period of the intact specimen (0.072 s) hardly changed after these shakings. After the first shaking with the 90% level motion, the fundamental period of the specimen increased by 0.018 second, indicating that some damage had occurred during the test. After three shakings with the 90%-level motions, it was observed that a few hairline flexural cracks initiated in the webs near the bottom of the two walls. The fundamental period measured from the white-noise tests increased to 0.107 s.

Test with MUL-120%

During the test with the 120%-level Mulholland motion, hairline cracks occurring in the last few tests opened and extended. Meanwhile, more flexural cracks initiated and propagated in the webs and flanges near the bottom of both walls, as shown in Figure 5-9. The fundamental period of the specimen increased from 0.107 to 0.166 s, which was largely attributed to the development of flexural cracks and the yielding of the vertical reinforcement near the wall base. As shown in Figure 5-10, during this motion, the maximum resistance developed by the structure reached 598 kN (134 kips) at a roof drift ratio of 0.35%. The maximum roof drift ratio reached in this test was 0.47%.

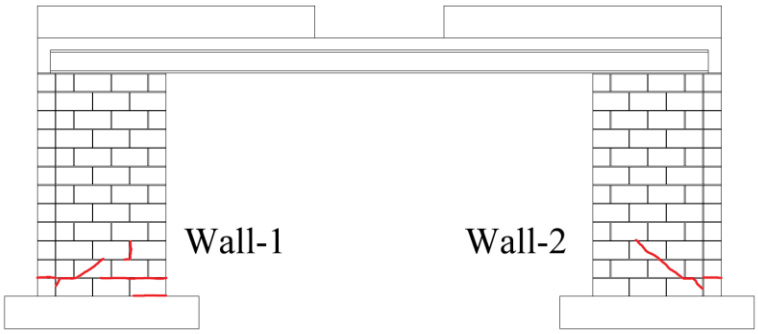

(a) South view

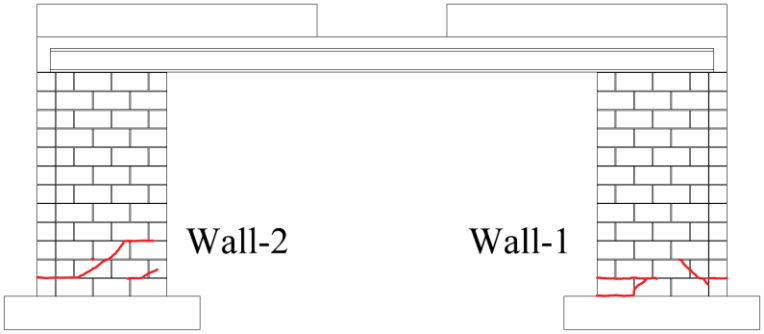

(b) North view

Figure 5-9. Crack patterns on Specimens 1 after MUL-120%

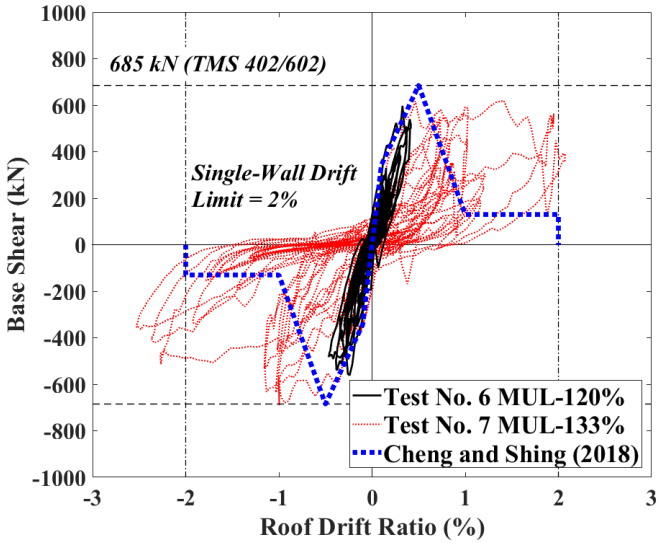

(a) Responses from the ground motion tests

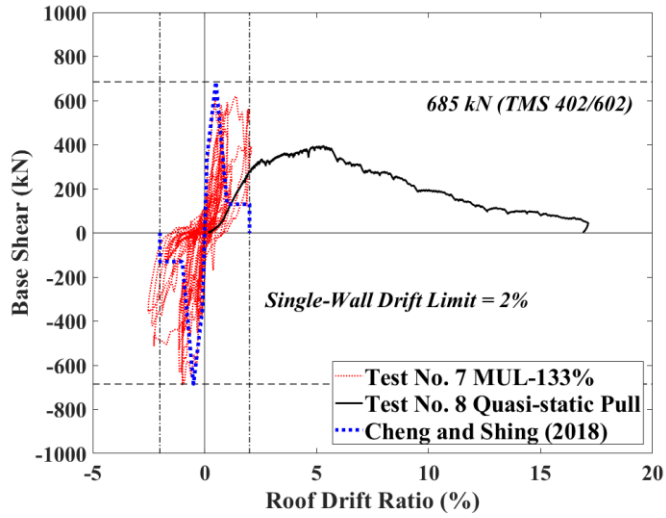

(b) Results from the quasi-static and last ground motion tests

Figure 5-10. Base shear-vs.-roof drift ratio curves for Specimen 1

Test with MUL-133%

The last dynamic test on Specimen 1 was conducted with a 133%-level Mulholland motion. In this test, the walls developed severe shear cracks. The specimen exhibited significant lateral drifts as the period of the structure elongated into the range in which the acceleration spectrum of the record peaked. The damage shifted the fundamental period of the structure from 0.166 to 0.751 s, as shown in Table 5-3, with the peak spectral acceleration of the ground motion occurring at 0.35 s after the similitude scaling. Figure 5-11 shows the severe diagonal shear cracks and the masonry spalling and crushing that developed in the webs of the T-walls. However, none of the diagonal cracks propagated into the flanges. As shown in Figure 5-11, Wall-2 (East T-Wall) also showed base crushing and subsequent buckling of the extreme vertical bar in the web near the wall base. The base shear-vs.-roof drift hysteresis curves for the structure (Figure 5-10) shows that the peak strength of 690 kN (155 kips) was reached at a roof drift ratio of about 1% in the negative (west) direction. A maximum roof drift ratio of 2.53% was reached in the west direction. At this drift level, the lateral resistance of the tested structure dropped to 340 kN (76.3 kips), which was about 50% of the peak strength.

Quasi-static pull test

After MUL-133%, to examine the maximum roof drift ratio that could be sustained by the structure before collapse, a quasi-static test was conducted by pulling the roof with steel cables. The quasi-static test was done instead of a dynamic test because of safety reasons. During the quasi-static test, the diagonal cracks in each wall continued to extend and open as the horizontal roof displacement increased. Severe crushing and spalling of

the masonry were observed. As shown in Figure 5-10(b), the lateral resistance of the wall system dropped to 44 kN (9.9 kips), which is 6% of the peak strength, when a roof drift ratio of 16.7% (42.4-cm roof horizontal displacement) was reached. Horizontal cracks were observed in the wall flanges, and a few diagonal cracks in the webs had extended into the flanges. As shown in Figure 5-12, at the roof drift ratio level of 16.7%, collapse was averted because the flanges were still able to carry the weight of the roof slab when the masonry in the wall webs had been severely crushed.

(a) South view of Wall-1

(b) North view of Wall-2

Figure 5-11. Damage in Specimen 1 after MUL-133%

Figure 5-12. Damage in Specimen 1 after the quasi-static pull test

5.5.2. Specimen 2

Tests up to MUL-133%

Specimen 2 was subjected to a similar sequence of ground motions as Specimen 1, which were 45%, 90%, 120% and 133%-level Mulholland motions, as shown in Table 5-3. An additional MUL-90% motion (test No. 4) was applied after the MUL-120% motion to check the instrumentation after the replacement of two faulty accelerometers. While flexural and shear cracks developed in Specimen 1 after the 120% and 133%-level Mulholland motions, there were no visible cracks observed in Specimen 2 after the MUL-133%. The fundamental period of Specimen 2 increased slightly from 0.090 to 0.097 s after the first MUL-90%.

Figure 5-13(a) shows the base shear-vs.-roof drift ratio curves for the 120% and 133%-level Mulholland motions applied to Specimen 2. During the test with MUL-120%, the specimen reached a maximum base shear of 598 kN (135 kips) at a drift ratio of 0.14%. The fundamental period increased to 0.121 s after this motion and remained unchanged after the following MUL-90%. Figure 5-13 also shows that the specimen developed nonlinearity during MUL-133%. The peak drift ratio reached in the test was 0.25%, while the maximum base shear developed was 726 kN (163 kips). The period of the specimen increased to 0.164 s, indicating some damage.

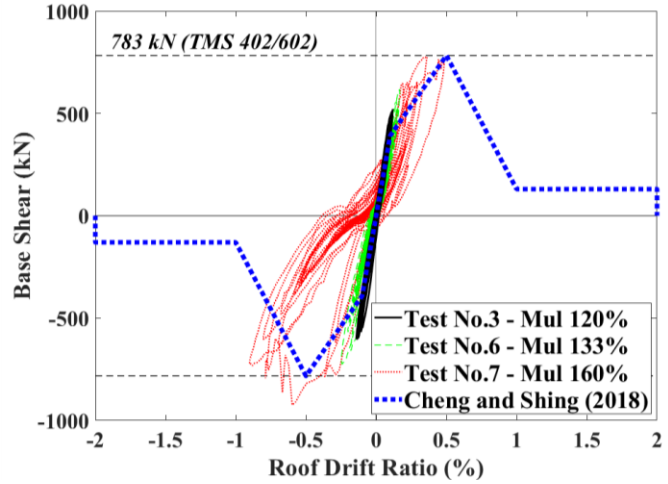

(a) Mulholland motions

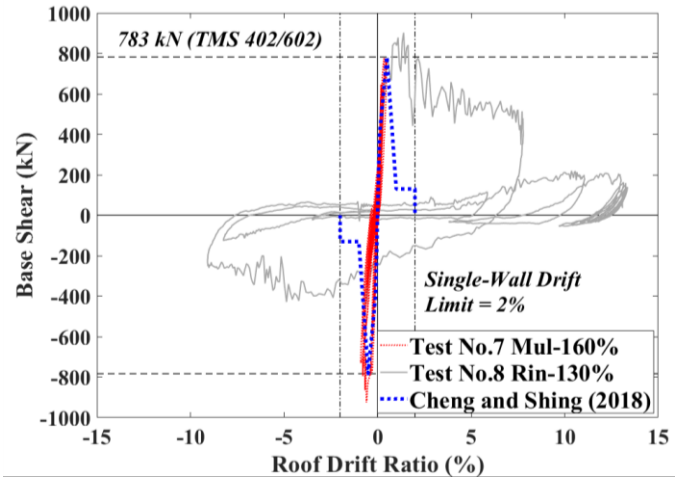

(b) Last two motions

Figure 5-13. Base shear-vs.-roof drift ratio curves for Specimen 2

Test with MUL-160%

During MUL-160%, the period of the specimen elongated from 0.164 to 0.328 s. A maximum drift ratio of 0.90% was reached. As shown in Figures 11(a) and (b), the base shear capacity of 925 kN (208kips) was reached at a roof drift ratio of 0.60% in the negative (west) direction. During the test, load degradation was relatively mild, about 22% with respect to the peak. Figure 5-14 shows the crack pattern obtained after MUL-160%.

Flexural and diagonal shear cracks occurred in the webs of the T-walls. As shown in Figure 5-14(a), in the web of Wall-1, a major diagonal crack extended from the top right corner to the wall flange above the fourth course of masonry units from the base, and then propagated as a horizontal crack in the flange. On the same wall, a crack developed along the flange-web interface, propagating from the end of the major diagonal crack down to the wall base. In Wall-2, major diagonal cracks extended into the toe of the web at one end and to the flange at an approximately 60-degree angle with respect to the horizontal at the other, propagating vertically up along the web-flange interface. Similar to Wall-1, one diagonal crack extended into the wall flange and formed a horizontal crack on the flange. Furthermore, several flexural cracks initiated and propagated in the lower part of the wall webs. Toe crushing occurred in the web of Wall-2. As shown in Figures 5-14(c) and (d), horizontal cracks developed at the top of the out-of-plane walls right below the lintel. For the two middle out-of-plane walls (Walls 4 and 7 as identified in Figure 5-1), no visible cracks were observed.

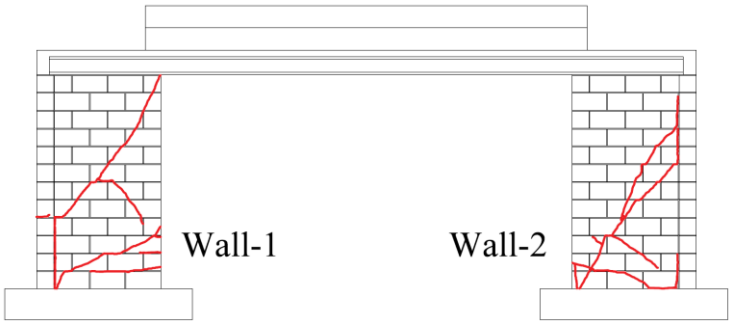

(a) South view of two T-walls

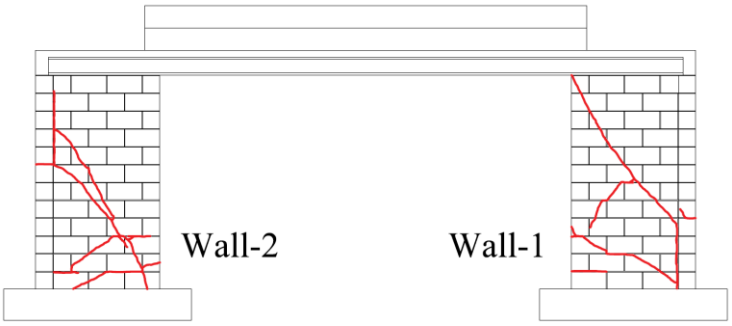

(b) North view of two T-walls

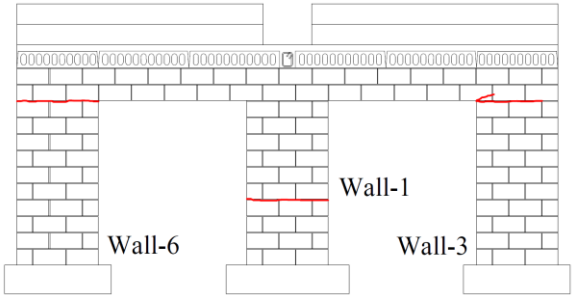

(c) West view of T-wall flange and out-of-plane walls

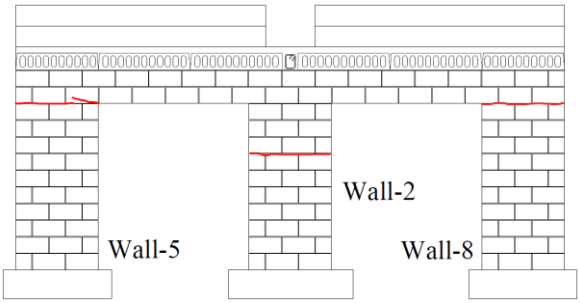

(d) East view of T-wall flange and out-of-plane walls

Figure 5-14. Crack patterns on Specimens 2 after MUL-160%

Test with RIN-130%

During RIN-130%, the T-walls developed severe damage. A maximum drift ratio of 13.4% was reached, but the structure did not collapse. The base shear-vs.-roof drift ratio curves in Figure 5-13(b) show that the maximum base shear reached 902 kN (203 kips) at a drift ratio of 1.39% in the positive (east) direction. The specimen developed a residual strength of 185 kN (41.6 kips), which was about 20% of the peak strength (208 kips) reached during MUL-160%. Figure 5-15 shows the damage of the specimen after the test. The diagonal cracks developed during MUL-160% extended further and were accompanied by the opening of new diagonal cracks in the webs of the T-walls. As in the quasi-static test of Specimen 1, severe masonry crushing occurred in the wall webs. The webs and flanges of the T-walls were practically separated. The failure of the 90-degree hooks connecting the flanges and webs was observed, along with the fracture of the horizontal bars crossing the flange-web interfaces. The flanges of the T-walls exhibited severe out-of-plane bending at the elevation of the horizontal cracks that developed in motion MUL-160%. Figure 5-15(e) shows that masonry spalling occurred on the east face of Specimen 2. Moreover, cracks radiated from the corners between the lintels and the out-of-plane rectangular walls, as shown in Figures 5-15(b) and (f). However, the roof slab remained practically intact during the test.

(a) South view of Specimen 2

(b) West view of Specimen 2

(c) South view of Wall-1

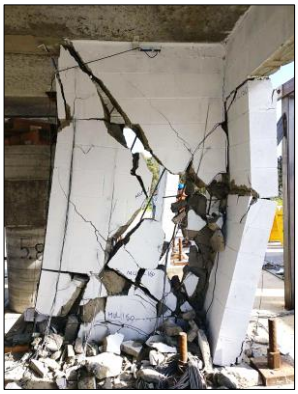

(d) South view of Wall-2

(e) Damage in the flange of Wall-2

(f) Cracks developed near the roof and the lintels

Figure 5-15. Damage in Specimen 2 after RIN-130%

5.6. Analysis of Test Results

5.6.1. Yielding and Fracture of Reinforcing Bars

Figures 5-16 and 5-17 show the sequence of yielding in the reinforcing bars in Specimens 1 and 2, respectively. Yielding in the reinforcing bars was determined by comparing the average yield strain obtained in the material sample tests and the strains recorded by the strain gauges attached to the bars.

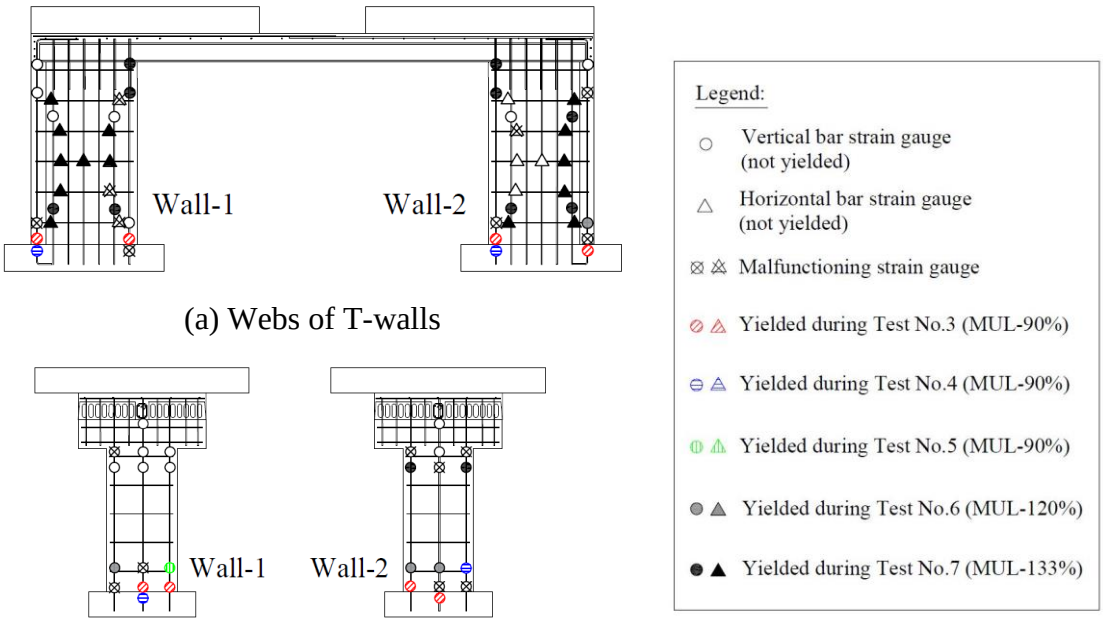

(a) Webs of T-walls

(b) Flange of Wall-1 (c) Flange of Wall-2

Figure 5-16. Yielding of reinforcing bars in Specimen 1

The first yielding in Specimen 1 occurred during the first MUL-90% (test No. 3) motion. The vertical bars at the two extreme sides of the two T-walls yielded in tension near the wall base, as shown in Figure 5-16. After three shakings with MUL-90%, three (out of six) vertical bars in the flanges had yielded at the first masonry course from the base. Moreover, both walls had one vertical bar in the flange yielded at the second course from the base. No yielding was detected in the vertical bars in the webs during the last two

MUL-90% tests. After the test with motion MUL-120%, most of the vertical bars in the flanges of both walls (5 out of 6) had yielded at the second course from the base. During the test with MUL-133%, most of the vertical and horizontal bars in the webs yielded at the locations where the major diagonal cracks developed. Yielding also occurred at the top of the extreme vertical bar near the free edge of each T-wall web. While there was no yielding detected near the top of the flange of Wall-1, two vertical bars in the flange of Wall-2 yielded near the top.

In Specimen 2, the vertical bar yielded in tension at the toe of the web of Wall-1 during test No.2 (with MUL-90% motion), as shown in Figure 5-17(a). In addition, the extreme vertical bar in the web of Wall-2 yielded in the region embedded in the concrete footing, indicating strain penetration. During MUL-133%, a vertical bar in the flange of Wall-2 yielded near the base. Yielding of the bars during these motions indicates that the walls were subjected to significant flexural deformation before the peak capacity was reached. During MUL-160%, with the initiation of diagonal cracks in the webs of the two T-walls, yielding occurred in the vertical and horizontal bars at locations intersected by diagonal shear cracks. Meanwhile, a few vertical bars in the wall flanges and the out-of-plane walls yielded. During the last test with RIN-130%, more bars in the webs of the T-walls yielded due to the opening of major diagonal cracks. After this test, most of the vertical bars at the top and bottom of each out-of-plane wall and T-wall flanges had yielded, showing that the walls were subjected to double-curvature bending.

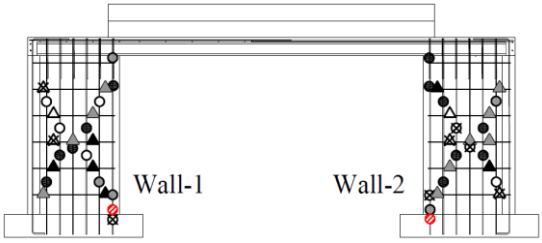

(a) Webs of T-walls

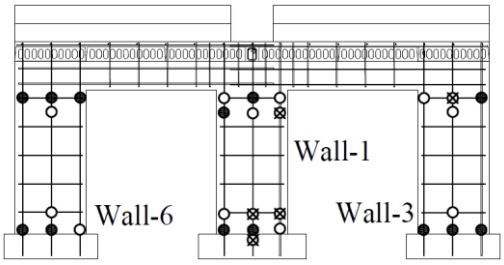

(b) Flange of Wall-1 and two west out-of-plane walls

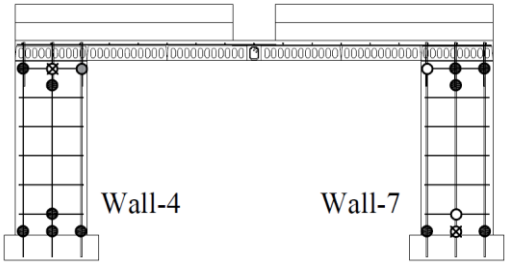

(c) Two middle out-of-plane walls

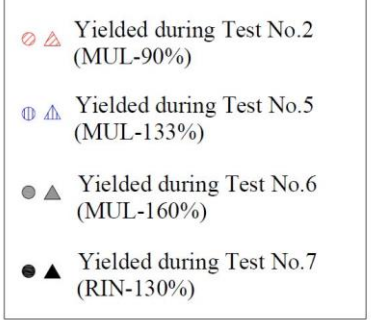

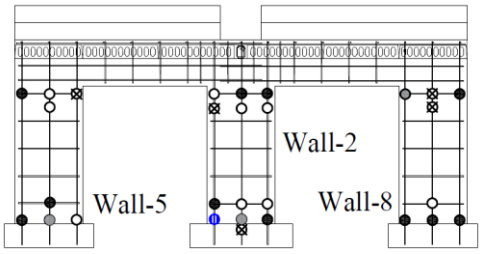

(d) Flange of Wall-2 and two east out-of-plane walls

Figure 5-17. Yielding of reinforcing bars in Specimen 2

The reinforcing bars in the two specimens had similar yielding sequences. Yielding first occurred in some of the vertical bars near the base of the two T-walls due to the flexural deformation. After the diagonal shear cracks opened, most of the horizontal and vertical bars in the webs of the T-walls yielded at the locations where the diagonal cracks passed. For Specimen 1, the opening of the diagonal shear cracks in the wall webs was accompanied by the yielding of the vertical bars near the top of the flange of Wall-2. For

Specimen 2, yielding was detected in most of the vertical bars near the top and bottom of the T-wall flanges and the out-of-plane walls during the last ground motion test.

Figure 5-18 shows the locations where bar fracture occurred during the tests. In Specimen 1, fracture occurred in two horizontal bars at the locations of major diagonal crack opening during the quasi-static test. In Specimen 2, all the horizontal bars (except the two top bars) in the webs of the T-walls fractured at the locations along the major shear cracks. It can also be observed that two of the horizontal bars in Wall-1 of Specimen 2 fractured at the location of the flange-web interface due to the opening of the vertical crack at that location during MUL-160%. Moreover, the vertical bar in Wall-2 fractured near the toe. Specimen 2 had significantly more fractured bars than Specimen 1 probably because the diagonal cracks in Specimen 1 were more closely spaced, while in Specimen 2 the diagonal cracks were more localized inducing larger tensile strains in the horizontal bars. Furthermore, it is likely that the quasi-static pull test conducted on Specimen 1 allowed more time for the reinforcing bars to slip, which reduced the tensile strains in the bars, when compared to a dynamic test.

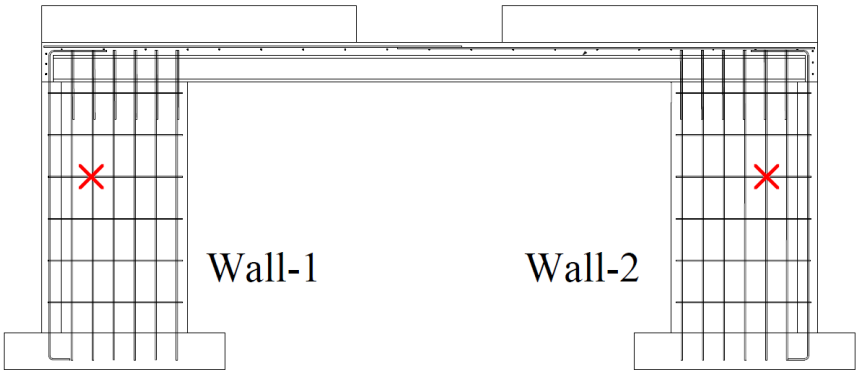

(a) Specimen 1 after the quasi-static pull test

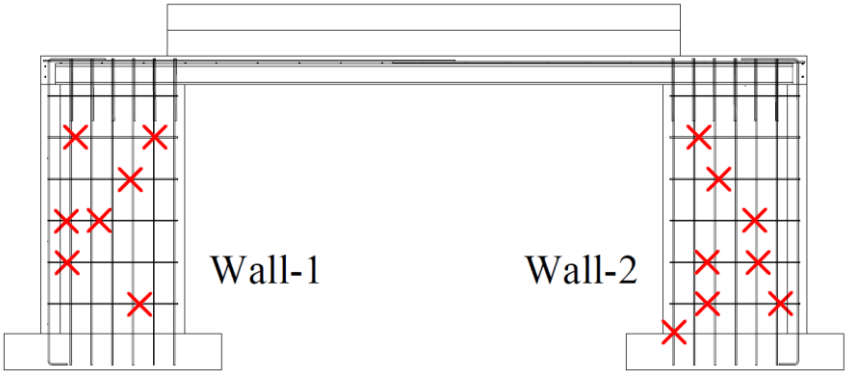

(b) Specimen 2 after Rin-130%

Figure 5-18. Fracture of reinforcing bars

5.6.2. Deformation Mechanism

Figure 5-19 shows the time histories of the drift ratios of the T-walls in the two specimens due to flexural deformation, shear deformation and wall sliding, respectively, for select tests in which these walls had noticeable flexural and shear cracks. The displacement due to flexural deformation is calculated from the curvature measured by the vertical displacement transducers mounted along the two sides of each wall. The sliding displacement is the sum of the sliding measured at the top and the base of the wall by the linear potentiometers. The shear deformation is calculated by subtracting the sliding and

the flexural deformation from the total roof displacement. The calculated shear deformation has been checked with the data acquired by the diagonal string potentiometers. The two sets of values show good consistency. Such data was not collected in the quasi-static test of Specimen 1 because the displacement transducers had been removed. The results for Specimen 2 under RIN-130% are not shown because some of the displacement transducers got damaged during that motion.

For Specimen 1, as shown in Figure 5-19(a), the displacement component due to flexure was significantly greater than the shear and sliding components during MUL-120. This is consistent with the flexural cracks observed and the absence of major diagonal cracks during that test, as shown in Figure 5-9. However, as shown in Figure 5-19(b), during MUL-133%, the shear deformation constituted a significant portion of the total roof drift, especially after the peak roof drift had been reached, due to the opening of diagonal shear cracks. For Specimen 2, during MUL-160%, the flexural components of the two T-walls accounted for 46.9% and 63.6% of the total peak roof drift, respectively, as shown in Figure 5-19(c). This indicates that the opening of the diagonal shear cracks was a bit delayed in Specimen 2 as compared to Specimen 1.

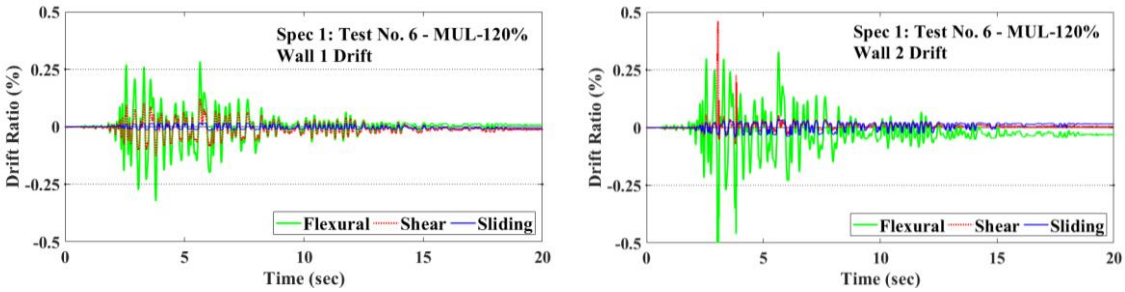

(a) Specimen 1 during MUL-120%

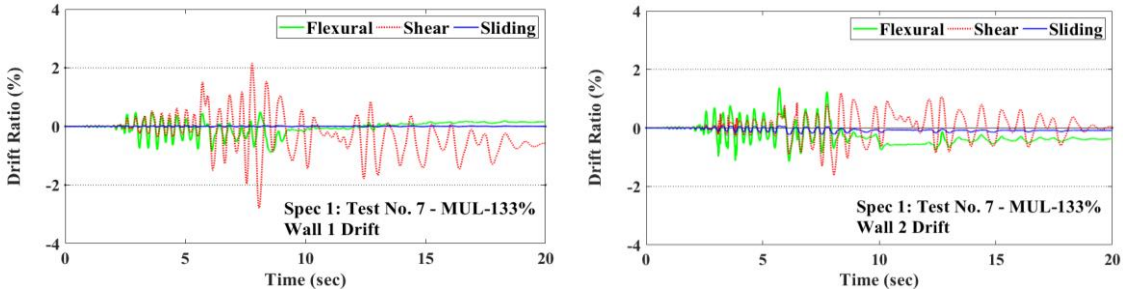

(b) Specimen 1 during MUL-133%

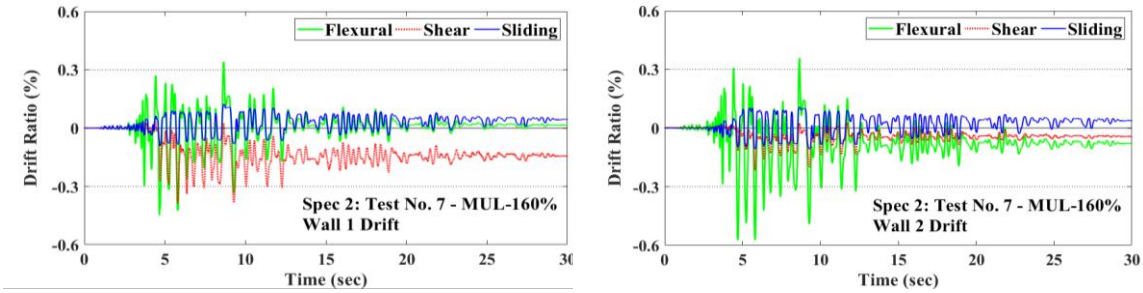

(c) Specimen 2 during MUL-160%

Figure 5-19. Drift time histories of the T-walls due to flexure, shear, and sliding

5.6.3. Lateral Strengths

The shear strength formula of TMS 402/602 (2016) is used to calculate the lateral resistance of the two specimens. In this calculation, the shear-span ratio ($M_u/(V_u d_v)$) of the T-walls is taken to be 0.86 with the assumption that the walls had no rotations at the top because of the stiff roof diaphragms. Figure 5-20 shows that the flexural curvatures measured by the linear potentiometers at the top and the bottom of the T-walls in Specimen 1 varied in opposite directions, indicating that the walls were deformed in double curvature. However, the curvatures measured at the top of the walls were a lot smaller than those at the bottom, implying that the rigid roof diaphragm assumption was not entirely correct. The above observation has no significant consequence here since the shear-span ratio assumed is already close to the upper limit of 1.0 specified in TMS 402/602 (2016). Furthermore, the axial load on each T-wall is assumed to be from the gravity load only, with the axial force introduced by the horizontal load ignored. This is a good assumption because the increase of the axial force in one wall due to the coupling effect of the roof diagonal is offset by a decrease in the other wall. The lateral resistance of Specimen 2 is assumed to be provided by the two T-walls only, and the flexural resistance of the six out-of-plane walls is ignored. The latter is relatively small. The masonry compressive strength and the yield strength of the horizontal reinforcing bars used in the calculations are based on the average values obtained from the masonry prism tests and the tensile tests of the bars, which are shown in Tables 5-1 and 5-2. For Specimen 1, the calculated shear strength is 685 kN (154 kips), which is almost identical to the peak strength of 689 kN (155 kips) reached in the test, as shown in Figure 5-10. For Specimen 2, the calculated strength is 783

kN (176 kips), which is 142 kN (32 kips) lower than the peak strength reached during MUL-160%, as shown in Figure 5-13.

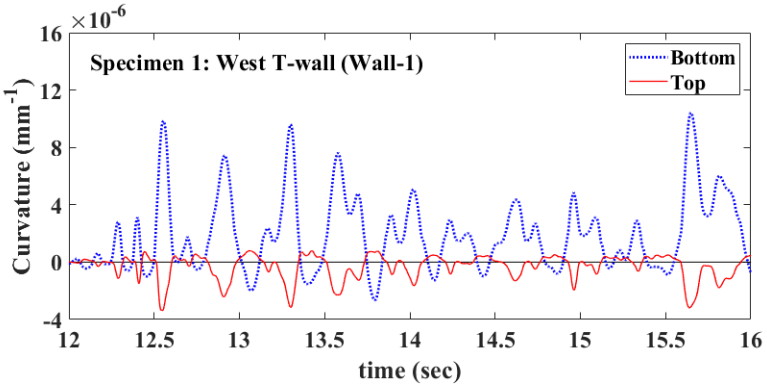

(a) West T-wall

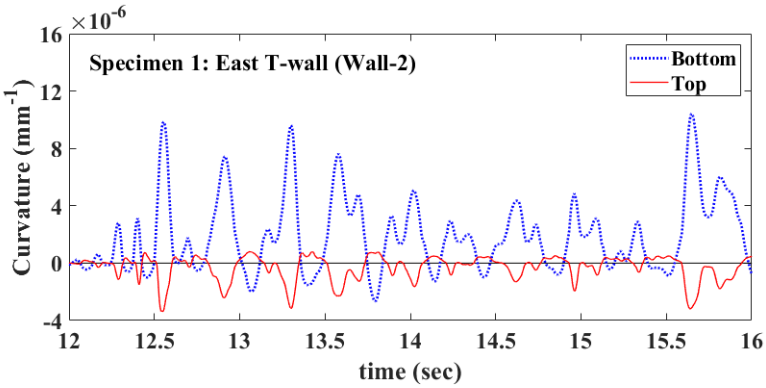

(b) East T-wall

Figure 5-20. Time histories of the measured curvature near the top and bottom of two T-walls of Specimen 1 during test MUL-120%

The higher lateral strength of Specimen 2, compared to Specimen 1, can be attributed to the flexural resistance and the axial restraint introduced by the six out-of-plane walls, as discussed in Mavros et al (2015). As the T-walls developed flexural deformation, they rocked on the footings because of the penetration of the tensile strains in the vertical bars into the region embedded in the footings. The rocking motion of the walls would push up the roof diaphragm, which was, however, restrained from moving up by the out-of-plane walls. Hence, the T-walls experienced increased axial compression when they rocked due

to the restraint of the out-of-plane walls. Figure 5-21 shows the plots of the strains in the center vertical reinforcing bars near the top of the out-of-plane walls against the roof drift during MUL-160%. It can be seen that the bars developed tension when the structure displaced in either direction. This is consistent with the flexure as well as the rocking restraint of the out-of-plane walls.

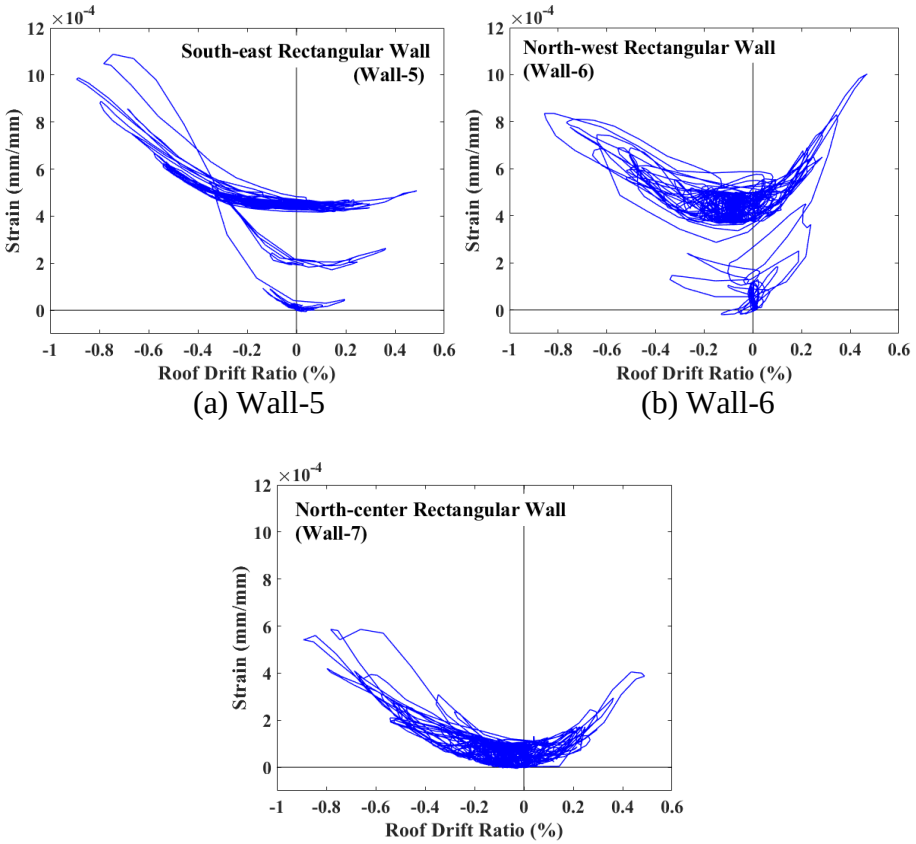

(a) Wall-5 (b) Wall-6

(c) Wall-7

Figure 5-21. Strains in the center vertical reinforcing bars near the top of the out-of-plane walls of Specimen 2 during MUL-160%

To assess the likelihood of each phenomenon, the following analyses have been conducted considering two scenarios. The results are shown in Table 5-6. In the first scenario, the shear resistance of the T-walls and the flexural resistance of the out-of-plane

walls are calculated with the gravity load only, with the roof weight distributed among the walls in proportion to their axial stiffness. The flexural resistance of the out-of-plane walls is calculated with a fixed-fixed end condition. The total lateral resistance is the sum of the shear resistance of the T-walls and the flexural resistance of the six out-of-plane walls. In the second scenario, the rocking of the T-walls is considered and the lateral resistance is assumed to be contributed by the shear strength of the T-walls only. In that case, the total axial compression exerted on the T-walls is calculated as the sum of the tensile forces developed by the vertical bars in the out-of-plane walls and the tributary gravity load. The tensile forces developed in the vertical bars that had not yielded during MUL-160% are calculated with the strains measured in the vertical bars near the top of each out-of-plane wall at the peak base shear. For those bars that had yielded, the average yield strength shown in Table 5-2 is used because the maximum tensile strains developed in those bars did not exceed the strain-hardening point. The flexural resistance of the out-of-plane walls is ignored based on the consideration that the flexural strength would diminish to zero as significant axial tension was developed in a wall. As shown in Table 5-6, the second scenario provides a significantly better match of the maximum lateral resistance developed in the test with a difference of only 0.3%. Hence, the higher lateral resistance of Specimen 2 is most likely due to the axial restraint of the out-of-plane walls, which is consistent to the observation of Mavros et al (2016).

Table 5-6. Calculated Lateral Resistance of Specimen 2

Wall Type	Axial Load Distribution 1		
	Wall Axial Load[a] [kN (kips)]	**Flexural Strength [kN (kips)]**	**Shear Strength [kN (kips)]**
Each T-wall	126 (28.3)	431 (96.9)	393 (88.3)
Each Out-of-plane Wall	58 (13.0)	18 (4.0)	0
Base Shear Capacity [kN (kips)]	893 (200.8)		
Wall Type	**Axial Load Distribution 2**		
	Wall Axial Load[b] [kN (kips)]	**Flexural Strength [kN (kips)]**	**Shear Strength [kN (kips)]**
Each T-wall	409 (91.9)	599 (134.7)	464 (104.3)
Each Out-of-plane Wall	0	0	0
Base Shear Capacity [kN (kips)]	928 (208.6)		

[a] Tributary roof weight proportional to the wall axial stiffness

[b] Half of the bar forces in the six out-of-plane walls plus half of the roof weight

5.6.4. Displacement Capacity

Figure 5-22 shows the damage states of the T-walls in the two specimens when the roof drift level reached 2%, 5%, and 10%, respectively. The respective strength degradations at these drift levels can be observed from the normalized base shear-vs.-roof drift ratio curves in Figure 5-23. At the drift level of 2%, the strength degradation was about 25% for both specimens, and diagonal shear cracks were visible in the webs, but they

were not significantly opened. Specimen 2 had more severe shear cracks, one of which propagated as a horizontal flexural crack into the flange of one T-wall. At the drift level of 5%, the strength degradation was about 50% for both specimens, and the webs of the T-walls had significant opening of the diagonal shear cracks. The webs of the T-walls in Specimen 1 exhibited severe masonry spalling, and some shear cracks propagated into the flanges. At 10% drift, the strength degradation was about 75% for both specimens, and the webs of the T-walls in both specimens had severe masonry crushing. Specimens 1 and 2 reached maximum roof drift ratios of 16.7% and 13.4%, respectively, without collapsing. At the end of the tests, the webs of the T-walls in both specimens had lost significant portions of the masonry due to crushing, and the roof weight was carried by the wall flanges, and, for the case of Specimen 2, also by the out-of-plane walls. For Specimen 1, at the roof drift level of 16.7%, the minimum lateral resistance required to resist the P-Δ effect of the roof weight is calculated to be 41 kN (9.2 kips). This resistance could be provided by the flexural strength of the wall flanges alone, which is estimated to be 44 kN (10 kips). For Specimen 2, at the roof drift level of 13.4%, the minimum lateral resistance required to resist the P-Δ effect is calculated to be 81 kN (18 kips), while the maximum resistance that could be provided by the flexural strengths of the flanges of the T-walls and the out-of-plane walls is calculated to be 152 kN (34 kips). At this damage state, the T-walls would not rock and the flexural strength of the out-of-plane walls could develop.

The tests have shown that RM wall systems with failure dominated by diagonal shear could develop significant lateral displacements without collapsing. The drift ratios attained and the ductility exhibited by the two specimens far exceed those observed from quasi-static tests conducted on shear-dominated planar wall segments (e.g., the tests of

Voon and Ingham, 2006; Shing et al., 1991; Ahmadi, 2012). Figure 5-13 compares the base shear-vs.-story drift ratio backbone curve developed by Cheng and Shing (2018) based on data from quasi-static wall tests to the hysteresis curves obtained from the shake-table tests. The difference in the displacement capacities is significant. The higher displacement capacity and more gentle load degradation exhibited by the shake-table test specimens can be attributed to several factors. One is the loading protocol. In typical quasi-static tests, wall specimens were normally subjected to a large number of displacement cycles with small to large amplitudes, which would introduce a more severe load degradation than what would have been experienced in an earthquake. The second is the presence of wall flanges and/or out-of-plane walls, which would carry the vertical load after the webs were severely damaged, in the shake-table test specimens, while there would be no alternative load paths for wall segments that had no flanges. However, it should be pointed out that the shake-table tests reported here had only unidirectional motion. In an earthquake, a building is subjected to excitation in multiple directions. In that case, walls oriented in different directions could suffer significant damage, and the displacement capacity of the structure will depend on the degree of damage in these walls as well as the presence or absence of gravity columns that can carry the gravity load after the vertical load carrying capacity of the walls has been depleted. Buildings with higher gravity loads could also be more vulnerable to collapse because of the more significant P-Δ effect. A recent numerical study using refined finite element models (Koutras, 2019) has shown that one- to four-story RM archetype buildings with shear-dominated wall behavior and steel gravity frames can develop story drift ratios exceeding 10% without collapsing when subjected to bidirectional horizontal ground motions.

(a) Spec. 1 at 2% Drift (Positive)

(d) Spec. 2 at 2% Drift (Positive)

(b) Spec. 1 at 5% Drift (Positive)

(e) Spec. 2 at 5% Drift (Positive)

(c) Spec. 1 at 10% Drift (Positive)

(f) Spec. 2 at 10% Drift (Negative)

Figure 5-22. North views of the damage in the T-walls at different roof drift levels

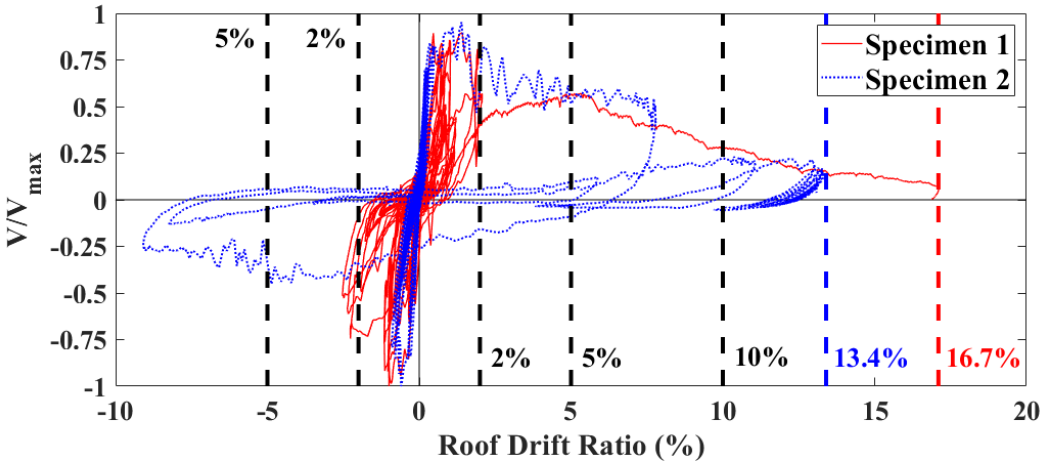

Figure 5-23. Normalized base shear-vs.-roof drift ratio curves for the test specimens

Chapter 5, in part, is a reprint of the material in a research paper titled "Evaluation of Collapse Resistance of Reinforced Masonry Wall Systems by Shake-Table Tests" that appears in the journal of *Earthquake Engineering and Structural Dynamics* in 2020. The authors of the research paper are: the author of the dissertation, Andreas A. Koutras, and P. Benson Shing. The author of the dissertation is the primary author and the main contributor of the work presented in the paper.

CHAPTER 6 A GENERALIZED FRAME ELEMENT FOR FLEXURE- AND SHEAR-DOMINATED REINFORCED MASONRY SHEAR WALLS

This chapter presents a three-dimensional beam-column model for simulating the nonlinear flexural and shear behaviors of RM walls. The proposed model is based on a three-field (force, strain, and displacement) mixed beam-column element formulation proposed by Taylor et al. (2003). This element formulation is free of shear locking, and allows a shear wall to be modeled with only one element, which improves computational efficiency. In the element, the nonlinear axial and flexural behaviors of an RM wall are modeled with distributed plasticity using a fiber-section approach. The shear deformation is assumed to be uniform along the element. A macro model is proposed to represent the nonlinear shear behavior of the wall in each loading direction. The interaction between the axial, flexural, and shear behaviors is also considered in the constitutive laws. The model is able to account for the influence of a wall flange on the shear response of the wall. The beam-column model has been calibrated and validated with the data of the past quasi-static tests and shake-table tests.

6.1. Element Formulation

6.1.1. Mixed Beam-Column Element with Shear Deformation

The mixed beam-column element proposed by Taylor et al. (2003) is selected to model the flexural as well as shear behavior of RM shear walls. This element adopts a three-field (displacement, strain, and force) mixed formulation based on the Hu-Washizu variational principle. It weakly enforces the equilibrium between the nodal and the internal forces at beam sections, the strain-displacement compatibility, and the material constitutive relations. This element formulation is free of shear locking, and allows an RM shear wall to be modeled with only one element, which significantly improves computational efficiency compared to displacement-based elements. The nodal displacements and rotations of a three-dimensional element in the local coordinate system with and without the rigid-body modes are shown in Figure 6-1. With the rigid-body modes excluded, the variational form of the mixed formulation including shear deformation can be expressed as follows.

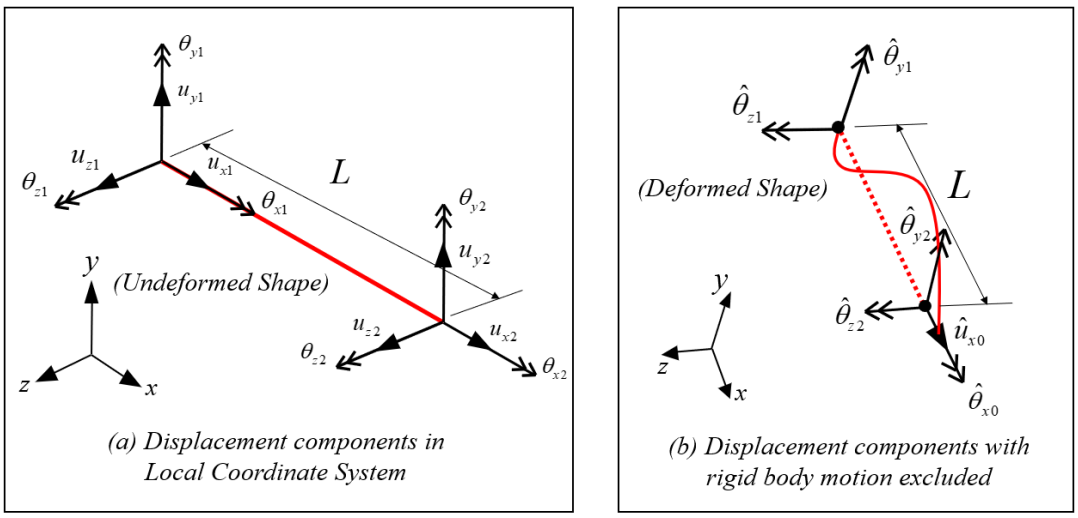

Figure 6-1. A three-dimensional frame element in local coordinate system

$$
\begin{aligned}
\delta\Pi_{HW} = & \int_L \{\delta\varepsilon[\bar{N}(\boldsymbol{\varepsilon}) - N] + \delta N(\frac{d\hat{u}_x}{dx} - \varepsilon) + \frac{d\delta\hat{u}_x}{dx} N\} dx \\
& + \int_L \{\delta\kappa_y[\bar{M}_y(\boldsymbol{\varepsilon}) - M_y] + \delta M_y(\frac{d\hat{\theta}_y}{dx} - \kappa_y) + \frac{d\delta\hat{\theta}_y}{dx} M_y\} dx \\
& + \int_L \{\delta\kappa_z[\bar{M}_z(\boldsymbol{\varepsilon}) - M_z] + \delta M_z(\frac{d\hat{\theta}_z}{dx} - \kappa_z) + \frac{d\delta\hat{\theta}_z}{dx} M_z\} dx \\
& + \int_L \{\delta\phi[\bar{T}(\boldsymbol{\varepsilon}) - T] + \delta T(\frac{d\hat{\theta}_x}{dx} - \phi) + \frac{d\delta\hat{\theta}_x}{dx} T\} dx \\
& + \int_L \{\delta\gamma_y[\bar{V}_y(\boldsymbol{\varepsilon}) - V_y] + \delta V_y(\frac{d\hat{u}_y}{dx} - \hat{\theta}_z - \gamma_y)\} dx \\
& + \int_L [(\frac{d\delta\hat{u}_y}{dx} - \delta\hat{\theta}_z) V_y] dx \\
& + \int_L \{\delta\gamma_z[\bar{V}_z(\boldsymbol{\varepsilon}) - V_z] + \delta V_z(\frac{d\hat{u}_z}{dx} - \hat{\theta}_y - \gamma_z)\} dx \\
& + \int_L [(\frac{d\delta\hat{u}_z}{dx} - \delta\hat{\theta}_y) V_z] dx + \delta\Pi_{bc} = 0
\end{aligned}
\tag{6-1}
$$

in which, L is the length of the element, as shown in Figure 6-1(b); $\boldsymbol{\varepsilon}$ is the strain vector defined as:

$$
\boldsymbol{\varepsilon} = \begin{bmatrix} \varepsilon & \kappa_y & \kappa_z & \phi & \gamma_{xy} & \gamma_{xz} \end{bmatrix}
$$

in which $\varepsilon, \kappa_y, \kappa_z, \phi, \gamma_{xy},$ and γ_{xz} are the axial strain, curvatures about the local *y* and *z* axes, torsional strain, and shear strains in the *x*-*y* and *x*-*z* planes, respectively; $\hat{u}_x, \hat{u}_y, \hat{u}_z, \hat{\theta}_x, \hat{\theta}_y,$ and $\hat{\theta}_z$ are the displacements and rotations in the respective directions; $N, T, M_y, M_z, V_y,$ and V_z are the axial force, torque, moments about the *y* and *z* axes, and shear forces in the *y* and *z* directions satisfying equilibrium; and

$\bar{N}, \bar{T}, \bar{M}_y, \bar{M}_z, \bar{V}_y$, and $\bar{V}_z$ are the axial force, torque, moments and shear forces given by constitutive relations .

With the assumption that no external loads are applied between the nodes, Π_{bc} is defined as the work done by the nodal forces:

$$\Pi_{bc} = \boldsymbol{u}^T \boldsymbol{F}$$

in which $\boldsymbol{u}$ is the nodal displacement vector:

$$\boldsymbol{u} = \begin{bmatrix} \hat{u}_{x0} & \hat{\theta}_{z1} & \hat{\theta}_{z2} & \hat{\theta}_{y1} & \hat{\theta}_{y2} & \hat{\theta}_{x0} \end{bmatrix}^T$$

in which $\hat{u}_{x0}, \hat{\theta}_{z1}, \hat{\theta}_{z2}, \hat{\theta}_{y1}, \hat{\theta}_{z2}$, and $\hat{\theta}_{x0}$ are the nodal axial displacement, rotations about the *z* and *y* axes, and torsional rotation, without the rigid-body modes; $\boldsymbol{F}$ is the vector of the corresponding applied nodal forces.

After applying integration by parts to the terms containing derivatives in Eq. (6-1) and the equilibrium conditions of a beam that has only nodal forces, Eq. (6-1) can be expressed as:

$$
\begin{aligned}
\delta\Pi_{HW} = & \int_L \{\delta\varepsilon[\bar{N}(\boldsymbol{\varepsilon}) - N] - \delta N\varepsilon\}dx + \int_L \{\delta\kappa_y[\bar{M}_y(\boldsymbol{\varepsilon}) - M_y] - \delta M_y\kappa_y\}dx \\
& + \int_L \{\delta\kappa_z[\bar{M}_z(\boldsymbol{\varepsilon}) - M_z] - \delta M_z\kappa_z\}dx + \int_L \{\delta\gamma_y[\bar{V}_y(\boldsymbol{\varepsilon}) - V_y] - \delta V_y\gamma_{xy}\}dx \\
& + \int_L \{\delta\gamma_{xz}[\bar{V}_z(\boldsymbol{\varepsilon}) - V_z] - \delta V_z\gamma_{xz}\}dx + \int_L \{\delta\phi[\bar{T}(\boldsymbol{\varepsilon}) - T] - \delta T\phi\}dx \\
& + \left(\delta\hat{N}_0\hat{u}_{x0} + \delta\hat{u}_{x0}\hat{N}_0\right) \\
& + \left(\delta\hat{M}_{y2}\hat{\theta}_{y2} + \delta\hat{\theta}_{y2}\hat{M}_{y2} - \delta\hat{M}_{y1}\hat{\theta}_{y1} - \delta\hat{\theta}_{y1}\hat{M}_{y1}\right) \\
& + \left(\delta\hat{M}_{z2}\hat{\theta}_{z2} + \delta\hat{\theta}_{z2}\hat{M}_{z2} - \delta\hat{M}_{z1}\hat{\theta}_{z1} - \delta\hat{\theta}_{z1}\hat{M}_{z1}\right) \\
& + \left(\delta\hat{T}_0\hat{\theta}_{x0} + \delta\hat{\theta}_{x0}\hat{T}_0\right) + \delta\Pi_{bc} = 0
\end{aligned}
\tag{6-2}
$$

in which $\hat{N}_0, \hat{T}_0, \hat{M}_{y1}, \hat{M}_{y2}, \hat{M}_{z1}$, and $\hat{M}_{z2}$ are the nodal axial force, torque, and moments about the *y* and *z* local coordinate axes.

6.1.2. Finite Element Approximation

It can be noted from Eq. (6-2) that to derive the stiffness matrix of the beam element, the strain and force fields have to be expressed in terms of the respective values at nodal or integration points using interpolation functions. The interpolation functions selected are shown in Figure 6-2. The equilibrium between the internal and nodal forces results in the following expressions for the force fields.

$$
\begin{aligned}
N &= N_0 \\
M_y &= M_{y1}(1-\frac{x}{L}) + M_{y2}\frac{x}{L} \\
M_z &= M_{z1}(1-\frac{x}{L}) + M_{z2}\frac{x}{L} \\
V_y &= \frac{M_{z1}-M_{z2}}{L} \\
V_z &= \frac{M_{y1}-M_{y2}}{L} \\
T &= T_0
\end{aligned}
$$

(6-3)

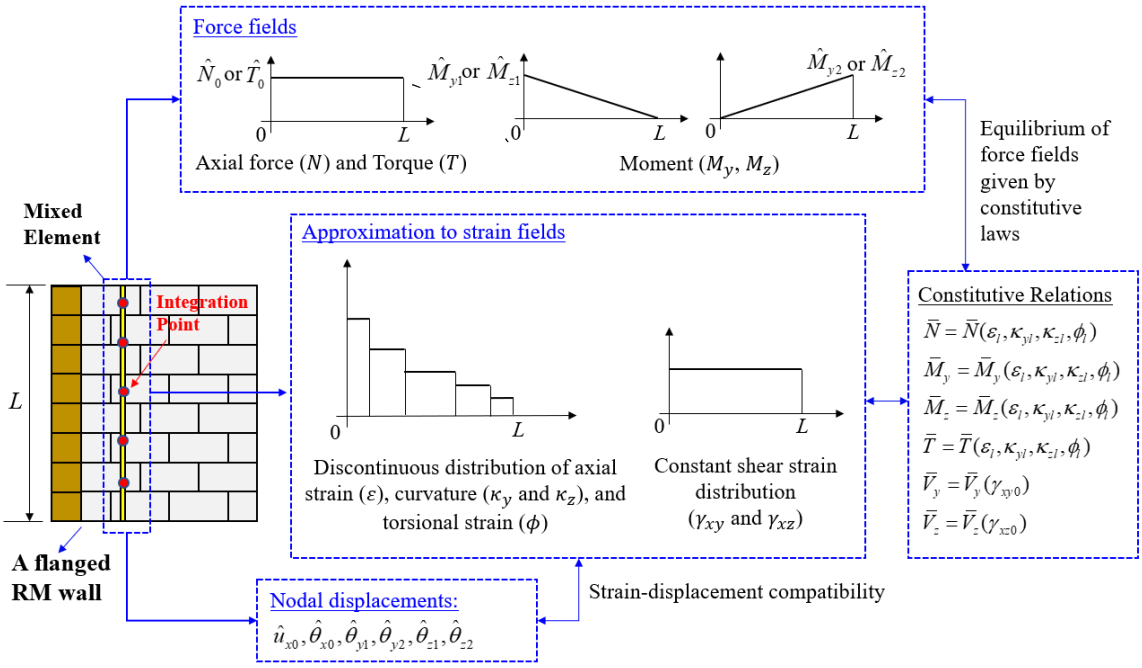

Figure 6-2. Finite element approximation in the mixed beam-column element

As shown in Figure 6-2, the curvatures (κ_y and κ_z), axial strain (ε) and torsional strain (ϕ) are approximated by discontinuous functions, as proposed by Taylor et al. (2003). The strain values are evaluated at each integration point along the element. One needs to select a sufficient number of integration points to capture the deformation of an RM wall accurately. The discontinuous strain functions result in a sparse stiffness matrix, which improves the computational efficiency. However, the shear strains are assumed to be constant for an RM wall. This is a reasonable assumption as the shear deformation of an RM wall is more or less uniform over the entire wall panel. By introducing the aforementioned approximate strain fields in Eq. (6-2), the integrals can be replaced by summations. Furthermore, after introducing the expressions in Eq. (6-3) for the force fields, Eq. (6-2) can be written as:

$$
\begin{aligned}
\delta\Pi_{HW} \approx & \sum_{l=1}^{n_s}\left\{\delta\varepsilon_l\left[\bar{N}(\varepsilon_l,\kappa_{yl},\kappa_{zl},\phi_l)-N_0\right]-\delta N_0\varepsilon_l\right\}W_l \\
& +\sum_{l=1}^{n_s}\left\{\delta\kappa_{yl}\left[\bar{M}_y(\varepsilon_l,\kappa_{yl},\kappa_{zl},\phi_l)-(1-\frac{x_l}{L})M_{y1}-\frac{x_l}{L}M_{y2}\right]-\left[(1-\frac{x_l}{L})\delta M_{y1}+\frac{x_l}{L}\delta M_{y2}\right]\kappa_{yl}\right\}W_l \\
& +\sum_{l=1}^{n_s}\left\{\delta\kappa_{zl}\left[\bar{M}_z(\varepsilon_l,\kappa_{yl},\kappa_{zl},\phi_l)-(1-\frac{x_l}{L})M_{z1}-\frac{x_l}{L}M_{z2}\right]-\left[(1-\frac{x_l}{L})\delta M_{z1}+\frac{x_l}{L}\delta M_{z2}\right]\kappa_{zl}\right\}W_l \\
& +\left\{\delta\gamma_{y0}[\bar{V}_y(\gamma_{y0})-\frac{1}{L}(M_{z1}-M_{z2})]-\frac{1}{L}(\delta M_{z1}-\delta M_{z2})\gamma_{y0}\right\}W_0 \\
& +\left\{\delta\gamma_{z0}[\bar{V}_z(\gamma_{z0})-\frac{1}{L}(M_{y1}-M_{y2})]-\frac{1}{L}(\delta M_{y1}-\delta M_{y2})\gamma_{z0}\right\}W_0 \\
& +\sum_{l=1}^{n_s}\left\{\delta\phi_l[\bar{T}(\varepsilon_l,\kappa_{yl},\kappa_{zl},\phi_l)-T_0]-\delta T_0\phi_l\right\}W_l \\
& +\left(\delta N_0\hat{u}_{x0}+\delta\hat{u}_{x0}N_0\right)+\left(\delta M_{y2}\hat{\theta}_{y2}+\delta\hat{\theta}_{y2}M_{y2}-\delta M_{y1}\hat{\theta}_{y1}-\delta\hat{\theta}_{y1}M_{y1}\right) \\
& +\left(\delta M_{z2}\hat{\theta}_{z2}+\delta\hat{\theta}_{z2}M_{z2}-\delta M_{z1}\hat{\theta}_{z1}-\delta\hat{\theta}_{z1}M_{z1}\right)+\left(\delta T_0\hat{\theta}_{x0}+\delta\hat{\theta}_{x0}T_0\right)+\delta\Pi_{bc}=0
\end{aligned}
\tag{6-4}
$$

in which n_s denotes the number of integration points along the element; x_l and W_l denote the coordinate and weight of the l^{th} integration point; and $\varepsilon_l, \phi_l, \kappa_{yl}, \kappa_{zl}$ are the axial strain, torsional strain, and curvatures at the l^{th} integration point. Since the shear strains along the element are assumed to be constant (γ_{y0} and γ_{z0}), the weights associated with the shear strains are taken as $W_0 = L$.

6.1.3 Matrix Form

To solve a nonlinear beam problem, Eq. (6-4) can be expressed in an incremental form as follows.

$$
\begin{bmatrix}\delta\boldsymbol{u}\\ \delta\boldsymbol{\sigma}\\ \delta\boldsymbol{\varepsilon}\end{bmatrix}\left(\begin{bmatrix}\mathbf{0} & \boldsymbol{H}^T & \mathbf{0}\\ \boldsymbol{H} & \mathbf{0} & \boldsymbol{Q}\\ \mathbf{0} & \boldsymbol{Q}^T & \boldsymbol{K}^e\end{bmatrix}\begin{bmatrix}\Delta\boldsymbol{u}\\ \Delta\boldsymbol{\sigma}\\ \Delta\boldsymbol{\varepsilon}\end{bmatrix}=\begin{bmatrix}\boldsymbol{R}_u\\ \boldsymbol{R}_\sigma\\ \boldsymbol{R}_\varepsilon\end{bmatrix}\right) \tag{6-5}
$$

in which $\left[\boldsymbol{R}_{\boldsymbol{u}}\ \boldsymbol{R}_{\boldsymbol{\sigma}}\ \boldsymbol{R}_{\boldsymbol{\varepsilon}}\right]^T$ is the residual error vector; $\Delta\boldsymbol{u}$ and $\Delta\boldsymbol{\sigma}$ are the incremental nodal displacement vector and incremental nodal force vector in the local element coordinate system without rigid-body modes, with

$$\boldsymbol{\sigma} = [\hat{N}_0\ \hat{M}_{z1}\ \hat{M}_{z2}\ \hat{M}_{y1}\ \hat{M}_{y2}\ \hat{T}_0]^T$$

and $\bar{\varepsilon}$ is the strain vector which consists of the axial strain, curvatures, and torsional strain at the integration points as well as two shear strain terms:

$$\bar{\boldsymbol{\varepsilon}} = [\varepsilon_1\ \kappa_{z1}\ \kappa_{y1}\ \phi_1 \ldots\ \varepsilon_{ns}\ \kappa_{zn_s}\ \kappa_{yn_s}\ \phi_{n_s}\ \gamma_{y0}\ \gamma_{z0}]^T$$

$\boldsymbol{H}$ is a 6×6 diagonal matrix defined as:

$$\boldsymbol{H} = \begin{bmatrix} 1 & 0 & 0 & 0 & 0 & 0 \\ 0 & -1 & 0 & 0 & 0 & 0 \\ 0 & 0 & 1 & 0 & 0 & 0 \\ 0 & 0 & 0 & -1 & 0 & 0 \\ 0 & 0 & 0 & 0 & 1 & 0 \\ 0 & 0 & 0 & 0 & 0 & 1 \end{bmatrix}$$

$\boldsymbol{Q}$ is a $6 \times (4n_s + 2)$ matrix:

$$\boldsymbol{Q} = \left[\boldsymbol{Q_1} \ldots \boldsymbol{Q_l} \ldots \boldsymbol{Q_{ns}}\ \boldsymbol{Q_{shear}}\right]$$

in which

$$\boldsymbol{Q_l} = W_l \begin{bmatrix} -1 & 0 & 0 & 0 \\ 0 & -(1-x_l/L) & 0 & 0 \\ 0 & -x_l/L & 0 & 0 \\ 0 & 0 & -(1-x_l/L) & 0 \\ 0 & 0 & -x_l/L & 0 \\ 0 & 0 & 0 & -1 \end{bmatrix},\ \boldsymbol{Q_{shear}} = W_0 \begin{bmatrix} 0 & 0 \\ -1/L & 0 \\ 1/L & 0 \\ 0 & -1/L \\ 0 & 1/L \\ 0 & 0 \end{bmatrix}$$

$\boldsymbol{K^e}$ is a sparse matrix defined as:

$$\boldsymbol{K^e} = \begin{bmatrix} W_1\boldsymbol{K}_{11}^e & 0 & \cdots & \cdots & 0 \\ 0 & \ddots & & & \vdots \\ \vdots & & W_{n_s}\boldsymbol{K}_{n_s n_s}^e & & \vdots \\ \vdots & & & W_0 K_{shear,y} & 0 \\ 0 & \cdots & \cdots & 0 & W_0 K_{shear,z} \end{bmatrix}$$

in which $\boldsymbol{K}_{ii}^e$ is the sectional axial and flexural stiffness matrix at integration point *i* and is defined as:

$$\boldsymbol{K}_{ii}^e = \begin{bmatrix} \left(\frac{\partial \bar{N}}{\partial \varepsilon}\right)_i & \left(\frac{\partial \bar{N}}{\partial \kappa_z}\right)_i & \left(\frac{\partial \bar{N}}{\partial \kappa_y}\right)_i & \left(\frac{\partial \bar{N}}{\partial \phi}\right)_i \\ \left(\frac{\partial \bar{M}_z}{\partial \varepsilon}\right)_i & \left(\frac{\partial \bar{M}_z}{\partial \kappa_z}\right)_i & \left(\frac{\partial \bar{M}_z}{\partial \kappa_y}\right)_i & \left(\frac{\partial \bar{M}_z}{\partial \phi}\right)_i \\ \left(\frac{\partial \bar{M}_y}{\partial \varepsilon}\right)_i & \left(\frac{\partial \bar{M}_y}{\partial \kappa_z}\right)_i & \left(\frac{\partial \bar{M}_y}{\partial \kappa_y}\right)_i & \left(\frac{\partial \bar{M}_y}{\partial \phi}\right)_i \\ \left(\frac{\partial \bar{T}}{\partial \varepsilon}\right)_i & \left(\frac{\partial \bar{T}}{\partial \kappa_z}\right)_i & \left(\frac{\partial \bar{T}}{\partial \kappa_y}\right)_i & \left(\frac{\partial \bar{T}}{\partial \phi}\right)_i \end{bmatrix}$$

and $K_{shear,y}$ and $K_{shear,z}$ are the two shear stiffness terms defined as:

$$K_{shear,y} = \frac{d\bar{V}_y}{d\gamma_{xy0}} \quad \text{and} \quad K_{shear,z} = \frac{d\bar{V}_z}{d\gamma_{xz0}}$$

The residual vector $\boldsymbol{R}_u$ is the difference between the applied nodal forces (***F***) and element nodal forces:

$$\boldsymbol{R}_u = \boldsymbol{F} - \boldsymbol{H}^T\boldsymbol{\sigma}$$

The term $\boldsymbol{R}_\sigma$ represents the error in the strain-displacement compatibility condition:

$$\boldsymbol{R}_\sigma = \boldsymbol{H}\boldsymbol{u} - \boldsymbol{Q}\bar{\boldsymbol{\varepsilon}}$$

The term $\boldsymbol{R}_\varepsilon$ represents the difference between the internal forces satisfying equilibrium with the nodal forces and the internal forces given by constitutive relations:

$$\boldsymbol{R}_\varepsilon = \boldsymbol{Q}^T\boldsymbol{\sigma} - \bar{\boldsymbol{\sigma}}$$

in which $\bar{\boldsymbol{\sigma}}$ is the interal force vector given by constitutive laws:

$$\bar{\boldsymbol{\sigma}} = \left[W_1 \bar{N}_1 \quad W_1 \bar{M}_{z1} \quad W_1 \bar{M}_{y1} \quad W_1 \bar{T}_1 \quad \cdots \quad W_{n_s} \bar{N}_{n_s} \quad W_{n_s} \bar{M}_{zn_s} \quad W_{n_s} \bar{M}_{yn_s} \quad W_{n_s} \bar{T}_{n_s} \quad W_0 \bar{V}_y \quad W_0 \bar{V}_z \right]^T$$

6.1.4. Solution Strategy

To implement the mixed beam formulation into a displacement-driven finite element code, the force and strain terms in Eq. (6-5) need to be condensed out. For this purpose, a solution strategy with condensation proposed in Taylor et al. (2003) will be presented below.

The incremental strain vector $\Delta\boldsymbol{\varepsilon}$ in Eq. (6-5) can be expressed as:

$$\Delta\boldsymbol{\varepsilon} = (\boldsymbol{K}^e)^{-1}(\boldsymbol{R}_{\boldsymbol{\varepsilon}} - \boldsymbol{Q}^T \Delta\boldsymbol{\sigma}) \tag{6-6}$$

By substituting Eq. (6-6) to Eq. (6-5), the strain-related terms in Eq. (6-5) can be eliminated, and the incremental form of the element formulation can be expressed as:

$$\begin{bmatrix} \delta\boldsymbol{u} \\ \delta\boldsymbol{\sigma} \end{bmatrix} \left(\begin{bmatrix} \boldsymbol{0} & \boldsymbol{H}^T \\ \boldsymbol{H} & -\tilde{\boldsymbol{K}}^{\boldsymbol{e}} \end{bmatrix} \begin{bmatrix} \Delta\boldsymbol{u} \\ \Delta\boldsymbol{\sigma} \end{bmatrix} = \begin{bmatrix} \boldsymbol{R}_{\boldsymbol{u}} \\ \tilde{\boldsymbol{R}}_{\boldsymbol{\sigma}} \end{bmatrix} \right) \tag{6-7}$$

in which

$$\tilde{\boldsymbol{K}}^{\boldsymbol{e}} = \boldsymbol{Q}(\boldsymbol{K}^e)^{-1}\boldsymbol{Q}^T \tag{6-8}$$

$$\tilde{\boldsymbol{R}}_{\boldsymbol{\sigma}} = \boldsymbol{R}_{\boldsymbol{\sigma}} - \boldsymbol{Q}(\boldsymbol{K}^{\boldsymbol{e}})^{-1}\boldsymbol{R}_{\boldsymbol{\varepsilon}} \tag{6-9}$$

The incremental force vector $\Delta\boldsymbol{\sigma}$ in Eq. (6-7) can be expressed as:

$$\Delta\boldsymbol{\sigma} = (\tilde{\boldsymbol{K}}^{\boldsymbol{e}})^{-1}(\boldsymbol{H}\Delta\boldsymbol{u} - \tilde{\boldsymbol{R}}_{\boldsymbol{\sigma}}) \tag{6-10}$$

With Eq. (6-10), the stress-related terms in Eq. (6-7) can be eliminated, and the incremental form of the element formulation can be expressed as:

$$\tilde{\boldsymbol{K}}_{\boldsymbol{a}}\Delta\boldsymbol{u} = \tilde{\boldsymbol{R}}_{\boldsymbol{a}} \tag{6-11}$$

in which $\tilde{\boldsymbol{K}}_{\boldsymbol{a}}$ is the condensed element stiffness matrix in the local coordinate system without rigid body mode, which is defined as:

$$\tilde{\boldsymbol{K}}_{\boldsymbol{a}} = \boldsymbol{H}^{T}(\tilde{\boldsymbol{K}}^{\boldsymbol{e}})^{-1}\boldsymbol{H} \tag{6-12}$$

is a condensed residual vector defined as:

$$\tilde{\boldsymbol{R}}_{\boldsymbol{a}} = \boldsymbol{H}^{T}(\tilde{\boldsymbol{K}}^{\boldsymbol{e}})^{-1}\tilde{\boldsymbol{R}}_{\boldsymbol{\sigma}} + \boldsymbol{R}_{\boldsymbol{u}} \tag{6-13}$$

It should be noted that the condensed element residual vector, $\tilde{\boldsymbol{R}}_{\boldsymbol{a}}$, will be equal to zero if and only if the three residual vectors in Eq. (6-5) ($\boldsymbol{R}_{\boldsymbol{u}}$, $\boldsymbol{R}_{\boldsymbol{\sigma}}$ and $\boldsymbol{R}_{\boldsymbol{\epsilon}}$) are all equal to zero. In the implementation of the mixed formulation, the residual vectors $\boldsymbol{R}_{\boldsymbol{\sigma}}$ and $\boldsymbol{R}_{\boldsymbol{\epsilon}}$ are checked in the element level, and the condensed element residual vector, $\tilde{\boldsymbol{R}}_{\boldsymbol{a}}$, is checked in the structure level. The implementation of the mixed element formulation is summarized below.

Element State Determination

1. Calculate the incremental displacement vector $\Delta \boldsymbol{u} = \boldsymbol{u} - \boldsymbol{u}_{old}$, in which $\boldsymbol{u}$ is the nodal displacement vector at the current step, and $\boldsymbol{u}_{old}$ is the nodal displacement vector from the last converged step.

2. Initialize the element force vector ($\boldsymbol{\sigma}$) and strain vector ($\boldsymbol{\varepsilon}$).

$$\boldsymbol{\sigma} = \boldsymbol{\sigma}_{old}$$

$$\boldsymbol{\varepsilon} = \boldsymbol{\varepsilon}_{old}$$

in which $\boldsymbol{\sigma}_{old}$ and $\boldsymbol{\varepsilon}_{old}$ are the element force vector and strain vector from the last converged step.

3. Calculate the incremental force vector, $\Delta\boldsymbol{\sigma}$ with $\Delta\boldsymbol{u}$ by Eq. (6-10), and update the force vector $\boldsymbol{\sigma} = \boldsymbol{\sigma} + \Delta\boldsymbol{\sigma}$.

4. Calculate the incremental strain vector, $\Delta\boldsymbol{\varepsilon}$ with $\Delta\boldsymbol{\sigma}$ by Eq. (6-16), and update the strain vector $\boldsymbol{\varepsilon} = \boldsymbol{\varepsilon} + \Delta\boldsymbol{\varepsilon}$.

5. Determine the stiffness matrix $\boldsymbol{K}^{\boldsymbol{e}}$ and the interal force vector $\bar{\boldsymbol{\sigma}}$ with constitutive laws:

   a. Loop over the integration points to determine the sectional states.

   b. Determinate the state of the two shear models.

6. Calculate the residual vectors $\boldsymbol{R}_{\boldsymbol{u}}, \boldsymbol{R}_{\sigma}$, and $\boldsymbol{R}_{\varepsilon}$ with updated $\boldsymbol{u}, \boldsymbol{\sigma}, \boldsymbol{\varepsilon}$, and $\bar{\boldsymbol{\sigma}}$.

7. Calculate the condensed stiffness matrix $\tilde{\boldsymbol{K}}_{\boldsymbol{a}}$ with Eqs. (6-8) and (6-12).

8. Calculate the condensed residual vector $\tilde{\boldsymbol{R}}_{\boldsymbol{a}}$ with Eqs. (6-9) and (6-13).

9. Check the element convergence with the following two conditions:

$$\left\|\boldsymbol{R}_{\varepsilon}\right\| < 10^{-4} \ \textit{and} \ \left\|\boldsymbol{R}_{\sigma}\right\| < 10^{-6}$$

If the element has not converged, go back to step 3. Otherwise, return the condensed element stiffness matrix ($\tilde{\boldsymbol{K}}_{\boldsymbol{a}}$) and output the force vector ($\boldsymbol{\sigma}$).

6.1.5. Geometric Nonlinearity

The element formulation and its incremental form are derived in the element local coordinate system without rigid-body modes. To introduce rigid-body modes, the nonlinear transformation scheme proposed by Sousa (2000) is applied. It accounts the geometric nonlinearity (i.e. P-Δ effect).

6.2. Model Idealization

This section presents the idealization scheme used to evaluate the element internal forces given by constitutive relations ($\bar{N}, \bar{T}, \bar{M}_y, \bar{M}_z, \bar{V}_y$, and $\bar{V}_z$). As shown in Figures 6-3 and 6-4, the axial and flexural responses at each integration point are evaluated with a fiber section model, in which uniaxial material laws are used to represent the nonlinear behaviors of masonry and vertical reinforcing steel.

With the assumption that the in-plane shear strain is uniform over a wall panel, as discussed in the previous section, the shear response of a wall is represented by a macro material model. Figure 6-3 shows the shear model for a wall with a rectangular cross-section. For the in-plane shear response, the shear force-vs.-shear strain relation ($\bar{V}_y - \text{vs.} - \gamma_{xy}$) is represented by a nonlinear curve that accounts for the behavior governed by diagonal shear cracking. For the out-of-plane direction, the shear response is assumed to be linearly elastic considering that the capacity of the wall in this direction is most likely dominated by flexure. Figure 6-4 shows the shear model for a flanged wall, which has two connected wall panels perpendicular to one another. It is assumed that the in-plane shear response of each panel is independent of that of the other. The response of each panel is

represented by a nonlinear shear force-vs.-shear strain relation, which accounts for the influence of the wall flange, as will be discussed in the next section. For flanged walls with two or more panels resisting shear in each direction, such as those with C-shaped or I-shaped sections, one shear force-vs.-shear strain relation is assigned to each panel.

As it will be described in detail in the next two sections, the interaction of the axial, flexural, and shear responses is considered through the constitutive relations. To account for the influence of the axial and flexural responses on the shear capacity of an RM wall, the shear resistance is assumed to be a function of the axial stress resultants (P_w and P_f) from the fiber section model, as shown in Figures 6-3 and 6-4. Furthermore, the compressive strength of masonry in the fiber model is reduced as the maximum shear strain attained increases, accounting for the spalling and crushing of masonry that could occur along diagonal shear cracks.

The torsional response of the element is assumed to be linearly elastic.

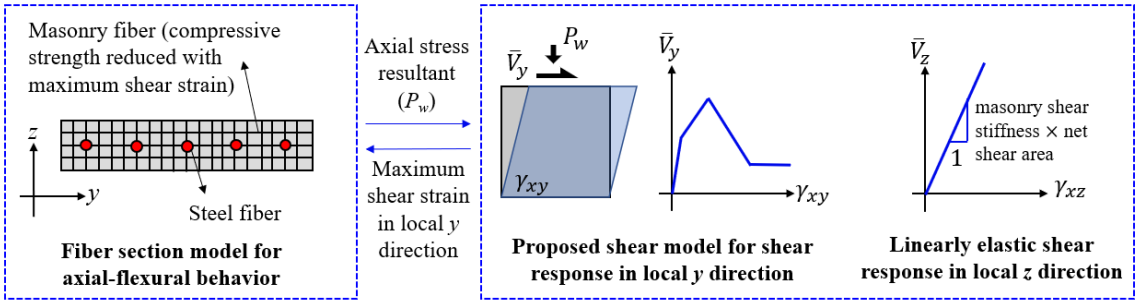

Figure 6-3. Model idealization for a planar RM wall

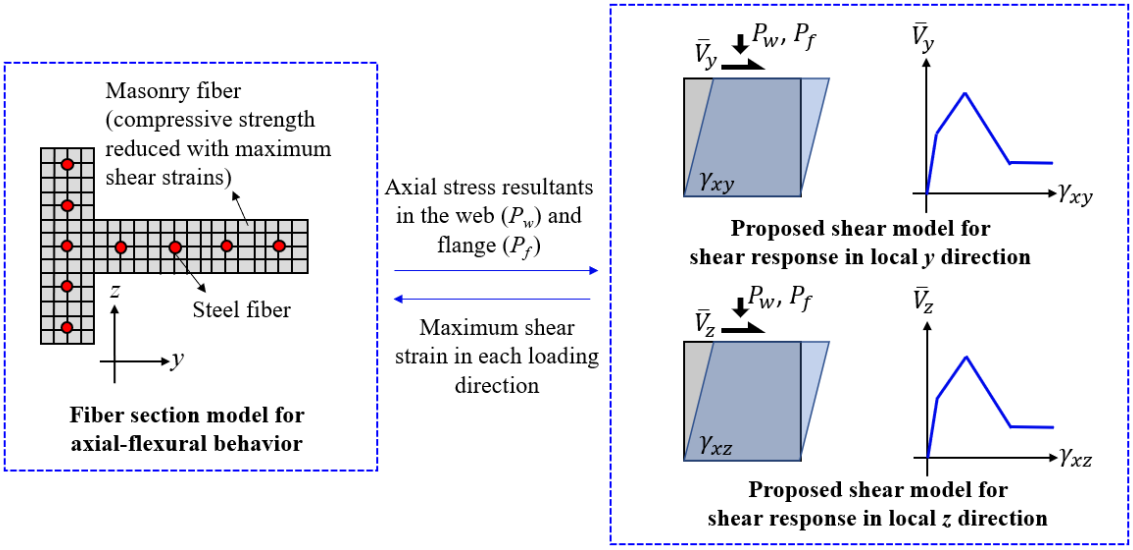

Figure 6-4. Model idealization for a flanged wall

6.3. Constitutive Relation for Shear Behavior

This section presents the constitutive model proposed to represent the shear behavior of an RM shear wall. The model is applicable to planar or flanged walls with different configurations (such as L-shaped, T-shaped, I-shaped, or C-shaped). For flanged walls, the wall panel(s) parallel to the lateral load direction considered is referred to as the web, while the panel(s) in the orthogonal direction is referred to as the flange, as shown in Figure 6-5. In the model, the shear resistance is considered to be provided by the in-plane action of the web(s), as well as the out-of-plane bending of the flange(s) once the shear deformation of the wall exceeds the point at which the peak shear strength is reached and the wall web starts to develop severe damage.

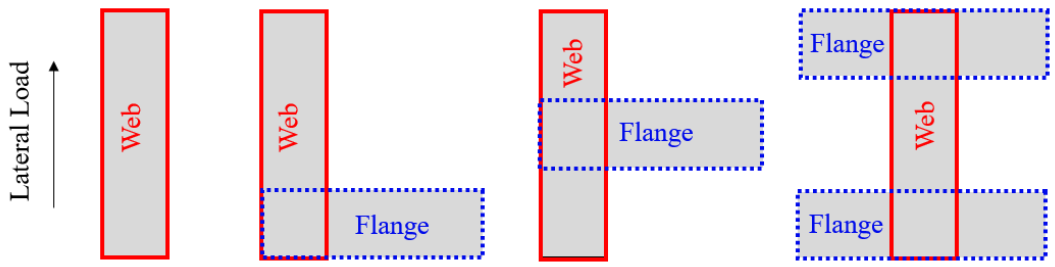

Figure 6-5. Definition of web and flange components for different types of wall section

6.3.1. Monotonic Shear Force-vs.-Shear Strain Envelope

Figure 6-6 shows the shear force-vs.-shear strain envelope of the proposed shear model, which represents the nonlinear shear response of an RM wall subjected to a monotonically increasing lateral load. As shown, the envelope is defined by three critical points, corresponding to the shear stress at the initiation of major diagonal cracks (V_{cr}),

the peak shear strength (V_p), and the attainment of the residual strength (V_{res}), respectively.

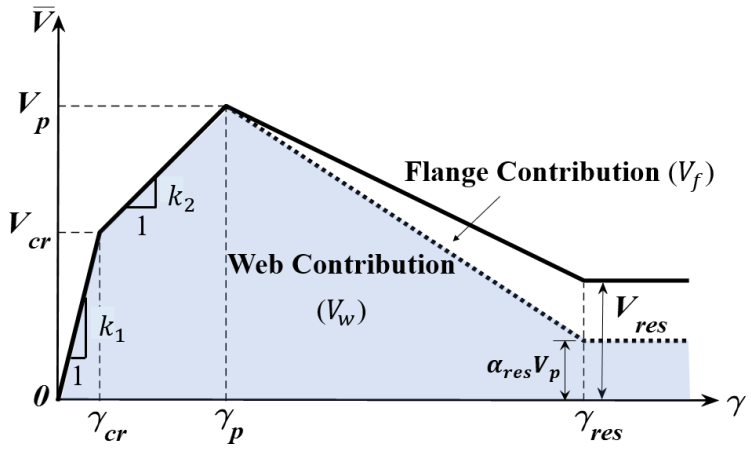

Figure 6-6**.** Envelope stress-vs-strain curve of the proposed shear model

The initial stiffness (k_1) of the envelope curve is taken as $0.40A_wG_m$, where A_w is the net area of the web and G_m is the shear modulus of masonry. The reduction factor of 0.40 is applied to account for fine cracks that may develop before the initiation of major diagonal shear cracks. Major diagonal cracks initiate at V_{cr} , which is assumed to be $0.70V_0$, where V_0 is the peak shear strength of the web panel under zero axial load calculated according to the strength design provision in TMS 402/602 (2016), including shear resistance provided by the shear reinforcement. In reality, the value of V_{cr} depends on the level of the axial load. However, for the range of the axial force that could occur in a typical masonry wall, the exact value of V_{cr} does not have a major influence on the overall shear response of a wall. Furthermore, igoring the influence of the axial load makes the numerical computation more stable and robust. When the wall is subjected to high tension induced by lateral seismic forces, its behavior will be governed by flexure and/or sliding, rather

than diagonal shear. The peak shear strength (V_p) is calculated according to TMS 402/602 (2016), considering only the wall web and the influence of the axial load applied to the web, with the following equation.

$$V_p = \max\left\{V_0 + 0.25P_w, 0.9V_0\right\} \tag{6-14}$$

in which P_w is the axial load in the web calculated from the fiber section, with the positive sign representing compression. The lower-bound value of $0.9V_0$ is to account for the fact that V_p cannot be lower than V_{cr}.

The second slope of the envelope curve in Figure 6-6 is specified as:

$$k_2 = \frac{V_0 - V_{cr}}{0.25\% - \gamma_{cr}} \tag{6-15}$$

in which γ_{cr} is the strain at which major diagonal cracks initiate. Hence, when P_w is zero, $V_p = V_0$ and γ_p is 0.25%. Because of the scarcity of test data on shear-dominated RM walls subjected to monotonically increasing loads, this stiffness is calibrated with quasi-static cyclic test data.(Shing et al., 1991; Voon and Ingham, 2006; Ahmadi, 2012) Since k_2 is assumed to be a constant, the value of γ_p changes with the axial load. This is consistent with the experimental observation of Voon and Ingham (2006).

After reaching the peak shear strength, the resistance is assumed to decrease linearly to a residual shear strength, V_{res}, as shown in Figure 6-6. The shear strain at which V_{res} is reached (γ_{res}) is taken as ($\gamma_p + 0.1$), which is based on the responses of two RM T-wall systems tested to the verge of collapse, as presented in Chapter 5. Most of the tests

in the literature did not reach such a large displacement level. The post-peak shear strength consists of the strength provided by the wall web (V_w) and, for flanged walls, flexural strength provided by the flange(s) (V_f), as shown in Figure 6-6. The calculation of these two terms will be discussed in the following two sub-sections.

6.3.1.1. Degradation of web shear strength

The rate of the degradation of the shear strength of the web due to the opening of diagonal cracks as well as masonry crushing and the fracture of the shear reinforcement depends on a number of factors. Test observations of Voon and Ingham (2006) have shown that for wall panels with the length-to-height ratio (*L/H*) less than or equal to 1, a higher axial compressive load will lead to more severe toe crushing and masonry spalling, and consequently more rapid degradation of the shear resistance. However, wall panels with a high length-to-height ratio (squat walls) are less prone to toe crushing. For these walls, a higher axial compressive load can lead to less rapid degradation of shear resistance because the increased friction resistance as well as the diagonal strut action. Based on these observations, the post-peak shear resistance provided by the wall web (V_w) is given by the following equation.

$$V_w(\gamma, \beta_w, \frac{L}{H}) = \alpha(\gamma, \beta_w, \frac{L}{H})V_p \qquad (\gamma \geq \gamma_p) \qquad (6\text{-}16)$$

in which β_w is the axial load ratio for the web, i.e., $\beta_w = P_w / A_w$, and α is a strength reduction factor considering the influence of the axial load ratio and aspect ratio (*L/H*) of the wall:

$$\alpha(\gamma, \beta_w, \frac{L}{H}) = \max\left[1 - \frac{1-\alpha_{res}(\beta_w, \frac{L}{H})}{0.1}(\gamma - \gamma_p),\ \alpha_{res}(\beta_w, \frac{L}{H})\right] \qquad (\gamma \geq \gamma_p) \qquad (6\text{-}17)$$

where α_{res} is the residual value of α given by the following equation:

$$\alpha_{res}(\beta_w, \frac{L}{H}) = C_0\left[1 + \frac{\max\left(1, \frac{L}{H}\right) - 2}{1 + C_1 \exp\left(C_2 \beta_w\right)}\right] \qquad (6\text{-}18)$$

The parameters C_0, C_1, and C_2 in the above equation are 0.2, 10 and -120, respectively, which have been determined with wall test data. Figure 6-7(a) shows the variation of the value of α with respect to the shear strain γ. Figure 6-7(b) shows how the value of the residual reduction factor α_{res} varies with β_w and *L/H*. As shown, when the wall is in tension except for β_w close to zero, the value of α_{res} is equal to 0.2, regardless of the value of *L/H*. The value of α_{res} can increase or decrease with the increase of the axial compressive load, depending on the aspect ratio of the wall. For walls with *L/H* less than 2, the value of α_{res} decreases with the axial compressive load, because these walls are vulnerable to toe crushing. For walls with *L/H* higher than 2, the value of α_{res} increases with the increase of the compressive load, because axial compression can enhance shear resistance in these walls. For *L/H* equal to 2, α_{res} is always 0.2.

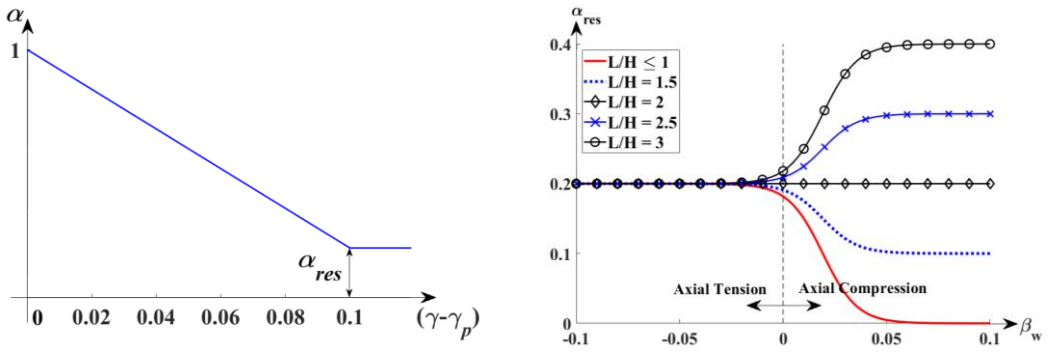

(a) (b)

Figure 6-7. (a) Relation between web damage factor and post-peak shear strain; (b) relation between residual web damage factor and web axial load ratio for web components with different depth-to-height ratios

6.3.1.2. Resistance of wall flange

For a flanged wall, the flange(s) can develop out-of-plane bending and thus flexural resistance (V_f) after severe damage has occurred in the web. As shown in Figure 6-6, it is assumed that the flexural resistance of the flange(s) will develop only when the shear strain has passed the point of the peak shear strength (V_p), and will increase linearly with the increase of the shear strain till reaching the full moment capacity when the shear strain reaches γ_{res}. The contribution of the wall flange to the residual shear strength, $V_f(\gamma_{res})$, can be calculated as follows.

$$V_f(\gamma_{res}) = \frac{M_f}{H_{eff}} \tag{6-19}$$

in which H_{eff} is the effective height of the wall, which is equal to the actual wall height for a cantilever wall, and is half of the wall height for a wall fixed from rotation at the top and the bottom; and M_f is the moment capacity of the flange section.

The value of M_f can be calculated with the equivalent stress block approach according to the recommendations in TMS 402 (2016). As shown in Figure 6-8, the equilibrium of the axial force and moment for the flange section can be expressed as:

$$P_f = 0.8(\alpha f'_m) b l_f - f_y A_{sf} \tag{6-20}$$

$$M_f = 0.8(\alpha f'_m) b l_f \frac{t_f - b}{2} \tag{6-21}$$

in which P_f is the axial force in the flange from the fiber-section model; t_f and l_f are the thickness and width of the flange, respectively; A_{sf} is the total area of all the vertical reinforcing bars in the flange and f_y is the yield strength of the bars; f'_m is the compressive strength of masonry; b is the depth of the compressive stress block; and α is the shear strength reduction factor defined in Eqs. (6-17) and (6-18) to account for the reduction of the moment capacity of the flange due to diagonal shear cracks induced in the flange by lateral loading parallel to the flange.

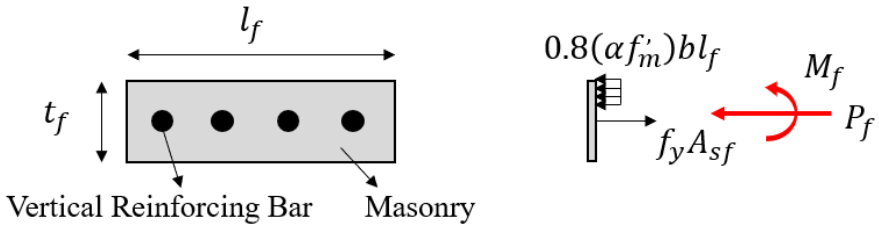

(a) cross section of a flange (b) sectional equilibrium

Figure 6-8. Axial force and moment equilibrium of a wall flange

6.3.2. Hysteretic Law

To model the shear response of RM walls subjected to cyclic load reversals, a

hysteretic law has been proposed with the envelope curve presented in the previous section as the baseline envelope. This law accounts for additional strength degradation induced by cyclic loading as well as the degradation of the stiffness during unloading and reloading. There are four main features in the hysteretic law: the pinching of the hysteresis loops, the degradation of the shear force-vs.-shear strength envelope due to damage caused by cyclic loading (in-cycle damage), the degradation of the unloading stiffness due to shear crack opening and closing, and the degradation of the reloading stiffness due to in-cycle damage, as described below.

6.3.2.1. Cyclic Unloading and Reloading

The hysteretic response of a shear-dominated RM wall often exhibits a pinching behavior. A tri-linear unloading-reloading law used in the Hysteretic Material Law in OpenSEES (McKenna et al. 2000) is adopted to represent the pinching behavior. Figure 6-9 shows an unloading-reloading curve for shear deformation towards the positive direction (path A-B-C-D). Once unloading starts (A in the figure), the shear force drops linearly to zero with the unloading stiffness k_{un}^{-} (path A-B). The value of k_{un}^{-} is equal to the initial stiffness (k_1) of the envelope curve if $\left|\gamma_{max}^{-}\right| \le \gamma_{cr}$, in which γ_{max}^{-} is the maximum shear strain attained in the negative loading direction. If $\left|\gamma_{max}^{-}\right| > \gamma_{cr}$, k_{un}^{-} has a reduced value given by the following equation to account for the stiffness degradation caused by the opening and closing of diagonal shear cracks.

$$k_{un}^{-} = k_1 \min\left[\left(\frac{\gamma_{cr}}{|\gamma_{max}^{-}|}\right)^{\eta}, 1.0\right] \tag{6-22}$$

in which η is a parameter governing the severity of stiffness degradation.

Reloading follows path B-C-D, as shown in Figure 6-9, which is a bilinear line that crosses the envelope curve at a point (point D) with the shear strain equal to the larger of γ_{cr} and $\gamma^{+}_{\max}$, where γ^{+}_{max} is the maximum shear strain attained in the positive loading direction in the previous loading cycle. As shown in the figure, the coordinates of the intermediate point (C) are determined with two parameters, *pinchX* and *pinchY*, whose values are between 0 and 1 and to be selected by user.

An unloading-reloading curve towards the negative direction can be constructed in a similar way.

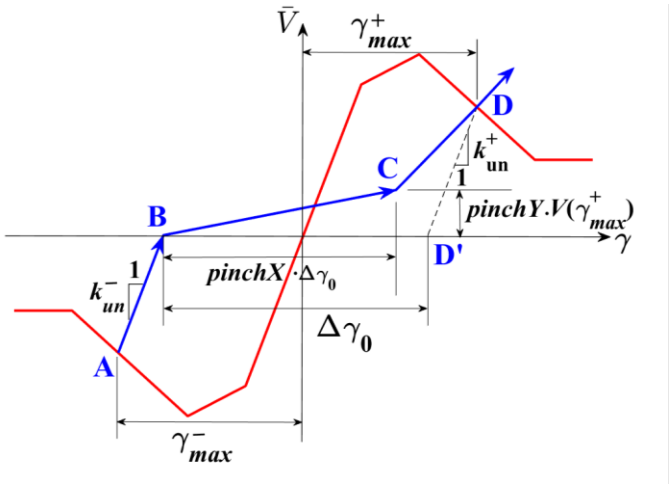

Figure 6-9. An unloading-reloading path constructed with the basic pinching model

6.3.2.2. Modeling of In-Cycle Damage

To account for the influence of in-cycle damage, two degradation modes as suggested by Ibarra et al (2005) are considered: degradation of the shear strength and the degradation of the reloading stiffness, as shown in Figure 6-10. As will be discussed below, the degradation laws proposed here are based on hysteretic energy dissipation.

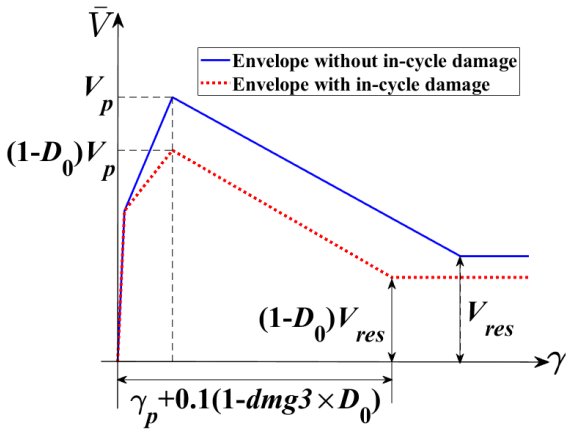

(a) Envelope stress

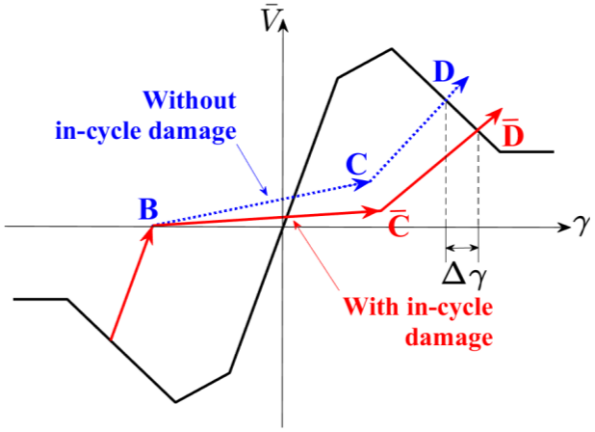

(b) Reloading stiffness

Figure 6-10. Deterioration models due to in-cycle damage

Shear Strength Degradation

The degradation of the shear strength due to in-cycle damage is controlled by a damage index (D_0) defined in the following equation. It is assumed that degradation will occur once the absolute maximum shear strain attained exceeds γ_{cr}.

$$D_0 = \begin{cases} dmg1 \times \dfrac{|\gamma_{max}| - \gamma_{cr}}{\gamma_{cr}} + dmg2 \times \dfrac{E_D}{E_A} & \text{if } |\gamma_{max}| > \gamma_{cr} \\ 0 & \text{if } |\gamma_{max}| < \gamma_{cr} \end{cases} \tag{6-23}$$

in which $|\gamma_{max}|$ is the absolute maximum shear strain reached in either loading direction in

the analysis; *dmg1* and *dmg2* are damage parameters, whose values are to be determined by user, E_D is the energy dissipated by the hysteretic model in all the previous cycles after $|\gamma_{max}|$ exceeds γ_{cr}, and E_A is a normalization constant given by:

$$E_A = 0.7V_0 \times \gamma_{cr} + 1.7V_0 \times (0.25\% - \gamma_{cr}) \tag{6-24}$$

As shown in Figure 6-10(a), the peak shear strength (V_p) and residual shear strength (V_{res}) are reduced by the factor ($1 - D_0$), and the shear strain at which the residual strength is first reach (γ_{res}), is reduced from $(\gamma_p + 0.1)$ as shown in Figure 6-7(a) to $\left[\gamma_p + 0.1(1 - dmg3 \times D_0)\right]$, in which *dmg3* is a damage parameter.

Reloading stiffness degradation

As shown in Figure 6-10(b), the degradation of the reloading stiffness is controlled by shifting point D, located at γ^+_{max} on the envelope curve to point $\overline{\mathrm{D}}$, located at $(\gamma^+_{max} + \Delta\gamma)$, where $\Delta\gamma$ is proportional to the energy dissipated in the previous cycle (E_{i-1}) as given in Eq. 6-25.

$$\Delta\gamma = dmg4 \times \gamma_{cr} \times E_{i-1} \tag{6-25}$$

in which *dmg*4 is a damage parameter. Point C is shifted accordingly to $\overline{\mathrm{C}}$, as shown in the figure.

6.3.3. Update of Envelope with Axial Force

When the mixed beam-column element is used to model a shear wall in a wall system subjected to lateral seismic forces, its axial force may vary due to the overturning moment induced on the wall system. To accurately account for the influence of the axial force on the shear resistance, the shear force-vs.-shear strain envelope curve is continuously updated based on the axial forces P_w and P_f calculated at the fiber section near the end where the flexural demand is most severe.

The envelope is updated in each incremental step of the analysis. The peak shear resistance V_p, the strain at the peak shear resistance γ_p, and the residual web strength reduction factor α_{res} are updated with the value of P_w calculated in the current step. For a flanged wall, the moment capacity of the flange(s), M_f, is updated with the value of P_f. However, once the maximum shear strain ($|\gamma_{max}|$) developed in the element in the last converged step exceeds the value of γ_p, the values of V_p and γ_p will be fixed, but the value of α_{res} will be continuously updated with P_w until $|\gamma_{max}|$ exceeds γ_{res} and remain constant afterwards. The value of the moment capacity of the flange(s), M_f, is continuously updated with the axial force P_f. This update strategy is adopted not to jeopardize the robustness of the numerical solution, and considers the fact that the axial force from the overturning moment cannot increase once the peak shear strength.

The update algorithm of the shear model is summarized on the next page.

Shear Model State Determination

1. If V_p and γ_p have not been fixed, update V_p and γ_p with axial stress resultant of the web P_w [Eq. (6-14)].
2. If $V_w(\gamma_{res})$ has not been fixed, calculate α_{res} and $V_w(\gamma_{res})$ with P_w [Eqs. (6-17) and (6-18)].
3. Calculate $V_f(\gamma_{res})$ with axial stress resultant of the flange P_f [Eqs. (6-19) to (6-21)].
4. Update the envelope curve with the values determined in steps 1-3.
5. If $\gamma_{max} > \gamma_{cr}$ or $\gamma_{min} < -\gamma_{cr}$, update the envelope with the accumulated in-cycle damage [Eqs. (6-23) and (6-24)].
6. If current shear strain $\gamma > \gamma_{max}$:
    a. Update γ_{max};
    b. If $\gamma > \gamma_p$, fix the values of V_p and γ_p;
    c. If $\gamma > \gamma_{res}$, fix the value of $V_w(\gamma_{res})$;
    d. Return the stress ($\bar{V}$) and tangent stiffness ($\frac{\partial \bar{V}}{\partial \gamma}$) on the positive envelope at γ.
7. If $\gamma < \gamma_{min}$:
    a. Update γ_{min};
    b. If $\gamma < -\gamma_p$, fix the values of V_p and γ_p;
    c. If $\gamma < -\gamma_{res}$, fix the value of $V_w(\gamma_{res})$;
    d. Return the stress ($\bar{V}$) and tangent stiffness ($\frac{\partial \bar{V}}{\partial \gamma}$) on the negative envelope at γ.
8. If $\gamma_{min} \leq \gamma \leq \gamma_{max}$:
    a. If $\gamma > \gamma_p$ or $\gamma < -\gamma_p$, fix the values of V_p and γ_p;
    b. If $\gamma > \gamma_{res}$ or $\gamma < -\gamma_{res}$, fix the value of $V_w(\gamma_{res})$;
    c. If the loading direction has reversed, start the construction of unloading-reloading path:
        i. Update the energy dissipated in the last cycle (E_{i-1}) and total energy dissipated (E_D).
        ii. If $\gamma_{max} > \gamma_{cr}$ or $\gamma_{min} < -\gamma_{cr}$, update the damage factor D_0 [Eqs. (6-23) and (6-24)].
        iii. Shift the γ_{max} or γ_{min} with E_{i-1}, depending on loading direction [Eq. (6-25)].
        iv. Calculate the unloading stiffness k_{un} with Eq. (6-22) and construct the unloading path.
        v. Construct the reloading path with pinching law.
    d. Calculate the stress ($\bar{V}$) and tangent stiffness ($\frac{\partial \bar{V}}{\partial \gamma}$) on the unloading-reloading path at γ.

6.4. Constitutive Relations for Fiber Section

This section presents the constitutive laws adopted for masonry and vertical reinforcing steel in the fiber section model. For masonry, the uniaxial stress-strain law proposed for concrete by Kent and Park (1971) is adopted. As shown in Figure 6-11(a), it is assumed that tensile strength of masonry is zero. The peak compressive strength, f'_m, is assumed to be reached at the compressive strain of 0.003. After the peak strength has been reached, the compressive stress drops linearly until it reaches $0.2 f'_m$ at a compressive strain of 0.006 to model crushing. Afterwards, a residual strength of $0.2 f'_m$ is maintained.

For a shear-dominated RM wall, severe spalling and crushing of masonry along diagonal cracks can result in the degradation of the flexural and axial compressive load carrying capacities. To model this phenomenon, the compressive strength of the masonry fibers within the web area is reduced with the increase of $|\gamma_{max}|$. As shown in Figure 6-11(a), f'_m is reduced by the α factor defined in Eq. (6-17) when $|\gamma_{max}| > \gamma_p$.

A bilinear elastic-plastic uniaxial law with kinematic strain hardening is adopted to model the vertical reinforcing bars in an RM wall section. As shown in Figure 6-11(b), the strain hardening ratio is assumed to be 0.1. This simple model does not account for the buckling and fracture of vertical bars that can be observed in walls suffering severe flexural damage. However, it provides a more stable condition for the numerical solution and is adequate for walls with the post-peak behavior dominated by shear. To model the behavior of walls predominately controlled by flexure, a steel model that can phenomenologically account for the buckling and fracture of vertical bars should be adopted.

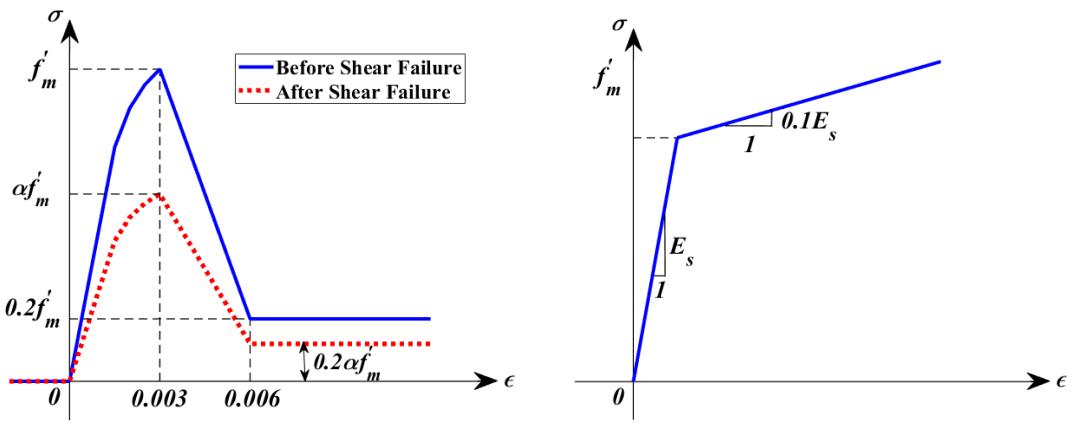

(a) Masonry (b) Vertical reinforcing steel

Figure 6-11. Uniaxial material constitutive laws used in fiber section model

6.5. Model Calibration and Validation

The mixed formulation, along with the proposed constitutive models, have been implemented into an open-source software platform, OpenSEES (McKenna et al. 2000). A number of experimental data have been selected to calibrate the parameters of the shear model, including the quasi-static cyclic tests on shear-dominated planar walls (Shing et al., 1990; Shing et al., 1989; Voon and Ingham, 2006; Ahmadi, 2012), the shake-table tests on a two-story RM structure by Mavros et al. (2016), and the shake-table tests on two one-story RM wall systems presented in Chapter 5. The parameters calibrated based on these test data are shown in Table 6-1. However, there is no test data available on RM structures subjected to bi-directional loads.

The numerical results obtained with the calibrated model are compared to the experimental results in the following sections. The compressive strength of masonry and the yield strength of the steel are based on the values reported in the experimental studies. In the analyses, the Gauss-Radau quadrature with five integration points is used for the

beam element.

Table 6-1. Calibrated model parameters

Type of Parameter	Parameter	Value	Note
Envelope	C_0	0.2	Parameter controlling web residual shear strength
	C_2	10.0	Parameter controlling web residual shear strength
	C_3	-120.0	Parameter controlling web residual shear strength
Hysteretic	*pinchX*	0.70	Pinching factor in hysteresis model
	pinchY	0.30	Pinching factor in hysteresis model
	η	0.60	Parameter controlling unloading stiffness degradation
	dmg1	0.0015	In-cycle damage factor
	dmg2	0.0050	In-cycle damage factor
	dmg3	0.2	In-cycle damage factor
	dmg4	1.5	In-cycle damage factor

6.5.1. Wall Segments Tested by Shing et al.

The proposed beam-column model was calibrated and validated with the test data of 17 shear-dominated RM wall specimens (Shing et al.,1991; Voon and Ingham, 2006; Ahmadi, 2012). The dimensions, reinforcement details, and axial load ratios of the selected wall specimens have been shown in Table 4-3.

Static cyclic analyses were performed with the models built for the selected wall specimens, with each wall modeled by one proposed mixed beam-column element. The comparisons of the results of static analysis with the proposed mixed element with the test data are shown in Appendix IV. Figures 6-12 show the comparisons of the three of the selected wall specimens: CU-3, CU-5, and CU-16. These cantilever planar walls had the same geometry. Walls CU-3 and CU-5 had the same reinforcement arrangement but were subjected to different levels of axial load. Walls CU-3 and CU-16 had the same amount of axial compressive load, but the latter specimen had higher amount of horizontal reinforcement. The results of analysis show good match with the test data. For all three cases, the responses of the models are dominated by shear. The lower shear strengths given by the models indicate that the shear strength formula in TMS 402/602 (2016) is conservative for these walls.

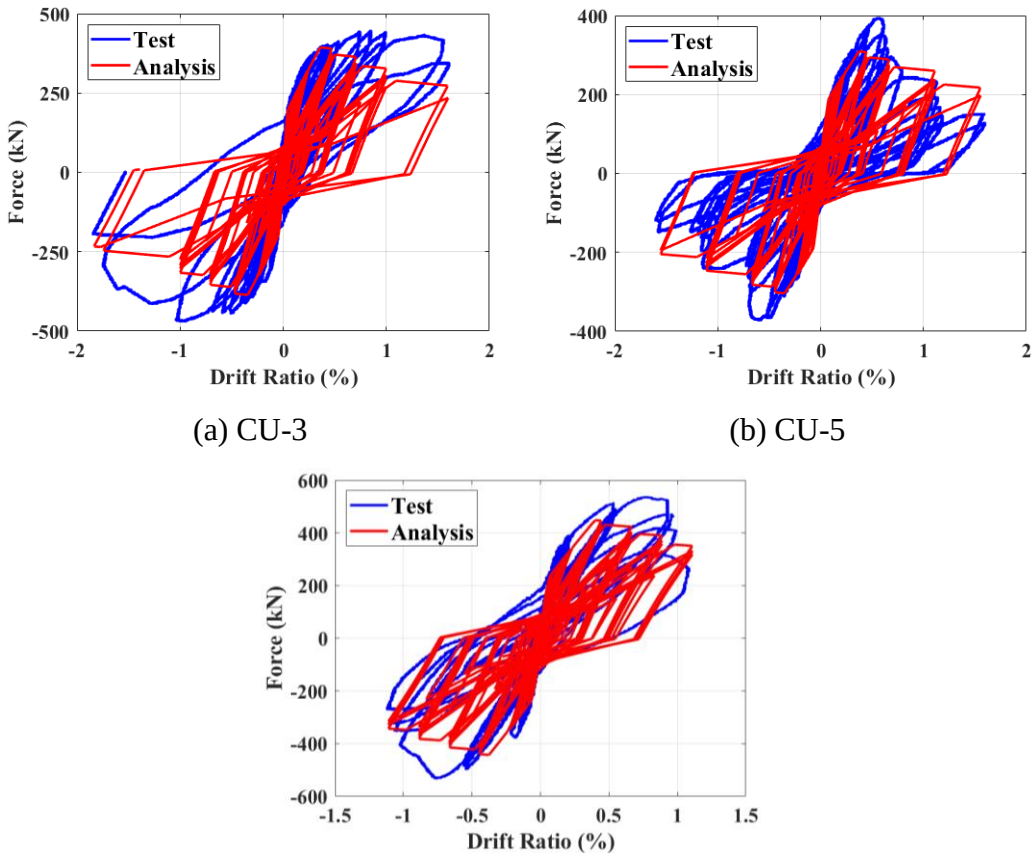

(a) CU-3 (b) CU-5

(c) CU-16

Figure 6-12. Comparison of numerical results with experimental data on shear-dominated walls

6.5.2. A Two-Story Structure Tested by Mavros et al.

The ability of the model to capture the dynamic response of an RM wall system under earthquake loading is evaluated with the two-story wall system tested by Mavros et al. (2016) with uni-directional earthquake motions on a shake table. Figure 6-13 shows the elevation view and plan view of the structure. In each story, the structure had two T-walls (Wall-1 and Wall-3) and one planar wall (Wall-2) that resisted the lateral seismic forces. In additional, there were four planar RM walls oriented perpendicular to the direction of shaking at the two ends of the structure. These four walls are referred to as out-of-plane

walls. The dimensions and reinforcement details of the walls are shown in Tables 6-2 and 6-3. The average material strengths obtained from sample tests are: f'_m = 15.6 MPa and f_y = 448 MPa.

A frame model has been developed for the two-story RM structure, as shown in Figure 6-14. All the elements in the model are located in a plane as the structure was subjected to uni-directional motions. In the first story, the two flanged walls (Wall-1 and Wall-3) at the two ends and the planar wall (Wall-2) are modeled with the mixed element. For each of the RM shear walls, the mixed beam-column element is located at the centroid of its section. The effective height (H_{eff}) is taken as half of the wall height due to the high bending stiffness of the horizontal diaphragm. Each of the four out-of-plane walls is modeled with five displacement-based beam-column elements of equal lengths. Fiber sections are used to compute the flexural resistance developed in the out-of-plane walls. Similar to the in-plane walls, masonry in the fiber section is modeled with the Kent-Park model (Concrete01 in OpenSEES), whereas the vertical reinforcement is modeled by a bilinear law with strain hardening (Steel01 in OpenSEES). As most of the inelastic deformation of the walls was localized in the first story, all the RM walls in the second story are modeled with elastic beam-column elements. The horizontal diaphragms and the RM panel zones connecting the wall segments are modeled with stiff elastic beam-column elements. The mass at roof and the 1st floor (including the masonry above and beneath the openings) was uniformly distributed at the nodes along the diaphragm elements. For each masonry wall component, half of the wall mass is lumped at each end.

In the test, the two-story RM structure was subjected to 9 El-Centro ground motion records obtained from the 1979 Imperial Valley Earthquake scaled to different intensities

until severe shear failure occurred. As the structure had little damage developed during the first six ground motions with its fundamental period increased from 0.077 to 0.084 sec, only the last three table motions are applied to the frame model, which are the El-Centro records scaled to 108%, 145% and 160% intensity levels. The motions were recorded table motions and are applied in sequence with quiet times inserted between records for the structure to rest before the next motion starts.

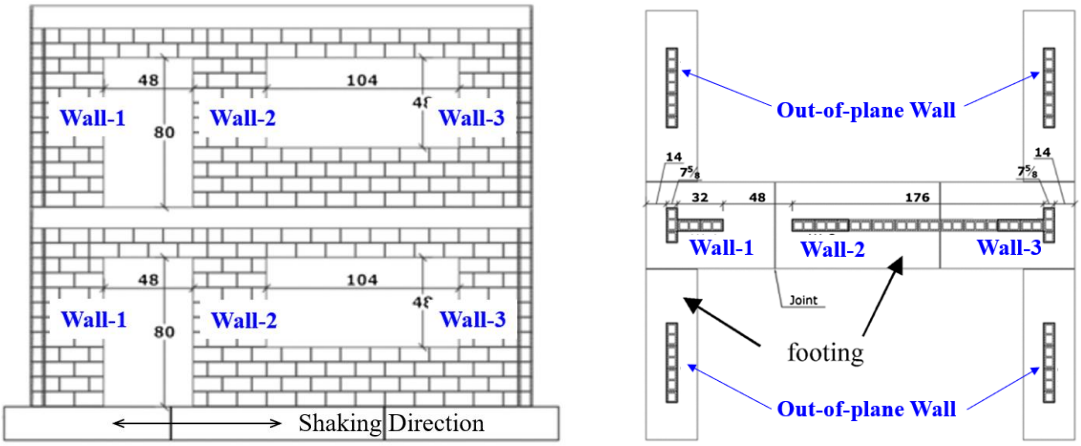

(a) Elevation view of interior walls (b) Plan view

Figure 6-13. Numbering of Walls in the two-story RM structure tested by Mavros et al.

Table 6-2. Dimensions of walls in the two-story RM structure tested by Mavros et al.

Wall ID	**Height (m)**	**Length of web (m)**	**Length of flange (m)**	**Width (m)**
Wall-1	2.03	0.81	0.61	0.194
Wall-3	1.22	0.81	0.61	0.194
	Height (m)	**Length (m)**		**Width (m)**
Wall-2	1.22	1.02		0.194
Out-of-plane Wall	2.44	1.42		0.194

Table 6-3. Reinforcement details of the two-story RM structure tested by Mavros et al.*

Wall ID	Horiz. reinf. in web	Vert. reinf. in web	Horiz. reinf. in flange	Vert. reinf. in flange
Wall-1	#4@41cm	#4@41cm	#4@20cm	#4@20cm
Wall-3	#4@41cm	#4@41cm	#4@20cm	#4@20cm
	Horiz. reinf.		**Vert. reinf.**	
Wall-2	#4@41cm		#4@41cm	
Out-of-plane Wall	#4@41cm		#4@61cm	

*#4 reinforcing bars have nominal diameter of 13 mm.

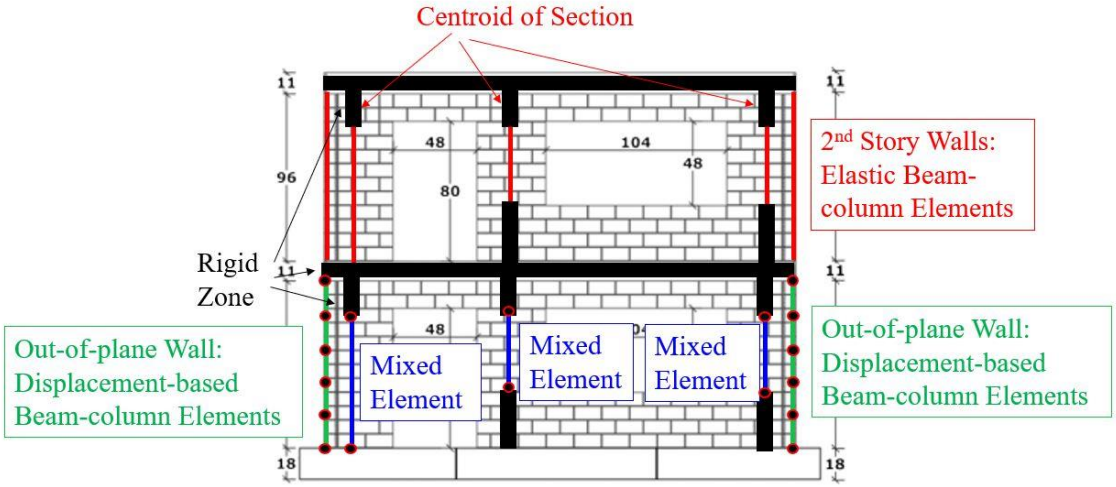

Figure 6-14. Frame model of the two-story RM structure tested by Mavros et al.

Rayleigh damping with a damping ratio of 0.5% for the 1st and 2nd modes is used. The stiffness proportional part of the damping matrix is based on the initial stiffness of the model calculated at zero displacement. As shown in Figure 6-15, the results of the analysis show a good agreement with the test results. However, comparing to the test, the model has a higher initial stiffness. The discrepancy is partly due to the omission of the first six lower-intensity motions, which induced slight damage to the structure.

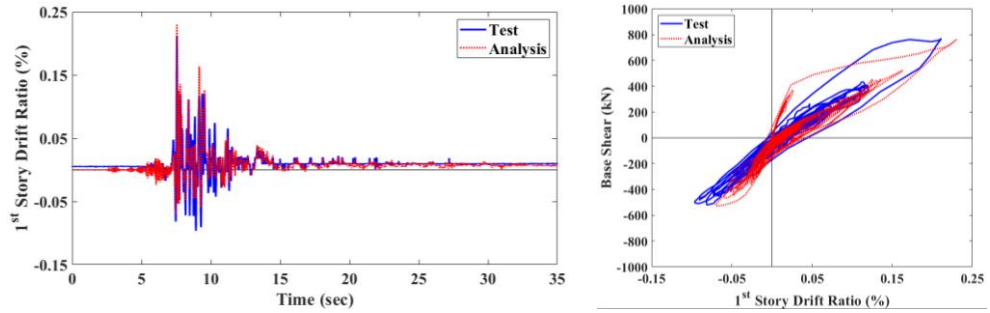

(a) El Centro 108%

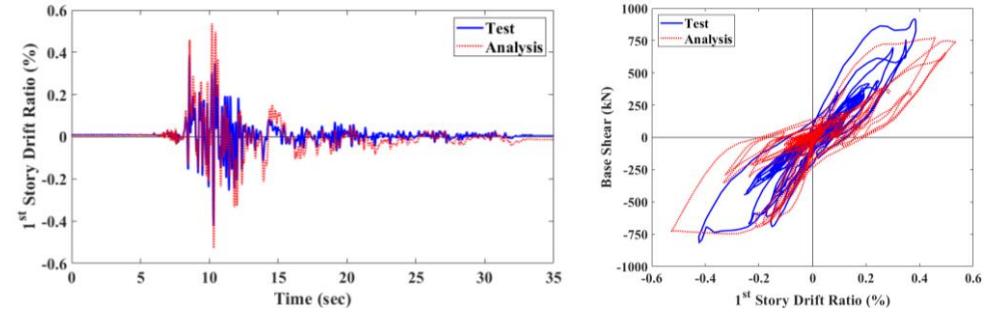

(b) El Centro 145%

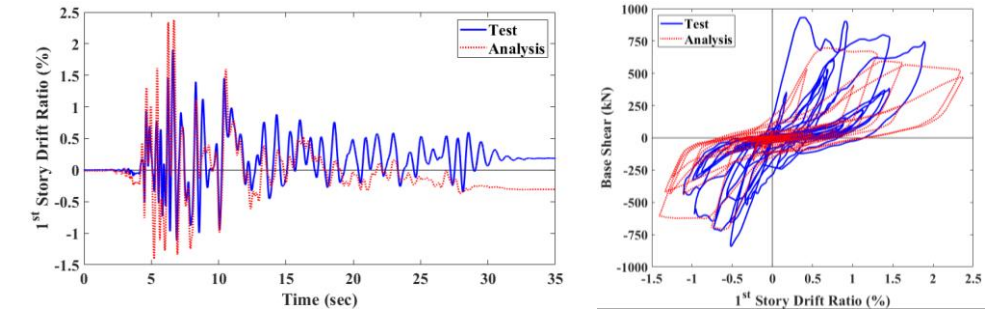

(c) El Centro 160%

Figure 6-15. Comparison numerical results with experimental data on the two-story RM structure tested by Mavros et al.

6.5.3. Two One-Story Structures Tested by the author

The two one-story RM structures presented in Chapter 5 have been selected to examine the ability of the model to simulate the response of a wall system up to the point of near collapse. The naming of the wall components of the two wall systems (Specimen 1 and Specimen 2) shown in Figure 5-1 has been adopted in this chapter. The dimensions and reinforcement details of these two structures are summarized in Tables 6-4 and 6-5.

Table 6-4. Dimensions of walls in the one-story RM structures presented in Chapter 5

Wall ID	**Height (m)**	**Length of web (m)**	**Length of flange (m)**	**Width (m)**
Specimen 1				
Wall-1	2.44	1.22	1.02	0.194
Wall-2	2.44	1.22	1.02	0.194
Specimen 2				
Wall-1	2.44	1.22	1.02	0.194
Wall-2	2.44	1.22	1.02	0.194
	Height (m)	**Length (m)**		**Width (m)**
Out-of-plane Wall	2.44	1.02		0.194

Table 6-5. Reinforcement details of the one-story RM structures presented in Chapter 5*

Wall ID	**Horiz. reinf. in web**	**Vert. reinf. in web**	**Horiz. reinf. in flange**	**Vert. reinf. in flange**
Specimen 1				
Wall-1	#3@41cm	#4@20cm	#3@41cm	#4@41cm
Wall-2	#3@41cm	#4@20cm	#3@41cm	#4@41cm
Specimen 2				
Wall-1	#4@41cm	#4@41cm	#3@41cm	#4@41cm
Wall-2	#3@41cm	#4@20cm	#3@41cm	#4@41cm
	Horiz. reinf.		**Vert. reinf.**	
Out-of-plane Wall	#3@41cm		#4@41cm`	

* #3 and #4 reinforcing bars have nominal diameters of 10mm and 13mm, respectively.

Frame models have been developed for the two one-story RM wall systems, with all the elements located in a plane. They are similar to the model discussed in the previous section. As shown in Figure 6-16, the mixed element is used to model the T-walls. For each T-wall, the mixed element is located at the centroid of the T-section. The effective height (H_{eff}) is taken as half of the wall height due to the high stiffness of the roof systems. For Specimen 2, the six out-of-plane walls are modeled with displacement-based beam-column elements with fiber sections. Each out-of-plane wall is modeled with five elements of the same length. The roof slabs in the two structures are modeled as stiff beam-column elements. For each specimen, the roof mass is distributed uniformly at the nodes along the roof. The mass of each RM wall (T-walls and out-of-plane walls) is lumped at the two ends of the wall.

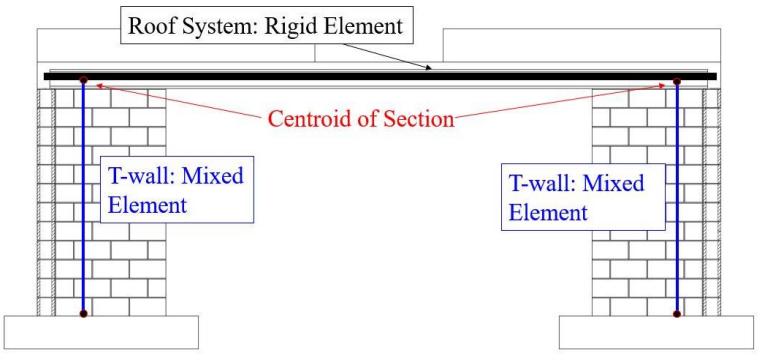

(a) Specimen 1

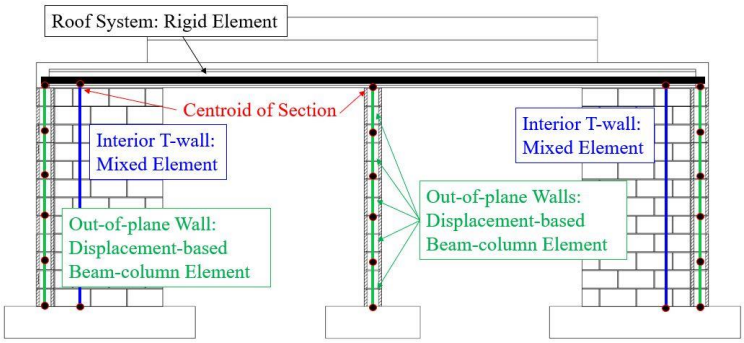

(b) Specimen 2

Figure 6-16. Frame models of the two one-story RM structures tested by the author

Time-history analysis was performed with the frame model of Specimen 1 using the table motions from the test, and it was followed by a static analysis pushing the roof to reach a drift ratio to 17%. The frame model of Specimen 2 was subjected to the same sequence of table motions recorded in the test. For both models, Rayleigh damping was used with the damping ratio equal to 0.4% for the 1st and 2nd modes, with the stiffness proportional part based on the initial stiffness. Figure 6-17 compares the numerical results for Specimen 1 with the experimental results from the last earthquake ground motion run and the quasi-static test. Figure 6-18 shows the comparison of the numerical and experimental results for Specimen 2 obtained with the last two motions (MUL-160% and RIN-130%). While the numerical results show good agreements with test data, the model for Specimen 2 significantly underestimates the residual drift ratio attained at the end of the test (RIN-130%). Capturing the residual drift is always difficult even with a refined nonlinear finite element model (Koutras and Shing, 2021).

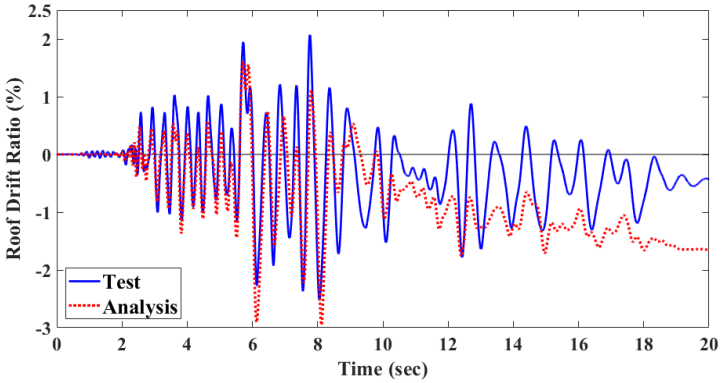

(a) Roof drift ratio time-history in MUL-133%

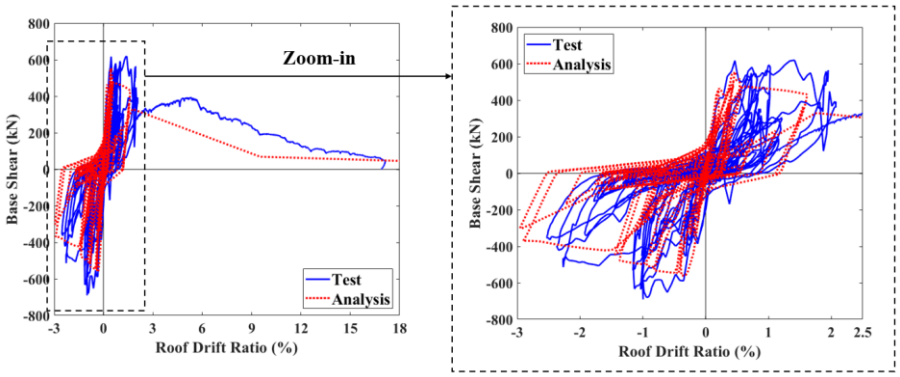

(b) Base shear-vs.-roof drift ratio response in MUL-133% and static pulling test

Figure 6-17. Comparison between numerical results and experimental data on Specimen 1 tested by the author.

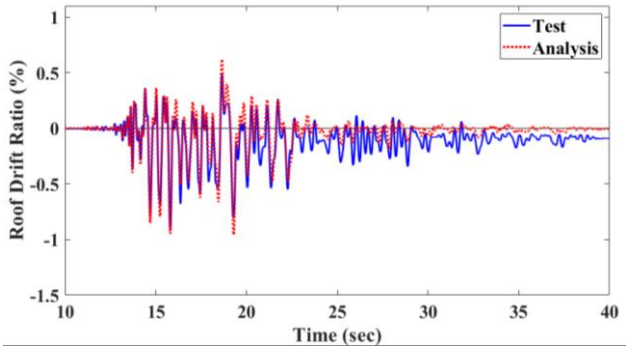

(a) Roof drift ratio time-history in MUL-160%

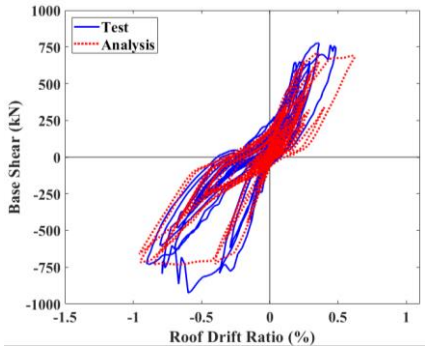

(b) Base shear-vs.-roof drift ratio response in MUL-160%;

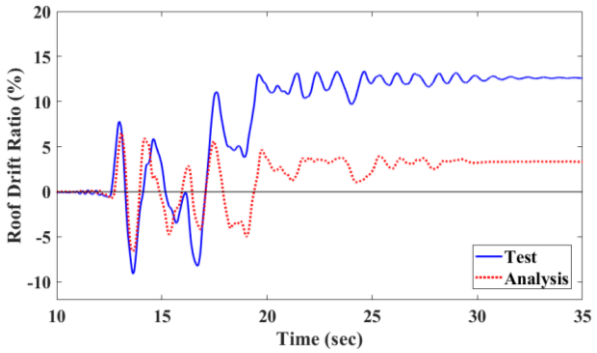

(c) Roof drift ratio time-history in RIN-130%

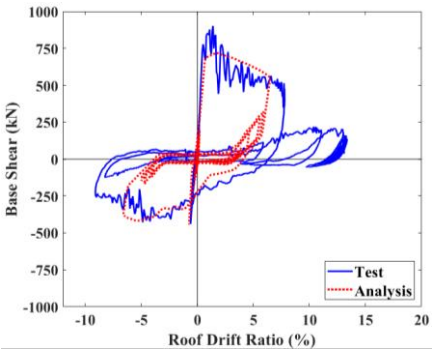

(d) Base shear-vs.-roof drift ratio response in RIN-130%

Figure 6-18. Comparison of numerical results with experimental data on Specimen 2 tested by the author

Chapter 6, in part, is a reprint of the material currently being prepared for submission for publication, Cheng, J. and Shing P. B. under the title “A Beam-Column Model for Nonlinear Flexural and Shear Behavior of Reinforced Masonry Walls”. The author of the dissertation is the primary author and the main contributor of the work presented in the paper.

CHAPTER 7 SUMMARY AND CONCLUSIONS

This dissertation presents a study aimed to acquire a better understanding of the nonlinear behavior of reinforced masonry RM shear wall systems under seismic loading, and to develop computationally efficient models to evaluate the seismic performance of these systems. In this study, beam-column element models have been developed to capture the nonlinear flexural and shear behaviors of RM shear walls, and large-scale shake-table tests were conducted to evaluate the strengths and displacement capacities of shear-dominated RM wall systems up to the verge of collapse.

7.1. Summary, Main Observations and Conclusions

7.1.1. Modeling of Flexure-Dominated Walls

Experimental data from wall tests have shown that the post-peak in-plane lateral load-vs.-displacement relation of a flexure-dominated RM wall is governed by a number of mechanisms, including the crushing of masonry at wall toes, the buckling of the vertical reinforcing bars, and the fracture of these bars due to low-cycle fatigue. To capture this relation accurately, a modeling approach that accounts for all these mechanisms has been presented in Chapter 3. In particular, a phenomenological material law has been proposed to model the buckling and fracture of reinforcing bars in a simple and efficient manner. The Kent-Park concrete model has been calibrated to model the behavior of masonry. The material models are calibrated with the assumption that the effective plastic-hinge length, in which plastic deformation is assumed to be uniformly distributed, is equal to 20% of the effective wall height. The modeling approach has been implemented in a force-based beam-column element with predefined plastic-hinge lengths and has been validated by data from cyclic, quasi-static, wall tests.

7.1.2. Force-vs.-Displacement Backbone Curves for RM Shear Walls

In Chapter 4, a general methodology has been presented for determining the lateral load-vs.-displacement backbone curves for flexure-dominated RM walls using the proposed material models. To allow the determination of these curves in a simple and efficient manner, values of non-dimensionalized critical moment and curvature parameters for different axial load and reinforcement conditions have been calculated and presented in tables, which can be used as analysis aids. The proposed method results in backbone curves that are far more accurate than those determined with current recommendations in ASCE 41 (ASCE, 2017). Even though the method has been derived and validated for fully grouted walls of rectangular and T sections, it can be applied to flanged walls in general as explained in Chapter 4. The use of these non-dimensionalized parameters for partially grouted walls needs validation with experimental data on flexure-dominated partially grouted walls, which are not currently available.

For shear-dominated RM walls, an empirical backbone curve has been proposed. The proposed backbone curve shows good agreement with test data of fully grouted, planar wall segments, whereas the curve constructed based on the current recommendations in ASCE 41(2017) shows overly brittle behavior.

7.1.3. Shake-Table Tests on RM Wall Systems

A study to investigate the collapse resistance of shear-dominated, fully grouted, RM wall systems designed for high seismic areas has been presented in Chapter 5. Two single-story specimens (Specimens 1 and 2), each having two RM T-walls as the seismic load resisting system, were tested on a shake table. Specimen 2 had six additional planar

walls (out-of-plane walls) perpendicular to the direction of shaking. Specimen 1 was first tested with a sequence of earthquake ground motions, and was finally subjected to quasi-static loading to the verge of collapse. The T-walls exhibited flexural behavior with the yielding of the vertical reinforcement during lower-level earthquake motions, but had failures eventually dominated by diagonal shear cracks. The maximum roof drift reached 2.52% in the ground motion tests. The maximum lateral resistance developed by the wall system is close to the sum of the shear strengths calculated for individual T-walls with the formula in TMS 402/602 (2016) based on the assumption that the axial force in each wall is due to the gravity load only. In the quasi-static test, the roof diaphragm was pulled to a maximum drift of 16.7%, at which the lateral resistance of the wall system dropped to 6% of the peak strength; but the structure did not collapse.

Specimen 2 was tested with a sequence of earthquake ground motions up to the verge of collapse. Compared to Specimen 1, Specimen 2 had a higher lateral resistance and had first cracks observed at a higher intensity ground motion. Specimen 2 also exhibited a much lower drift ratio at comparable ground motion levels. The specimen survived the last motion without collapse. The maximum roof drift reached 13.4%, at which the residual strength dropped to 20% of the peak strength. When the shear strength of the two T-walls is calculated with the TMS 402/602 (2016) formula with the consideration of the axial compression exerted by the out-of-plane walls, which restrained the rocking of the T-walls, the calculated value matches the maximum lateral resistance measured in the test well.

The two test specimens exhibited significantly higher displacement capacities than shear-dominated planar wall segments tested in previous studies under quasi-static cyclic loads. This could be partly attributed to a smaller number of large-amplitude displacement

cycles experienced by the two specimens compared to those tested under quasi-static loads. However, the higher displacement capacities can be largely attributed to the presence of wall flanges and, for the case of Specimen 2, the out-of-plane walls, which provided an alternative load path to carry the gravity load when the webs of the T-walls had been severely damaged.

Reinforced masonry buildings often have flanged walls and walls in different directions, and may also have gravity frames, which can provide an alternative load path to carry the gravity load as well as additional axial compression on the in-plane walls when the latter rock. These systems can sustain significant lateral displacements before the P-Δ effect of the gravity load would induce collapse. In general, the displacement capacity of a building system depends on a number of factors, including the wall configuration, wall failure mechanism, presence or absence of gravity frames, the P-Δ effect of the gravity load, and the severity of wall damage induced in each direction by bidirectional earthquake ground motions. These all need to be taken into consideration to assess the collapse vulnerability of a building.

7.1.4. Beam-Column Element for Modeling Flexural and Shear Behaviors of RM Walls

A beam-column element for modeling the nonlinear flexural and shear behaviors of RM shear walls has been presented in Chapter 6. The model is based on a three-field (force, strain, and displacement) mixed formulation, which is free of shear locking and allows an RM wall to be modeled with one element. A fiber-section model is used to simulate the axial and flexural behaviors, while a macro phenomenological model has been proposed to represent the shear behavior of a wall. The axial-flexural-shear interaction is

considered through the constitutive models. The shear model has a stress-vs.-strain envelope updated with the axial stress resultant from the fiber-section model, and the compressive strength of the masonry fibers in the fiber-section model is reduced with the development of shear damage.

The model has been calibrated and validated with experimental data from shear-dominated planar wall specimens and the two wall systems tested on a shake-table tests. The numerical and experimental results have shown good agreement. However, the ability of the proposed model in capturing the behavior of RM wall systems subjected to bi-directional horizontal loading has not been examined due to the lack of experimental data.

7.2. Recommendations for Future Research

The extension of the method presented in Chapter 4 for determining the force-vs.-displacement backbone curves for flexure-dominated fully grouted RM walls to partially grouted walls has not been thoroughly validated. This is because of the lack of experimental data. Most of the partially grouted RM walls that were tested exhibited shear- or shear-sliding-dominated behaviors. More experimental data on the flexure-dominated, partially grouted RM shear walls are needed.

In spite of the good agreement with test data, the empirical backbone curve for shear-dominated RM walls presented in Chapter 4 is only applicable to planar walls. A more rational methodology to construct the backbone curves for shear-dominated walls with different configurations is needed.

For the mixed beam-column element presented In Chapter 6, the nonlinear shear response is modeled by a phenomenological model. In spite of the good agreement of the

numerical results with the test data, the model does not explicitly consider the physics of the shear-dominated failure mechanisms, such as the opening and closing of the diagonal cracks, the compression strut mechanism, and the yielding and fracture of the horizontal reinforcement. A more physics-based shear model is desirable. Furthermore, the modeling of the flexural behavior in the element needs to be improved to account for the rebar buckling and fracture, as described in Chapter 3. This will entail the improvement of the numerical solution scheme to handle the added load degradation mechanisms.

Furthermore, the beam-column model presented in Chapter 6 is only calibrated with the test data of RM shear walls subjected to in-plane cyclic loads and uni-directional ground motions. The ability of the model in representing the behaviors of RM shear walls and shear wall systems subjected to multi-directional ground motions has not been verified by experimental data. More experimental data are needed on the behavior of RM walls and wall systems with multi-directional earthquake loads.

APPENDIX I COMPARISON OF NUMERICAL RESULTS WITH TEST DATA FOR FLEXURE-DOMINATED PLANAR WALLS

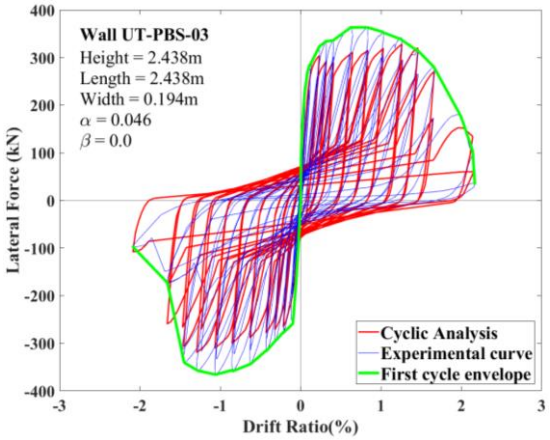

UT-PBS-03

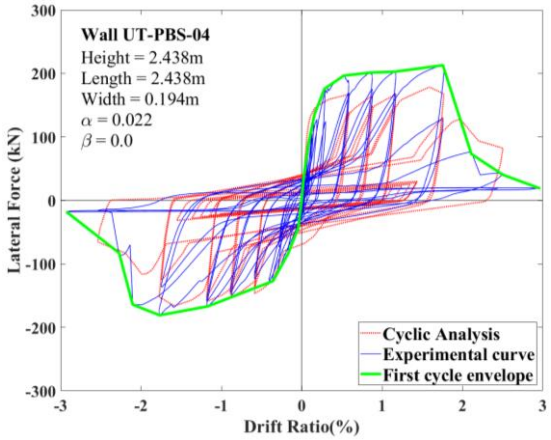

UT-PBS-04

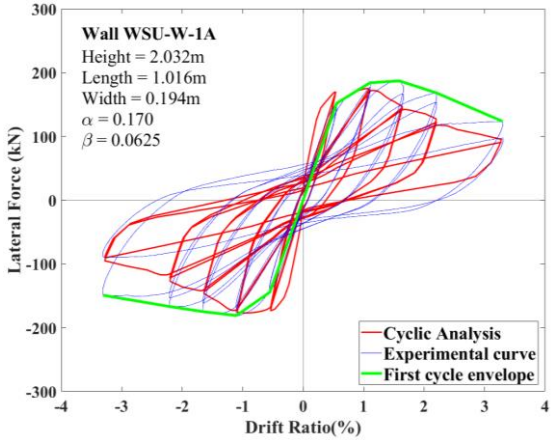

WSU-W-1A

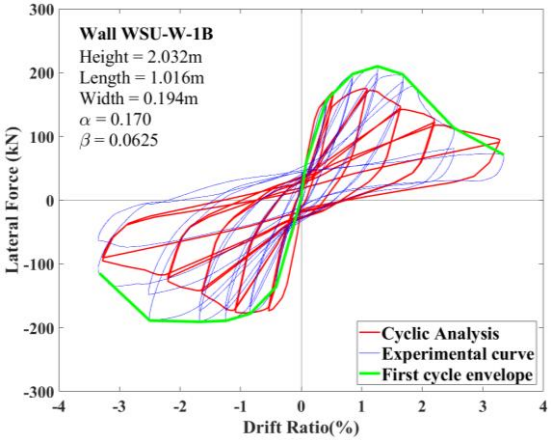

WSU-W-1B

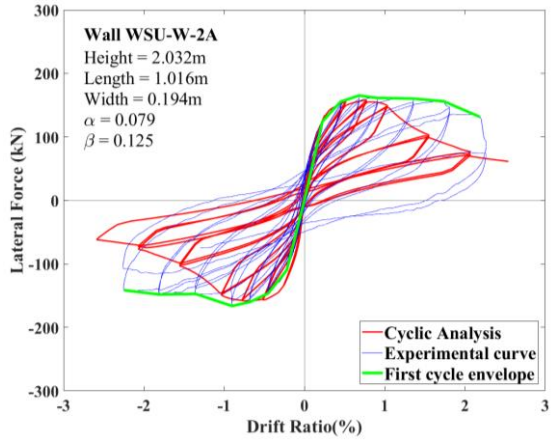

WSU-W-2A

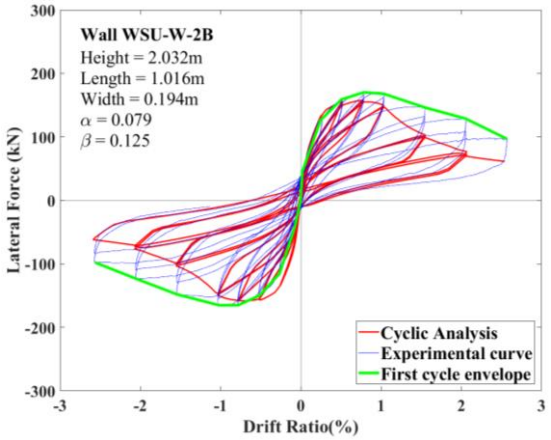

WSU-W-2B

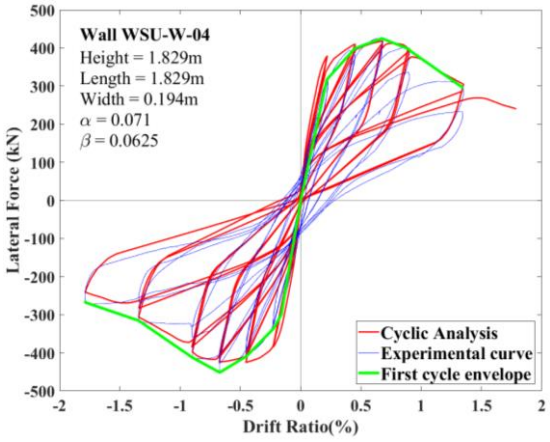

WSU-W-04

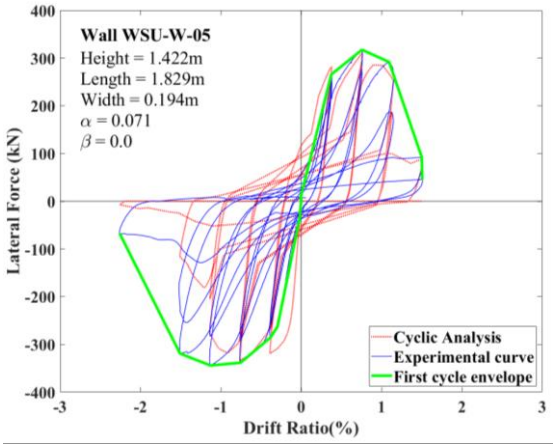

WSU-W-05

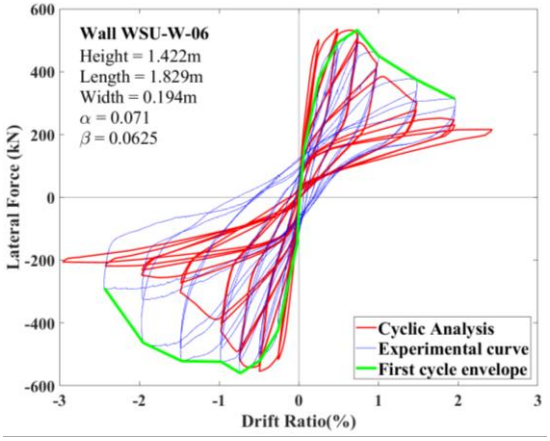

WSU-W-06

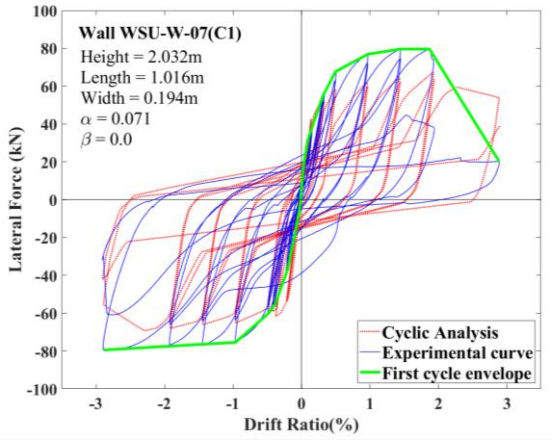

WSU-W-07(C1)

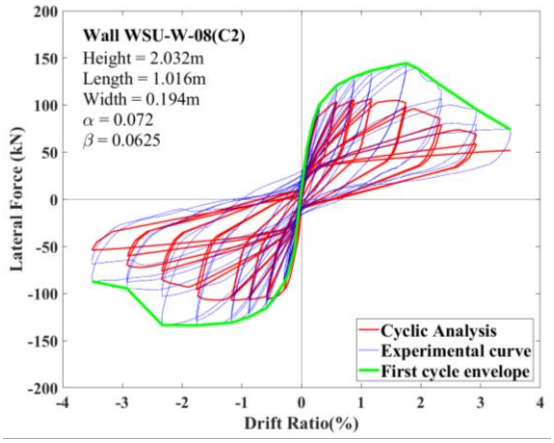

WSU-W-08(C2)

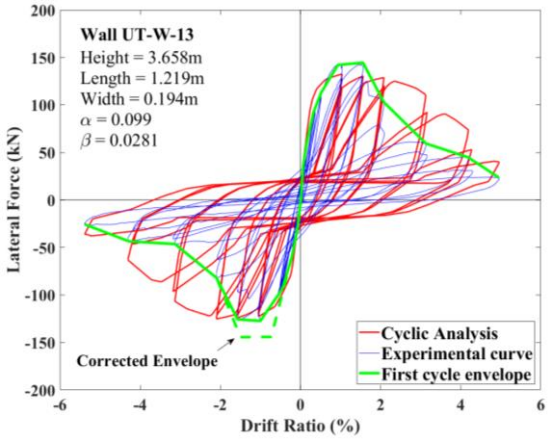

UT-W-13

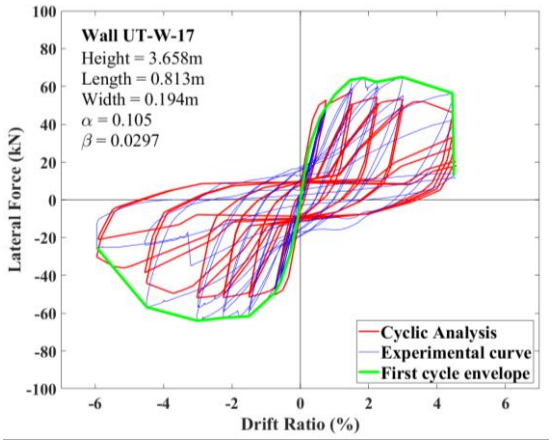

UT-W-17

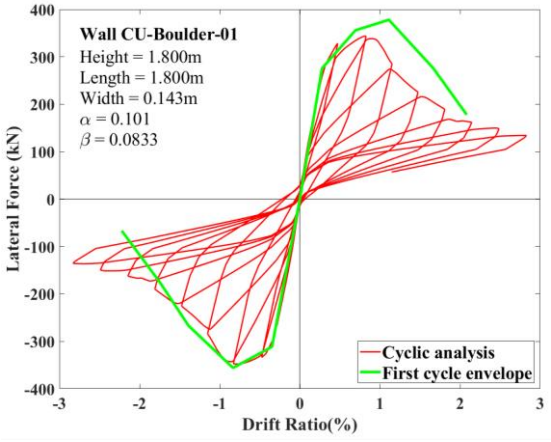

CU-Boulder-1

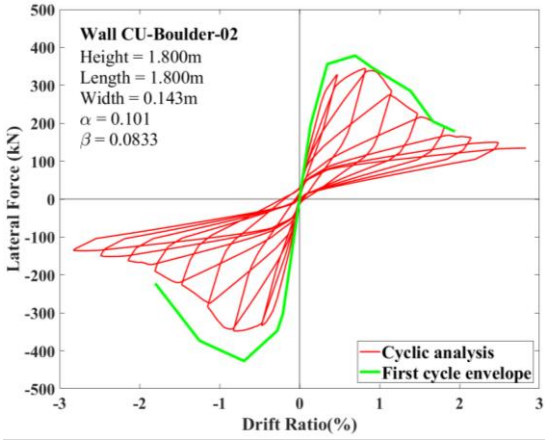

CU-Boulder-2

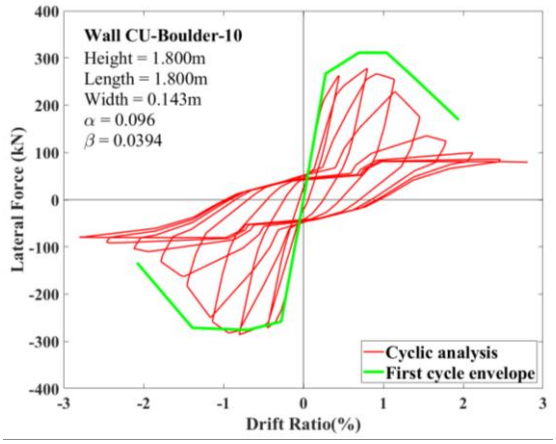

CU-Boulder-10

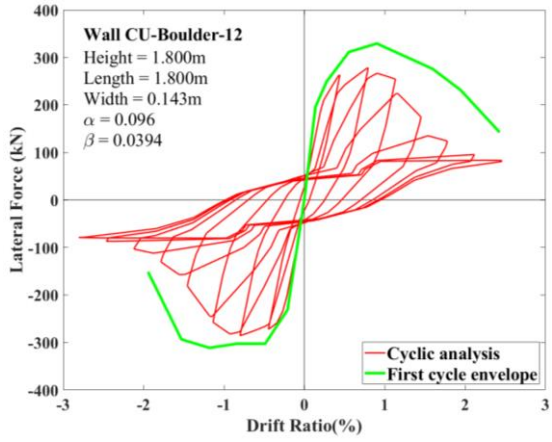

CU-Boulder-12

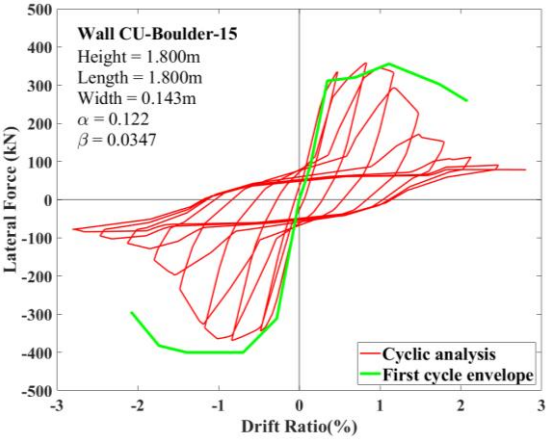

CU-Boulder-15

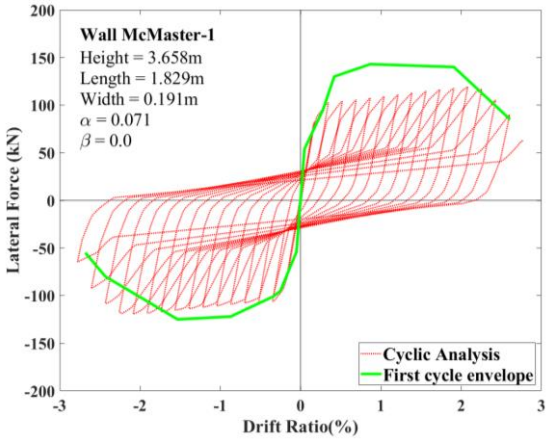

McMaster-1

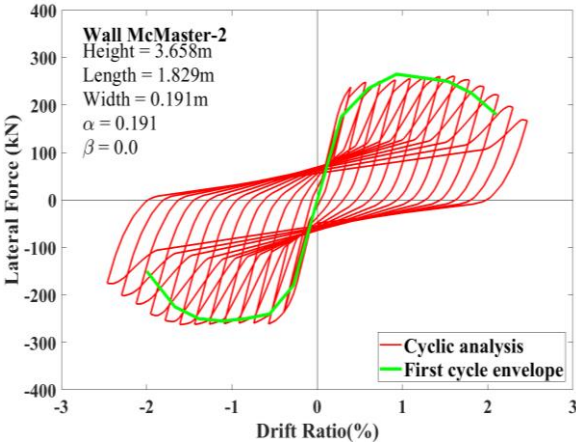

McMaster-2

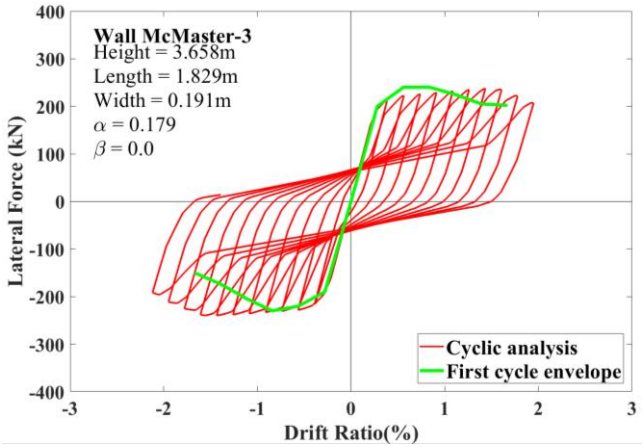

McMaster-3

APPENDIX II COMPARISON OF BACKBONE CURVES WITH TEST DATA FOR FLEXURE-DOMINATED RECTANGULAR-SECTIONED CANTILEVER WALLS

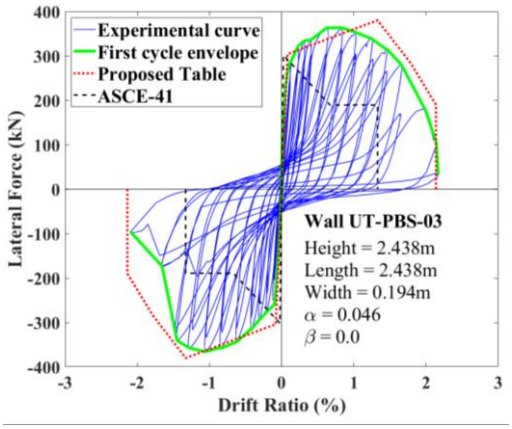

UT-PBS-03

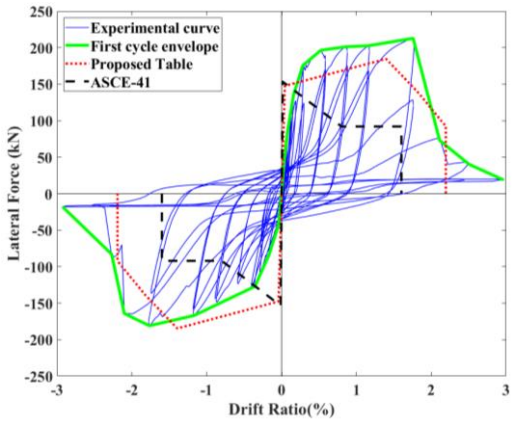

UT-PBS-04

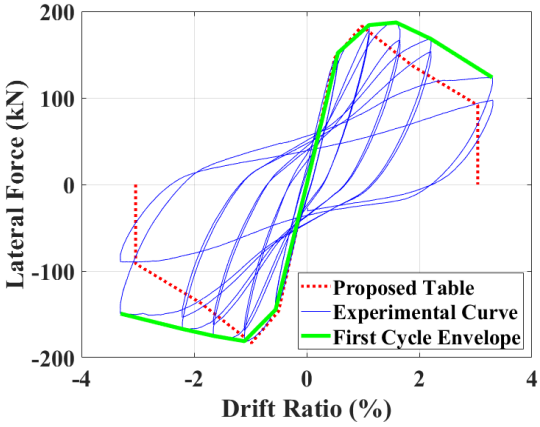

WSU-W-1A

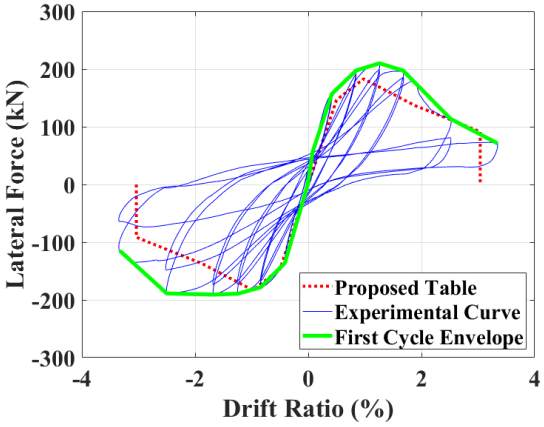

WSU-W-1B

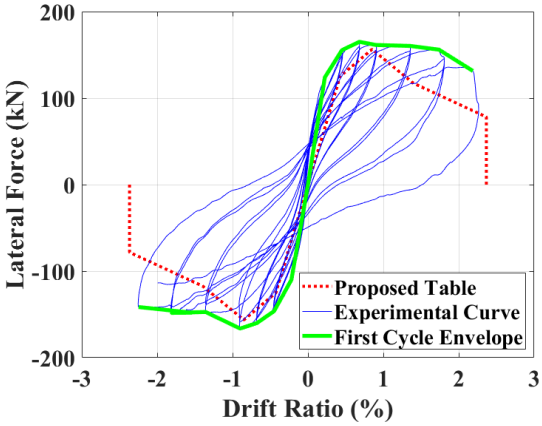

WSU-W-2A

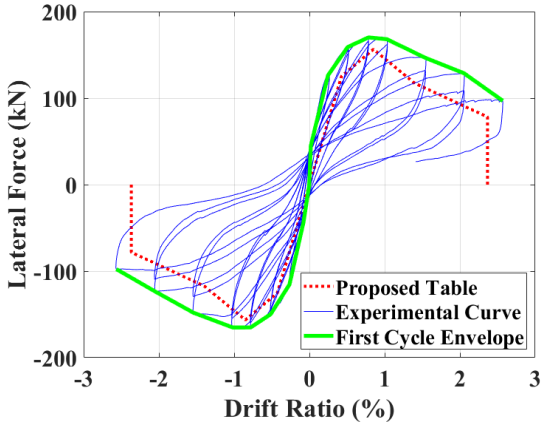

WSU-W-2B

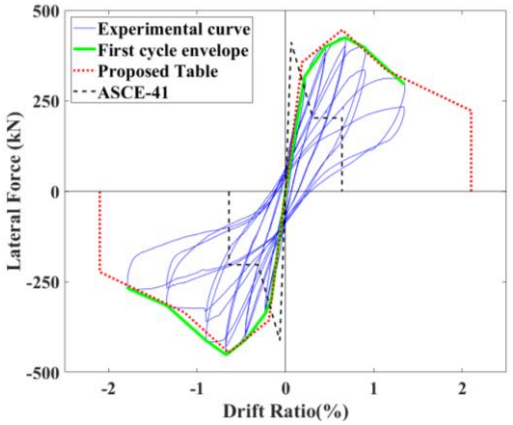

WSU-W-04

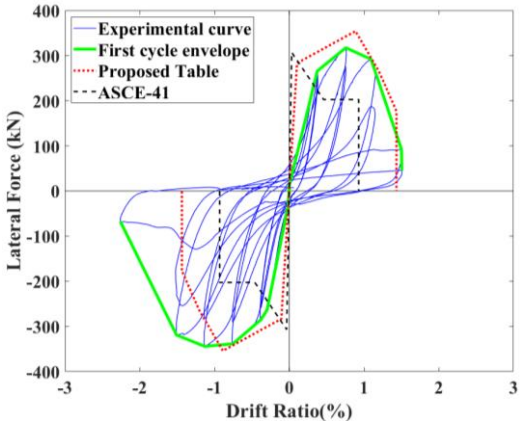

WSU-W-05

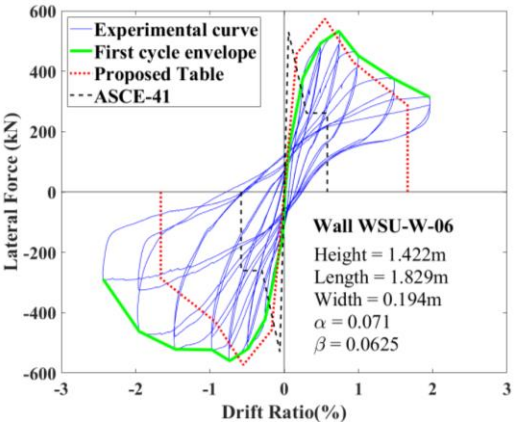

WSU-W-06

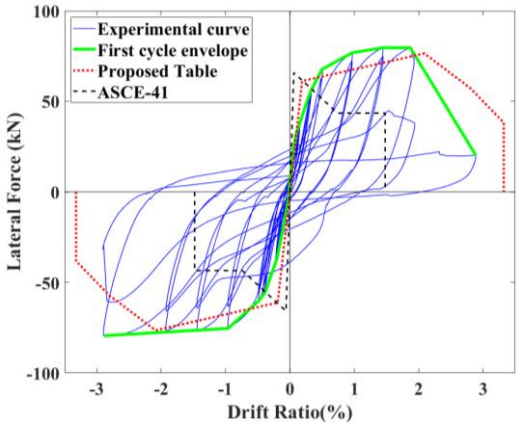

WSU-W-07(C1)

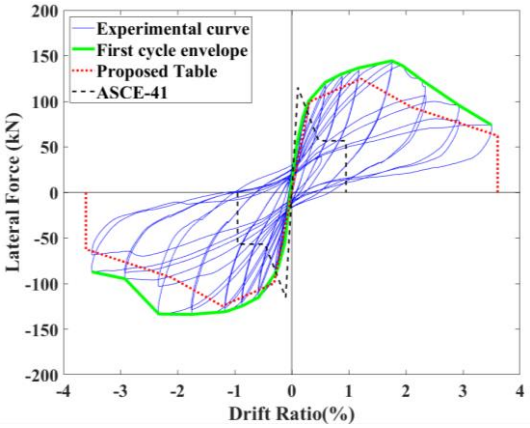

WSU-W-08(C2)

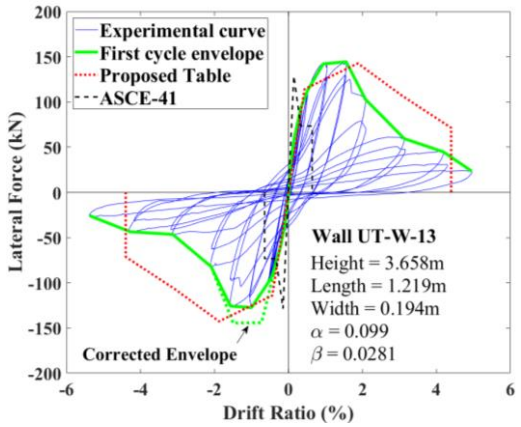

UT-W-13

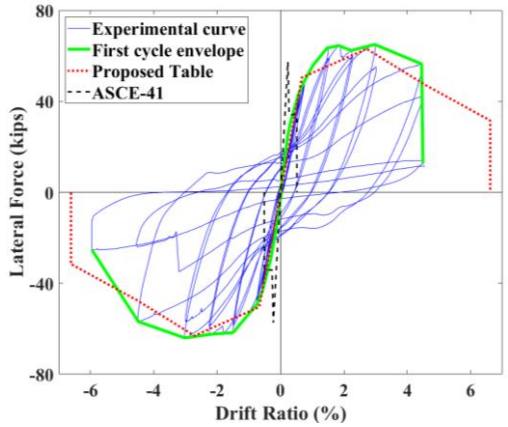

UT-W-17

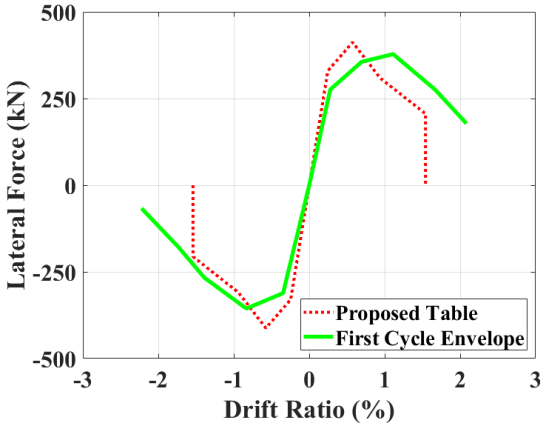

CU-Boulder-1

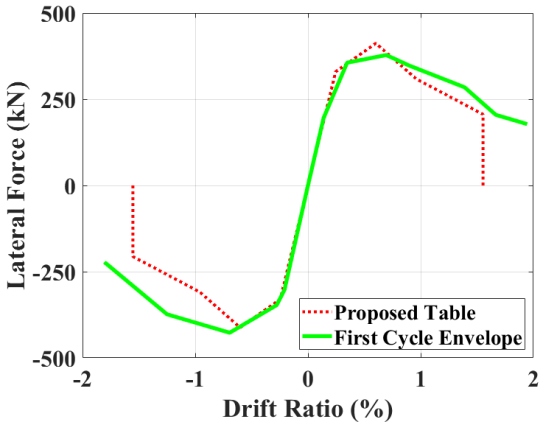

CU-Boulder-2

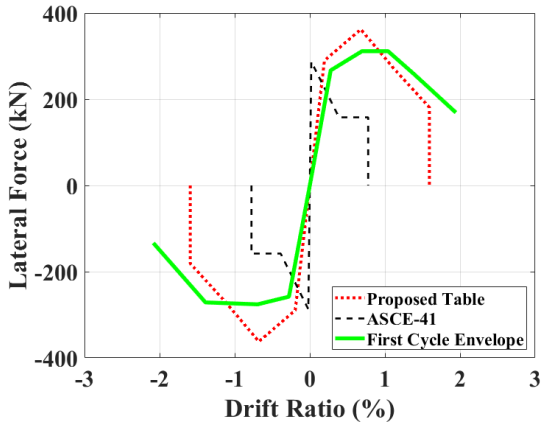

CU-Boulder-10

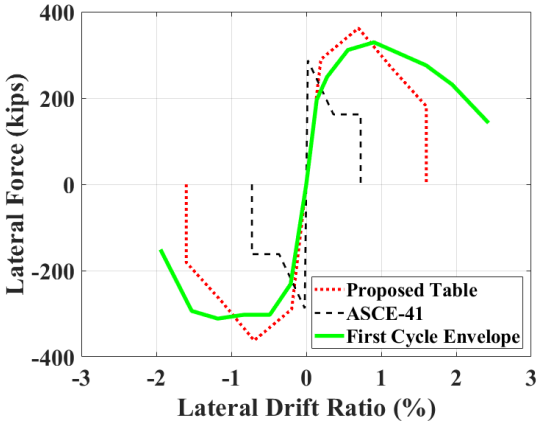

CU-Boulder-12

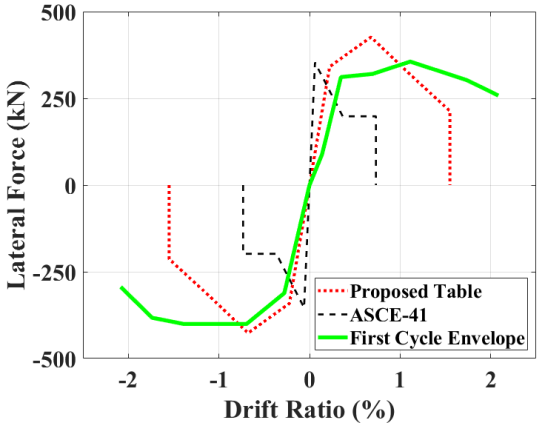

CU-Boulder-15

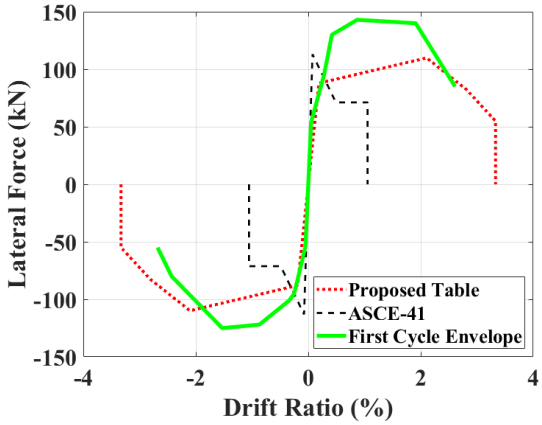

McMaster-1

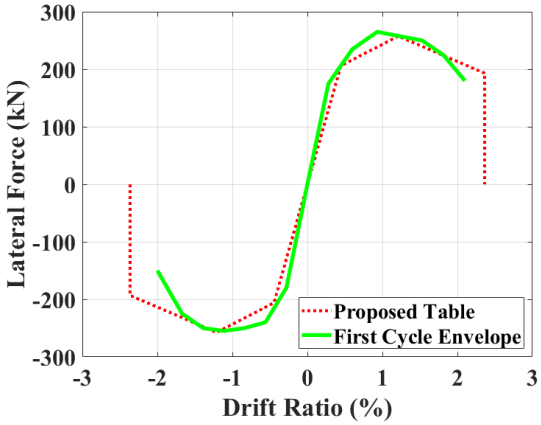

McMaster-2

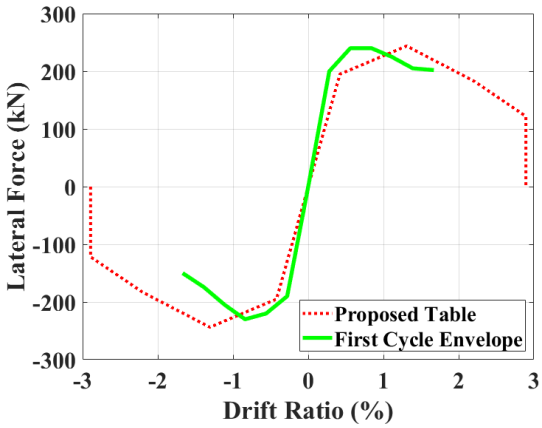

McMaster-3

APPENDIX III COMPARISON OF BACKBONE CURVES WITH TEST DATA FOR FLEXURE-DOMINATED RECTANGULAR-SECTIONED CANTILEVER WALLS

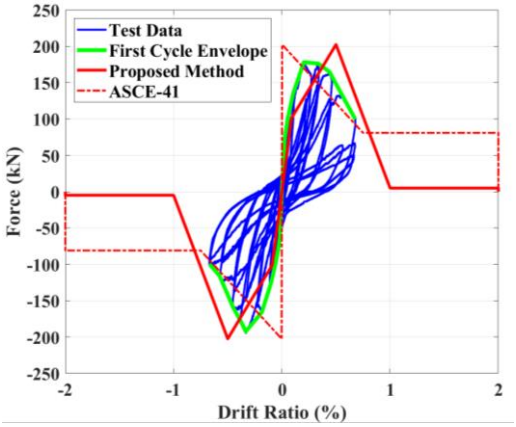

Auck-02

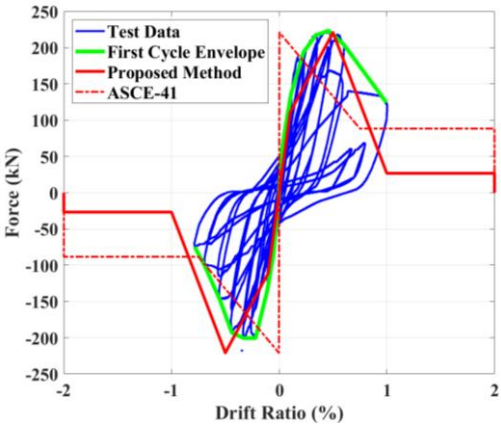

Auck-04

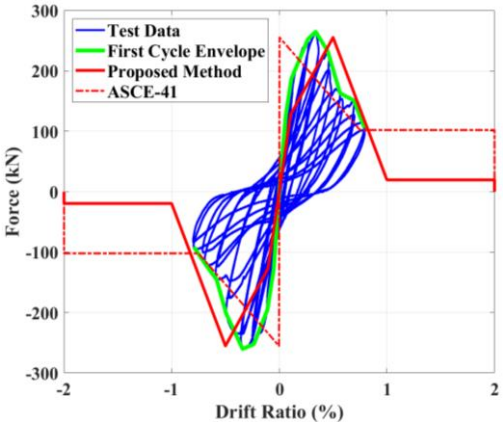

Auck-07

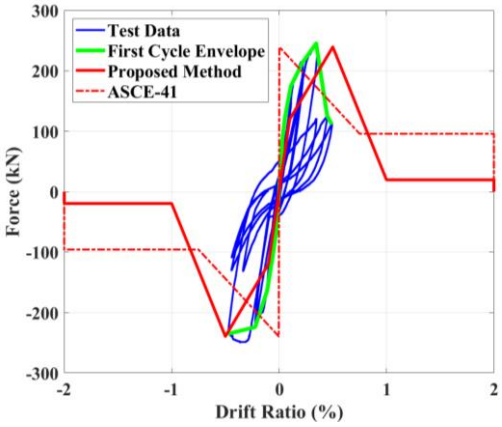

Auck-08

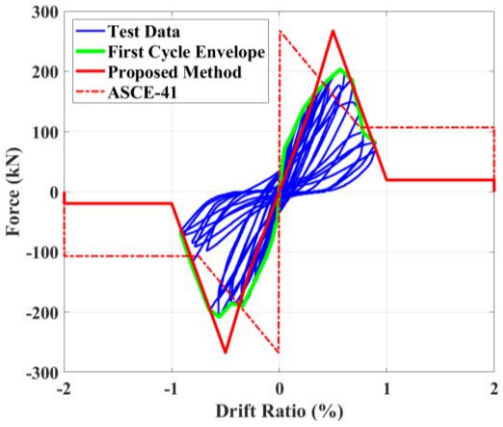

Auck-09

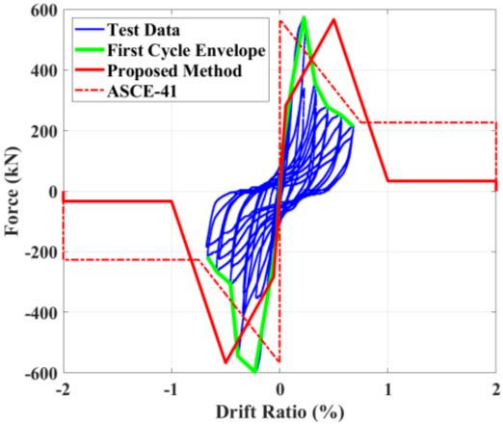

Auck-10

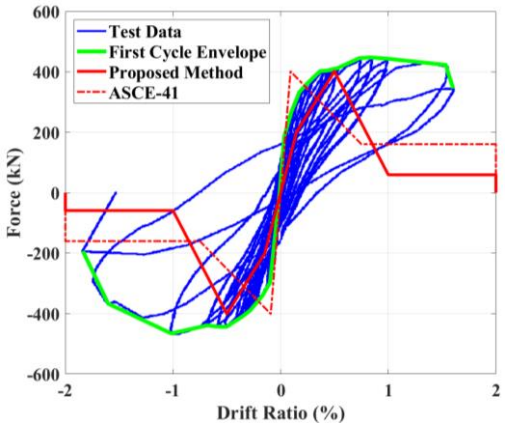

CU-3

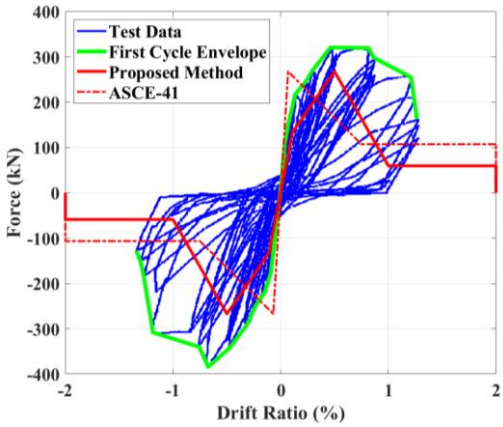

CU-4

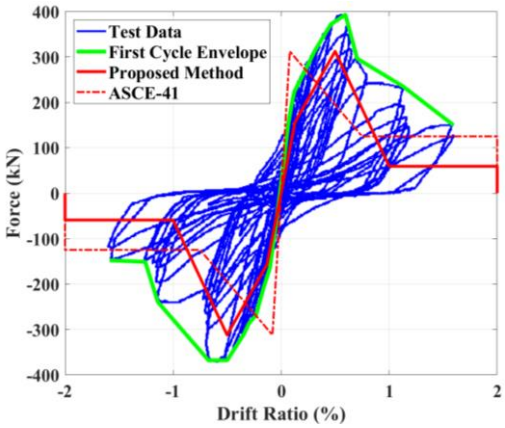

CU-5

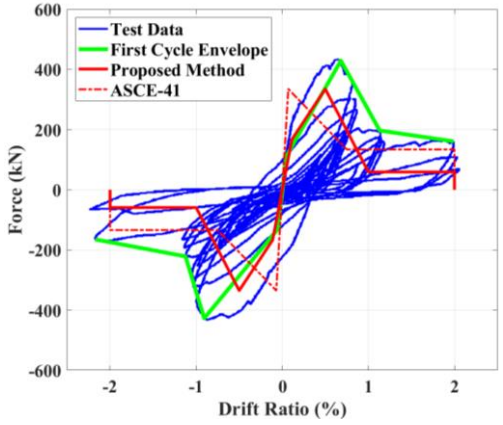

CU-7

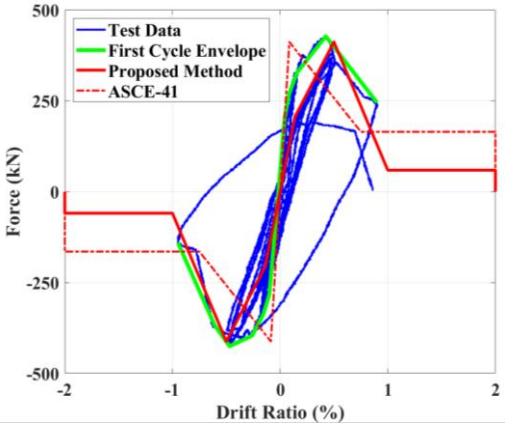

CU-9

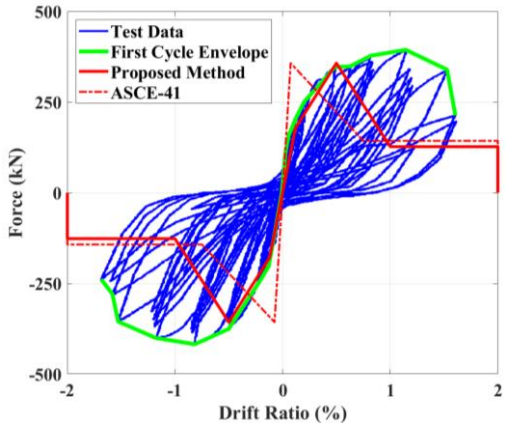

CU-11

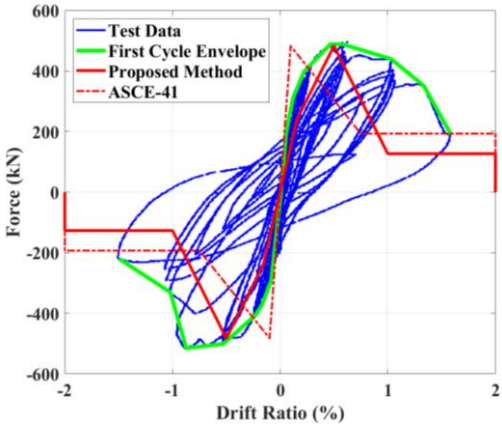

CU-13

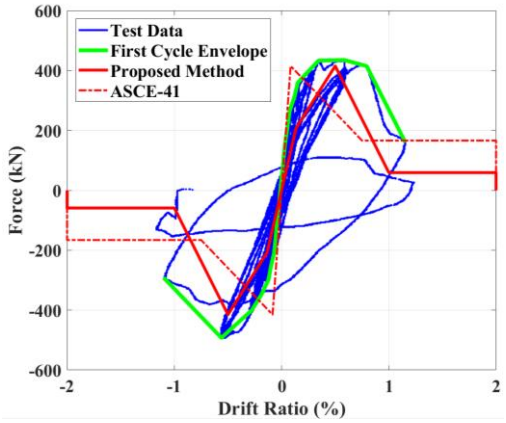

CU-14

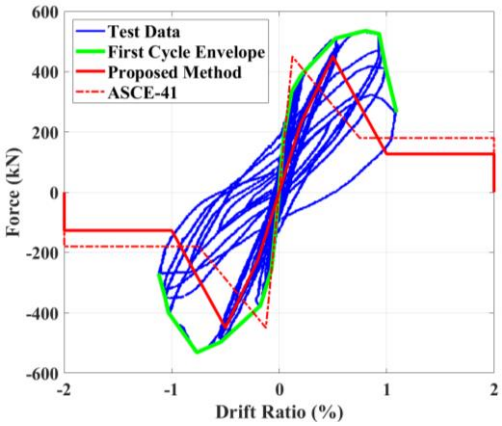

CU-16

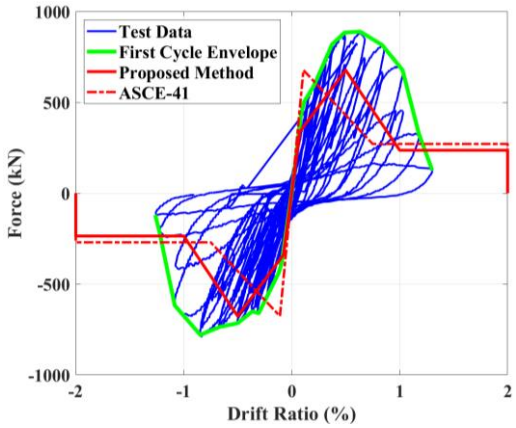

UT-PBS-01

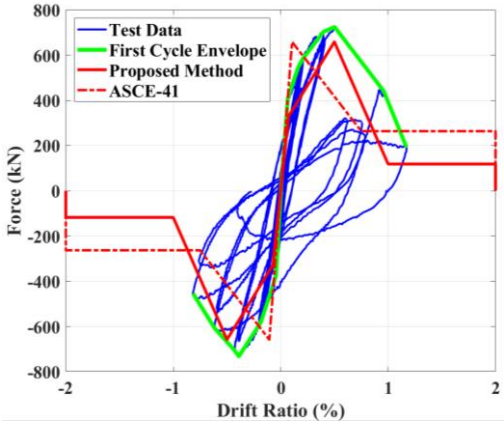

UT-PBS-02

APPENDIX IV COMPARISON OF NUMERICAL RESULTS WITH TEST DATA FOR SHEAR-DOMINATED PLANAR WALLS

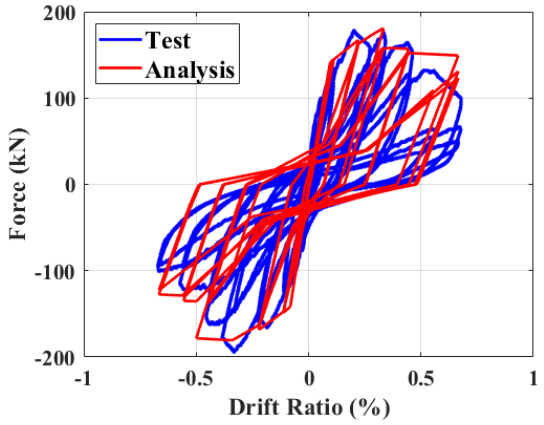

Auck-02

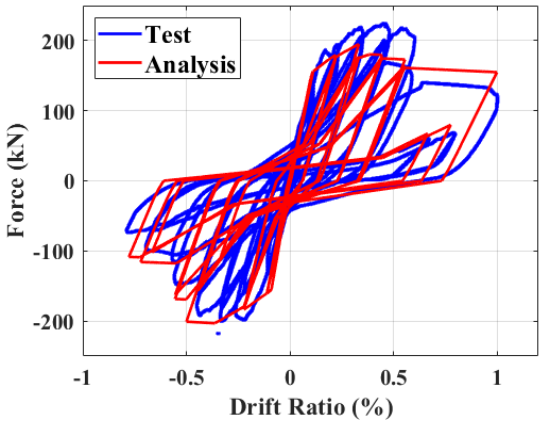

Auck-04

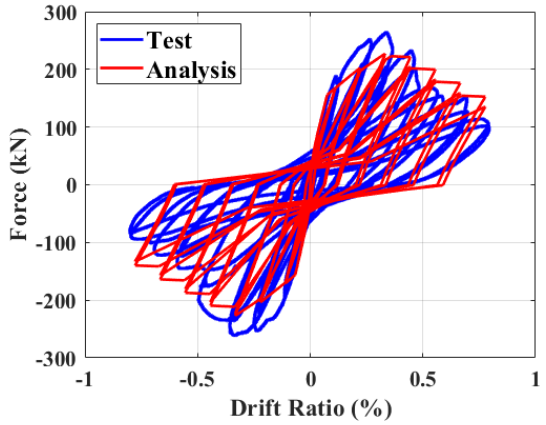

Auck-07

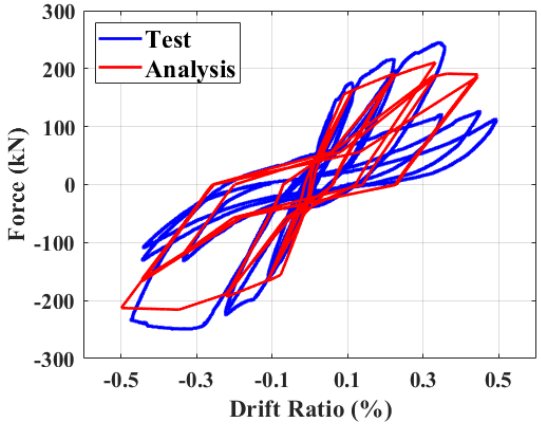

Auck-08

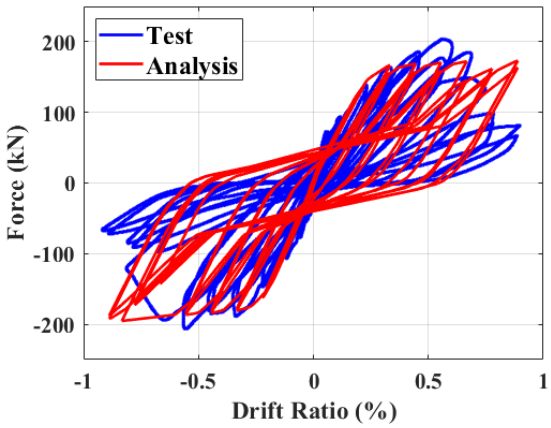

Auck-09

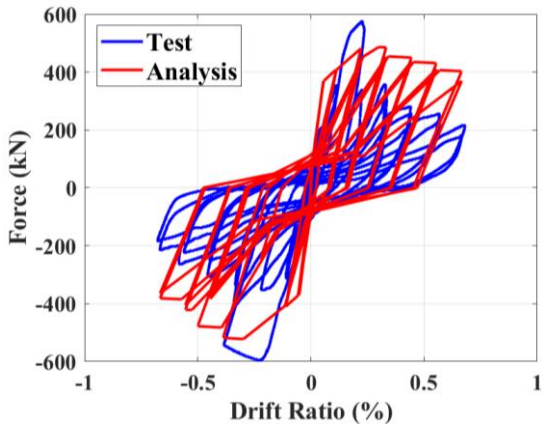

Auck-10

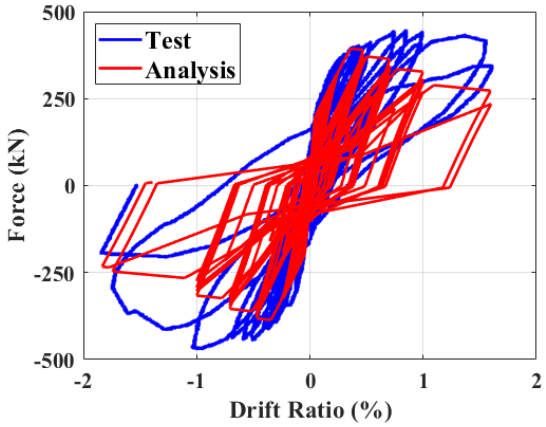

CU-3

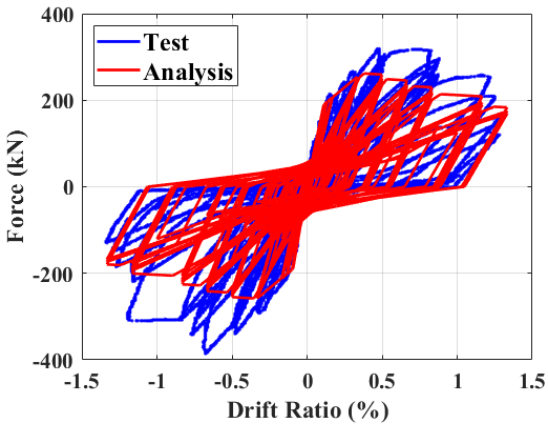

CU-4

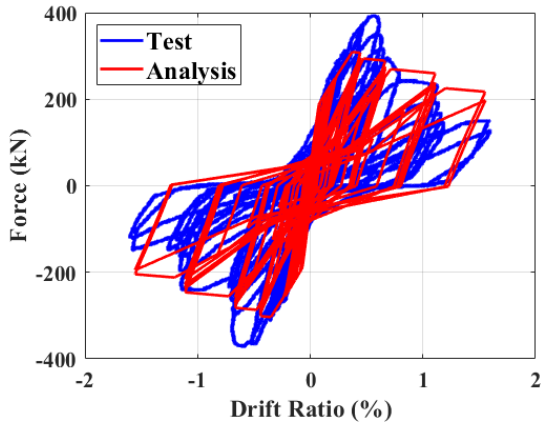

CU-5

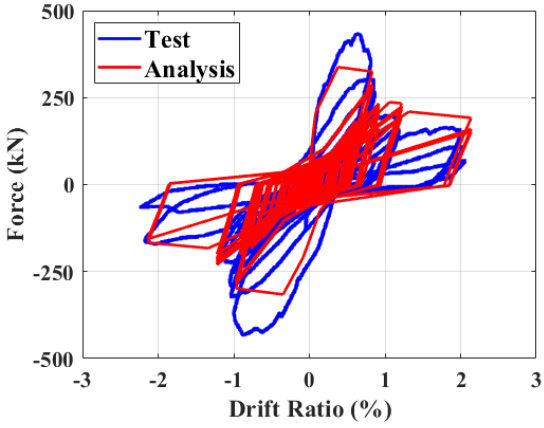

CU-7

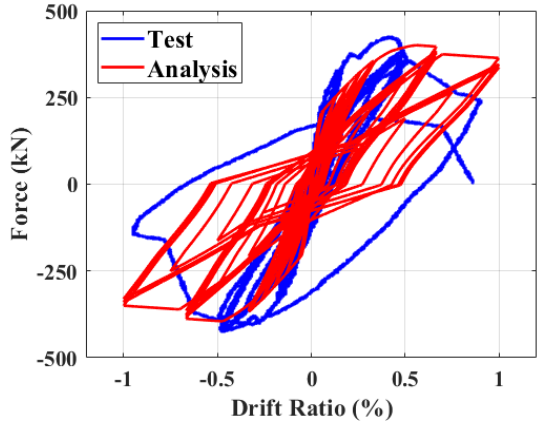

CU-9

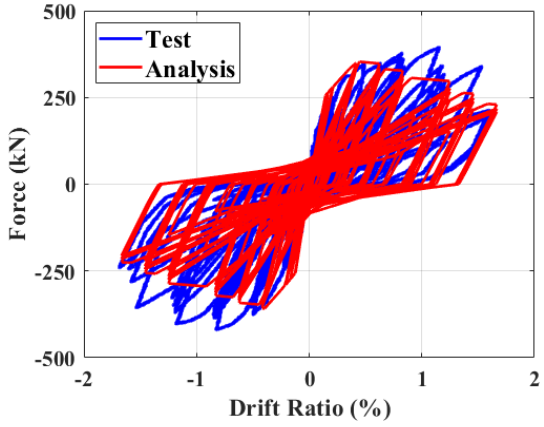

CU-11

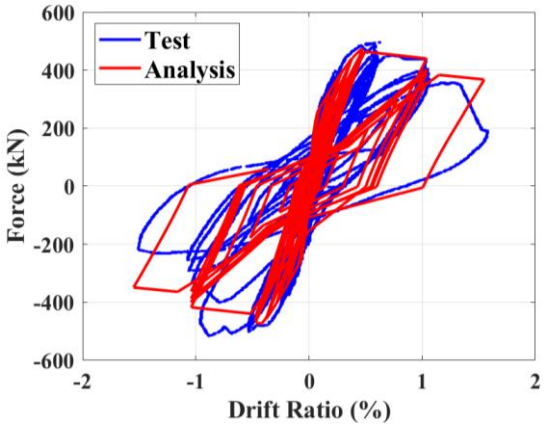

CU-13

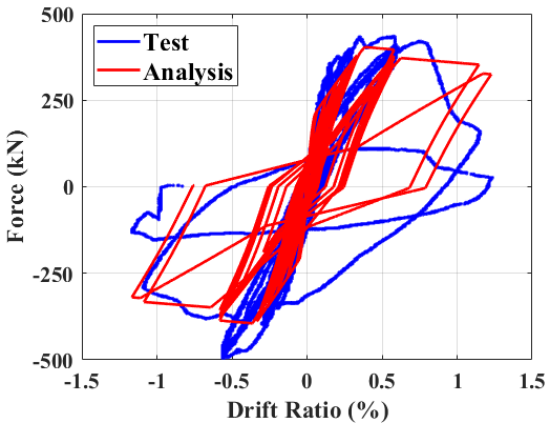

CU-14

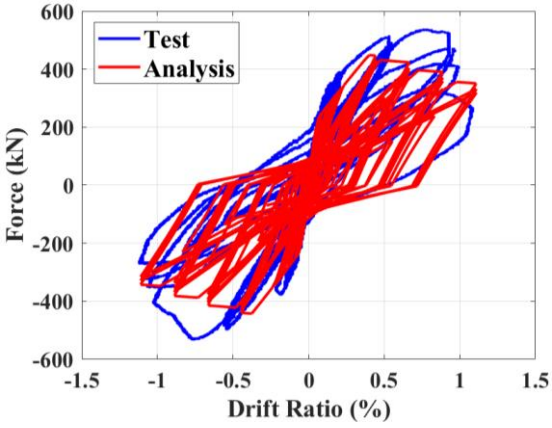

CU-16

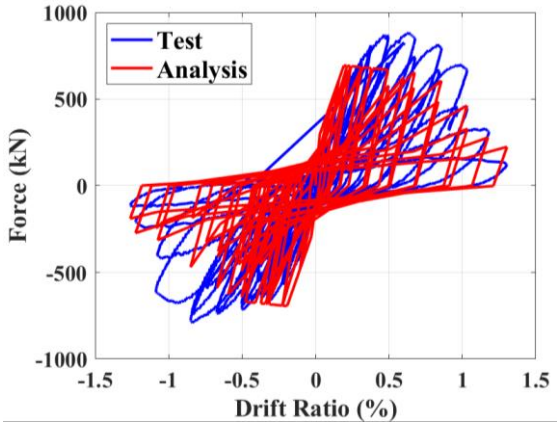

UT-PBS-01

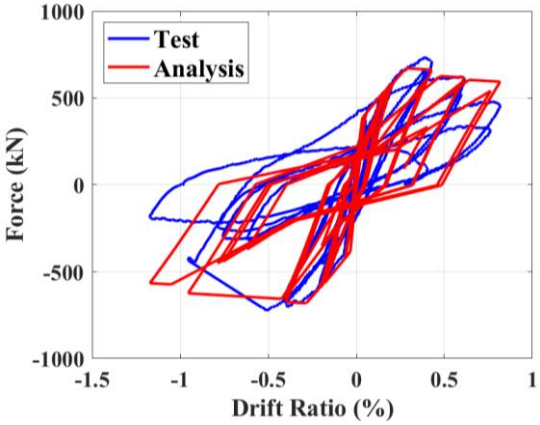

UT-PBS-02

REFERENCES

ACI Committee. *Building Code Requirements for Structural Concrete (ACI 318-14) and Commentary (ACI 318R-14).* American Concrete Institute, Farmington Hills, MI, 2014

Ahmadi, F. *Displacement-based seismic design and tools for reinforced masonry shear-wall structures*. Ph.D. Dissertation, Department of Civil Engineering, University of Texas at Austin, Austin, TX, 2012.

ASCE 7-16. *Minimum Design Loads and Associated Criteria for Buildings and Other Structures*, American Society of Civil Engineers, Reston, VA,2017.

ASCE/SEI 41-17. *Seismic evaluation and retrofit of existing buildings.*, American Society of Civil Engineers, Reston, VA, 2017.

Ashour, A., El-Dakhakhni, W., and Shedid, M. Experimental evaluation of the system-level seismic performance and robustness of an asymmetrical reinforced concrete block building. *J Struct Eng.* 2016, Apr 26;142(10):04016072.

ASTM A615/A615M-09b: *Standard Specification for Deformed and Plain Carbon-steel Bars for Concrete Reinforcement*. ASTM, West Conshohocken, PA, 2009.

Atkinson, R. H., and Kingsley, G. R. A comparison of the Behavior of Clay and Concrete Masonry in Compression. Atkinson-Noland & Associates, 1985.

Banting, B. R., and El-Dakhakhni, W. W. "Force-and displacement-based seismic performance parameters for reinforced masonry structural walls with boundary elements". *J Struct Eng.* 2012, 138(12):1477-91.

Banting, B. R., and El-Dakhakhni, W. W. Seismic performance quantification of reinforced masonry structural walls with boundary elements. *J Struct Eng.* 2014, 140(5):04014001.

Bažant, Z. P., and Oh, B. H. "Crack Band Theory for Fracture of Concrete." *Mater. & Struct*. 1983, 16: 155-177.

Bolhassani, M. *Improvement of Seismic Performance of Ordinary Reinforced Partially Grouted Concrete Masonry Shear Walls.* PhD Dissertation, Drexel University, Philadelphia, PA, 2015.

Ceresa, P., Petrini, L., Pinho, R., and Sousa, R. A fibre flexure–shear model for seismic analysis of RC-framed structures. E*arthq Eng Struct Dyn.* 2009;38(5):565-86.

Cheng, J., and Shing, P. B. *Proposed Update of Nonlinear Models for Reinforced Masonry Shear Walls in ASCE 41.* 11th National Conference on Earthquake Engineering, CA, 2018.

Coleman, J. and Spacone, E. Localization Issues in Forced-Based Frame Elements. *J Struct Eng*. 2001; 127(11): 1257-1265.

D'Ambrisi, A., and Filippou, F. C. Modeling of cyclic shear behavior in RC members. *J Struct Eng.* 1999;125(10):1143-50.

De Souza, R. M. *Force-based finite element for large displacement inelastic analysis of frames.* PhD Dissertation, University of California Berkeley, Berkeley, CA, 2000.

Ezzeldin, M., Wiebe, L., and El-Dakhakhni, W. Seismic collapse risk assessment of reinforced masonry walls with boundary elements using the FEMA P695 methodology. *J Struct Eng.* 2016; 142(11):04016108.

Ezzeldin, M., El-Dakhakhni, W., and Wiebe, L. Reinforced masonry building seismic response models for ASCE/SEI-41. *J Struct Eng*. 2018; 144(1):04017175.

FEMA. *NEHRP Quantification of Building Seismic Performance Factors.* FEMA P695, Federal Emergency Agency: Washington, DC, 2009.

He, L., and Priestley, N. J. *Seismic behaviour of flanged masonry shear walls*. Final report, US-Japan Coordinated Program for Masonry Building Research, Department of Applied Mechanics and Engineering Sciences, University of California San Diego, CA, USA. 1992.

Heerema, P., Shedid, M., Konstantinidis, D., and El-Dakhakhni, W. System-level seismic performance assessment of an asymmetrical reinforced concrete block shear wall building. *J Struct Eng*. 2015 Mar 13;141(12):04015047.

Ibarra, L. F., Medina, R. A., and Krawinkler, H. Hysteretic models that incorporate strength and stiffness deterioration. *Earthq Eng Struct Dyn*. 2005 Oct;34(12):1489-511.

Kapoi, C. M. *Experimental performance of concrete masonry shear walls under in-plane loading flexure-dominated wall tests*. Master Thesis, Washington State University, Pullman, Washington, 2012.

Kent, D. C., and Park, R. Flexural members with confined concrete. *J Struct Div*. 1971.

Kolozvari, K., Orakcal, K., and Wallace, J. W. Modeling of cyclic shear-flexure interaction in reinforced concrete structural walls. I: Theory. *J Struct Eng*. 2015 May 1;141(5):04014135.

Koutras, A. A. *Assessment of the seismic behavior of fully and partially grouted reinforced masonry structural systems through finite element analysis and shake-table testing.* PhD Dissertation, University of California San Diego, La Jolla, CA, 2019.

Koutras, A. A., and Shing, P. B. Seismic behavior of a partially grouted reinforced masonry structure: Shake-table testing and numerical analyses. *Earthq Eng Struct Dyn*. 2020;49:1115-1136.

Koutras, A. A., and Shing, P. B. Finite-element modeling of the seismic response of reinforced masonry wall structures. *Earthq Eng Struct Dyn.* 2021 Apr;50(4):1125-46.

Koutromanos, I., and Shing, P. B. Cohesive crack model to simulate cyclic response of concrete and masonry structures. *ACI Struct J*. 2012; 109(3):349-355.

Lotfi, H. R., and Shing, P. B. An appraisal of smeared crack models for masonry shear wall analysis. *Comput Struct*. 1991;41(3):413-425.

Lourenço, P. B., Avila, L., Vasconcelos, G., Alves, J. P., Mendes, N., and Costa, A. C. Experimental investigation on the seismic performance of masonry buildings using shaking table testing. *Bull Earthquake Eng*. 2013 Aug 1;11(4):1157-90.

Lu, Y., and Panagiotou, M. Three-dimensional cyclic beam-truss model for nonplanar

reinforced concrete walls. *J Struct Eng*. 2014 Mar 1;140(3):04013071.

Martinelli, L. Modeling shear-flexure interaction in reinforced concrete elements subjected to cyclic lateral loading. *ACI Struct J*. 2008 Nov 1;105(6):675.

Mavros, M. *Experimental and Numerical Investigation of the Seismic Performance of Reinforced Masonry Structures.* PhD Dissertation, University of California San Diego, La Jolla, CA, 2015.

Mavros, M., Ahmadi, F., Shing, P. B., Klingner, R. E., McLean, D., and Stavridis, A. Shake-table tests of a full-scale two-story shear-dominated reinforced masonry wall structure. *J Struct Eng*. 2016 May 3;142(10):04016078.

Mazzoni, S., McKenna, F., and Fenves, G. L. *OpenSees command language manual*. Pacific Earthquake Engineering Research (PEER) Center, 264, 2005.

McKenna, F. OpenSees: a framework for earthquake engineering simulation. *Comp Sci Eng*. 2011 Jun 27;13(4):58-66.

McKenna, F., Fenves, G. L., and Scott, M. H. *Open system for earthquake engineering simulation*. University of California, Berkeley, CA, 2000.

Merryman, K. M., Leiva, G., Antrobus, N., and Klingner, R. E. *In-plane seismic resistance of two-story concrete masonry coupled shear walls*, Report No. 3.1(c)-1, US-Japan Coordinated Program for Masonry Building Research, University of Texas at Austin, Austin, TX, 1990.

Minaie, E., Mota, M., Moon, F. L., and Hamid, A. A. In-plane behavior of partially grouted reinforced concrete masonry shear walls. *J Struct Eng.* 2010, 136(9), 1089-1097.

Mojiri, S., El-Dakhakhni, W. W., and Tait, M. J. Shake table seismic performance assessment of lightly reinforced concrete block shear walls". *J Struct Eng*. 2015; 141(2):04014105.

NIST. *Evaluation of the FEMA P-695 methodology for quantification of building seismic performance factors.* NIST GCR 10-917-9, National Institute of Standards and Technology, Gaithersburg, MD, 2010.

NIST. *Recommended modeling parameters and acceptance criteria for nonlinear analysis in support of seismic evaluation, retrofit, and design.* NIST GCR 17-917-45, National Institute of Standards and Technology, Gaithersburg, MD, 2017.

Orakcal, K., and Wallace, J. W. Flexural modeling of reinforced concrete walls-experimental verification. *ACI Mat J.* 2006 Mar 1;103(2):196.

Paulay, T., and Priestley, M. J. N. *Seismic design of reinforced concrete and masonry buildings.* 1992.

Peruch, M., Spacone, E., and Shing, P. B. Cyclic analyses of reinforced concrete masonry panels using a force-based frame element. *J Struct Eng*. 2019;145(7):04019063.

Petrangeli, M., Pinto, P. E., and Ciampi, V. Fiber element for cyclic bending and shear of RC structures. I: Theory. *J Eng Mech*. 1999 Sep;125(9):994-1001.

Petrangeli, M. Fiber element for cyclic bending and shear of RC structures. II: Verification. *J Eng Mech*. 1999 Sep;125(9):1002-9.

Priestley, M. J. N., Calvi, G., and Kowalsky, M. *Displacement-based seismic design of structures*, Istituto Universitario di Studi Superiori (IUSS), Pavia, Italy, 2007.

Saritas, A., and Filippou, F. C. Analysis of RC walls with a mixed formulation frame finite element. *Comp Concrt*. 2013 Oct 1;12(4):519-36.

Saritas, A., and Filippou, F. C. Numerical integration of a class of 3d plastic-damage concrete models and condensation of 3d stress-strain relations for use in beam finite elements. *Eng Struct.* 2009 Oct 1;31(10):2327-36.

Scott, M. H., and Fenves, G. L. Plastic hinge integration methods for force-based beam–column elements. *J Struct Eng*. 2006; 132(2):244-52.

Seible, F., Priestley, M. J., Kingsley, G. R., and Kürkchübasche, A. G. Seismic Response of Full-scale Five-story Reinforced-Masonry Building. *J Struct Eng*. 1994 Mar;120(3):925-46.

Shedid, M. T., Drysdale, R. G., and El-Dakhakhni, W. W. Behavior of fully grouted reinforced concrete masonry shear walls failing in flexure: Experimental results. *J Struct Eng*. 2008 Nov;134(11):1754-67.

Shedid, M. T., and El-Dakhakhni, W. W. Plastic hinge model and displacement-based seismic design parameter quantifications for reinforced concrete block structural walls. *J Struct Eng*. 2014; 140(4):04013090.

Sherman, J. D. *Effects of key parameters on the performance of concrete masonry shear walls under in-plane loading.* Master Thesis, Washington State University, Pullman, Washington, 2011.

Shing, P. B., Schuller, M. P., and Hoskere, V. S. In-Plane Resistance of Reinforced Masonry Shear Walls, *J Struct Eng*. Reston, VA, Vol. 116, No. 3, March 1990b, pp. 619-640.

Shing, P. B., Noland, J. L., Spaeh, H. P., Klamerus, E. W., and Schuller, M. P. *Response of single-story reinforced masonry shear walls to in-plane lateral loads*. Department of Civil, Environmental and Architectural Engineering University of Colorado, Boulder, CO, 1991.

Siyam, M. A., El-Dakhakhni, W. W., Shedid, M. T., and Drysdale, R. G. Seismic response evaluation of ductile reinforced concrete block structural walls. I: Experimental results and force-based design parameters. *J Perf Const Fac.* 2016; 30(4):04015066.

Spacone, E., Filippou, F. C., and Taucer, F. F. Fibre beam–column model for non-linear analysis of R/C frames: Part I. Formulation. *Earthq Engrg & Struct Dyn.* 1996; 25(7):711-25.

Spacone, E., Filippou, F. C., and Taucer, F. F. Fibre beam–column model for non-linear analysis of R/C frames: part II. Applications. *Earthq Engrg & Struct Dyn.* 1996; 25(7):727-42.

Stavridis, A., Ahmadi, F., Mavros, M., Shing, P. B., Klingner, R. E., and McLean, D. Shake-table tests of a full-scale three-story reinforced masonry shear wall structure. *J Struct Eng.* 2016 Apr 28;142(10):04016074.

Stavridis, A., and Shing, P. B. Finite-element modeling of nonlinear behavior of masonry-infilled RC frames. *J Struct Eng.* 2010;136(3):285-96.

Taylor, R. L., Filippou, F. C., Saritas, A., and Auricchio, F. A mixed finite element method for beam and frame problems. *Comp Mech*. 2003 May 1;31(1-2):192-203.

Thomsen, J. H., and Wallace, J. W. *Displacement-based design of RC structural walls: an experimental investigation of walls with rectangular and T-shaped cross-sections*. Clarkson University, Department of Civil Engineering; 1995.

TMS 402/602. *Building Code Requirements for Masonry Structures*. The Masonry Society, Boulder, CO. 2016.

Tomaževič, M., Lutman, M., and Petković, L. Seismic behavior of masonry walls: experimental simulation. *J Struct Eng*. 1996 Sep;122(9):1040-7.

Tomaževič, M., and Weiss, P. Seismic behavior of plain-and reinforced-masonry buildings. *J Struct Eng*. 1994 Feb;120(2):323-38.

Voon, K. C., and Ingham, J. M. Experimental in-plane shear strength investigation of reinforced concrete masonry walls. *J Struct Eng*. 2006 Mar;132(3):400-8.